GEOCHEMISTRY AND PETROLOGY OF DIORITIC ROCKS FROM AUR ISLAND, MERSING, JOHOR

FATIN 'IZZANI HAZAD

FACULTY OF SCIENCE
UNIVERSITY OF MALAYA
KUALA LUMPUR

2015

GEOCHEMISTRY AND PETROLOGY OF DIORITIC ROCKS FROM AUR ISLAND, MERSING, JOHOR

FATIN 'IZZANI HAZAD

THESIS SUBMITTED IN FULFILMENT OF THE REQUIREMENTS FOR THE DEGREE OF MASTER OF SCIENCE

DEPARTMENT OF GEOLOGY
FACULTY OF SCIENCE
UNIVERSITY OF MALAYA
KUALA LUMPUR

2015

UNIVERSITY OF MALAYA

ORIGINAL LITERARY WORK DECLARATION

Name of Candidate: (I.C/Passport No:)

Registration/Matric No:

Name of Degree:

Title of Project Paper/Research Report/Dissertation/Thesis ("this Work"):

Field of Study:

I do solemnly and sincerely declare that:

(1)   I am the sole author/writer of this Work;
(2)   This Work is original;
(3)   Any use of any work in which copyright exists was done by way of fair dealing and for permitted purposes and any excerpt or extract from, or reference to or reproduction of any copyright work has been disclosed expressly and sufficiently and the title of the Work and its authorship have been acknowledged in this Work;
(4)   I do not have any actual knowledge nor do I ought reasonably to know that the making of this work constitutes an infringement of any copyright work;
(5)   I hereby assign all and every rights in the copyright to this Work to the University of Malaya ("UM"), who henceforth shall be owner of the copyright in this Work and that any reproduction or use in any form or by any means whatsoever is prohibited without the written consent of UM having been first had and obtained;
(6)   I am fully aware that if in the course of making this Work I have infringed any copyright whether intentionally or otherwise, I may be subject to legal action or any other action as may be determined by UM.

Candidate's Signature   Date:

Subscribed and solemnly declared before,

Witness's Signature   Date:

Name:

Designation:

ABSTRACT

Smaller granitoid occurrences of Late Cretaceous magmatism can be identified in the Central and Eastern Belts of Peninsular Malaysia. Study area, Aur and its surrounding islands (Dayang and Lang), is located 65km east coast off Mersing, Johor are the most easterly exposed Eastern Belt granitoids. The dioritic rocks from the study area have been dated as Late Cretaceous age (~80±1Ma), and the lithology of these islands consists entirely of plutonic rocks, without any observation of volcanic or metamorphic rock. Aur diorite was classified using QAP modal percentages, and the rocks fall into diorite, quartz monzodiorite and granodiorite field. Aur composite pluton can be distinguished into two members; mafic-end member: diorite and quartz monzodiorite (SiO_2: 54.6-59 wt.%) and the felsic-end member: granodiorite (SiO_2: 61-65.7 wt.%). The mafic-end members: diorite and quartz monzodiorite show the typical ophitic and sub-ophitic texture often found in mafic rock, with their major mafic phase are made of clinopyroxene and orthopyroxene, with minor biotite and hornblende. The felsic-end member: granodiorite shows a markedly different observation. Granodiorite has the typical hypidiomorphic granular texture, with hornblende and biotite as its major mafic phase. The contact between these two different members could not be distinguished clearly in the field but the rocks are gradational from a more mafic composition at the northern part of Aur Island to a more felsic composition at the southern and central part of the island. Aur pluton displays mafic and felsic magma interaction with the presence of rounded to ellipsoidal MME heterogeneously distributed throughout the pluton. Magma mixing texture; anti-rapakivi can only be observed in granodiorite, suggesting that there may have been an interaction between these two magmas at one point during magmatic evolution. Generally, the pluton is I-type, metaluminous with the mafic-end member showing high-K calc-alkaline trend while the felsic-end member shows shoshonitic trend. Both members show distinct geochemical differences on Harker diagram and the chondrite

normalized REE patterns are fractionated [(La/Yb)N=6.52-11.92] with weak negative Eu anomalies (Eu/Eu*=0.602-1.008). Both members show variable depletion at Rb, P, Zr, Sm and Eu, with a pronounced negative Nb and Ti anomaly. LIL modelling show that the mafic-members magmatic evolution are controlled by clinopyroxene, hornblende and plagioclase; and the felsic-end magmatic evolution are controlled by plagioclase, K-feldspar and biotite. A multi sources and different origins for both end members can be seen from geochemical and petrographic evidences, suggesting they were probably made up of individual batches of melt. However, continuous trend seen for both members on Rb/Sr vs SiO$_2$, Sr vs CaO and REE patterns suggests that a connection exist between all of the rocks at some stage of their magmatic evolution. Geochemical plots, petrographic evidence and presence of MME rule out pure crustal derived magma genesis and suggest mixed-origin of magma generations.

ABSTRAK

Magmatism Kretaceous lewat dapat dikenal pasti di beberapa lokasi di Jalur Tengah dan Timur wilayah granitoid Semenanjung Malaysia. Kawasan kajian, Aur dan pulau sekitarnya (Dayang dan Lang) terletak 65km dari pesisir pantai Mersing, Johor, adalah batuan Jalur Timur yang paling jauh. Batuan dioritik Aur telah ditarikhkan sebagai Lewat Kretaceous (~80Ma), dan batuan di kawasan kajian cuma terdiri daripada batuan dioritik tanpa kehadiran batuan volkanik atau metamorfik. Batuan dioritik Aur dikenal pasti melalui modal peratusan QAP, dan ia terdiri daripada diorit, kuarza monzodiorit dan granodiorite. Pluton Aur yang pelbagai boleh dikenal pasti kepada dua komposisi berbeza iaitu: ahli mafik yang terdiri daripada: diorit dan kuarza monzodiorite (SiO_2: 54.6-59%), dan ahli felsik: granodiorite (SiO_2: 61-65.7%). Ahli mafik: diorit dan kuarza monzodiorite menunjukkan tekstur ophitik dan sub-ophitik yang sering dijumpai dalam batuan mafik, dengan fasa mafik utama mereka adalah klinopyroxene dan orthopyroxene. Ahli yang lebih felsik: granodiorit menunjukkan pemerhatian petrogafi yang berbeza, ia mempunyai tekstur berbutir hypidiomorphik granular, dengan fasa mafik utama mereka adalah hornblende dan biotit. Batuan dioritik Pulau Aur berubah daripada komposisi mafik di utara Pulau Aur terhadap komposisi yang lebih felsik di bahagian selatan dan tengah pulau. Aur Pluton menunjukkan bukti interaksi magma mafik dan felsik dengan kehadiran elipsoid enclaves (MME) dijumpai di lapangan. Mikrotekstur percampuran magma; anti-rapakivi hanya boleh diperhatikan dalam granodiorite, menunjukkan bahawa ada interaksi antara kedua-dua magma pada satu ketika semasa evolusi magmatik. Secara umumnya, batuan dioritik Pulau Aur adalah jenis 'I', metaluminous dengan ahli mafic akhir menunjukkan tren tinggi K-Calc-alkali manakala ahli felsic akhir menunjukkan trend shoshonitik. Keduanya menunjukkan perbezaan geokimia di gambarajah Harker. Tren REE chondrite menunjukkan pemeringkatan berperingkat [$(La/Yb)N$= 6.52-11.92] dengan anomali Eu negatif yang kecil (Eu/Eu^*= 0.602-1.008). Kedua-dua ahli mafik dan

felsik akhir menunjukkan anomali negatif berbeza pada Rb , P, Zr , Sm dan Eu , dengan anomali negatif Nb dan Ti yang ketara. Keduanya dikawal oleh pengfraksian mineral yang berbeza (ahli mafik: klinopyroxene, plagioclase, hornblende, dan ahli felsik: plagioclase, biotite, K-feldspar). Sumber yang pelbagai dan asal-usul yang berbeza untuk kedua-dua anggota akhir boleh dilihat dari bukti-bukti geokimia dan petrografi, menunjukkan mereka berasal daripada nadi magma yang berbeza. Bagaimanapun, tren berterusan yang dapat dilihat pada plot seperti Rb/Sr vs. SiO_2, Sr vs. CaO dan tren REE menunjukkan ada hubungan di antara kedua ahli pada satu tahap evolusi magma. Plot geokimia, data petrografi dan kehadiran MME menolak asalan tulen kerak bumi sebagai sumber magma, tetapi mencadangkan sumber magma adalah daripada generasi percampuran antara dua magma, iaitu mantel dan kerak bumi.

ACKNOWLEDGEMENTS

To my supervisor, Prof. Dr. Azman Abd Ghani.

Your neverending dedications and guidance, though having such a troubled student amazed me. May Allah shows His mercy upon you and your family, may you be guided and rewarded with a castle in Jannah.

To my late father, ibu, family, close friends, and lecturers;

I pray that Allah will always be guiding all of us,

That the mirage of this dunya will not own our hearts,

And one day we will all return to Him with peace in our hearts.

To Ahmad Faiz,

Thank you for being, my husband.

To **you**,

May the love, and compassions you give to others come back to you tenfold.

I pray good things will always come to you.

Ameen Ya Rabb.

<div align="right">

With good thoughts and love,

Fatin Hazad.

</div>

TABLE OF CONTENTS

LIST OF FIGURES

LIST OF TABLES

LIST OF APPENDICES

CHAPTER 1: INTRODUCTION

1.1   Introduction

This chapter briefly describes the study area, objectives of study, methodology, and overall thesis framework. Objectives mentioned in this chapter are foundations for the contents that will be discussed thoroughly in the next chapters.

1.2   Study Area

Granitoid provinces of Peninsular Malaysia have petrological and geochronological characteristics that allow them to be divided into three belts of north-south elongated provinces (Figure. 1.1), which is the; (1) Western Belt Main Range granite, (2) Central Belt and (3) Eastern Belt granite province (Hutchison and Tan, 2009). Smaller occurrences of Cretaceous plutons with I-type affinities are also commonly found within the Central and Eastern Belt granitoid province. Aur Island, a small circular pluton located southeast coast of Mersing, Johor, which is the most easterly exposed of the Eastern Belt granitoid provinces will be the main focus in this research.

Aur Island that lies about 65 km from mainland Mersing, Johor, is part of the group of islands archipelago along the east coast of Johor (Figure 1.2). These groups of islands offshore of Johor consist of famous islands such as Tioman, Pemanggil, Sibu, Rawa and Tinggi have been well known as a major tourist attraction and has been appointed as a preserved national park. There is a smaller island up north, Dayang Island, which is separated from Aur Island by a narrow channel of about 400 m width at the narrowest point (Figure 1.3). There are also two nearby islets, Pinang and Lang Islands, located southeast and northwest respectively from Pulau Aur. The rocks from Dayang and Lang Island will also be included in this study.

Covering approximately 20km^2 areas, the lithology of these islands consists entirely of plutonic rocks without any association of volcanic, metamorphic or sedimentary rocks. Almost 80% of Aur Island is bounded by a hilly topography, covered with tropical rain forests. Along the coastline, Quaternary sediments of beach deposits can be found together with agricultural plots of coconut trees. Detailed geological accounts of study area will be described further on Chapter Two.

1.3   Objectives of Study

The main objectives of study that will be the guidelines in conducting this research are:

  i.   To systematically study the petrology and geochemical aspects of the dioritic rocks from study area.

  ii.   To compare the petrogenesis of dioritic rocks of Pulau Aur and Pulau Pemanggil based on the geochemical data.

  iii.   Interpreting the petrogenesis of the dioritic rocks based on petrography and geochemical results.

Data accumulated and conclusions derived from this study will contribute towards a better understanding of the petrogenesis, geochemistry, and finally the tectonic and geological history of the study area.

1.4   Methodology

Methods used in conducting this research study involved desk study, field work and laboratory work. Desk study involves doing literature review, reviewing previous published and unpublished works about the study area, studying maps, and aerial photographs of the study area. Literature review is done prior to field work as an early preparation before going to the field. Field works were carried out in two ways: (1)

geological mapping of study area by using tape and compass traversing method, (2) collecting rock samples while traversing across the study area. Geological mapping was carried out, and rock samples for petrography and geochemical analysis were collected.

Lab analysis is the next important method where selected samples that have been crushed into powder form were analysed to obtain geochemical data for major elements, trace elements and rare earth elements (REE) by using the X-Ray Fluorescence (XRF method) and Inductive Coupled Plasma Spectrometry (ICPMS method). Some of these selected samples were made into thin section for petrographic analysis. By using the thin section, the petrography of the rock were analysed and microphotograph of the rock will be taken, as it will be useful in the petrogenetic study of the rock. Modal analyses of the rocks were made by using mechanical point counter together with petrographic observation. The analysed data from both petrography and geochemical analysis are discussed and interpreted in term of the rocks petrogenesis and magma evolution.

1.5 Previous Works

Not many detailed studies have been done in this area. Tan (1977) stated that the earliest recorded geological account of the area was written by Willbourn (1926). Willbourn (1926) stated that Pulau Aur is dominated by hornblende granite in which some parts, contains pyroxene and also grades into syenites. A 1957 Malaysian Geological Survey map shows that Pulau Aur to be built of syenite. A revised edition published in 1972 indicates that Pulau Aur are made up of diorites. Tan (1977) also stated that Pulau Aur is made up of quartz diorite, quartz monzonite and quartz syenite, and texturally, the diorite found is different from the quartz diorite of Pulau Pemanggil. The study made by Tan (1977) however focuses more on the geochemical analysis of seafloor sediment of Pulau Aur and surrounding islands such as Pulau Tioman and Pulau Pemanggil, not the igneous petrology, petrogenesis and geochemical studies of igneous rock at Pulau Aur.

1.6   Thesis Framework

Chapter Two will discussed the general geology and field relation of study area. Petrographic observation of the rocks from study area, the classification and description of the rocks based on macroscopic and microscopic observation, and the differences between the varieties of rocks found will be described thoroughly in Chapter Three. Chapter Four will discussed the results obtained from the geochemical analysis of the rocks, the major elements, trace elements and rare earth element. Description of various geochemical plots and the discussion of geochemical aspects will also be discussed. Chapter Five will be focusing on the comparison of the dioritic rocks from the study area, with the dioritic rocks from nearby island, Pulau Pemanggil. The last chapter, Chapter Six is the discussion and conclussions where the magmatic processes involved, petrogenesis and the possible tectonic setting for Aur dioritic rocks will be discussed and concluded.
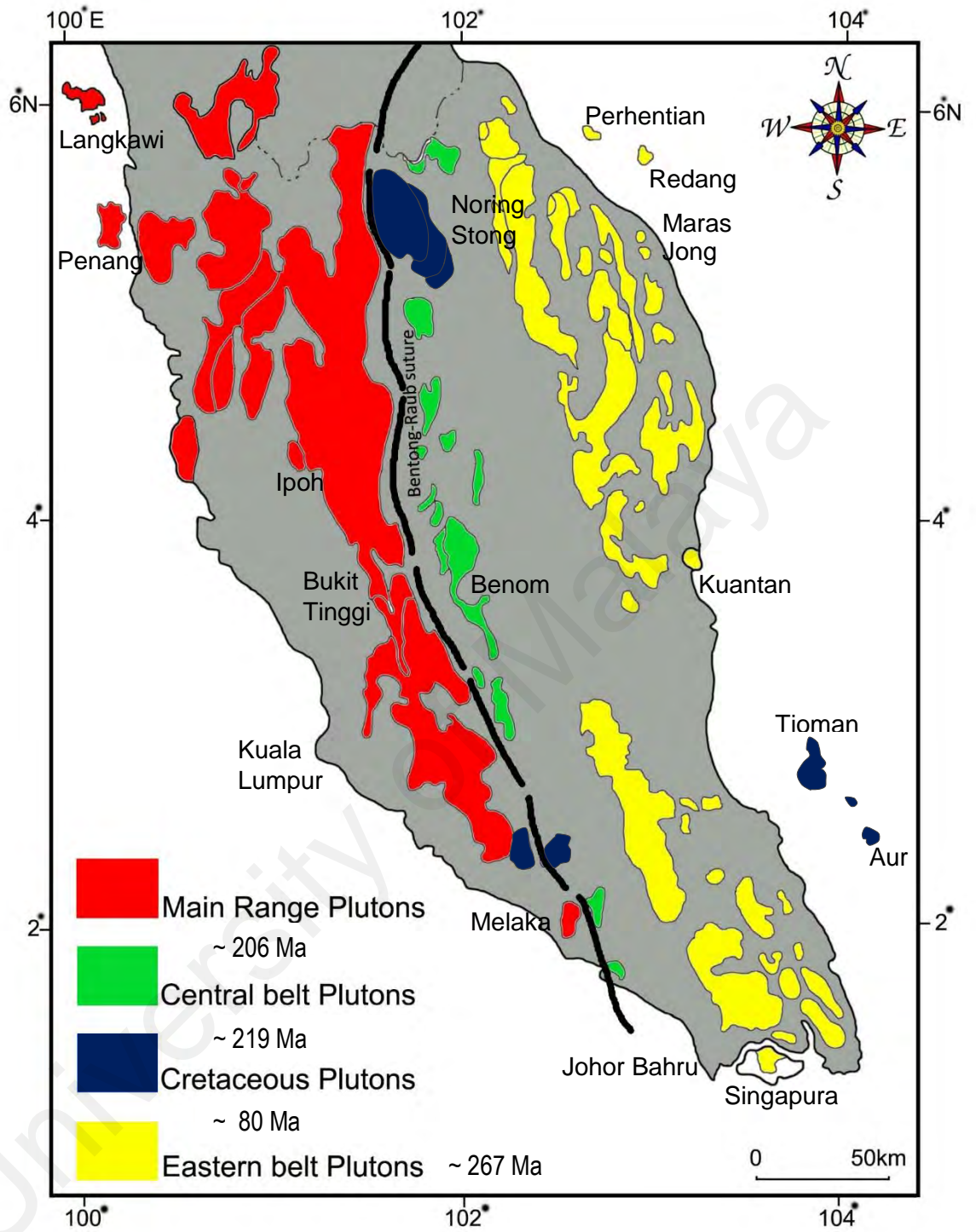
Figure 1.1 Map showing the distribution of granitoid provinces of
Peninsular Malaysia.

Figure 1.2 Location map of study area
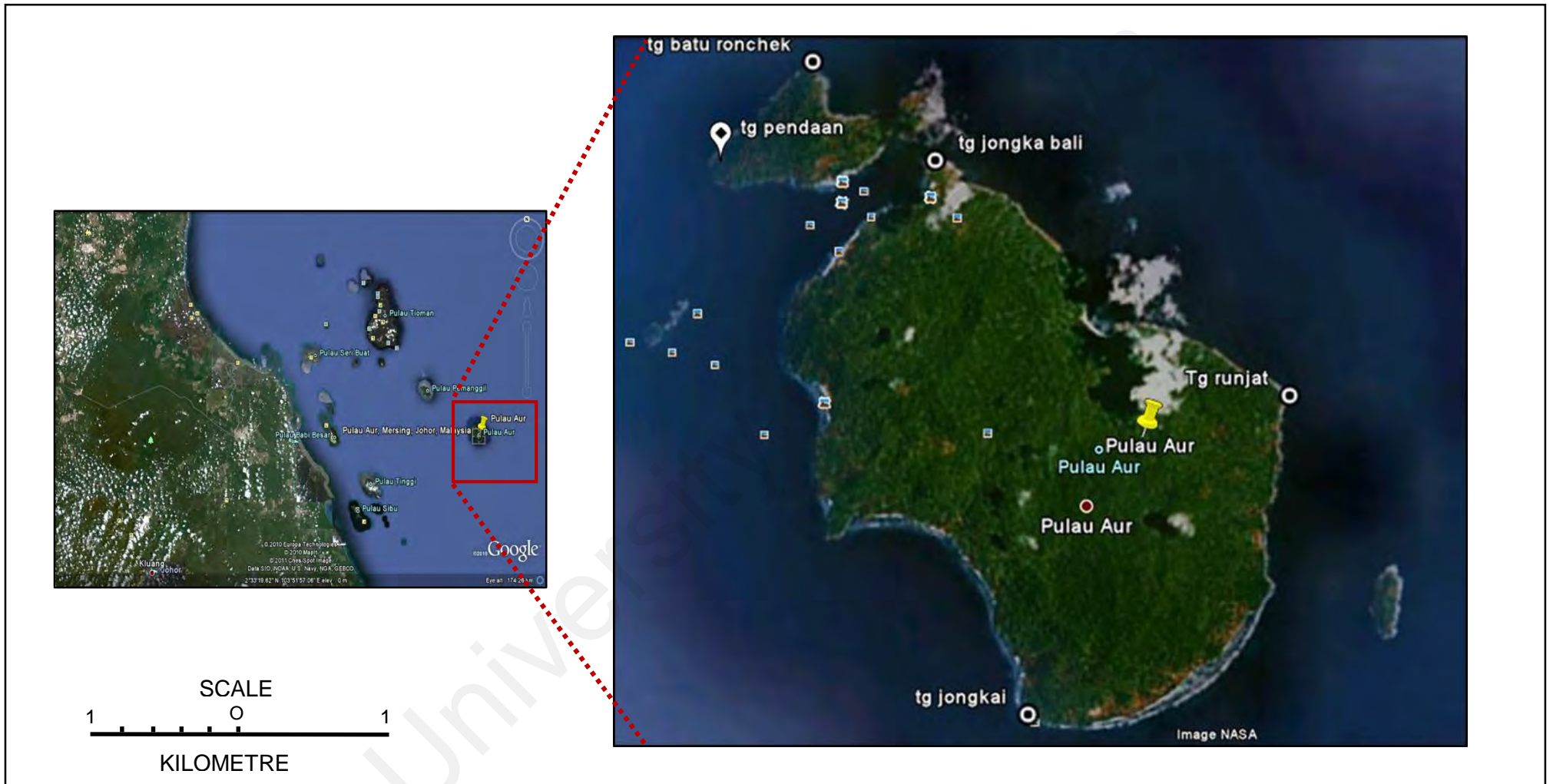
Figure 1.3   Satellite image of study area (Source: Google Earth, 2012)

Figure 1.4   Topography map of Aur Island and the nearby islands, Dayang, Lang, and Pinang Island
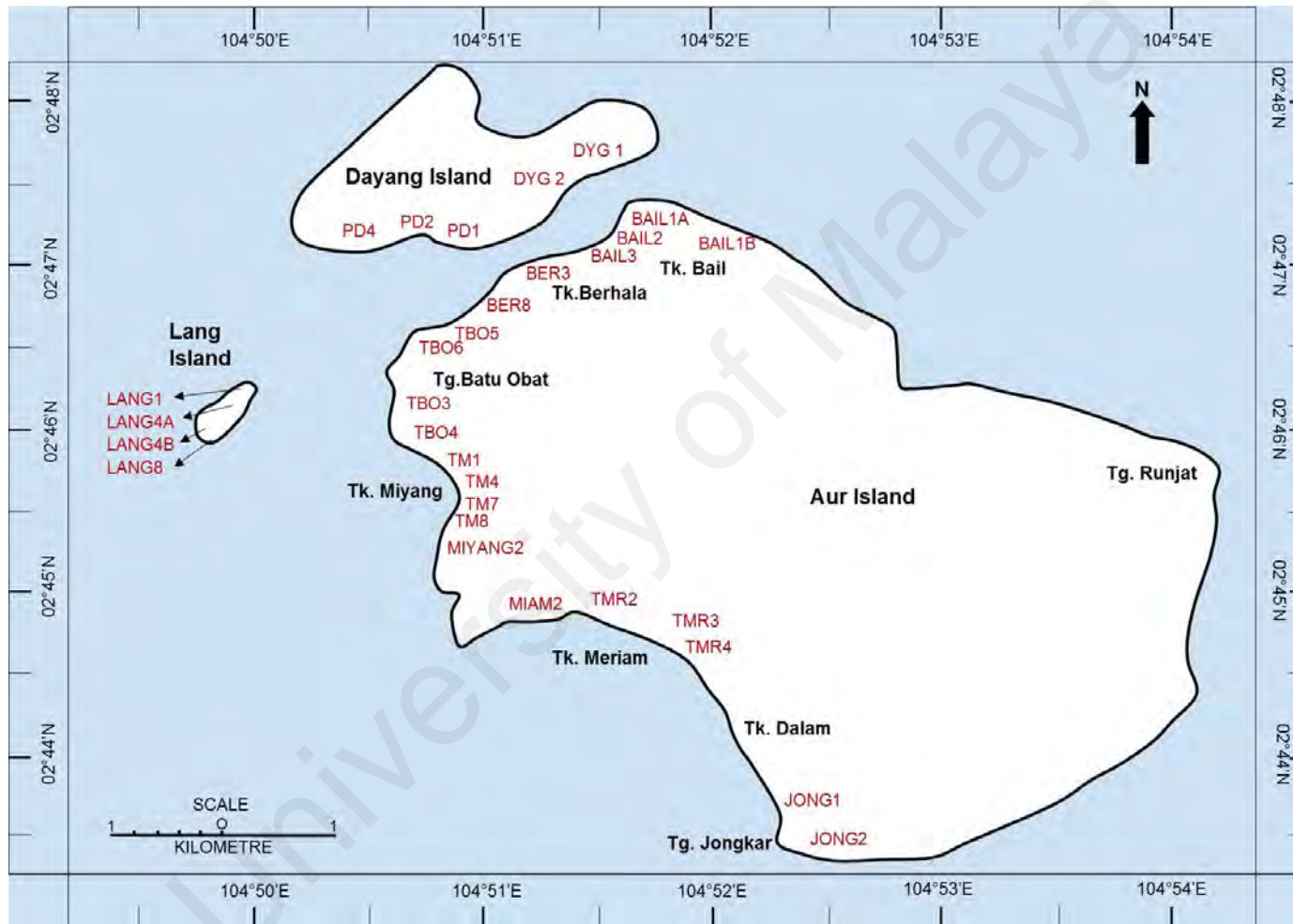
Figure 1.5   Location map of sample taken from study area

CHAPTER 2: GENERAL GEOLOGY

2.1   Introduction

In this chapter, regional geological setting and the spatial distribution of the granitoids of Peninsular Malaysia particularly from the Eastern Belt and Cretaceous plutons, along with the general geology of the study area, together with field observation will be discussed. The varieties of the different rocks will be discussed in terms of the lithological boundary, the different compositional varieties, their association, field relation and observation.

2.2   Regional Geological Setting

Peninsular Malaysia, with a total area of 130 268km^2 forms an integral part of Southeast Asian continental core of Sundaland (Metcalfe, 2011). Sundaland is the partly submerged southeast extension of the Asian continent, and comprises of the South China block, Indochina block, Sibumasu block, West Burma block, West Sumatra block and SW Borneo block. The basement geology of mainland SE Asia is composed of complex amalgamation of tectonic plates derived from Gondwana/Pangea during Paleozoic and Mesozoic, accreted to the Asia continent in the Late Paleozoic to Cenozoic (Metcalfe, 1998; Metcalfe, 2011).

Peninsular Malaysia comprises of two tectonic blocks; the Sibumasu Block in the west and Indochina Block in the east, which were amalgamated together during collision in the Late Triassic. This broad tectonic framework is relatively well understood, but the detailed geology; in particular the timing, extent and polarity of subduction zones are still poorly constrained in Peninsular Malaysia. Although there are extensive database of biogeographic, tectonostratigraphic, palaeoclimatic, detrital zircon provenance and the whole-rock geochemistry and isotope data of granites, Peninsular Malaysia is

characterized by lack of chronological precision and incomplete coverage (Cobbing et al., 1986, 1992, Krahenbuhl, 1991, Ghani, 2009, Oliver et al., 2013).

Based on distinct differences and characteristics in stratigraphy, structure, magmatism, geophysical signatures and geological evolution, Peninsular Malaysia can be divided into four tectonostratigraphic regions (Hutchison and Tan, 2009); which is the Western Belt, Central and Eastern Belt, and the Bentong Raub Suture which marks the boundary of Sibumasu (Western Belt) and Indochina Terrane (Central and Eastern Belt), (Figure 2.1a).

The Western Belt (including the Northwestern Block) is part of the Sibumasu Terrane, derived from the NW Australia Gondwana margin when the Meso-Tethys Ocean basin opened in the late Early Permian. Lower Paleozoic rocks are confined to the western belt, and the oldest dated rocks on Sibumasu are middle Cambrian to Early Ordovician clastics shallow sedimentary sequence of the Machinchang and Jerai Formations in NW Peninsular Malaysia of Gondwana affinity containing cold water brachiopods and glacial drop stones (Lee, 2009). Collisional crustal thickening, coupled with slab break off and rising hot asthenosphere produced the Main Range Late Triassic- Early Jurassic S-Type granitoids that intrudeD the Western Belt and Bentong-Raub Suture zone.

The Central and Eastern Belts of Peninsular Malaysia were regarded as a single tectonic block, the East Malaya Block (Metcalfe, 2000, 2013). They represent the Indochina Block, which was located in an equatorial position in the Carboniferous-Permian and was derived from Gondwana during Devonian when the Palaeo-Tethys Ocean opened. The Central Belt consists of thick sequences of shallow marine Permian argillites with minor Carboniferous limestones, associated with calc-alkaline rhyolite-
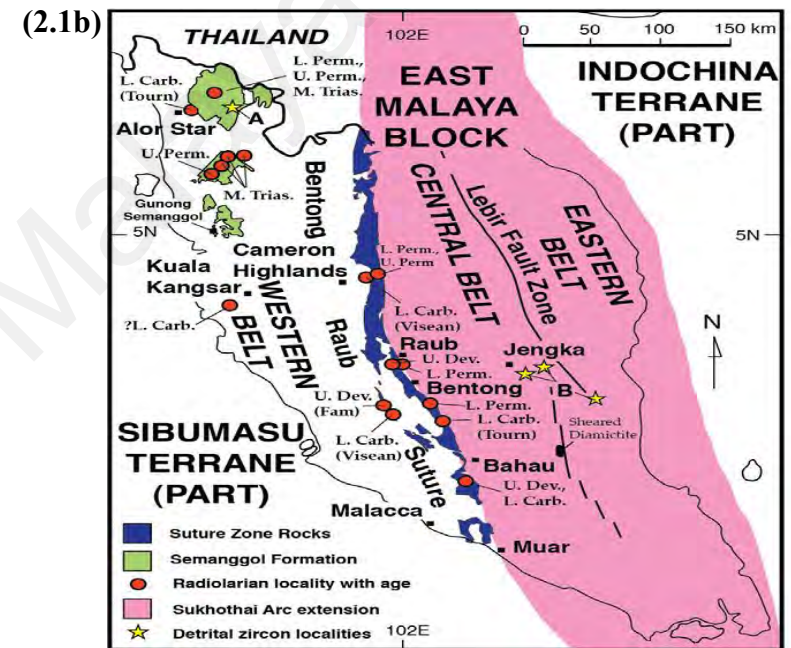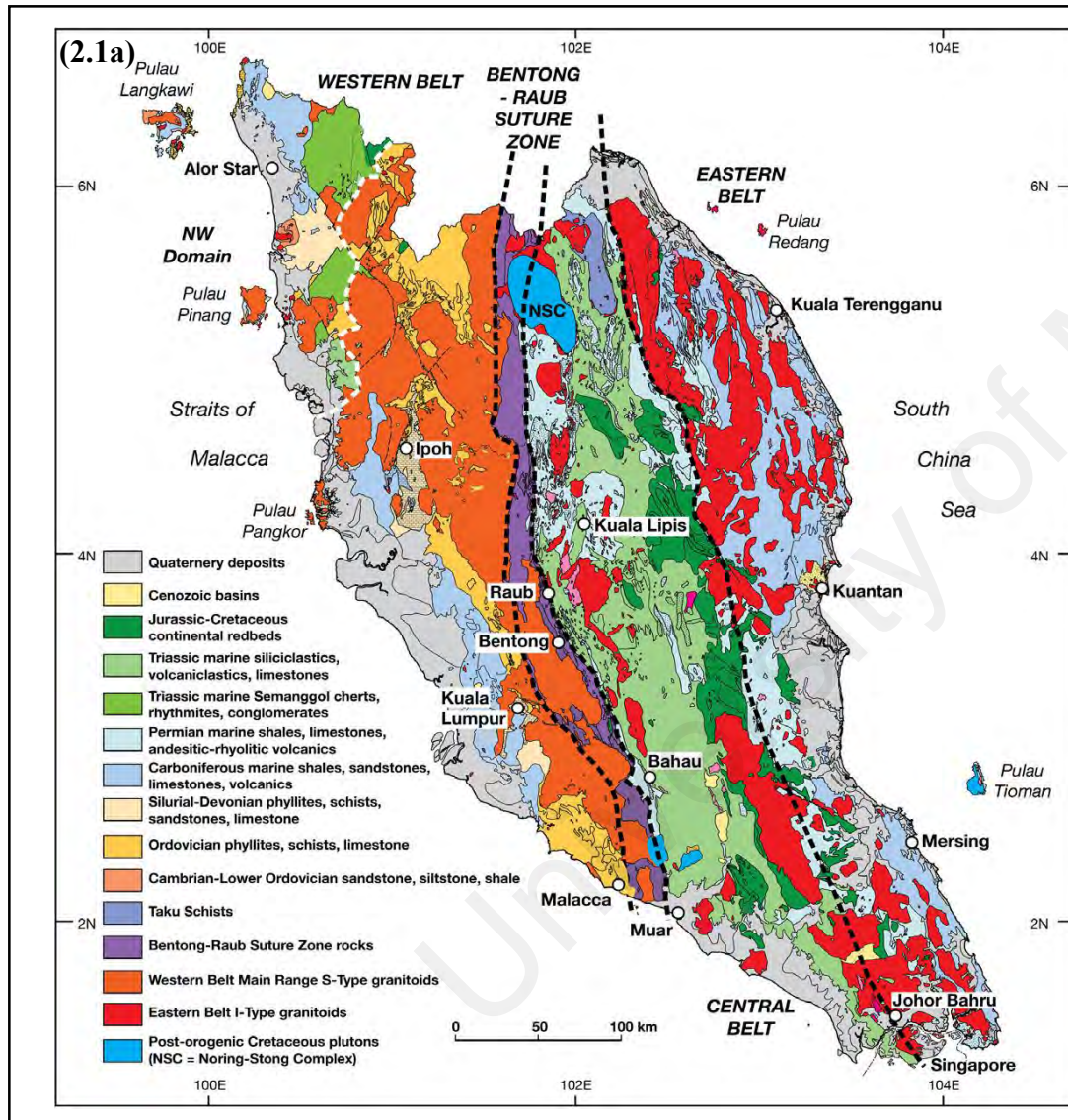
Figure 2.1a Simplified geological map showing the four main tectonostratigraphic regions of Peninsular Malaysia (after Tate et al., 2009)

Figure 2.1b Map showing the distribution of the Sibumasu Terrane (Western Belt) and Indochina Terrane (East Malaya Block), the Palaeo-Tethys Bentong-Raub Suture Zone. After Metcalfe (2000, 2011a, 2011b). Also in this map is the Lebir fault, marking the boundary between Central and Eastern belt on the East Malaya block (after Metcalfe, 2013)

andesitic volcanics, whilst the Eastern Belt composed of shallow marine Carboniferous sedimentary rocks, minor Permian conglomerates with associated rhyolite-andesite volcanics. Evidences of Permian warm climate plant fossils indicate the warm equatorial latitude and Cathaysian fauna affinities in contrast to the Permian glacial marine dropstones and cold water brachiopods of Gondwana from the Western Belt. Central and Eastern Belts are clearly separated by the Lebir Fault in the north but less clearly in the south (Lee, 2009) (Figure 2.1b).

Bentong-Raub Suture preserves remnants of the Paleo-Tethys Ocean which was opened during Devonian-Permian when Indochina and other Chinese blocks separated from Gondwana (Metcalfe, 2000). Paleo-Tethys Ocean was destroyed during the northward subduction beneath Indochina Block, which causes the Permian–Triassic andesitic volcanism and I-Type granitoids observed in the Central and Eastern Belts of the Malay Peninsula. The collision between Sibumasu and Indochina began in Early Triassic times and was finally completed by the Late Triassic.

2.3   Granitoids of Peninsular Malaysia

Granite and granitoid batholiths are widely distributed in the Southeast Asian region, and are the result of major plate tectonic processes that have affected this area. The granitoids of Peninsular Malaysia can be divided into three belts, (1) the Western Belt Main Range Granite that is separated from the Central Belt by the Bentong-Raub Suture; (2) Central Belt and (3) the Eastern Belt (Hutchison and Tan, 2009).

The Western Belt Main Range granite of Peninsular Malaysia forms the backbone of mountain ranges, and represent the Central Granitoid Province of SE Asia, extending northwards to Thailand and southwards into the Indonesian Tin Islands. It has been classified as dominantly tin bearing S-type granites of mainly Triassic age. The Main Range Granite is also enriched in uranium and thorium. U–Pb zircon emplacement ages

for the granites range from Late Triassic (230~9 Ma) to the earliest Jurassic (207~14 Ma), with a peak at around 210 Ma (Liew and Page, 1985; Cobbing et al., 1986; Darbyshire, 1988; Hutchison, 1989; Cobbing et al., 1992). Initial $^{87}Sr/^{86}Sr$ ratios are high, ranging from 0.7159 to 0.7512, indicating a continental source for the granites (Liew and McCulloch, 1985; Cobbing et al., 1992).

Central Belt is separated from the Eastern Belt along the Lebir Fault (Tate et al., 2008), containing plutons having age and geochemistry similar to the Eastern Belt granitoids, having low initial ratio of $^{87}Sr/^{86}Sr$ (<0.712) with biotite and/or hornblende varieties. Central Belt yields a Middle Triassic Rb-Sr ages, and are much older than the Late Triassic Western Belt Main Range granites but younger than those of the Early Permian and Early Triassic granitoids of the Eastern Belt granitoids.

The Eastern Belt granite province consists of dominantly Permian-Triassic I-type hornblende-biotite-granites with subordinate S-type plutons and A-type syenites-gabbros. The Eastern Belt plutons are older than the Western Belt Main Range Granite and represent the magmatism associated with the subduction of an ancient ocean (i.e. the Paleo Tethys Ocean) under the Central and Eastern Belts (Indochina Block). Rb-Sr whole rock and U-Pb zircon ages indicate emplacement of the Eastern Belt granites broadly ranges from Permian to Triassic. The granitoids ages of Eastern and Central belts show a general younging trend towards the Bentong-Raub Suture. Hutchison (2009a) also noted that the ages in the Eastern and Central Belts show a general trend of younging towards the Bentong-Raub Suture.

Late Cretaceous magmatism are also identified in the Central and Eastern Belt granitoid provinces where Cretaceous granite plutons have been reported and dated from the Stong Complex, Batang Melaka, Gunung Ledang, Gunung Pulai and Pulau Tioman (Garson et al., 1975; Bignell & Snelling 1977; Mitchell, 1977; Beckinsale et al., 1979;

Cobbing, 1986, 1992, Krahenbuhl, 1991; Searle et al., 2012). This smaller I-type plutons found within the Peninsular Malaysia are in common with the Cretaceous magmatism of the Western Thailand-Myanmar/Burma province that consists of hornblende-biotite I-type granodiorite-granites. The subduction and closure of Paleo-Tethys Ocean during the final collision between Sibumasu plate and Indochina terrane during the Late Triassic might have continued up to Middle Cretaceous, when this subduction-influenced, late stage and post collisional granites were emplaced in Phuket in the west and the Tioman Islands granite in the east (Searle et al., 2012).
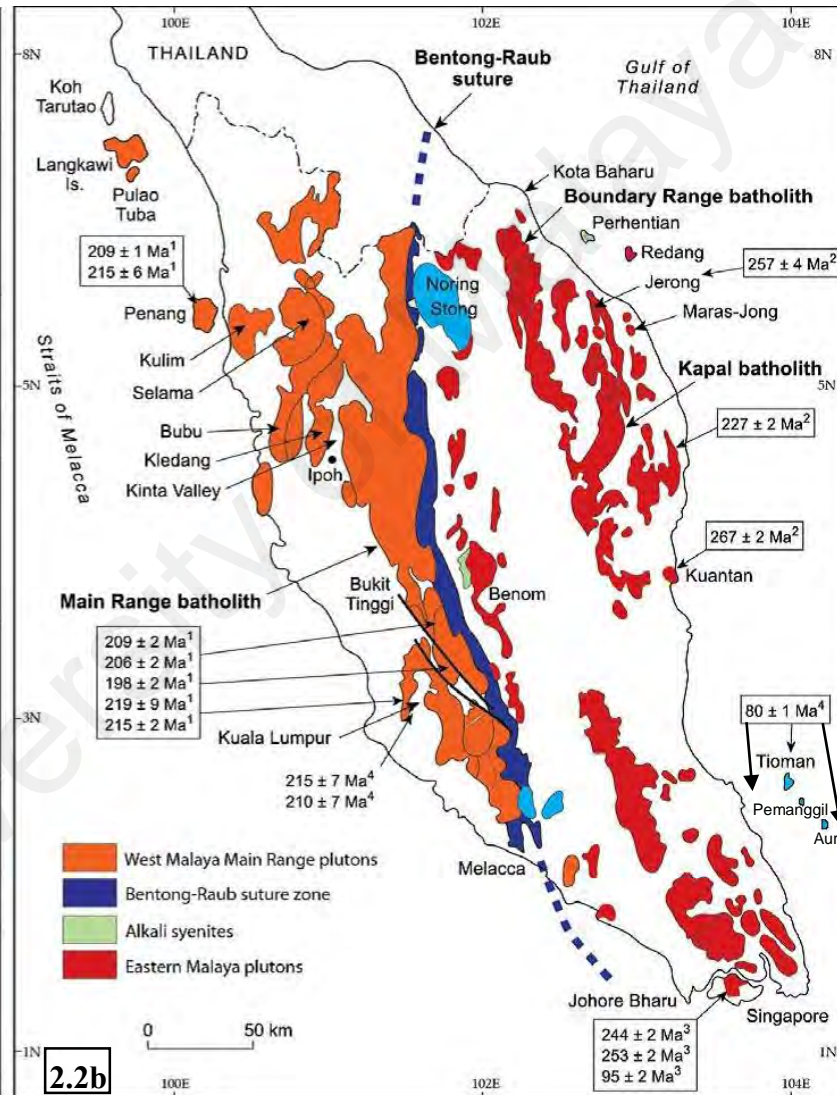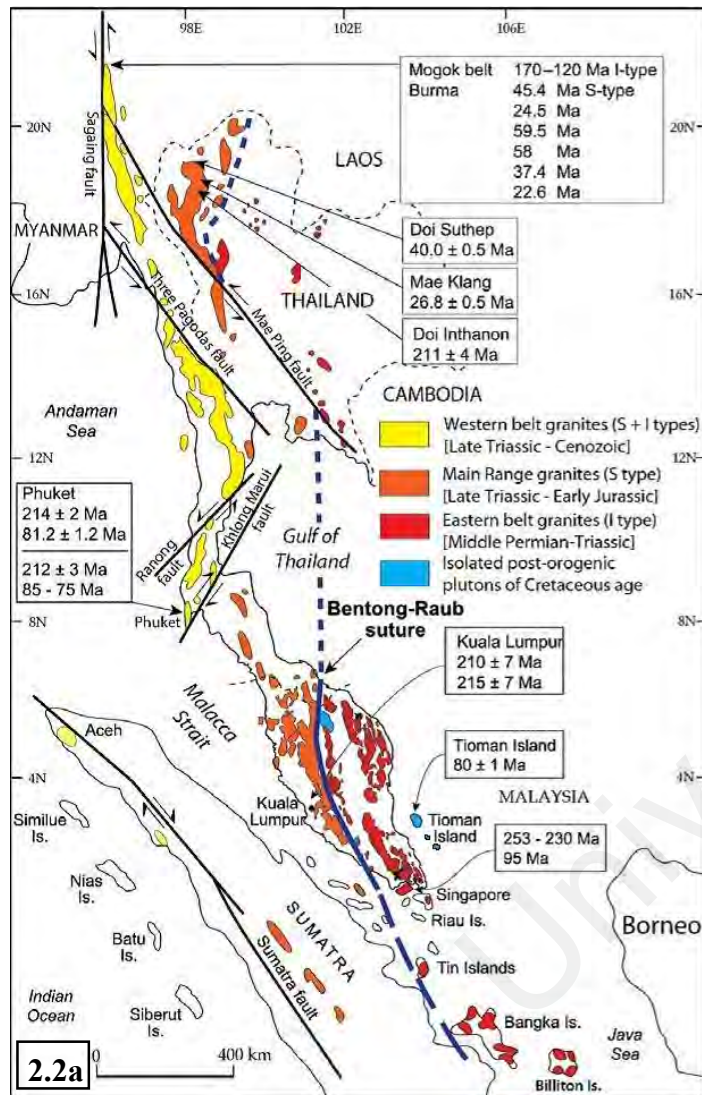
Figure 2.2a Map showing the three main granite provinces of SE Asia (after Searle et al., 2012)

Figure 2.2b Granite plutons and age of the Peninsular Malaysia granite of the Western Belt Main Range plutons, Eastern Belt and smaller Cretaceous plutons both on shore and offshore Peninsular Malaysia.
(Ages for (a) and (b) are from Searle et al. (2012); Ages for the Malay Peninsular; Liew and Page (1985); Liew and McCulloch (1985); Hotson et al. (2011) Oliver et al. (2011); Searle et al. (2012)).

2.4   General Geology and Tectonic Setting

The study area, Aur Island and the surrounding islands (Dayang and Lang) are located 65 km south east coast of Peninsular Malaysia, and they are part of the islands archipelago along the Johor's offshore territory. Geologically, the Johor Islands Archipelago which consists of the well-known: Tioman, Pemanggil, Aur, Besar, Hujung, Tengah, Rawa, Sibu and Tinggi Islands are the most easterly exposures of the Eastern Belt granitoids. These islands are composed of by variety of igneous rocks, ranging from granitic, syenitic, monzonitic and dioritic in compositon. Majority of these plutonic rocks intruded the earlier volcanic rocks consisting mainly of felsic to intermediate pyroclastic and lava.

The Eastern belt granitoid province extends from the eastern part of Malaysia towards NE Thailand and into Laos (Cobbing et al., 1986) are broadly dated as Permian to Triassic of age, related to the oceanic subduction of the Palaeo-Tethys Ocean beneath the Indochina block. These groups of islands archipelago, however, are characterized by a lack of geochronological precisions, and the age of the plutonic and volcanic rocks of the islands are still poorly constrained. Some of this islands off the east coast of Johor are probably part of the Eastern Belt, where rhyolite from Sibu Island yields a U-Pb zircon age of 276±5 Ma (Oliver et al., 2013), Ar-Ar whole rock of pyroclastic from Sibu Island yields an age of 296± 0.7 Ma (Ghani, in preparation); however some of these islands have very different U-Pb ages where Cretaceous magmatism has also been reported and are common within the Eastern Belt granitoid province (Bignell and Snelling, 1977; Darbyshire, 1985, Ghani et al., 1999; Searle et al., 2012). Cretaceous magmatism is recorded from the biotite K-feldspar granites of the Tioman Island that yields a zircon age of 80± 1Ma (Searle et al., 2012) and unpublished U-Pb zircon of the dioritic rocks from both Pemanggil and Aur Island give an age of about 80 ± 1Ma. (Ghani, unpublished data). The Cretaceous plutons of Tioman, Pemanggil and Aur Islands form several linear chain aligned NNW and SSE to one another (Fig. 2.2b).

The lithology of Aur Island consists entirely of plutonic rocks, without any association of volcanic or metamorphic rock. It forms a single pluton consists of diorite, quartz monzodiorite and granodiorite. The contacts between these three types of rock could not be distinguished clearly on field, but the rocks are grading from a more mafic composition (diorite and quartz monzodiorite) at the northern part, with pyroxenes as the main mafic phase, towards a more felsic composition (granodiorite) at the southern part, where the mafic constituent are dominated by hornblende and biotite.

Dayang Island which is located north to Aur Island, where it is separated from Aur Island by a narrow channel with width about 400m, on the other hand consists of diorite. It is the most mafic rock in the study area, mesocratic in appearance, greyish to dark grey in colour with mafic mineral abundances of about 55%. The rocks are typically medium grained, phaneritic with grain size of average 5mm where occurrences of mafic minerals are very prominent. Aplite dikes are found intruding diorite body at Dayang Island (**Fig. 2.4a**).

Quartz monzodiorite is found on Lang Island, and on Aur Island it is found near: Teluk Bail, Teluk Berhala, and Tanjong Batu Obat where it is found as rock boulders mainly at the northern part of Aur Island. In hand specimens, the rocks are phaneritic, medium grained with size ranging from 1-4 mm and grey in colour. Quartz monzodiorite and diorite of Dayang Island are quite similar in texture and colour indexes but there is an obvious different amount of K-feldspar, quartz and the mafic minerals when observed under a petrographic miscroscope.

Granodiorite is found largely at the central and southern part of Aur Island as in the form of rock boulders. About 70% of the pluton consists of granodiorite bodies, whereas the more mafic quartz monzodiorite is found towards the northern part. In hand specimen, granodiorite is light grey in colour, with elongated grains of hornblende and small biotite grains are abundant.

Mafic microgranular enclaves (MMEs) common in Eastern Belt granitoids are evident and can be found in abundance within the rock bodies throughout Aur Island. The MMEs generally have sharp contacts and are darker in colour and finer grained compared to the host rock bodies. They can be found in the quartz monzodiorite bodies on the northern part of Pulau Aur, and also towards the southern part, enclosed within the most evolved rock in study area, the granodiorite. MMEs range in size from 3 cm to almost 30 cm and are well rounded, ellipsoidal, flattened and even sub-angular in shape (**Fig. 2.4h**).
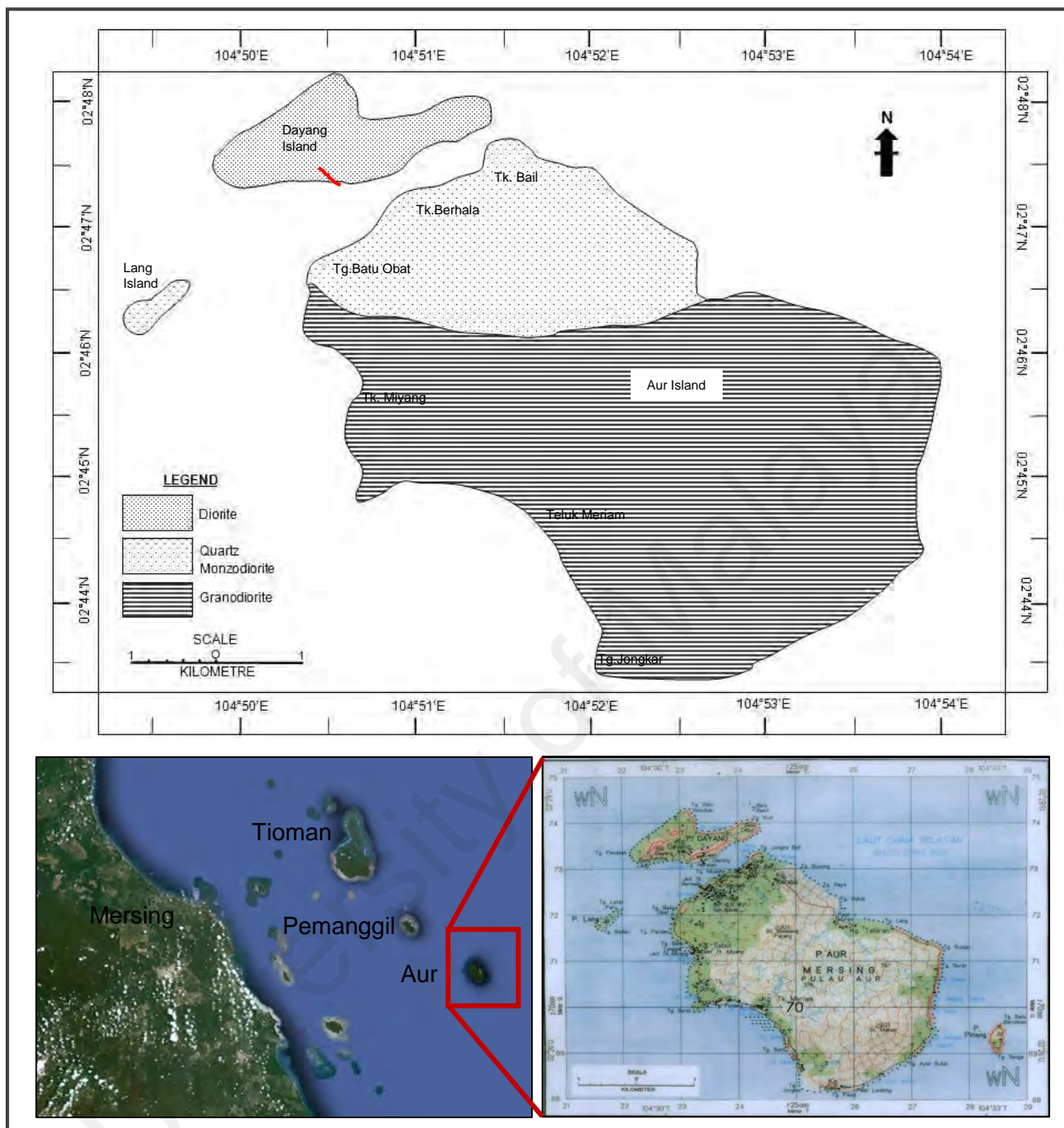
Figure 2.3 Geological map of Aur Island
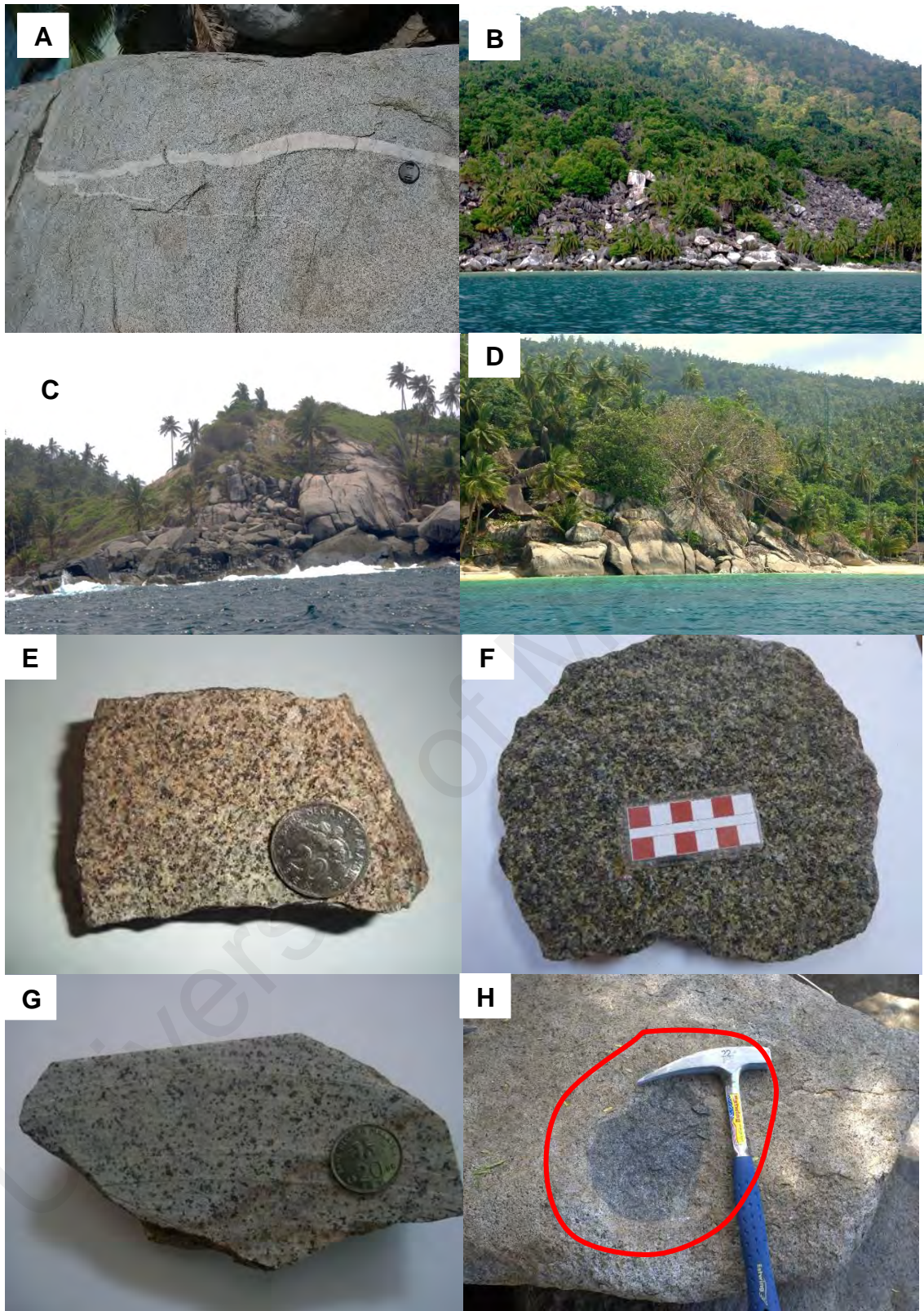
Figure 2.4 Field and hand specimen photographs showing the rock types found at study area **(a)** aplite dike cutting across diorite body at Dayang Island **(b-d)** typical outcrop of rock boulders along Aur Island **(e)** diorite sample from Dayang Island (PD4) **(f)** quartz monzodiorite sample from Teluk Bail (BAIL1A) **(g)** granodiorite sample from Teluk Meriam (TMR2) **(h)** MME observed in rock outcrop, rounded, showing sharp contacts with host rock

2.5   Summary

1) The varieties of dioritic rock found from the study area are ranging from diorite – quartz monzodiorite – granodiorite could have originated from the same magmatic source that grades into one another.

2) Field observation however does not show any contact between the occurrences of the more mafic quartz monzodiorite association at the northern part of Aur Island and the granodiorite at the southern part of Aur Island.

3) The occurrences of Mafic Microgranular Enclaves (MME) found within the quartz monzodiorite and granodiorite bodies could be suggestive of magma mixing processes that might have played an important role in the genesis of the dioritic rocks at the study area.

CHAPTER 3: PETROGRAPHY

3.1   Introduction

This chapter discusses the aspects of petrography and petrology of the rocks from the study area. The differences of rocks collected from different localities will be described based on detailed petrographic examinations, which involve field, macroscopic and microscopic observation.

3.2   Method of Study

A total of fourteen thin sections of dioritic and associated rocks from Aur and the nearby islands (Dayang and Lang Islands) were available for petrographic analyses (Fig. 1.5). Detailed examinations on thin sections were done to identify minerals, estimating mineral abundances and textural features of the selected samples.

3.2.1   Grain Size Classification

The grain size classification being used to identify and approximately measure the size of the crystals are (Williams et al., 1954 and Moorhouse, 1956).

Fine – grained	:	< 1 mm
Medium – grained	:	1 – 5 mm
Coarse – grained	:	5 mm – 3 cm
Very coarse grained	:	> 3 cm

3.2.2   Modal Analysis

All fourteen samples were point counted using Swift point counter. Estimations of mineral abundances were obtained by this point counting method, and approximately one thousand points were counted in each thin section. Modal analysis of the minerals present in the rock was then recorded in percentages, results presented in (Table 3.1). QAP diagram (Fig. 3.1) was plotted to classify the rocks of study area, where the samples
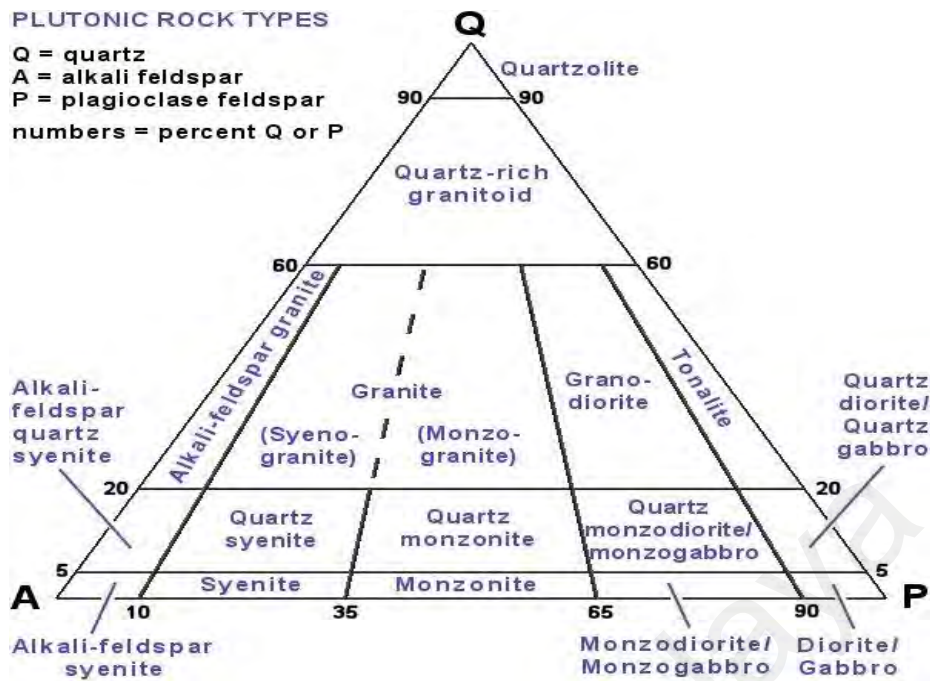
Figure 3.1   QAP diagram after Streckeisen (1976) used for classification of rocks at study area.
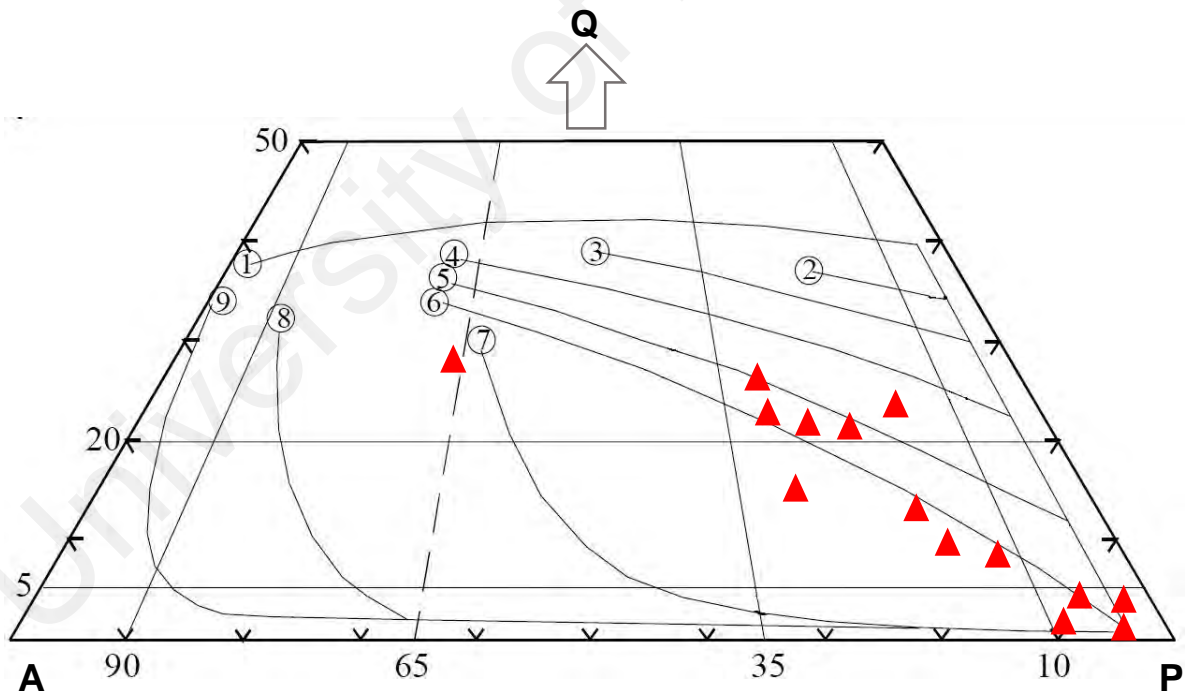
Figure 3.2   Main trends of plutonic type series based on QAP modal mineralogy. Trends with circled numbers are: 1-tholeiitic series, 2-calc-alkaline trondhjemitic series, 3-6-various calc-alkaline granodiorite series, 7-monzonitic series, 8-9-various alkaline series (Lameyre and Bowden, 1982; Lameyre and Bonin, 1991).

plot in the diorite, quartz monzodiorite and granodiorite field according to Streckeisen (1976).

3.2.3   Quartz-Alkali Feldspar-Plagioclase Feldspar (QAP) Diagram

QAP modal classification is also useful to determine the nature of a main magmas series (Lameyre and Bowden, 1982; Lameyre and Bonin, 1991). In magmatic arcs, the calc-alkaline series trend of plutonic rock can be subdivided into several classifications and trends which is; (1) tonalitic-trodjemitic calc alkaline series, (2) granodioritic calc-alkaline series and (3) monzonitic calc-alkaline series (Lameyre and Bowden, 1982). Based on the modal mineralogy, the rocks from study area fall in the various granodioritic calc-alkaline series (Fig. 3.2).

3.3   Petrology Description

Detailed petrographic description were made to the different types of rocks which have been classified earlier according to modal analysis and QAP method (Streckeisen, 1976). The different types of rocks are:

(i)   Diorite
(ii)   Quartz monzodiorite
(iii)   Granodiorite
(v)   Aplite vein
(vi)   Mafic microgranular enclaves (MME)

Petrographic description of the (v) aplite vein of various orientation and thickness found on diorite body at Dayang and Island and (vi) mafic microgranular enclaves (MME) found abundance within the rock outcrops at Aur Island will also be mentioned here.

Table 3.1 Results of point counting

Rock Type	Diorite			Quartz Monzodiorite				Granodiorite					Aplite Dike	MME
Sample	PD1	PD4	DYG1	TBO5	TBO6	Bail1A	Lang4	TMR3	TMR4	TM4	TM7	JONG1	PD2	TM7
Quartz	4.1	2.5	3.0	7.4	5.2	8.0	5.8	15.0	17.2	17.7	17.7	18	32.2	2.1
K-feldspar	2.3	2.3	2.3	15.6	15.9	17.7	14.2	8.0	9.8	10.0	11.3	12.8	26.3	3.6
Plagioclase	66.5	74.4	66.8	53.0	60.0	54.0	55.0	50.0	60.0	47.3	55.0	48.2	39.2	67.4
Clinopyroxene	18.1	14.8	17.4	12.3	16.5	12.4	14	-	-	-	-	-	-	-
Orthopyroxene	4.0	2.3	1.0	1.3	3.2	1.1	5.8	3.0	-	-	3.4	2.1	-	8.3
Hornblende	-	1.6	5.3	4.1	2.0	2.0	3.0	13.8	9.3	12.8	14.0	12.3	-	9.7
Biotite	5.0	2.1	4.2	6.4	3.2	4.0	3.2	10.2	3.7	8.2	7.6	5.2	-	8.9
Zircon	-	-	0.3	0.7	0.2	0.6	0.5	0.6	0.5	0.4	0.7	0.3	7	-
Sphene	-	-	-	0.3	-	-	-	0.9	0.7	-	-	0.6	-	-
Apatite	0.3	0.5	0.2	0.5	0.4	0.5	0.3	1.2	1.1	1.4	1.3	1.5	0.8	0.6
Opaque oxide	0.5	0.4	0.6	0.7	0.9	0.6	0.6	0.8	0.8	0.7	0.5	0.7	0.6	0.6

Table 3.2 Modal composition of rock samples for QAP classification based on Streickesen (1976)

Sample	Location	Quartz	Alkali Feldspar	Plagioclase Feldspar	Recalculated to 100%			Rock Type
					Q	A	P	
PD1	Dayang Island	4.1	2.3	66.5	6	3	91	Diorite
PD4	Dayang Island	2.5	2.3	74.4	3	3	94	Diorite
DYG1	Dayang Island	3.0	2.3	66.8	4	3	93	Diorite
TBO5	Tg. Batu Obat	7.4	15.6	53.0	9	21	70	Quartz Monzodiorite
TBO6	Tg. Batu Obat	5.2	15.9	60.0	6	19	74	Quartz Monzodiorite
Bail 1A	Tk. Bail	8.0	17.7	54.0	10	22	68	Quartz Monzodiorite
Lang4	Lang Island	5.8	14.2	55.0	8	13	73	Quartz Monzodiorite
TMR3	Tk. Meriam	15.0	8.0	50.0	21	11	68	Granodiorite
TMR4	Tk. Meriam	17.2	9.8	60.0	20	11	69	Granodiorite
TM4	Tk. Miyang	17.7	10.0	47.3	24	13	63	Granodiorite
TM7	Tk. Miyang	17.7	11.3	55.0	21	13	65	Granodiorite
JONG1	Tk. Jong	18.0	12.8	48.2	23	16	61	Granodiorite
PD2	Dayang Island	32.2	26.3	39.2	33	27	40	Granite
TM7	Tk. Miyang	2.1	3.6	67.4	3	5	92	Diorite/Gabbro

3.3.1 Diorite

Diorite consists dominantly of plagioclase feldspar (67-74 %), clinopyroxene (15-18%), orthopyroxene (1-4%), biotite (2-5%), quartz (3-4%) and K-feldspar (2%). Accessory mineral phases found are; zircon (0.8-1.2%), apatite (0.2-0.5%) and subordinate opaque mineral (0.4-0.6%). On petrographic observations, diorite shows the typical hypidiomorphic granular texture. Ophitic texture, typically found in mafic rocks can also be observed. Sometimes when plagioclase are only found abutted against the large subhedral clinopyroxene, and not fully enclosed by the clinopyroxene, forming sub-ophitic texture.

Plagioclase feldspar is the most abundant minerals in this rock. Plagioclases are euhedral to subhedral in shape, with size ranging from 0.5-3 mm. Plagioclase occurrences can be found in two forms, (1) as a small euhedral to subhedral inclusions randomly distributed within a larger subhedral clinopyroxene forming ophitic texture (Fig. 3.3b) and (2) as a large subhedral to euhedral lath-shaped crystal. Large plagioclase crystals (~2.5-3mm) often contains many inclusions of clinopyroxenes and opaque minerals (Fig. 3.3f). Plagioclase often displays sharply defined polysynthetic albite twin and zoning are rarely observed.

Clinopyroxenes are the primary mafic phase in diorite. They are typically euhedral to subhedral in shape with size ranging between 0.5-3.0 mm. Large clinopyroxene (2-3 mm) often encloses other minerals, (e.g. plagioclase and opaque mineral). Clinopyroxene prevails over orthopyroxene, and clinopyroxene can be distinguished based on its higher birefringence, 2nd order interference colour (blue) and inclined extinction under cross nicol. Both clinopyroxene and orthopyroxene typically shows brassy yellow colour under plane polarized light, lack of distinct pleochroism and a good near to 90° cleavage can be observed.

Biotite occurs as subhedral to anhedral crystal, with size ranging from 0.05-1.0 mm and it is usually found associating with clinopyroxene, forming mafic clots. It can be identified based on its brown to dark brown pleochroism, bird's eye extinction and pleochroic halos. In few of the samples, hornblende can also be observed. Hornblende found in diorite are only minor in amount, occurring as anhedral crystal, with size ranging from 0.2-0.6 mm. Hornblende has partly replaced, and may have formed by replacement of clinopyroxene.

Quartz and K-feldspar are anhedral in shape, forming interstitially between the earlier formed minerals. Zircon, apatite and subordinate opaque minerals are the common accessory phases found, usually associated with clinopyroxene and biotite. Minor to weak alteration of plagioclase to sericite can be observed, and chloritization is rarely observed.
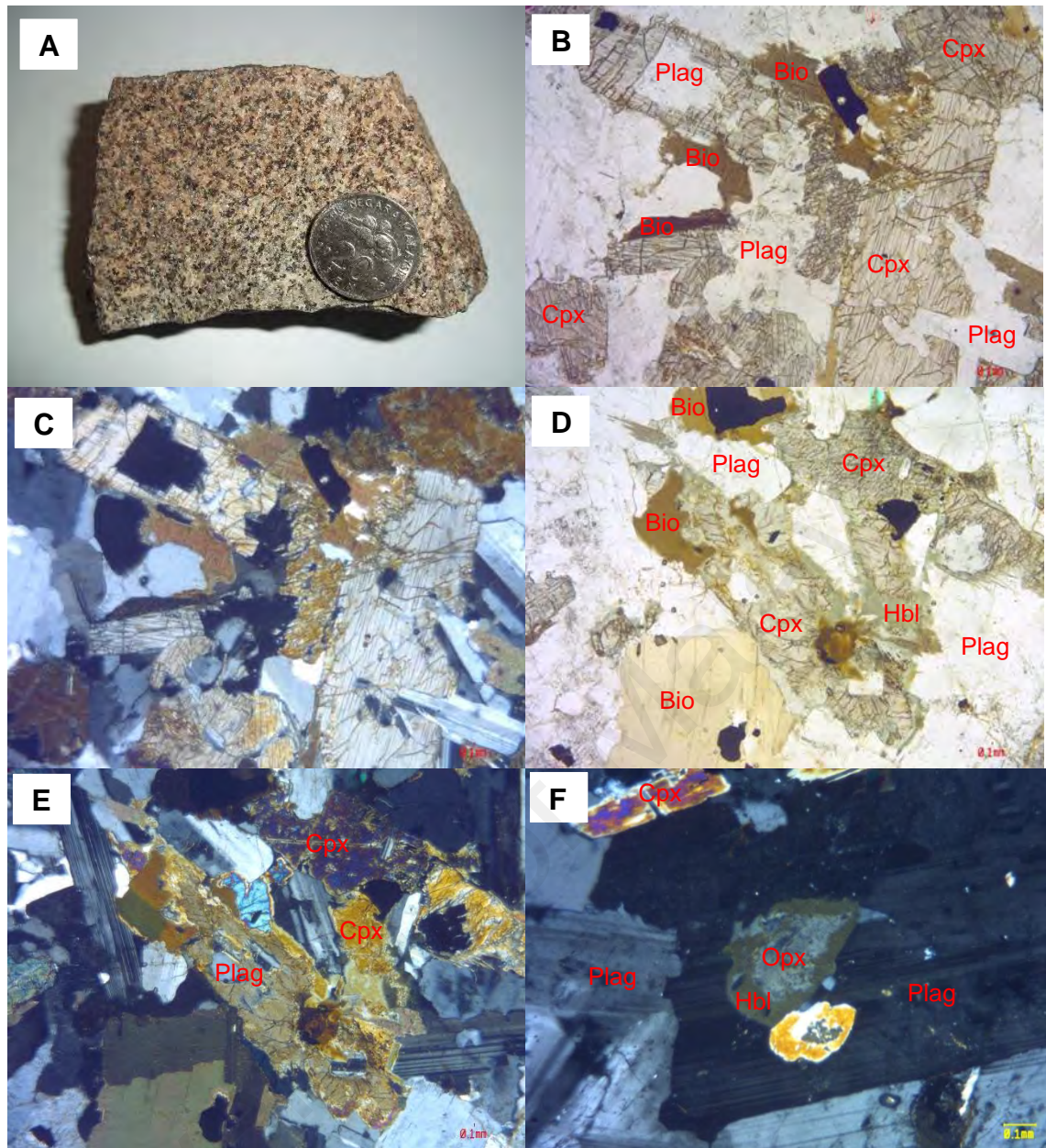
Figure 3.3

(a)   Hand specimen of diorite from Pulau Dayang.
(b)   Photomicrograph showing typical hypidiomorphic granular texture in diorite, opaque mineral are usually euhedral, smaller plagioclase inclusions and orthopyroxene are or euhedral to subhedral in shape. Notice at the bottom right, the occurrences of sub-ophitic texture where plagioclase are abutted against euhedral pyroxene
(c)   Photomicrograph of Fig. 3.3.1 (b) in cross nicol.
(d)   Photomicrographs showing subhedral clinopyroxene enclosing euhedral to subhedral plagioclase inclusion, forming ophitic texture. Notice the anhedral hornblende with no crystal faces, probably formed from replacement of clinopyroxene.
(e)   Photomicrograph of Fig. 3.3.1 (d) in cross nicol. Biotite and clinopyroxene are often found together forming mafic clots.
(f)   Photomicrograph showing inclusions of anhedral hornblende which has overgrown, or replaced orthopyroxene inside a plagioclase.

51
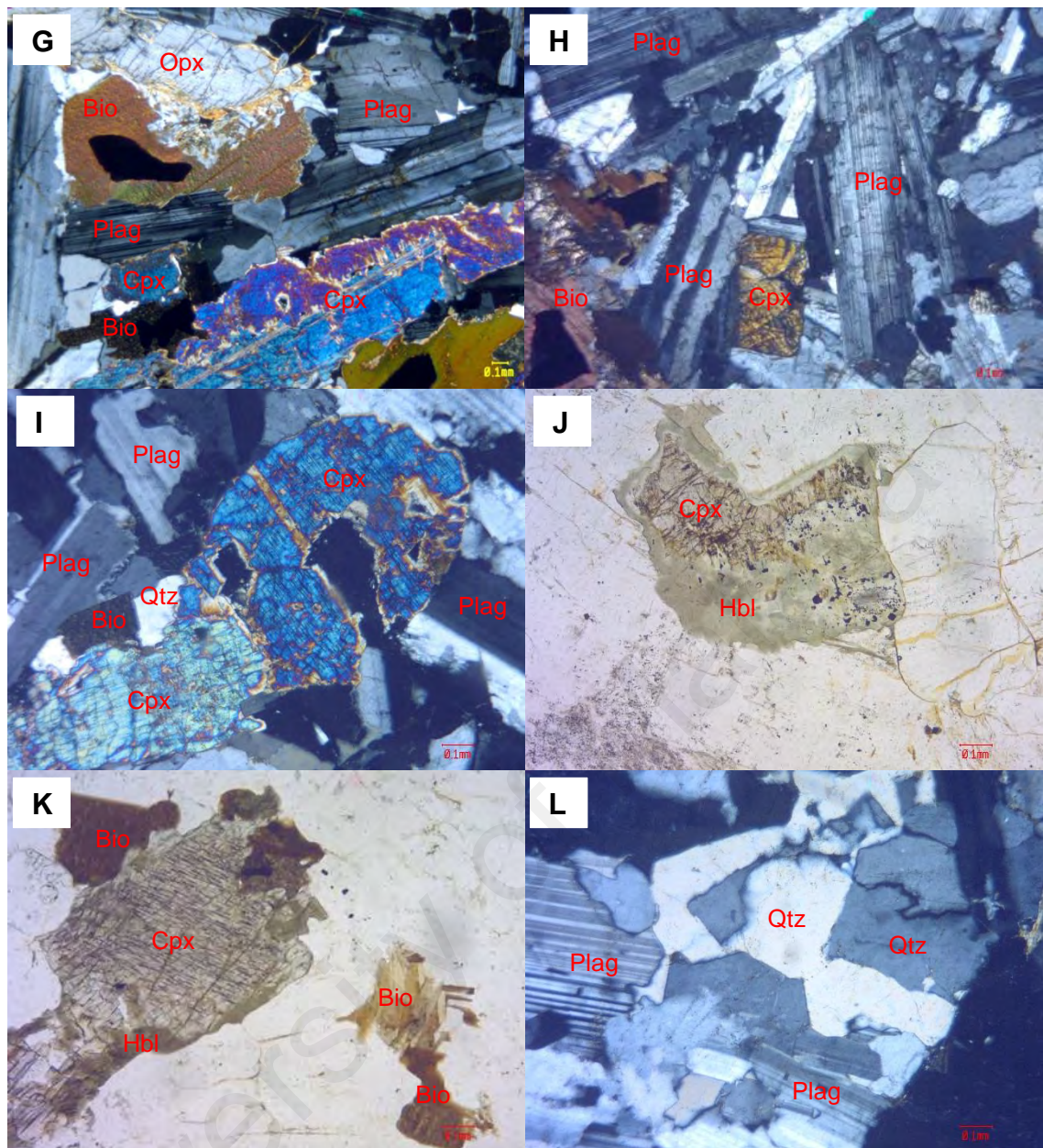
Figure 3.3 (cont.)

(g)   Photomicrograph showing occurrences of subhedral to anhedral clinopyroxene, orthopyroxene, plagioclase,   biotite and opaque mineral.

(h)   Photomicrograph showing typical spatial distribution and shapes of plagioclase, showing sharply defined albite twinning. Euhedral clinopyroxene crystal can also be observed.

(i)   Photomicrograph showing anhedral clinopyroxene, showing simple twinning and high birefreingence.

(j)   Photomicrograph showing remnants of clinopyroxene, with brassy yellow colour, fully enclosed by anhedral hornblende.

(k)   Photomicrograph showing spatial occurrences of clinopyroxene, biotite and hornblende. Subhedral clinopyroxene with two directions of cleavage ~ 90' intersecting with one another can be clearly seen. Hornblende and biotite are found along the edges of larger clinopyroxene crystal.

(l)   Photomicrograph showing quartz are found interstitially within the earlier forming crystals.

52

3.3.2 Quartz Monzodiorite

On petrographic observation, quartz monzodiorite consists of the essential plagioclase feldspar (53-60%), clinopyroxene (12-16%), orthopyroxene (1-6%), biotite (3-6%), hornblende (2-3%), quartz (5-8%) and K-feldspar (14-18%). Accessory mineral phases are zircon (0.2-0.7%), apatite (0.3-0.5), opaque oxide (0.6-0.9) and in some samples, sphene can be observed. It has the typical hypidiomorphic granular texture, and sub-ophitic texture are common.

Plagioclase is the dominant feldspar, euhedral to subhedral shape, occurring as equant tabular crystal with size ranging from 0.3-1.5 mm. Plagioclase are distinguished by polysynthetic albite twins, displaying sharply defined lamellae or only a few lamellae that are diffuse, and sometimes plagioclase found may show concentric patterns of zoning when viewed under cross polarizer light.

Clinopyroxene are still the dominant mafic phase in quartz monzodiorite. It can be found in two forms; (1) as large euhedral to subhedral crystal (individual or associated with other mafic minerals) and (2) as smaller broken and isolated subhedral crystal. The size ranges from 0.2-2.5 mm. In some sample, corroded grains of early clinopyroxene are frequently found enclosed, and altered by hornblende. Orthopyroxene are present, but they are only subordinate to clinopyroxene, ranging much smaller in size, 0.5-1.2 mm.

Biotite is found as subhedral to anhedral crystal, showing the typical brown to dark brown pleochroism. It is often associated with clinopyroxene and hornblende, rarely as individual crystal. The size range are 0.5-2 mm. Hornblende can be found in two occurrences; (1) subhedral to euhedral individual crystal with perfect crystal faces and (2) anhedral shaped hornblende enclosing earlier crystallized clinopyroxene crystal, where it may have partly replaced and formed from clinopyroxene. Hornblende can be identified based on its pale green to dark green pleochroism, two directions of cleavage that are

characteristics of amphiboles can be observed, while some display only a single direction or none at all.

K-feldspar and quartz are among the last mineral to form, and occur interstitially between the earlier forming minerals. Both quartz and K-feldspar size ranges are from 0.1-1.5 mm. One distinct observation are the increasing abundances of K-feldspar and quartz in quartz monzodiorite and its larger grain size, 0.1-1.5 mm.

Apatite occurs as inclusions in the early subhedral to euhedral individual hornblende, or closely associate as inclusions in late minerals, biotite, which points to a wide temperature interval for apatite crystallization. Subordinate opaque mineral are euhedral to subhedral shape and found abundance as inclusions or enclosed by clinopyroxene and amphibole.

In some samples, chloritization, in which mafic minerals association: clinopyroxene, biotite and hornblende were replaced by chlorite are very prominent. Chlorite can be identified based on its yellowish green colour, anhedral, having no crystal shape and low order anomalous interference colour. Weak alteration of plagioclase and K-feldspar to fine grain sericite can also be observed.
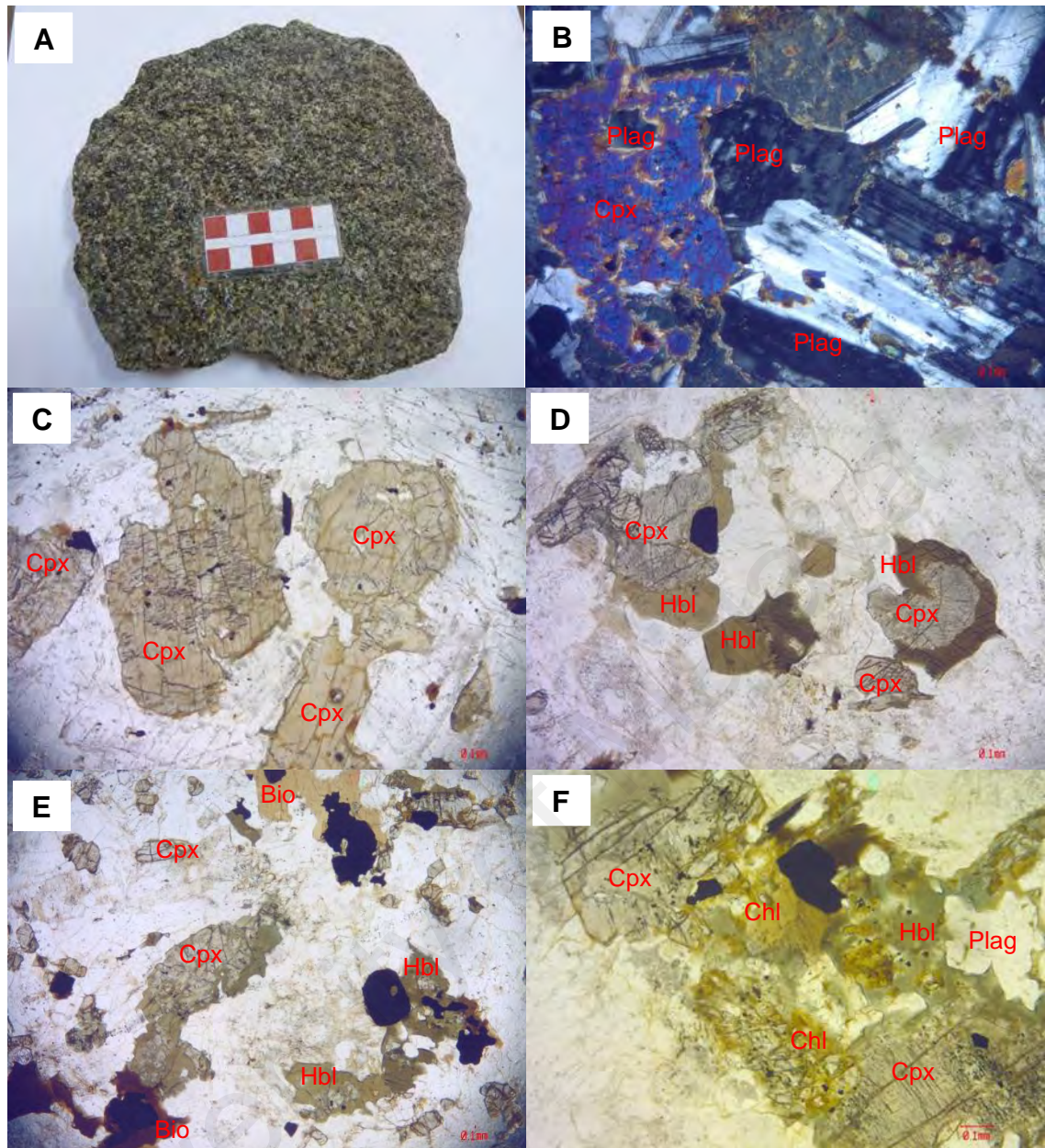
Figure 3.4

(a)   Hand specimen of quartz monzodiorite

(b)   Photomicrograph showing anhedral plagioclase inclusion in clinopyroxene forming ophitic texture. Inclusions of smaller anhedral clinopyroxene in larger plagioclase crystal can also be observed. Notice the serrated plagioclase contact with other mineral grains, plagioclase are commonly showing weak, diffuse twinning.

(c)   Photomicrograph showing occurrences of clinopyroxene as larger grain, with visible ~90° cleavage can be observed, often found showing brassy yellow colour.

(d)   Photomicrograph showing occurrences of euhedral to subhedral hornblende as individual crystal or found associated with clinopyroxene. Typical cleavages of hornblende ~124/56 are clearly visible.

(e)   Photomicrograph showing typical spatial distribution of mafic mineral abundances; clinopyroxene, hornblende, biotite and subordinate opaque mineral. Notice the occurrences of smaller and individual and isolated subhedral to anhedral clinopyroxene

(f)   Photomicrograph showing yellowish green chlorite, anhedral in shape replacing along edges of clinopyroxene and hornblende.
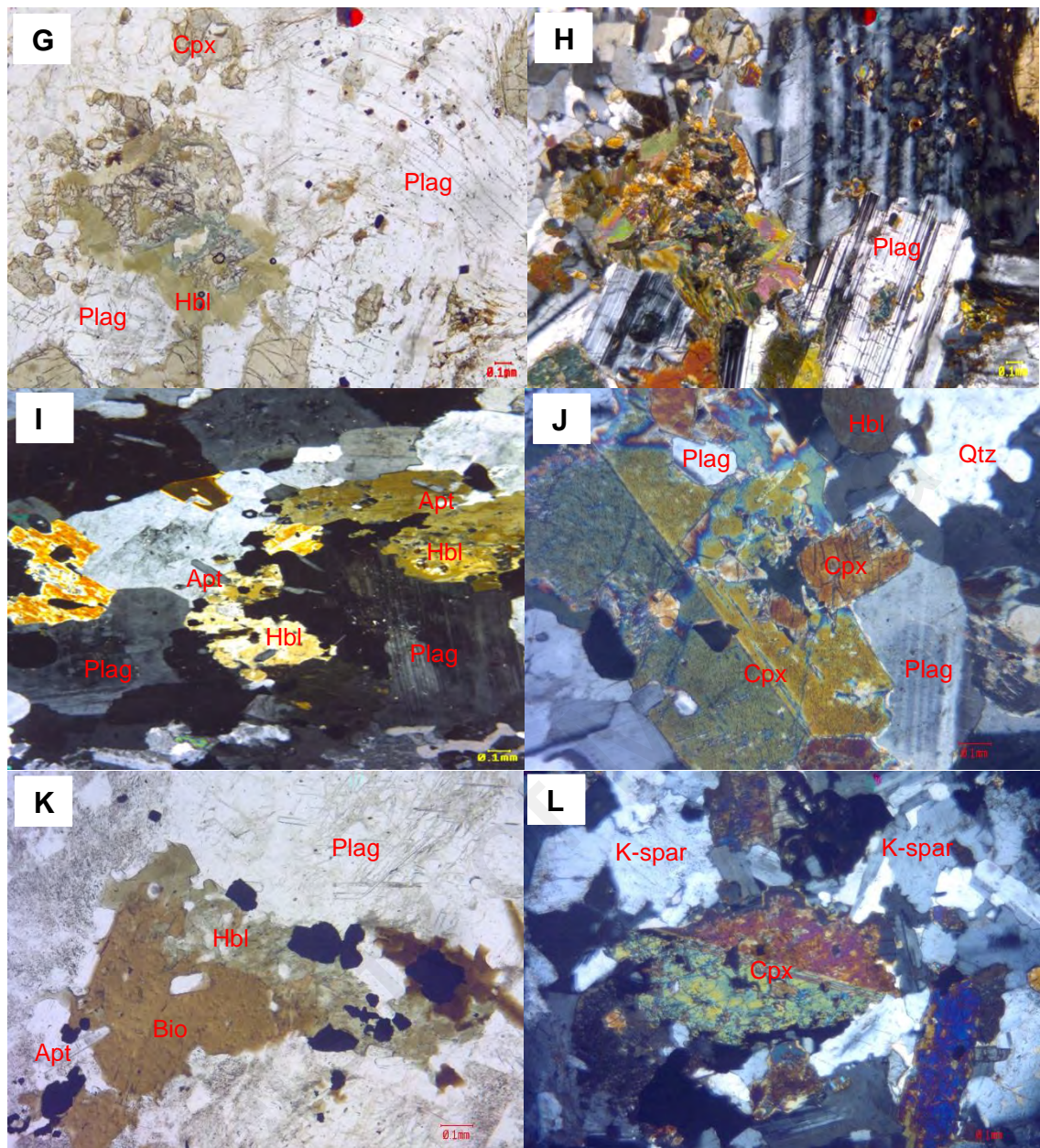
Figure   3.4 (cont.)

(g)   Photomicrograph showing cluster of fibrous amphibole with green to pale green pleochroism enclosing the remnant bits of pyroxene.

(h)   Photomicrograph of Fig. 3.3.2 (g) under cross nicol showing inclusions of opaque mineral, pyroxne inside a zoned and twinned plagioclase. Hornblende aggregates at the left of the plagioclase crystal shows variable interference colour due to hornblende which has overgrown or replaces part of what is originally a euhedral prism of orthopyroxene.

(i)   Photomicrograph showing inclusions of needle shape, hexagonal apatite inside plagioclase and hornblende. Notice the abundances of apatite.

(j)   Photomicrograph showing clinopyroxene showing simple twinning, euhedral clinopyroxene abutted against the larger subhedral pyroxene.

(k)   Photomicrograph showing brown to dark brown aggregates of anhedral biotite closely associated with hornblende and opaque oxide.

(l)   Photomicrograph showing quartz and K-feldspar forming interstitially, anhedral in shape. Notice the abundances of K-feldspar observed than what is found in diorite.

56

3.3.3 Granodiorite

Microscopically, it consists of plagioclase (47-55 %), quartz (15-18%) and K-feldspar (17.3%). Mafic phases are well-formed hornblende (9-14%) and biotite (4-10%). Minor amount of orthopyroxene (2-3%) are also found in some samples, found associated with hornblende and biotite. Accessory phases found are zircon (0.3-0.7%), sphene (0.6-0.9), apatite (1.1-1.5%) and opaque oxide (0.5-0.8%). Granodiorite shows the typical hypidiomorphic granular texture. Anti-rapakivi texture, where plagioclase feldspar are mantled by K-feldspar are also common.

Plagioclase is still the most abundant feldspar, sometimes showing diffuse lamellae and sharply defined albite twin. Zoning are common, which is indicative of the fractional crsytallization processes during magmatic evolution. The shape are elongated, subhedral to anhedral in shape with size ranging from 0.2-0.8 mm.

K-feldspar are identified based on its grainy and greyish appearance, anhedral shape with size ranging from 0.1-1.2 mm. Perthite texture, intergrowth of K-feldspars and plagioclase feldspar (Na rich-albite) are also common in granodiorite. Quartz forms interstitially, anhedral in shape with size ranging from 0.03-0.8 mm. Quartz and K-feldspar are abundant and present as anhedral phase that is sparsely distributed.

Hornblende is common in granodiorite, and it is the major mafic phase observed together with biotite. It occurs as subhedral to anhedral shape, occurring as individual crystal and sometimes associated with biotite forming mafic clots. The size range from 0.4-1.5 mm, showing pale green to dark green pleochroism. Few show the two directions of cleavage that are characteristic of amphiboles, but others display only a single direction or none at all. Some hornblende may have formed by replacement of orthopyroxene, where hornblende clearly has enveloped and may have partly replaced magmatic orthopyroxene.

Biotite are euhedral to subhedral in shape, with size ranging from 0.5-1.5 mm. It is pleochroic from dark brown to pale yellowish brown. Biotite can be found occurring as individual crystals, and also commonly associated with hornblende and opaque mineral.

Accessory phases; apatite are found especially abundance in hornblende and biotite, both in basal and prismatic forms, identified by its fairly high relief and colorless and low order grey interference colour. Sphene is found as euhedral to subhedral crystal, sometimes as a smaller broken wedge shape with high positive relief. Opaque mineral are also abundant, subhedral to euhedral in shape, forming interstitially within other mineral. K-feldspars are often altered to sericite, and occasionally show intergrowth with quartz.
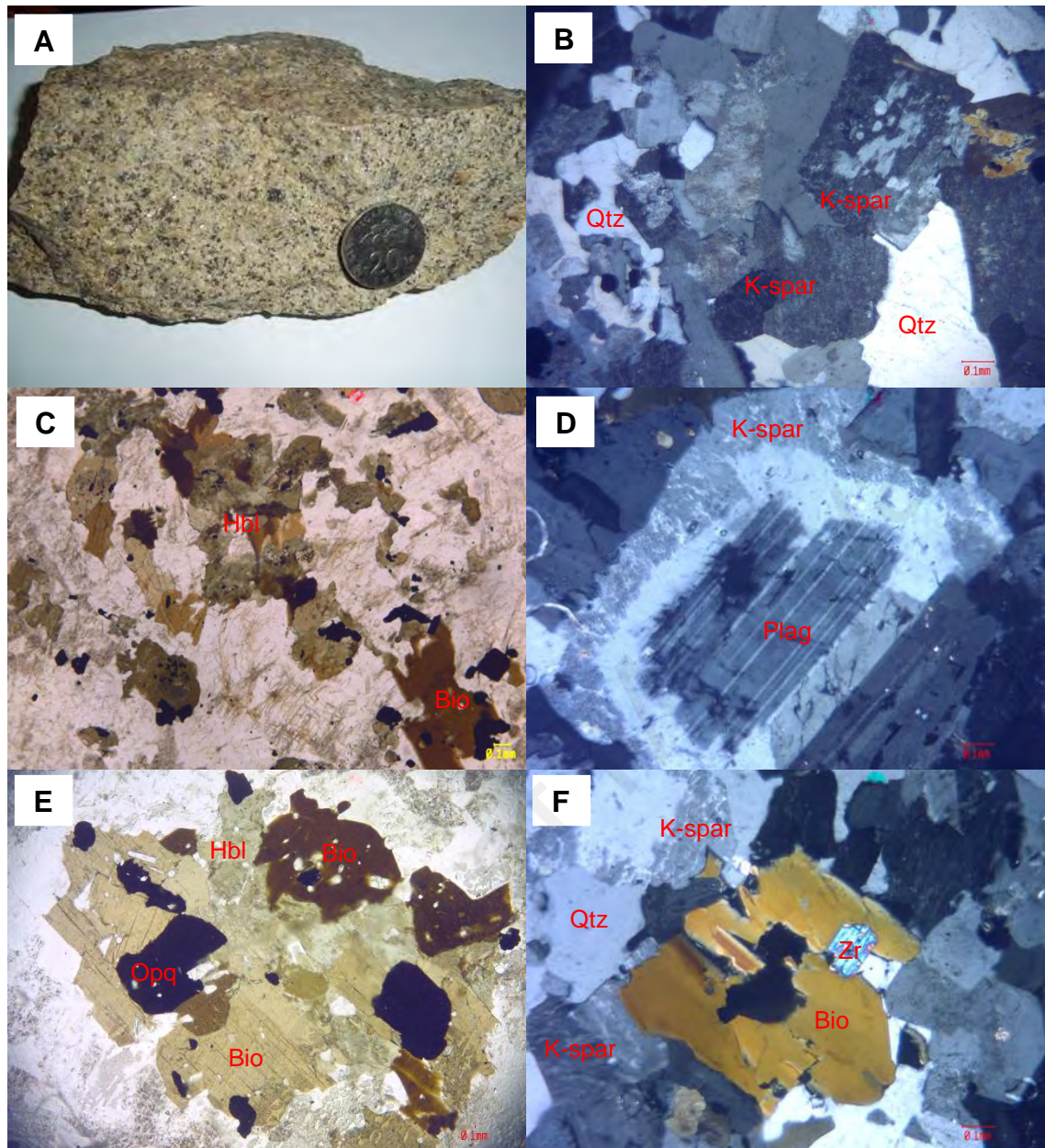
Figure   3.5

(a)   Hand specimen of granodiorite sample from Teluk Meriam
(b)   Photomicrograph showing hypidiomorphic granular texture observed in granodiorite, notice the typical spatial distribution of K-feldspar and quartz.
(c)   Photomicrograph showing abundances of hornblende and biotite, some of the hornblende has been altered to biotite. Opaque oxide can be seen abutted against the grains of biotite and hornblende.
(d)   Photomicrograph showing anti-rapakivi texture where occurrences of plagioclase feldspar with polysynthetic twinning are ringed by K-feldspar.
(e)   Photomicrograph showing mafic clots of subhedral-anhedral biotite and hornblende associations. Opaque oxide can be seen enclosed within the mafic clot.
(f)   Photomicrograph showing subhedral biotite with euhedral individual zircon and opaque oxide fully enclosed in it.
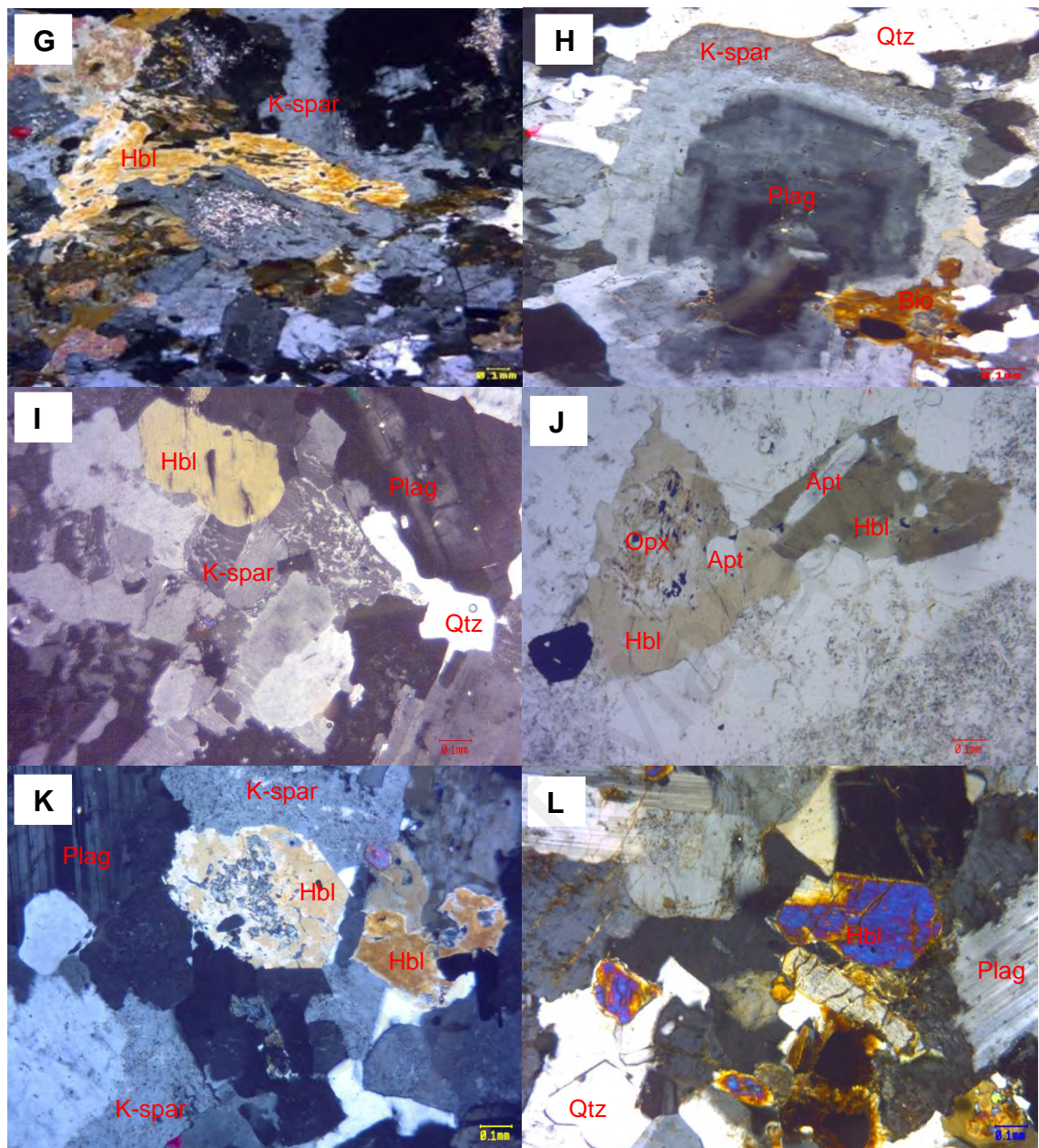
Figure 3.5 (cont.)

(g)   Photomicrograph showing plagioclase which has been highly sericitized at the center, resulting in occurrences of secondary muscovite.

(h)   Photomicrograph showing plagioclase feldspar showing zoning are ringed by K-feldspar, anti-rapakivi.

(i)   Photomicrograph showing irregular, mottled appearance of K-feldspar, showing perthite texture.

(j)   Photomicrograph showing anhedral hornblende on the left has overgrown, or replaced, part of euhedral prism of orthopyroxene. Inclusions of prismatic needle shape and hexagonal apatite inside hornblende. Notice the abundances of apatite.

(k)   Photomicrograph showing inclusions of plagioclase inside a subhedral hornblende.

(l)   Photomicrograph showing euhedral individual crystals of hornblende showing maximum interference colour. Anhedral biotite can be seen closely associated with the hornblende at the center lower part of the photograph

60

3.3.4 Aplite Veins

Aplite veins are found at Dayang Island, across the diorite body. The aplitic veins have varying orientation and thickness, with its thickness ranging from 5 cm to 10 cm and the lateral dimensions of the aplite vein extends about 5m. The colour is light grey, very fine grain, giving 'sugary texture' appearance to the rock.

Microscopically, aplite has the same composition as granite, and it shows the typical hypidiomorphic granular texture. The main mineral compositions of aplite are quartz, alkali feldspar and plagioclase feldspar. Biotite is the only mafic mineral found and apatite and opaque oxide are the only accessory minerals observed. Quartz and alkali feldspar found are usually anhedral while the plagioclase and biotite are typically subhedral to euhedral in shape.

Quartz constitutes about 65 % of the rock composition, with size ranging from 1.0 mm to 3.5 mm. It is anhedral in shape and sometimes occurs as interstitial within other minerals. K-feldspar is subhedral to anhedral with size range from 1.0-3.0 mm. It shows typical frosted surface and grey colour. K-feldspar shows distinct microperthite texture. Plagioclase feldspar is euhedral to subhedral, with size relatively smaller than the alkali feldspar. Plagioclase size range from 0.5 to 2 mm, showing normal zoning and polysynthetic twinning is sometimes clearly observed.

Biotite size ranges from 0.2 mm 1.0 mm and it can be found in two occurrences, (1) as a smaller inclusion inside plagioclase feldspar; (2) individual subhedral mineral. Biotite found is less than 8% of the total composition and it is randomly distributed within the rock. Based on petrographic observation on the contact between the aplite dike and the diorite host and the texture observed, the aplite dikes are magmatic in origin.
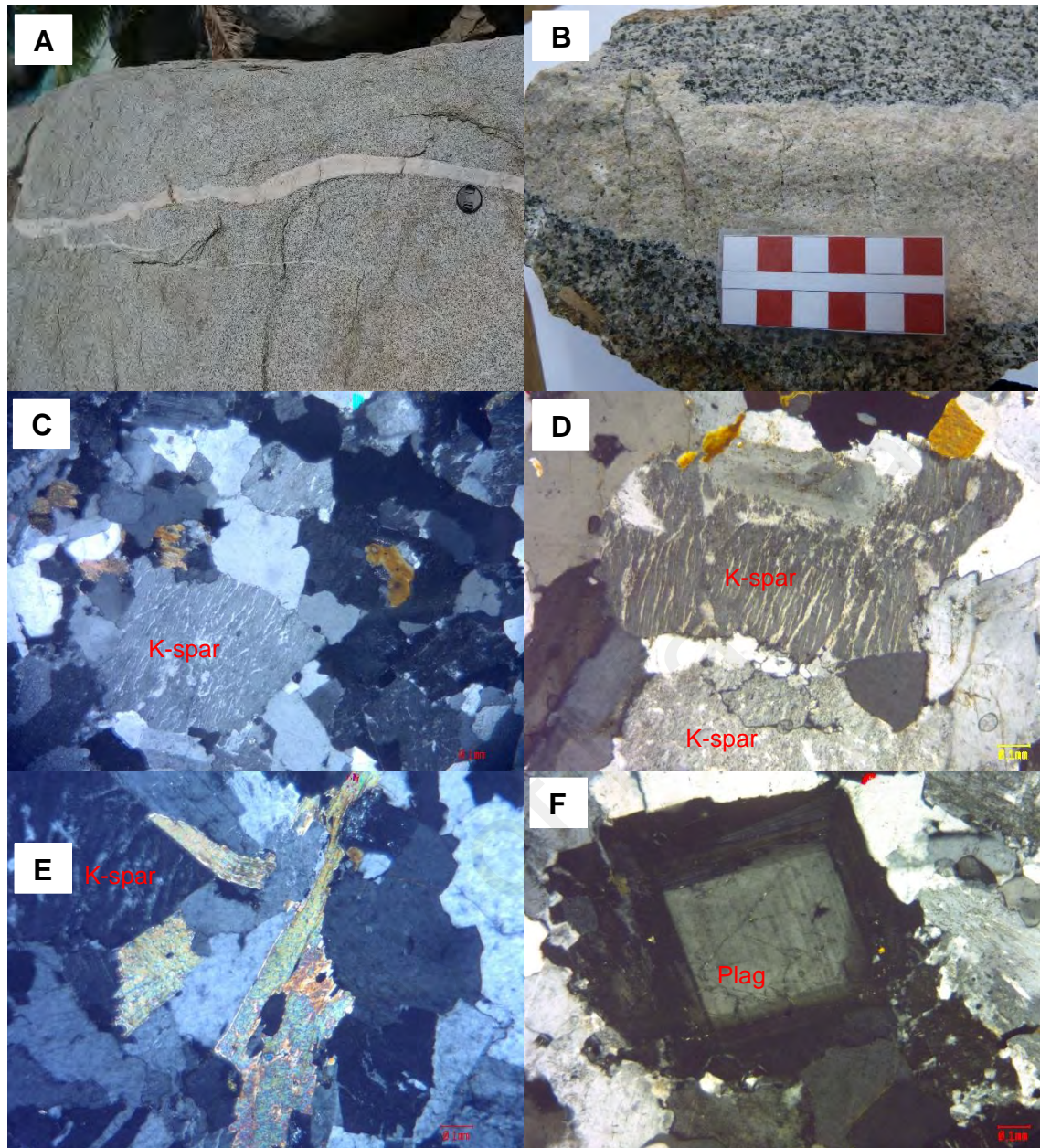
Figure 3.6

(a)   The extend of aplite cutting through the diorite body in Dayang Island.
(b)   Close up view of the aplite vein, notice the lighter colour and finer grain size of the aplite dike.
(c)   Photomicrograph showing hypidiomorphic granular texture observed in thin section. (XN: 5X)
(d)   Photomicrograph showing perthite texture shown by K-feldspar (XN: 10X)
(e)   Photomicrograph showing subhedral elongated biotite, showing maximum birefringence and bird's eye extinction (XN: 5X)
(f)   Photomicrograph showing subhedral plagioclase feldspar showing a distinctive pattern of rectangular-shaped zoning is surrounded with alkali feldspar showing perthitic texture and quartz, (XN: 10X)
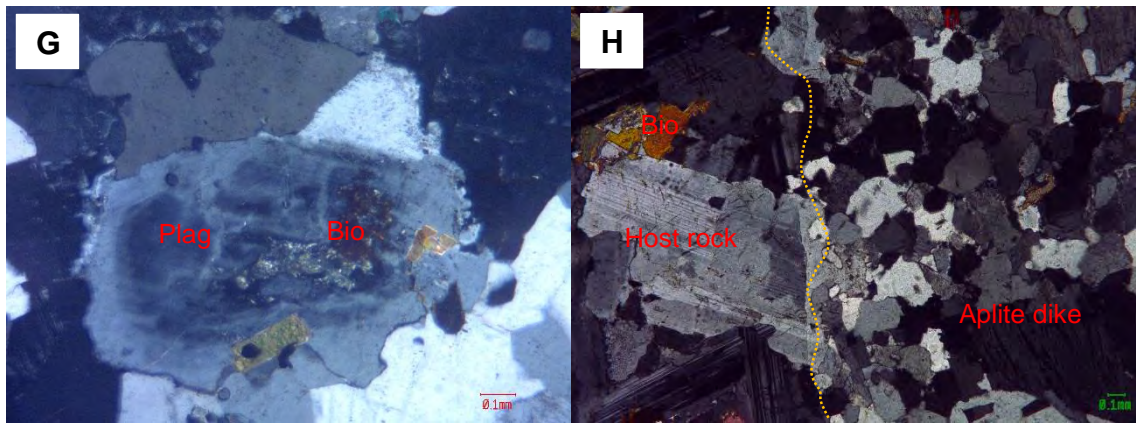
Figure   3.6 (cont.)

(g)   Photomicrogrph showing small euhedral biotite inclusions inside plagioclase showing zoning (XN: 10X)

(h)   Photomicrograph showing contact between aplite dike on the right side and the host rock, diorite on the left side. Notice that the aplite is much smaller in grain size compared to the porphyritic diorite. (XN: 5X)

3.3.5   Mafic Microganular Enclaves (MME)

Mafic microgranular enclaves are common in calc-alkaline granitoids (Didier and Barbarin, 1991). Although the enclaves represent only 1-2 vol% of granitoid plutons, the study of such inclusions is a valuable tool to investigate the initiation and evolution of calc-alkaline granitoid magmas. MMEs are commonly found in the Eastern Belt, where the occurrences of the MMEs are usually from 1-50 cm in diameter, finer grained, darker coloured, and showing sharp contacts with the host rock (Kumar, 1995).

Microgranular enclaves in host rocks are commonly interpreted as the product of mixing and mingling of mantle- and crust derived magmas (Vernon, 1983, 1991; Dorais et al., 1990; Castro et al., 1990; Barbarin and Didier, 1992 and Kumar et al., 2004). Petrographic evidence of enclaves are important as to differentiate enclaves from the residues of partial melting or samples of unmelted, refractory materials from the source region (restite); (Chappell, 1996; White and Chappell, 1977; Chen et al., 1989). However, to distinguished the existence of the MMEs and the host rock, detailed chemical and isotopic compositions of both enclaves and host rock are important, but for the means of this study, only the petrographical aspects of the enclaves will be studied.

MME are widespread and can be found in abundance within the rock bodies throughout Pulau Aur. It can be found in the quartz monzodiorite bodies on the northern part of Pulau Aur, and also towards the southern part, enclosed within the most evolved rock in study area, the granodiorite. MME can be distinguished macroscopically in which they are finer grained, and darker coloured compared to their host rock. The size of the MME range from 3 cm to almost 30 cm. Contacts between the MME and host rock are sharp and rounded. The shapes of the MME are well rounded, ellipsoidal, flattened and even sub-angular in shape. All these macroscopic features of the MME suggest the plastic behaviour at the moment of their incorporation into the host magma are due to the plastic rheology of the MME (Frost and Mahood, 1987, Poli and Tommasini, 1991)

Petrographic observation shows that the MME are diorite in composition with similar mineral assemblages as the host rock, but in different proportions, and the MME are porphyritic under petrographic observation. The MMEs contain higher ferromagnesian phases (orthopyroxene, hornblende, biotite) and plagioclase, but lower in quartz and K-feldspar than those of the host rocks. They are composed of plagioclase (55-70%), hornblende (5-15%), biotite (3-15%), pyroxene (5-10%), orthoclase (2-6%), quartz (2-6%) and opaque oxide and apatite as the accessory phases. Contacts between the MMEs and host rock on petrographic observation have granular fine grained magmatic textures with decreasing crystal size of the MMEs towards the contact.

Plagioclase in the MMEs occur as anhedral to subhedral, rounded and corroded phenocryst and in the matrix as plagioclase laths. The size range of the plagioclase phenocrsyt are 1.5 mm to 2.5 mm. It normally shows diffuse lamellae twin, sharply defined polysynthetic albite twin and sometimes zoning.

Mafic minerals consist of orthopyroxene, hornblende and biotite that occur as smaller subhedral to anhedral crystal within the groundmass and sometimes found as inclusions, enclosed within the plagioclase phenocryst. Orthopyroxene, hornblende and biotite are often found together forming mafic clots.

Accessory minerals include apatite and opaque oxide. Interestingly, apatite in the MMEs tend to be acicular, needle like shape and rarely as stubby hexagonal inclusions as in the host rock. The presence of acicular apatite as inclusions in plagioclase reflect on the rapid cooling of MMEs and the magma mixing processes associated during the generation of the MMEs (Poli and Tommasini, 1991). The enclaves show minor alteration of feldspar to sericite. and opaque oxide occurrences along cleavage and as inclusions are common.
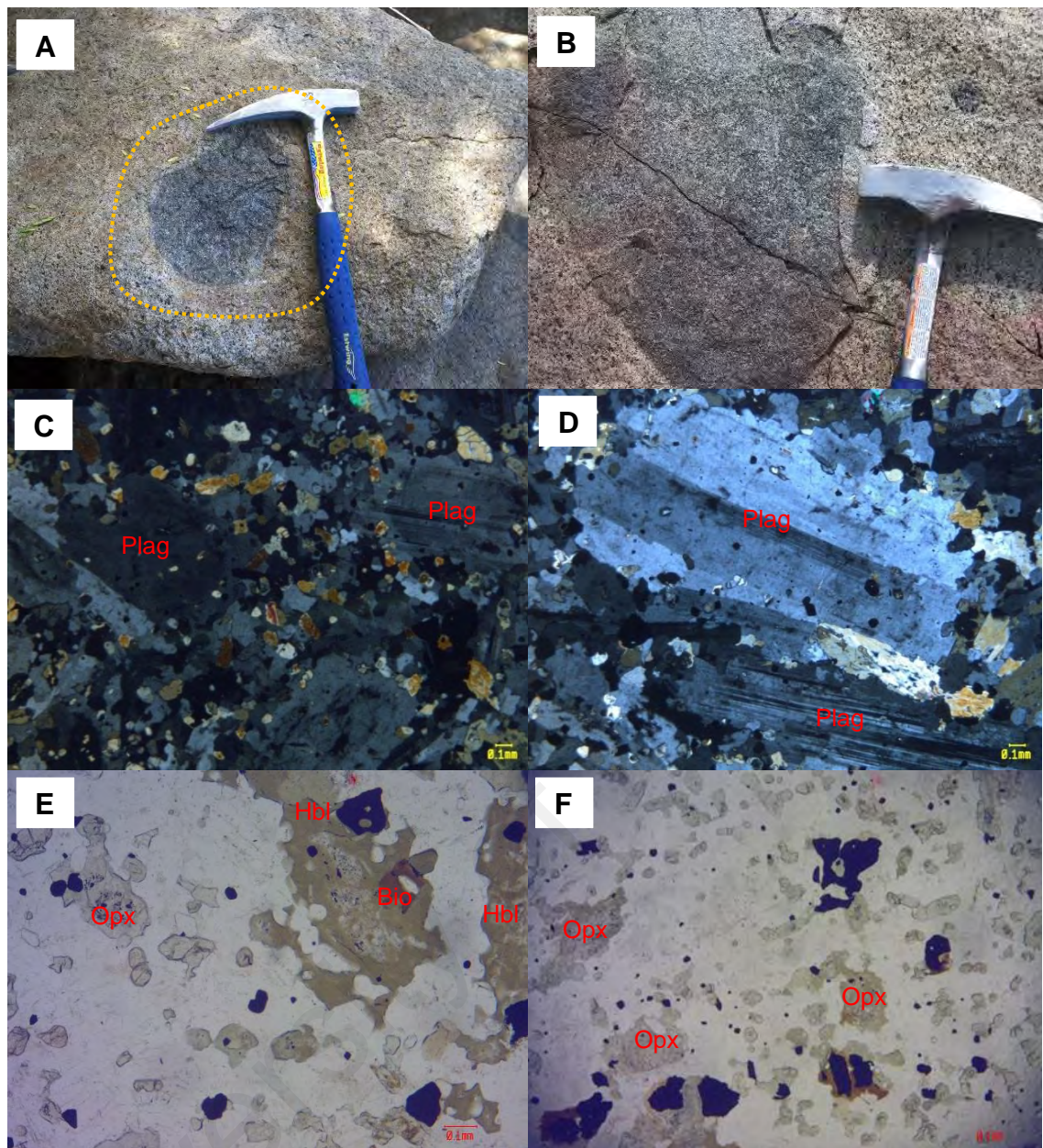
Figure 3.7

(a, b)   MMEs observed in rock outcrop, rounded, showing sharp contacts with host rock.

(c)   Photomicrograph showing porphyritic texture observed of the MME where plagioclase usually forms as the phenocryst, within the groundmass of finer grained subhedral to anhedral biotite, hornblende, quartz and K-feldspar.

(d)   Photomicrograph showing large plagioclase phenocryst, where the edges of the plagioclase crystal are serrated and abutted by other minerals.

(e)   Photomicrograph showing mafic mineral association, biotite as inclusions in pyroxene-hornblende pseudomorph, where original orthopyroxene are completely enclosed by hornblende.

(f)   Photomicrograph showing spatial distribution of mafic mineral and opaque oxide within the groundmass.

3.4   Discussion of petrographic observation

The lithology of study area, Aur and the surrounding islands (Dayang and Lang) consist entirely of plutonic rocks, without any association of volcanic or metamorphic rock. Based on petrographic observation of the mineralogy and texture observed in the dioritic rocks from study area, the rocks have undergone slow cooling and long crystallization history, producing ranges of intermediate rock in composition; (1) diorite (2) quartz monzodiorite and (3) granodiorite.

The contacts between these three types of rock could not be distinguished clearly on field, but based on petrographic observation, the rocks are grading from a more mafic composition (diorite and quartz monzodiorite) at the northern part, with clinopyroxene and orthopyroxene as the major mafic phase, towards a more felsic composition (granodiorite) at the southern part, where the mafic constituent are dominated by hornblende and biotite.

Overall, the mineralogy of dioritic rocks from study area have more or less the same mineral assemblages, but in different amounts. Based on modal mineralogy and mineral assemblages, the dioritic rocks from study area form two different units, (1) the mafic-end member with clinopyroxene as its mafic constituent for diorite and quartz monzodiorite, and (2) the felsic-end member: granodiorite, where the main mafic phase are hornblende and biotite.

Among the distinguishing characteristics that can be observed between the two members are: (1) the dominant mafic phases (2) ophitic and sub-ophitic texture observed in diorite and quartz monzodiorite (3) perthite texture observed in granodiorite and (4) anti-rapakivi texture observed in granodiorite.

Diorite and quartz monzodiorite are quite similar in texture and colour indexes but there is an obvious different amount of K-feldspar, quartz and the mafic minerals amount under petrographic observation. Clinopyroxene prevails over orthopyroxene in diorite

and quartz monzodiorite. Hornblende and biotite are only subordinate to clinopyroxene, lesser in amount in both types of rock. Ophitic and sub-ophitic texture, typical texture of mafic rocks where large ferromagnesium minerals, clinopyroxene encloses random plagioclase laths are often observed in these mafic-end members. Hornblende are anhedral in shape, occurring along the edges of the earlier formed clinopyroxene. Hornblende might have form from the alteration of clinopyroxene. One distinct difference are the occurrences of hornblende in isolated, individual forms showing the characteristic 124/56 cleavage with subhedral-euhedral shape in quartz monzodiorite, which are not observed in diorite.

Granodiorite show different mineral assemblages, where there is no occurrences of clinopyroxene and the lack of individual orthopyroxene. Orthopyroxene are only found as remnants in a hornblende pseudomorph, having no crystal shape. Granodiorite major mafic phases are well-formed biotite and hornblende. Anti-rapakivi texture, an important magma mixing texture where plagioclase are ringed by K-feldspar are only observed in granodiorite. This occurrences of anti-rapakivi texture might have given a clue on the magma mixing processes that might play an important role during magmatic evolution of the dioritic rocks from study area. Perthite texture is only observed in granodiorite, suggesting that the magma forming granodiorite was more siliceous and richer in sodium and potassium. Perthite formed due to exsolution or unmixing of alkali feldspar, which is the process of K-feldspar separation due to different compositions at low temperature or below the temperature of solidus. During cooling, homogenous melt will be separated into two phases, which is (1) Na-rich solidus phase and (2) K-rich solidus phase, following the solvus curve. Perthite is albite (Na-rich) inside orthoclase (K-rich), where albite forms exsolution lamellae. Based on this, the cooling process is slow, whereby permitting this texture to occur and perthite texture further supports that the magma comes from the melting of igneous source material.

Minerals that have euhedral shape or as inclusions in other minerals are early crystallising minerals, having enough spaces to crystallized, thus forming perfect euhedral shape. Minerals that crystallizes later, forming interstitially between other minerals are subhedral to anhedral in shape, as these minerals have no free space to form perfect crystal faces. (Shand, 1950). As magmatic evolution proceeds and slow cooling of magma takes place, crystals that grow and form eventually touching and coming into contacts with each other, preventing crystal faces from forming properly or at all.

Plagioclase is the first major mineral to crystallize based on their euhedral lath shape and there is occurrences of plagioclase as inclusions in other minerals, such as clinopyroxene and orthopyroxene, forming ophitic texture. Plagioclase exist in ranges of temperature and zoning of plagioclase can be observed occurring in all the different rock types at study area. Zoning in plagioclase can be seen because of the different extinction angle of albite and anorthite when rotated under crossed nicol. Zoning indicates fractional crystallization that plays an important role during magmatic evolution. It occurs due to lowering of temperature during magma cooling, resembling the unstable condition during crystallization, and plagioclase zoning is an indicator of thermal history of rock crystallisation (Shelley, 1993; Vernon et al., 2004).

Mafic mineral that is the first to crystallize are; clinopyroxene, orthopyroxene, followed by hornblende and biotite. This is evident by the occurrences of hornblende rim around pyroxene. This replacement of clinopyroxene by hornblende or mantling process occur due to abrupt changes in temperature during crystallization. Clinopyroxene that have crystallized earlier reacted with the remaining magma, forming hornblende, as observed in diorite and quartz monzodiorite. The time of which clinopyroxene, orthopyroxene, hornblende and biotite crystallized might be long enough to produce ranges of shape, from euhedral to anhedral crystal. The lack of clinopyroxene and

individual crystal of orthopyroxene in granodiorite might reflect the different magma composition forming that of granodiorite.

Three distinct types of biotite can be distinguished petrographically: (1) dark brown laths and euhedral crystals with textural relationships that suggest they are probably early formed and magmatic in origin; (2) brown to red-brown laths or aggregates that replace clinopyroxene or hornblende; and (3) colorless to light-brown laths which are more phlogopitic in composition and which form veins and replacements (Ayres and Bamford, 1976). The occurrences of biotite in rocks found at study area are type (1) and (2). Biotite of type (1) is found as individual, subhedral to anhedral shape while type (2) is anhedral, and often found associated with clinopyroxene and hornblende. Biotite crystallizes after hornblende and it occurs along the edge of hornblende crystal. This shows that hornblende might have altered to biotite during crystallisation.

During the crystallization of early minerals; plagioclase, pyroxene, hornblende and biotite, the elements of calcium, magnesium and ferum are being used up, causing the remaining magma melt to be richer in siliceous and alkaline material. Quartz and K-feldspar are among the last minerals to crystallize, forming between the earlier formed minerals, occurring interstitially and anhedral in shapes. The crystallization of the minerals of the rocks from study area follows that of the Bowen Series.

Accessory minerals such as apatite, zircon and opaque mineral are among the earliest mineral to crystallize, having euhedral to subhedral shape. Opaque mineral are found randomly distributed and abundance in all the three different rock types. It can be found as inclusions in other minerals; hornblende, plagioclase, biotite, quartz and alkali feldspar. Zircon are rarely found in diorite, and only found in small amount and shapes. During the early crystallization stage, the magma contains high percentages of elements such as phosphorus and zirconium, thus allowing the formation of apatite and zircon as accessory minerals in the rock.

Hydrothermal alteration and metasomatism processes are evident from the occurrences of secondary minerals; chlorite and sericite. Chlorite forms from alteration of ferromagnesium mineral e.g. orthopyroxene, hornblende and biotite, and can be observed in quartz monzodiorite and granodiorite. Sericite, alteration product of feldspars that appears as fine grained dust in feldspar can be seen common in the three rock types. Sericite is often found occurring at the center and rims of plagioclase grain. Sericitization occur mostly at the centre of plagioclase which is more calcic in composition, when K+ cation brought by hydrothermal solution enters the fractured plagioclase, causing the replacement of Ca2+ ion by K+. Sericitization occurs more easily in zoned plagioclase in a magma rich with anorthite content and hydrothermal solution, followed by metasomatism process (Shelley,1993). Sericitization are more intense in granodiorite, possibly reflecting the stronger metasomatism processes that may have affected the rock.

3.5 Summary

Based on petrographic observation, several conclusions can be made:

1. QAP modal classification shows that the dioritic and intermediate rocks from study area consisted of (i) diorite, (ii) quartz monzodiorite and (iii) granodiorite.

2. Based on modal mineralogy and mineral assemblages, the rocks from study area form two different units; (1) the mafic-end member with clinopyroxene as its major mafic constituent for diorite and quartz monzodiorite, and (2) the felsic-end member: granodiorite, where the main mafic phase are made up of hornblende and biotite.

3. Among the distinguishing characteristics that can be observed between the two members are: (1) the difference of major mafic mineral phases (2) ophitic and sub-ophitic texture observed in diorite and quartz monzodiorite (3) perthite and anti-rapakivi texture observed in granodiorite.

4. Magma from which the two-end members have crystallised are I-type, coming from igneous source melt, due to the presence of major minerals like: clinopyroxene, hornblende, biotite, and accessory minerals like: sphene and apatite.

5. The magma from which the mafic-end member unit crystallizes are much more mafic, resembling possible mantle source contribution, due to the abundances of clinopyroxene as its major mafic phase. Clinopyroxene is dominant mafic minerals in diorite and quartz monzodiorite, but totally disappears in granodiorite.

6. The more felsic-end member: granodiorite are more siliceous and richer in alkaline minerals due to the presence of perthite, anti-rapakivi texture, and the increasing abundances and size of quartz and K-feldspar observed in granodiorite. The major mafic phase are made up of hornblende and biotite.

7. The presence of anti-rapakivi texture, an important magma mixing texture where plagioclase are ringed by K-feldspar are only observed in granodiorite. This occurrences of anti-rapakivi texture might have given a clue on the magma mixing processes that

might play an important role during magmatic evolution of the dioritic rocks from study area. (Hibbard, 1995)

8.   MMEs are diorite/gabbro in composition, having similar mineral assemblages as the host rock, but in different proportions, and the MME are porphyritic under petrographic observation. MME occurrences that can be found abundance within the rock bodies throughout Aur Island, gives an important clue of the possible magma mixing/mingling between mantle-derived basaltic magma and crustal derived granitic magma.

Table 3.3   Summary of petrographic descriptions of dioritic rocks from study area

Characteristics		Diorite	Quartz Monzodiorite	Granodiorite
Macroscopic Observation				
Grain Size		Phaneritic, medium grained ~ 5 mm	Phaneritic, medium grained ~ 3 mm	Phaneritic, medium grained ~ 3-5 mm
Colour		Light to dark grey	Light to dark grey	Light grey
Field Description		Occupy about 10% of the pluton, Dayang Island	Occupy about 15% of the pluton, covering northern part of Aur Island and Land Island	Occupy about 75% of the pluton, covering central and southern part of Aur Island
Microscopic Observation				
Petrographic Description		Medium grained, hypidiomorphic granular texture Ophitic texture: cpx encloses subhedral-euhedral lath shaped plag are common Sub-ophitic texture: cpx not fully encloses, and plag are only abutted against the edges of cpx Primary mafic phase are cpx	Medium grained, hypidiomorphic granular texture Sub-ophitic texture: opx not fully encloses, and plag are only abutted against the edges of opx	Medium grained, hypidiomorphic granular texture Mafic phases are: well-formed hbl and bio Anti-rapakivi texture, where plagioclase are mantled by K-feldspar
Mafic Phase	Clinopyroxene Amount Size Shape/form Description	9-15% 0.5-3 mm Euhedral-subhedral Prevails over orthopyroxene Associated with bio forming mafic clots In a few samples cpx partially replaced by hbl	3-6% 0.2-2.5 mm Euhedral-subhedral Prevails over orthopyroxene Form as (1) large crystal often associated with bio and hbl or as (2) smaller, broken euhedral to subhedral isolated crystal	Not observed
	Orthopyroxene Amount Size Shape/form Description	1-4% 0.2-2 mm Euhedral-subhedral Only subordinate to cpx	1-6% 0.5-1.2 mm Subhedral-anhedral Only subordinate to cpx	2-3% Anhedral in shape 0.3-1 mm Mantled by hornblende Occurrences as individual crystal are not observed Only found as remnants in a hornblende pseudomorph.
	Hornblende Amount	2-4%	4-8%	9-14%

	Size Shape/form Description	0.2-0.6 mm Anhedral, no crystal shape Partly replaced, may have formed by replacement of cpx	0.4-1 mm Subhedral to anhedral Occurrences of hbl (1) Individual hornblende with visible crystal shape and cleavages can be observed, (2) Hbl associated with opx, probably formed from replacement of opx	0.5-2.5 mm Subhedral to anhedral Occur as individual/ isolated crystal or accompanied by biotite forming mafic clots With inclusions of opaque oxide and apatite
	Biotite Amount Size Shape/form Description	2-5% 0.2-1.2 mm Subhedral to anhedral shape Not found as single individual crystal, rather found associated with cpx and opx, forming mafic clots	3-6% 0.2-1.2 mm Subhedral to anhedral Rarely found as individual crystal, associated with hbl and opx, forming mafic clots Usually encloses anhedral opaque oxide	4-10% 0.4-1.5 mm Subhedral to anhedral Occurrences as isolated, and/or associated with hbl forming mafic clots
Felsic Phase	Plagioclase Amount Size Shape/form Description	66-74% 0.5-3 mm Euhedral-subhedral lath shaped crystals Large plag crystals often contains many inclusions of cpx, opaque minerals Smaller euhedral-subhedral lath shaped plag occur as inclusions inside cpx and opx	53-60% 0.3-1.5 mm Diffuse lamellae twin, sharply defined albite twin Concentric compositional zoning common Euhedral-subhedral lath shaped	47-60% 0.2-0.8 mm Diffuse lamellae twin, sharply defined albite twin Concentric, compositional zoning are common Alteration to sericite are common, fairly intense
	Quartz Amount Size Shape/form Description	2-4% 0.1-0.7 mm Anhedral Interstitial grain	5.8% 0.1-0.7 mm Anhedral Interstitial grain	15-18% 0.03-0.8 mm Interstitial, anhedral in shape Abundant, sparsely distributed
	K-feldspar Amount Size Shape/form Description	2.3% 0.1-0.5 mm Anhedral Interstitial grain	16% 0.1-1.5 mm Anhedral Interstitial grain Increasing amount of K-feldspar than observed in diorite	8-13% 0.1-1.2 mm Perthite texture are common Often altered to sericite, occasionally show intergrowth with quartz Abundant, sparsely distributed
	Zircon	0.3 %	Euhedral-subhedral zircon	Euhedral-subhedral zircon are abundance

Accessory Phases		Small, subhedral grains	Short and small prismatic crystal	Short, small prismatic crystals
	Apatite	Inclusions inside plagioclase, acicular	Acicular apatite are found as inclusions in hbl and bio	Often found as inclusions in hbl and bio Both prismatic and acicular apatite can be observed
	Sphene	Not observed	Not observed	Sphene are common Isolated broken wedge shape, with high relief
	Opaque oxide	Shapes and size are variable, ranging from 0.03-0.2 Usually encloses by bio, as inclusions in other minerals, e.g cpx Subhedral to anhedral	Subhedral-anhedral Associated with other minerals, encloses by biotite, as inclusions in other minerals	Euhedral to subhedral Associated with other minerals, encloses by biotite, as inclusions in other minerals
Secondary/ Alteration Minerals		Minor to weak alteration of plagioclase to sericite Alteration of ferromagnesium to chlorite are rarely observed	Minor to weak alteration of plagioclase to sericite Alteration of ferromagnesium minerals are observed, clinopyroxene and hornblende alterations to chlorite	Alteration of plag and K-spar to fine grain secondary sericite are more intense and common

76

Table 3.3 Summary of petrographic descriptions of rocks from study area (cont.)

Characteristics		Aplite Vein	Mafic Microgranular Enclaves (MME)
Macroscopic Observation			
Grain Size		Aphanitic, fine grained < 1 mm	Aphanitic, fine grained < 1 mm
Colour		Very light grey	Dark grey
Field Description		Aplitic veins having varying orientation and thicknesses are common Very fine grain Sharp contact with host rock	Can be distinguished based on its rounded to sub-angular shape, finer and darker coloured compared to their host rock Size: 3-30 cm Sharp contact between host rock and MMEs
Microscopic Observation			
Petrographic Description		Hypidiomorphic granular texture Similar composition as a granite	Diorite/gabbroic in composition (QAP modal percentages) Similar mineral assemblages as host rock, but in different proportions, MMEs higher in ferromagnesian minerals (opx, hbl, bio) and high percentages of plagioclase Porphyritic texture: plagioclase as phenocryst, and opx, hbl, bio qtz and K-spar as smaller finer grain n the groundmass
Mafic Phase	Clinopyroxene	Not observed	X
	Orthopyroxene	Not observed	8% Size range: 0.1-1.0 mm Subhedral to anhedral Occur as smaller individual crystal within groundmass, or associated/mantled by hornblende
	Hornblende	Not observed	9.7% Subhedral to anhedral Often associated with orthopyroxene and biotite
	Biotite	7% Size range 0.2-1.0 mm Can be found as inclusions inside plagioclase and as individual subhedral mineral	9% Anhedral Occasionally alteration to chlorite are common
Felsic Phase	Plagioclase	39% Subhedral to euhedral in shape	67% Subhedral to anhedral shape, 1.5-2.5 mm

		0.5-2 mm, size relatively smaller than K-spar Polysynthetic albite twin, and zoning are common,	Irregular contacts of large plag phenocrsyt are common, edges of plag are serrated and abutted by smaller minerals Often contains inclusions of other minerals (hbl, opx, opaque oxide)
	Quartz	32% Anhedral in shape, interstitial between other minerals 1-3.5 mm	2% Lower compared to host rock Anhedral, interstitial between other minerals that makes up groundmass
	K-feldspar	26% Anhedral in shape, interstitial between other minerals 1-3 mm Microperthite texture common	3% Lower compared to host rock Anhedral, interstitial between other minerals that makes up groundmass
Accessory Phase	Zircon	Not observed	Not observed
	Apatite	Apatite, long acicular apatite can be observed as inclusions in plagioclase	Long, acicular apatite as inclusions in plagioclase Rarely stubby/prismatic apatite as seen in host rock
	Sphene	Not observed	Not observed
	Opaque oxide	Anhedral in shape Usually associated with biotite, as inclusions in biotite or other minerals, e.g. K-spar	Abundant opaque oxide Small, subhedral to anhedral opaque oxide along cleavages and as inclusion in other minerals

CHAPTER 4: GEOCHEMISTRY

4.1 Introduction

This Chapter will discuss the petrogenesis and genetic relationship of the varieties of dioritic rocks from study area based on geochemical data that have been obtained. Description of geochemical attributes will be described to study the origin, type and evolution of crystallising magma.

4.2 Methodology/Analytical Techniques

For whole rock major and trace element geochemical analyses, thirty samples were selected carefully from Aur Island, and the nearby islets, Dayang and Lang. $1 - 3$ kg of the fresh rock samples were crushed in jaw crusher. The samples were then grinded to a fine powder using tungsten swing mill at the Department of Geology, University of Malaya, Kuala Lumpur, Malaysia.

Whole rock geochemistry compositions were determined at ACME Analytical Laboratories Ltd. in Vancouver, Canada. Major element compositions were obtained by X-ray fluorescence (XRF) while other trace elements and rare earth elements (REE) were determined by inductively couple plasma spectrometry (ICP-MS). Major elements were determined by XRF using a Philips PW 1404/10 X-ray spectrometry by fusing with lithium tetraborate and casting into glass discs. The trace elements Zr was also measured by X-ray fluorescence using pellets of pressed rock powder. Precision was of 2-5% for major elements, except Mn and P (5-10%) and for Zr, (2-5%).

ICP-MS has been successfully used for direct determination of trace elements in geological samples. It is a powerful and sensitive tool to determine total metal content in rocks and it is required to use sample preparation methods that result in the total dissolution of the sample. Hydroflouric (HF) and nitric acids (HNO_3) were used for the digestion of silicate samples. Both HF and HNO_3 are easily purified by sub-boiling

distillation to give low reagent blanks and correspondingly low analyte limits of detection. The use of HF and HNO_3 for digestion of silicate samples is well established and has been applied to the dissolution of basalts, soils and other rocks. Use of this approach is however problematic since Zr and Hf do not always go into solution. Granites often contain accessory minerals such as zircon, which are very difficult to dissolve (Liang et al. 2000).

4.3   Geochemical Results

Whole rock major and trace elements data for the selected 30 samples of dioritic rocks from study area are listed in Table 4.1. These samples were collected from the diorite (4), quartz monzodiorite (12), granodiorite (13) and aplite dike (1). The range and mean of SiO_2 (in percentages) of the different units of the dioritic rocks are: diorite (54.6-55.6), quartz monzodiorite (56.1-59), granodiorite (61-65.7) and aplite dike (70.4). SiO_2 content increases from diorite→quartz monzodiorite→granodiorite.

Major oxide elements that have been obtained are SiO_2 (54.6-65.7%), Al_2O_3 (15.36-17.06 %), Fe_2O_3 (4.7-8.32%), CaO (2.68-7.65 %), MgO (1.4-4.05 %), Na_2O (4.15-4.97 %), K_2O (1.76-4.64 %), TiO_2 (1.02-1.44%), P_2O_5 (0.27-0.66%) and MnO (0.05-0.16%).

Trace elements concentrations (in ppm) that have been obtained for the rocks are; Ba (606-1134), Rb (41.7-174.7), Sr (378.8-1297.6), U (1.2-5.2), V (73-208), W (0.7-5.1), Zr (118.1-450.6), Y (24.4-44.6), Ta (0.4-1.2), Th (4.3-21.2), Cu (9.5-51.6), Pb (2.3-28.5), Zn (17-77), Ni (4.2-14.3), Ga (16.1-18.8), Nb (8.9-19.4), Co (7.9-22.9), Cs (1.2-10.5), Hf (3.6-11.7), Mo (0.6-7.2), Be (1-4), Sn (<1-4), and As (0.7-8.6).

From the geochemical data, the normative values and recalculation for chemical ratios and elements are being also calculated using the CIPWNORM program, result shown in Table 4.2.

4.4 Major and Trace Elements Geochemistry

Dioritic rocks of study area distinguished earlier based on petrographic observation (Chapter Three) are diorite, quartz monzodiorite and granodiorite. The range and mean for major and selected trace elements for these three different rocks are shown in Table 4.3. The range of SiO_2 for the rocks are: diorite (54.6-55.6%), quartz monzodiorite (56.1-59 %) and granodiorite (61-65.7 %). Although the range of SiO_2 does not overlap between different rock types, diorite and quartz monzodiorite show similar range and values for most major and trace elements concentration. Granodiorite however, shows a significantly different composition.

From Table 4.3, it can be seen that granodiorite has a significantly lower amount of Fe_2O_3, CaO, MgO, with an average of 5.46, 3.33 and 1.75 respectively. Both diorite and quartz monzodiorite have higher average value for these three major elements, where Fe_2O_3 for diorite and quartz monzodiorite respectively are 8.21 and 7.44, CaO; (diorite: 7.54, quartz monzodiorite: 5.83) and MgO (diorite: 4, quartz monzodiorite: 3.27). K_2O and Na_2O are the highest in granodiorite, with an average of 4.5 and 4.21 respectively. This gives the high TAS content in granodiorite, ranging from 8.49 to 8.91 %. Most trace elements concentrations such as Ba, Rb, Zr, Nb, Pb, Th are the highest in granodiorite, with a significantly low Sr concentrations. Sr content for granodiorite ranges only from 378.8 to 545 ppm. The high K_2O, Na_2O and Ba contents reflect the abundance of K-feldspar and biotite in granodiorite compared to the other two rocks.

Table 4.1 Major (wt. %) and trace elements (ppm) data

Sample	PD2	PD1	PD4	DYG1	DYG2	LANG1	LANG4A	LANG4B	LANG8	BAIL1A
Rock type	Dike	Dr	Dr	Dr	Dr	QMzd	QMzd	QMzd	QMzd	QMzd
SiO_2	70.4	55.7	55.6	54.6	55	57.5	58.6	57.8	58.1	57.7
Al_2O_3	14.2	17.06	16.94	16.95	16.79	15.97	16.15	15.7	16.01	16.72
Fe_2O_3	2.78	8.08	8.32	8.2	8.22	7.91	7.56	8.15	7.88	7.07
CaO	2.25	7.65	7.59	7.55	7.34	5.72	5.62	5.72	5.6	5.97
MgO	1.03	3.99	4.05	4.03	3.95	3.3	3.15	3.18	3.25	3.49
Na_2O	3.71	4.2	4.13	4.2	4.15	4.31	4.42	4.34	4.39	4.21
K_2O	4.87	2.12	2.17	1.94	2.11	2.63	2.69	2.73	2.69	2.6
MnO	0.05	0.14	0.14	0.13	0.14	0.13	0.13	0.13	0.13	0.12
TiO_2	0.55	1.3	1.29	1.27	1.29	1.27	1.25	1.44	1.3	1.13
P_2O_5	0.18	0.64	0.66	0.63	0.52	0.56	0.52	0.59	0.52	0.4
LOI	0.18	0	-0.02	0.01	0.02	0.15	0.23	0.15	0.22	0.24
TOTAL	100.2	100.88	100.87	99.51	99.53	99.45	100.32	99.93	100.09	99.65
A/NK	1.25	1.85	1.85	1.88	1.84	1.61	1.59	1.56	1.58	1.72
A/CNK	0.92	0.74	0.74	0.75	0.75	0.79	0.79	0.77	0.79	0.81
Na_2O/K_2O	0.76	1.98	1.9	2.16	1.97	1.64	1.64	1.59	1.63	1.62
TAS	8.58	6.32	6.3	6.14	6.26	6.94	7.11	7.07	7.08	6.81
mg#	42.33	49.45	49.09	49.33	48.77	45.27	45.22	43.6	45	49.44
Ba	563	801	763	682	662	720	749	744	743	634
Be	3	2	1	<1	2	3	1	3	2	4
Co	6.1	22.9	22	21.5	20.5	20.5	17.2	18.8	17.9	18.4
Cs	4.9	1.6	2	1.2	1.9	2	3.1	1.9	2.4	2.2
Ga	14.5	17	17.5	18.5	18.7	18.4	17.8	17.9	18.7	18.7
Hf	6.8	5.2	3.7	4	4.2	3.6	4.4	6.4	5.2	5.7
Nb	15.5	10.1	11.1	8.9	9.6	11.8	12.4	13.2	11.3	11.4
Rb	201.8	51.1	54.8	41.7	46.8	63.9	69.1	66.8	65.5	68.4
Sn	2	2	2	<1	1	2	2	2	2	2
Sr	423	1260.5	1297.6	1201.7	1155.4	760.7	755	757.3	770.9	640.7
Ta	1.1	0.5	0.6	0.5	0.4	0.6	0.7	0.7	0.7	0.7
Th	29	6	5.9	4.7	4.6	7	8.3	7.3	7.1	8.9
U	5.3	1.4	1.4	1.2	1.3	1.7	2.1	2.2	2.1	2.1
V	55	208	199	151	137	130	118	143	127	115
W	4.4	3.7	0.7	1.1	0.7	1.2	0.8	1.2	1.2	1.8
Zr	180.1	195.1	118.1	214.9	205	146.7	207.2	331.2	238.2	269.9
Y	26.2	26.6	25.4	25.4	26.2	30.4	29.3	31.7	32	26.3
Mo	0.7	0.6	1	1	0.9	1.5	1.5	1.3	1.1	1.3
Cu	10.3	31.8	39.1	33.4	44	29	28.7	29	23.8	20
Pb	7.9	3.1	2.8	2.4	2.7	3.6	3.1	2.6	2.7	2.6
Zn	17	27	26	30	33	29	26	25	22	29
Ni	4.5	10.5	12.8	12	12.3	14.3	11.3	10.2	11.2	17
As	1	1.1	1	0.7	0.9	0.7	0.9	0.9	0.8	1.1

Table 4.1 Major (wt. %) and trace elements (ppm) data (cont.)

Sample	BAIL1B	BAIL2	BAIL3	BER3	BER8	TBO5	TBO6	TBO3	TBO4	TM3
Rock type	QMzd	QMzd	QMzd	QMzd	QMzd	QMzd	QMzd	Gd	Gd	Gd
SiO_2	57.6	59	57.7	57.4	57.7	56.1	56.9	63.6	62.1	62.6
Al_2O_3	16.85	16.67	16.91	16.9	16.61	16.91	16.55	15.84	15.82	15.72
Fe_2O_3	7.04	6.65	7.18	6.95	7.33	7.89	7.63	5.21	5.76	5.5
CaO	6.11	5.45	6.16	5.87	5.64	6.53	5.52	3.4	3.43	3.21
MgO	3.59	3.05	3.65	3.14	2.91	3.51	3.07	1.66	2	1.72
Na_2O	4.33	4.39	4.44	4.52	4.41	4.88	4.55	4.5	4.45	4.48
K_2O	2.48	2.89	2.41	2.67	2.76	1.76	3.57	4.27	4.1	4.32
MnO	0.12	0.12	0.12	0.12	0.12	0.16	0.15	0.11	0.11	0.1
TiO_2	1.06	1.02	1.06	1.17	1.34	1.4	1.39	1.09	1.16	1.07
P_2O_5	0.37	0.37	0.39	0.37	0.46	0.51	0.47	0.34	0.37	0.35
LOI	0.04	0.15	0.01	0.21	0.15	0.55	0.58	0.44	0.83	0.49
TOTAL	99.59	99.76	100.03	99.32	99.43	100.2	100.38	100.46	100.13	99.56
A/NK	1.72	1.61	1.71	1.64	1.62	1.7	1.46	1.32	1.35	1.3
A/CNK	0.81	0.82	0.8	0.8	0.81	0.78	0.77	0.87	0.88	0.88
Na_2O/K_2O	1.75	1.52	1.84	1.69	1.6	2.77	1.27	1.05	1.09	1.04
TAS	6.81	7.28	6.85	7.19	7.17	6.64	8.12	8.77	8.55	8.8
mg#	50.25	47.61	50.18	47.23	44.02	46.85	44.35	38.7	40.75	38.25
Ba	639	659	636	727	695	606	823	935	1027	1007
Be	<1	2	2	4	3	2	2	3	3	3
Co	18	16.7	17.5	17.5	16	17.4	17.8	10.3	12.4	9.9
Cs	2.3	3.2	2.1	1.6	1.9	2.2	2	3.3	2.6	3.8
Ga	18	18.8	18.3	18	17.9	17.7	17.1	16.6	16.7	17.3
Hf	5.2	6.7	5.3	6.9	7.5	6.2	6.2	9.9	10.1	9.5
Nb	11.2	11.4	10.6	11.1	12.7	15.1	16	17.8	16.6	18.3
Rb	61.4	83.7	61.3	67.8	72.4	58.5	95.4	133.3	124.1	152.9
Sn	2	1	<1	<1	2	3	2	3	3	3
Sr	675.5	621.7	676.4	640	617.7	704.1	574.9	476.7	489.7	502
Ta	0.8	0.8	0.7	0.7	0.8	1	0.9	1	1	1.1
Th	6.6	9	7	7.3	8.3	4.3	4.7	15.3	12.7	12.8
U	2.2	2.4	1.8	2	2.4	1.3	1.4	3.6	3.4	3.2
V	105	94	106	105	98	177	149	88	100	94
W	1.4	1.4	2	1.8	1.8	3.7	2.1	2.2	1.2	2.5
Zr	233.5	290.2	258.9	288.6	327.5	227.3	257.2	423.1	393.2	374.4
Y	25.7	25.8	24.4	27.6	30.7	34.6	36.4	31.6	41.3	33.3
Mo	1	1.1	1	1.3	1.5	4.1	1.4	2.1	2.4	1
Cu	17.6	18.4	18.4	19	17.2	25.8	19.7	17.1	25.8	24.5
Pb	2.3	5.1	2.5	3.3	4	16	12.2	13.3	18.7	17.2
Zn	17	26	19	26	27	48	56	47	90	58
Ni	11.5	11.9	12.6	11.3	6.3	9	7.9	7.3	8.1	7.3
As	1	1.4	0.9	1.3	1.5	6.6	4.8	6.2	8.6	6.5

Table 4.1 Major (wt. %) and trace elements (ppm) data (cont.)

Sample	TM4	TM6	TM7	MYA2	JONG1	JONG2	MIAM2	TMR2	TMR3	TMR4
Rock type	Gd	Gd	Gd	Gd	Gd	Gd	Gd	Gd	Gd	Gd
SiO_2	61	63.2	62	63.1	62.1	61.7	65.7	62.6	64.4	63.9
Al_2O_3	15.36	15.89	16.1	15.89	15.82	15.76	15.58	15.57	15.42	15.66
Fe_2O_3	6.53	5.34	5.73	4.87	5.48	5.49	4.7	5.65	5.19	5.47
CaO	3.43	3.52	3.86	3.47	3.39	3.41	2.68	3.17	3.04	3.24
MgO	1.75	1.89	1.99	1.62	1.75	1.99	1.4	1.7	1.56	1.69
Na_2O	4.97	4.56	4.6	4.65	4.53	4.35	4.18	4.38	4.38	4.5
K_2O	3.76	4.17	4.08	4.01	4.03	4.14	4.64	4.29	4.53	4.33
MnO	0.15	0.11	0.09	0.08	0.1	0.1	0.11	0.16	0.12	0.1
TiO_2	1.4	1.1	1.21	0.96	1.06	1.04	0.87	1.08	1.02	1.06
P_2O_5	0.47	0.35	0.38	0.33	0.35	0.33	0.27	0.35	0.32	0.35
LOI	0.59	0.68	0.38	0.59	0.38	1.01	0.53	0.57	0.4	0.34
TOTAL	99.41	100.81	100.42	99.57	98.99	99.32	100.66	99.52	100.38	100.64
A/NK	1.25	1.32	1.34	1.33	1.34	1.35	1.31	1.31	1.27	1.3
A/CNK	0.83	0.86	0.85	0.87	0.88	0.88	0.93	0.88	0.87	0.87
Na_2O/K_2O	1.32	1.09	1.13	1.16	1.12	1.05	0.9	1.02	0.97	1.04
TAS	8.73	8.73	8.68	8.66	8.56	8.49	8.82	8.67	8.91	8.83
mg#	34.68	41.22	40.76	39.72	38.75	41.8	37.11	37.35	37.32	37.98
Ba	982	978	1134	844	939	901	764	1052	927	900
Be	3	3	3	2	<1	1	5	2	4	3
Co	8.4	9.7	10.8	7.9	8.4	8.9	10.5	9.2	10.7	11
Cs	2.7	3.5	3.9	2.3	3.2	2.7	10.5	4.6	7	5
Ga	16.6	16.1	17.2	17.5	17.8	18.7	18.5	16.7	16.5	16.8
Hf	9.8	11.7	11.6	9.5	9.2	9.9	10.7	9.9	10.9	11.4
Nb	18.5	18.3	17.7	15.8	16.8	14.9	15.7	18.8	19.4	18.4
Rb	123	142.8	124.6	130.4	121.7	124.1	173.7	162	174.7	169.7
Sn	3	3	3	4	3	3	4	4	3	3
Sr	498.7	486.6	545	449.1	504.2	479.6	378.8	508.3	422.4	447.4
Ta	1.2	1.2	1.1	1	1	1.1	1.1	1	1.2	1.2
Th	13.4	17.6	16	12.2	11.4	13.4	21.2	15.3	21.1	18.5
U	3.8	3.4	3.6	3.7	5.2	3.7	5.7	2.5	4.1	5.1
V	104	97	112	73	98	96	61	96	85	93
W	2.3	1.4	4.6	1.8	0.8	1.8	2.2	1.8	2.1	5.1
Zr	374.6	423.8	432.5	446.6	439.5	427.5	450.6	405.3	419	420.3
Y	44.6	35.7	29.9	32.8	30.6	38.5	38.9	32.5	34.7	34.6
Mo	2	0.9	0.9	1.2	2.5	2	7.2	0.8	2.9	3.5
Cu	51.6	18.2	20	23.8	9.5	10.6	24.1	25.6	9.7	21.4
Pb	23.8	15.6	16.8	16.5	12.4	17.4	28.5	20.7	19.5	16
Zn	51	50	26	33	37	60	77	75	48	38
Ni	4.2	7.6	7.9	6.1	6.9	8	5.1	7.5	7.2	7.2
As	5.8	4.4	4.9	5.3	3.8	6.1	4.7	5.6	5.7	5.6

Table 4.2 Calculated normative mineral values in weight percentages

SAMPLE	Q	Or	Ab	An	Di	Hy	Il	Hm	Tn	Ru	Ap	Sum
PD2	24.82	28.78	31.39	7.71	0.43	2.36	0.12	2.78	1.21	0	0.43	100.03
PD1	5.29	12.53	35.54	21.44	6.50	6.92	0.3	8.08	2.80	0	1.52	100.92
PD4	5.44	12.82	34.95	21.27	6.32	7.16	0.3	8.32	2.78	0	1.56	100.93
DYG 1	4.86	11.46	35.54	21.67	6.04	7.24	0.28	8.2	2.76	0	1.5	99.53
DYG 2	5.24	12.47	35.12	20.95	6.32	6.91	0.3	8.22	2.78	0	1.23	99.54
LANG1	8.55	15.54	36.47	16.46	3.38	6.65	0.28	7.91	2.76	0	1.33	99.33
LANG4A	9.1	15.9	37.40	16.28	3.39	6.27	0.28	7.56	2.71	0	1.23	100.12
LANG4B	8.77	16.13	36.72	15.29	3.68	6.22	0.28	8.15	3.18	0	1.4	99.81
LANG8	8.7	15.9	37.15	16.03	3.37	6.53	0.28	7.88	2.83	0	1.23	99.9
BAIL1A	8.11	15.37	35.62	19.04	3.5	7.07	0.26	7.07	2.44	0	0.95	99.43
BAIL1B	7.4	14.67	36.64	19.22	4.29	6.97	0.26	7.04	2.27	0	0.88	99.57
BAIL2	8.82	17.08	37.15	17.24	3.34	6.05	0.26	6.65	2.17	0	0.88	99.63
BAIL3	7.04	14.24	37.57	19.09	4.44	7.04	0.27	7.18	2.27	0	0.92	100.04
BER3	6.57	15.78	38.25	17.94	4.02	5.96	0.27	6.95	2.54	0	0.88	99.13
BER8	8.0	16.31	37.32	17.37	2.65	6.2	0.26	7.33	2.96	0	1.09	99.31
TBO5	5.36	10.40	41.29	19.04	4.5	6.66	0.34	7.89	2.99	0	1.21	99.68
TBO6	3.88	21.1	38.5	14.19	4.57	5.53	0.32	7.63	3.0	0	1.11	99.83
TBO3	13.2	25.23	38.08	10.41	0.68	3.82	0.24	5.21	2.37	0	0.81	100.04
TBO4	12.0	24.23	37.65	11.08	0	4.98	0.24	5.76	2.48	0.03	0.88	99.32
TM3	12.33	25.53	37.91	10.02	0.22	4.18	0.21	5.5	2.35	0	0.83	99.09
TM4	10.25	22.22	42.05	8.5	0.9	3.94	0.32	6.53	3.02	0	1.11	98.85
TM6	12.34	24.64	38.59	10.57	0.94	4.27	0.23	5.34	2.4	0	0.83	100.15
TM7	10.64	24.11	38.92	11.23	1.23	4.39	0.19	5.73	2.72	0	0.9	100.06
MYA2	12.74	23.7	39.35	10.64	1.08	3.53	0.17	4.87	2.14	0	0.78	99.0
JONG1	12.22	23.82	38.33	10.93	0.24	4.25	0.21	5.48	2.33	0	0.83	98.63
JONG2	11.97	24.47	36.89	11.25	0.22	4.85	0.21	5.49	2.28	0	0.78	98.33
MIAM2	16.88	27.42	35.37	10.04	0	3.49	0.24	4.7	1.05	0.32	0.64	100.15
TMR2	13.07	25.35	37.06	10.15	0.12	4.18	0.34	5.65	2.21	0	0.83	98.97
TMR3	14.50	26.77	37.06	9.03	0.68	3.57	0.26	5.19	2.17	0	0.76	100.0
TMR4	13.55	25.59	38.08	9.74	0.58	3.94	0.21	5.47	2.33	0	0.83	100.32

Both diorite and quartz monzodiorite show similar concentrations for most major and trace elements, having the highest percentages of Al_2O_3, Fe_2O_3, CaO, MgO, TiO_2 and P_2O_5. They have significantly lower TAS contents than granodiorite, ranging from 6.14 to 6.32 % for diorite and 6.64-7.28 % for quartz monzodiorite. They are characterised by low concentrations for most trace elements, with an exceptionally high Sr content, ranging as high as 1155 - 1297 ppm for diorite and 574 - 770 ppm for quartz monzodiorite.

Harker diagrams for major oxide elements are shown in Fig. 4.1. From the diagrams, all the rocks exhibit a linear-like trend for most major elements. However it is noticeable that diorite and quartz monzodiorite lies in the silica-undersaturated end, but granodiorite lies on the silica-saturated end. Both diorite and quartz monzodiorite as the mafic-end members has SiO_2 ranging from 54.6 to 59%, and the felsic-end member: granodiorite has SiO_2 ranging from 61 to 65.7%, with a gap of 2% between these two members. This silica gap and the significantly different range of Fe_2O_3, CaO, MgO between these two members show that diorite-quartz monzodiorite are the results of fractional crystallisation from the same magma whereas granodiorite crystallizes from a different magma.

The linear-like trend and geochemical variations seen from Harker plot suggest the importance of fractional crystallisation for these two members. With increasing SiO_2 content and magmatic evolution from diorite→quartz monzodiorite→granodiorite, Fe_2O_3, CaO, MgO and P_2O_5 generally show decreasing trends, suggesting the importance of fractional crystallisation and the removal of ferromagnesium and Ca-bearing plagioclase during magmatic evolution. Na_2O and TiO_2 show a separate negative trends for diorite-quartz monzodiorite and granodiorite. Al_2O_3 shows a vague decreasing trend and K_2O is the only major element displaying positive correlation with increasing SiO_2 content.

Table 4.3 Range and average of selected major and trace elements
of the dioritic rocks from study area

Rock units	Diorite (4 samples)		Quartz Monzodiorite (12 samples)		Granodiorite (13 samples)	
Major Elements (wt. %)	Range	Average	Range	Average	Range	Average
SiO_2	54.6-55.7	55.23	56.1-59	57.68	61-65.7	62.92
Al_2O_3	16.79-17.06	16.94	15.7-16.91	16.5	15.36-16.1	15.73
Fe_2O_3	8.08-8.32	8.21	6.65-8.15	7.44	4.7-6.53	5.46
CaO	7.34-7.65	7.53	5.45-6.53	5.83	2.68-3.86	3.33
MgO	3.95-4.05	4	2.91-3.59	3.27	1.4-2	1.75
Na_2O	4.13-4.2	4.17	4.21-4.88	4.43	4.18-4.97	4.5
K_2O	1.94-2.17	2.09	1.76-3.57	2.66	3.76-4.64	4.21
MnO	0.13-0.14	0.14	0.12-0.16	0.13	0.08-0.16	0.11
TiO_2	1.27-1.3	1.29	1.02-1.44	1.24	0.87-1.16	1.09
P_2O_5	0.52-0.66	0.61	0.37-0.59	0.46	0.27-0.47	0.35
Trace Elements (ppm)	Range	Average	Range	Average	Range	Average
Ba	662-801	727	606-823	697.92	764-1134	953.08
Rb	41.7-54.8	48.6	58.5-95.4	69.52	121.7-174.7	142.85
Sr	1155.4-1297.6	1228.8	574.9-770.9	682.91	378.8-545	476.04
Zr	118.1-214.9	183.275	146.7-290.2	256.37	374.4-450.6	417.72
Y	25.4-26.6	25.9	24.4-36.4	29.58	29.9-44.6	35.31
Zn	26-33	29	17-56	29.17	33-90	53.08
Pb	2.4-3.1	2.75	2.5-16	5	12.4-28.5	18.18
Ni	10.5-12.8	11.9	6.3-14.3	11.21	4.2-8.1	6.95
Nb	8.9-11.1	9.93	10.6-16	12.35	14.9-19.4	17.46
Ta	0.4-0.6	0.5	0.6-1	0.76	1-1.2	1.09
Th	4.6-6	5.3	4.3-9	7.15	11.4-21.2	15.45
Hf	3.7-5.2	4.28	3.6-7.5	5.78	9.2-11.7	10.32
U	1.2-1.4	1.33	1.3-2.4	1.98	2.5-5.1	3.92
V	137-208	173.75	94-177	122.25	61-112	92.08
W	0.7-3.7	1.55	0.8-3.7	1.7	0.8-5.1	2.29
Mo	0.6-1	0.88	1-4.1	1.51	0.8-2.9	2.26
Cu	31.8-44	37.08	17.2-29	22.22	9.5-51.6	21.68
Co	20.5-22.9	21.73	16-20.5	17.81	7.9-12.4	9.71
Cs	1.2-1.9	1.68	1.6-3.2	2.24	2.3-10.5	4.24
Ga	17-18.7	17.93	17.1-18.8	18.11	16.1-18.7	17.15
As	0.7-1.1	0.93	0.7-6.6	1.83	3.8-8.6	5.63
A/CNK	0.74-0.75	0.74	0.77-0.81	0.79	0.83-0.93	0.87
K_2O+Na_2O	6.14-6.32	6.26	6.64-7.28	7.09	8.49-8.91	8.71
K_2O/Na_2O	0.46-0.53	0.5	0.36-0.78	0.6	0.86-1.11	0.94
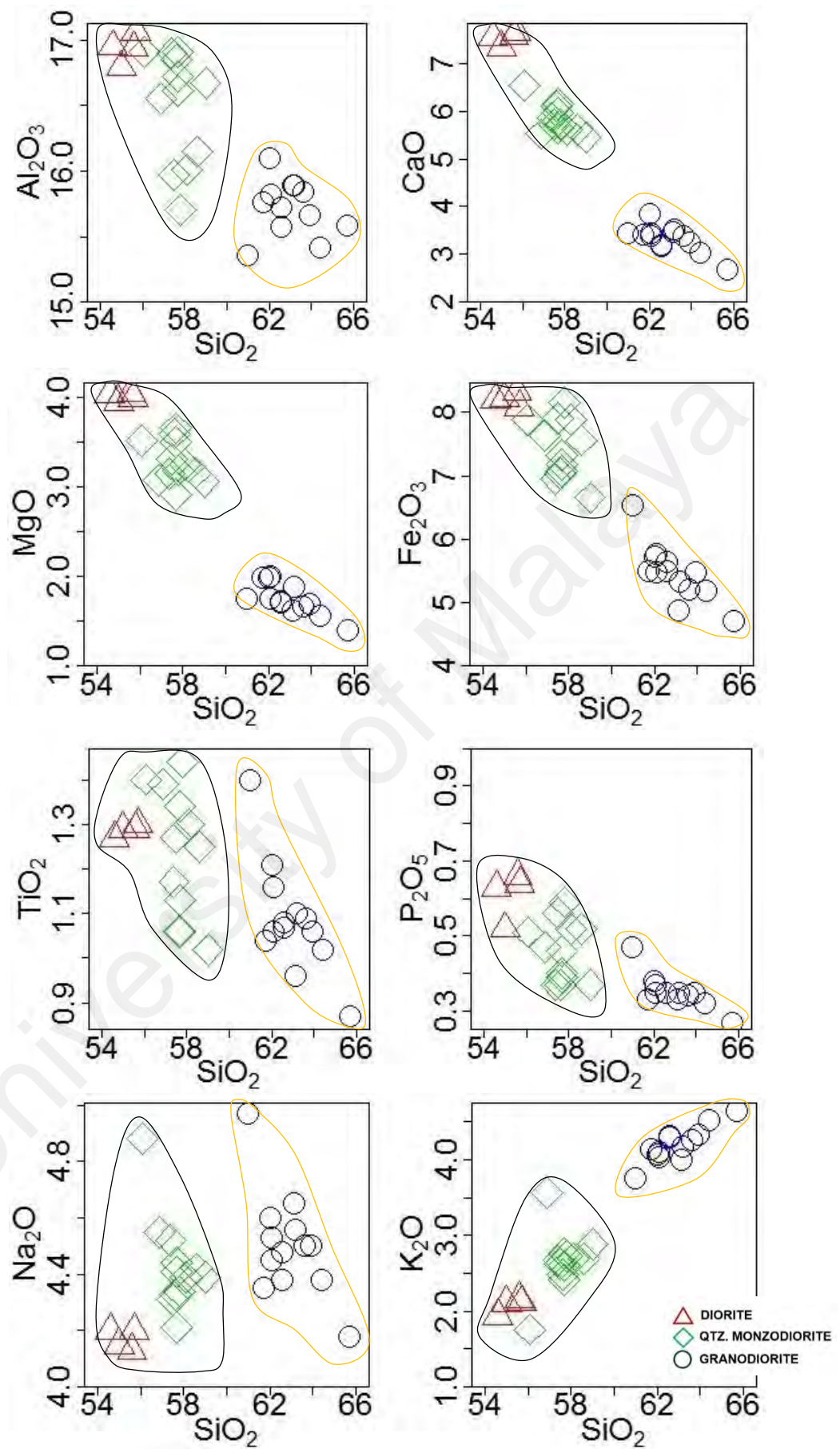
Figure 4.1 Harker variation diagram for major elements

Harker diagram for trace elements are shown in Fig. 4.2. The different trends seen on most trace elements with increasing SiO_2 between the two mafic-end members (diorite, quartz monzodiorite) and felsic-end members (granodiorite) further supports that the rocks are made up of at least two different individual batches of melt.

Ba shows different trends, (1) forming a similar trend for both diorite and quartz monzodiorite. This suggest that Ba remains fairly constant and low in concentration, ranging from 662 to 801 and ranging between 606 to 823 for diorite and quartz monzodiorite respectively. A linear negative trend are clearly seen for granodiorite, where with increasing SiO_2, Ba decreases drastically. Granodiorite has the highest value and wide range of Ba concentration; 764-1134 ppm. Again, these high values of Ba and K_2O reflect the importance of biotite and K-feldspar during magmatic evolution for the granodiorite.

Sr exhibit a complicated trends where from the Harker plot, it can be seen that all the three rocks show different trends, where (1) Sr shows positive trend for diorite, (2) Sr forms a cluster and remains fairly constant for quartz monzodiorite and (3) Sr clearly shows negative linear trend with increasing SiO_2 content. As Sr is a compatible trace element in plagioclase, fractionation of plagioclase would have causes decreasing Sr with increasing SiO_2 content (Wilson, 2007).

Rb, U, Th and Pb show a linear positive trend from diorite→quartz monzodiorite→granodiorite with increasing SiO_2 content. V, Co, Mo and Cs decreases with increasing SiO_2 content. Most of the trace elements however, lack clear linear correlation with SiO_2 where for W, Y, Ta, Nb, Hf, Zn, Ga, Ni, Be and As, no discernible trends could be identified.

Variable and different trends seen from Harker diagram for most major and trace elements each with a pronounced compositional gap between the two members provides evidences that both are made up of individual batches of melt.
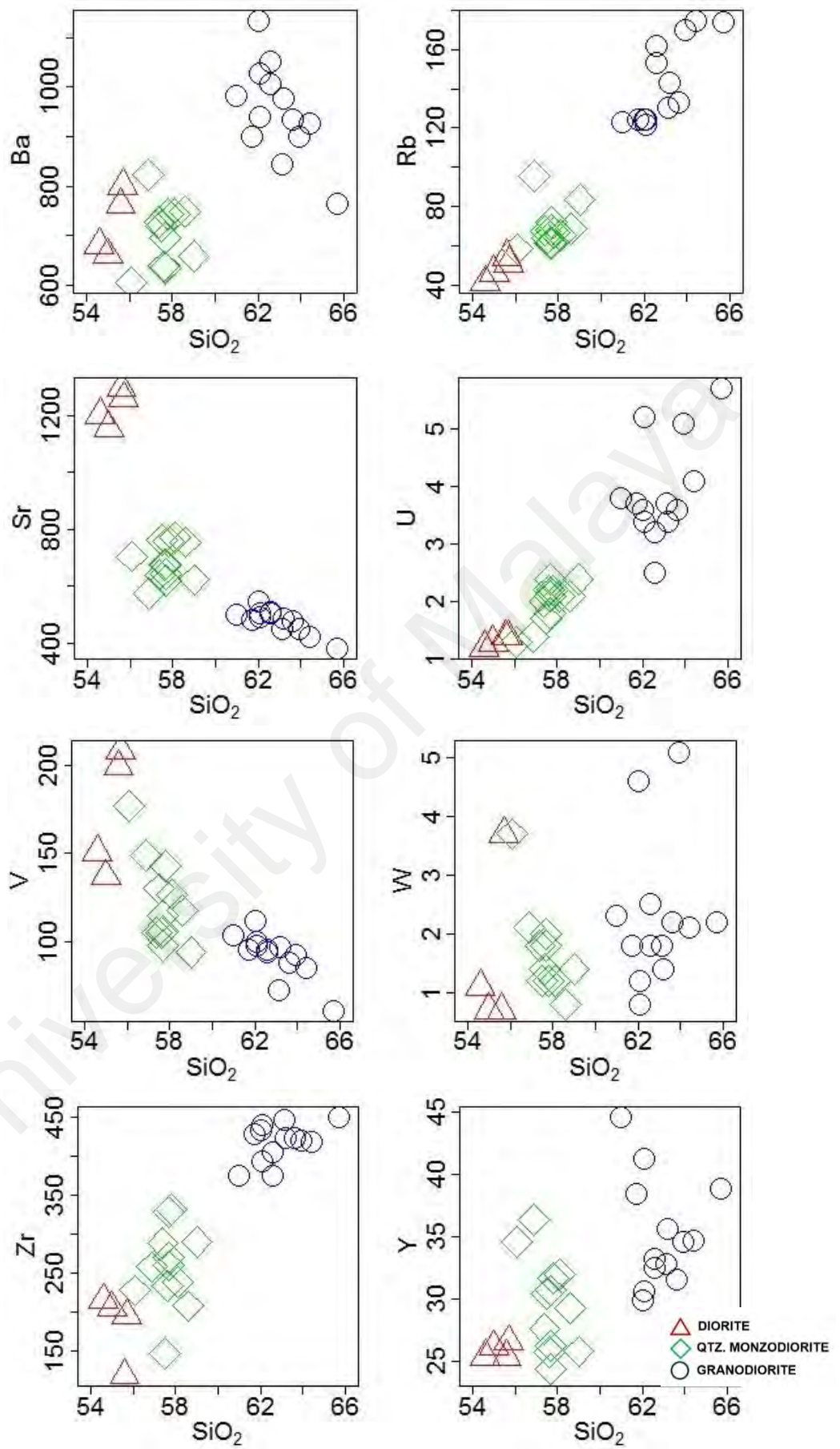
Figure 4.2 Harker variation diagram for trace elements
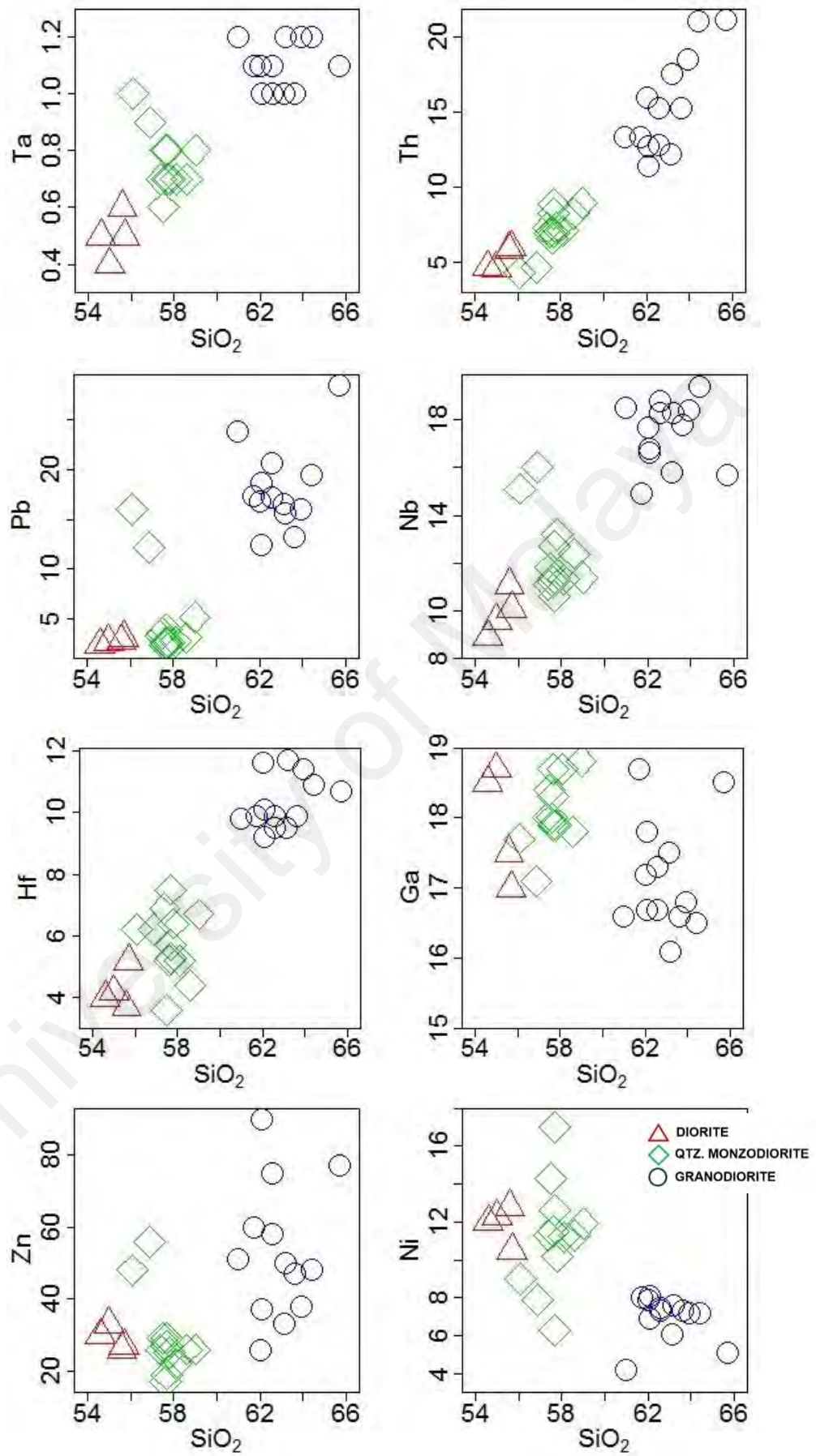
Figure 4.2 Harker variation diagram for trace elements (cont.)
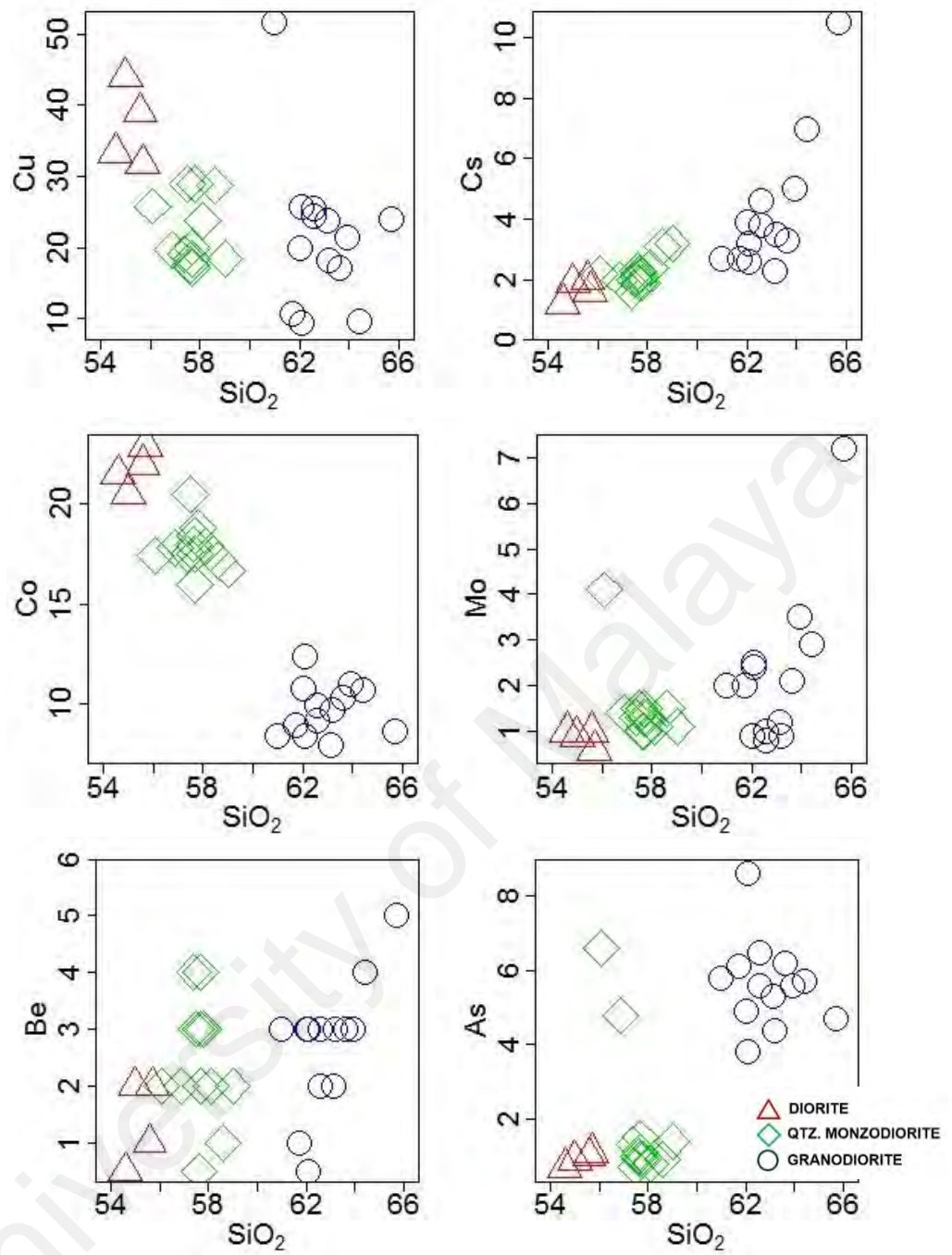
Figure 4.2 Harker variation diagram for trace elements (cont.)

4.4.1 Spider Plot

Normalised multi-element diagram (spider diagram) of trace elements for the dioritic rocks were plotted to compare the concentration of elements and whole compositions of a sample on a same diagram. Rocks from the study area were normalised to N-MORB-normalized values given according to (Sun and McDonough, 1989).

Based on the combined N-MORB-normalized multi element diagrams of all the three rock types, (Fig. 4.4) there is a notable difference of trace elements patterns between the mafic-end members (diorite, quartz monzodiorite) and the felsic-end member (granodiorite). While most of the trace element do show similar patterns that display a gentle decrease in element abundances with decreasing compatibility, one feature that distinguishes between the two members are Pb enrichment of granodiorite. Additionally, both members showed variable depletion at Rb, Nb, P, Zr, Sm, Eu and Ti. They are characterized by high concentrations of incompatible trace elements (LILE and LREE) and pronounced by significant Nb, Zr, P and Ti anomalies, resembling those of volcanic arc granitoids. Negative Ti anomaly is commonly related to ilmenite or titanite fractionation, whereas negative P anomaly is attributed to apatite separation.

All the samples show negative Nb-Ti anomalies, which reflect involvement of subduction related component (Pearce et al., 2005; Hemond et al., 2006). Slab derived fluid is enriched in highly mobile elements (Ba, U, Pb) due to low T dehydration at shallow emplacement levels, and partial melting of mantle metasomatized by such fluid would produce magmas with high Ba/Th ratios of more than 50 (Pearce et al., 2005). This high Ba/Th ratio can be seen in all rock samples, especially for diorite and quartz monzodiorite (61.1-175) and granodiorite (36-82.4).

Since HFSE (such as Nb and Ta) are depleted in the lithospheric mantle relative to the LREE, high Nb/La ratios ($\sim >1$) indicate an OIB-like asthenospheric mantle source for basaltic magmas and lower ratios ($\sim <0.5$) indicate a lithospheric mantle source.

Accordingly, Nb/La ratio of all the rock samples, range from (0.19 – 0.47), suggesting a lithospheric mantle source (Bradshaw and Smith, 1994; Smith et al., 1999). Enrichment in LILE and LREE with negative Nb-Ti anomalies are characteristics of subduction related magmas and are commonly attributed to the mantle source, which has been previously enriched in LILEs over HFSE by metasomatic activity of fluids derived from the subducted slab or sediments (e.g. Pearce, 1983; Hawkesworth et al., 1997; Elburg et al., 2002; Cameron et al., 2003). High LIL/HFSE ratios and negative Nb and Ti anomalies can also be characteristics of magma originated from an enriched sub-continental lithospheric mantle caused by earlier subduction events. Mantle enrichment events could have probably formed at great depth during the period of subducting Paleo-Tethys Ocean during the Middle-Late Triassic. During such case, a large amount of fluids and/or sediments caused metasomatization of the depleted mantle. An important feature of subduction related metasomatism is the formation of hydrous mineral phase such as amphibole (Beccaluva et al., 2004).
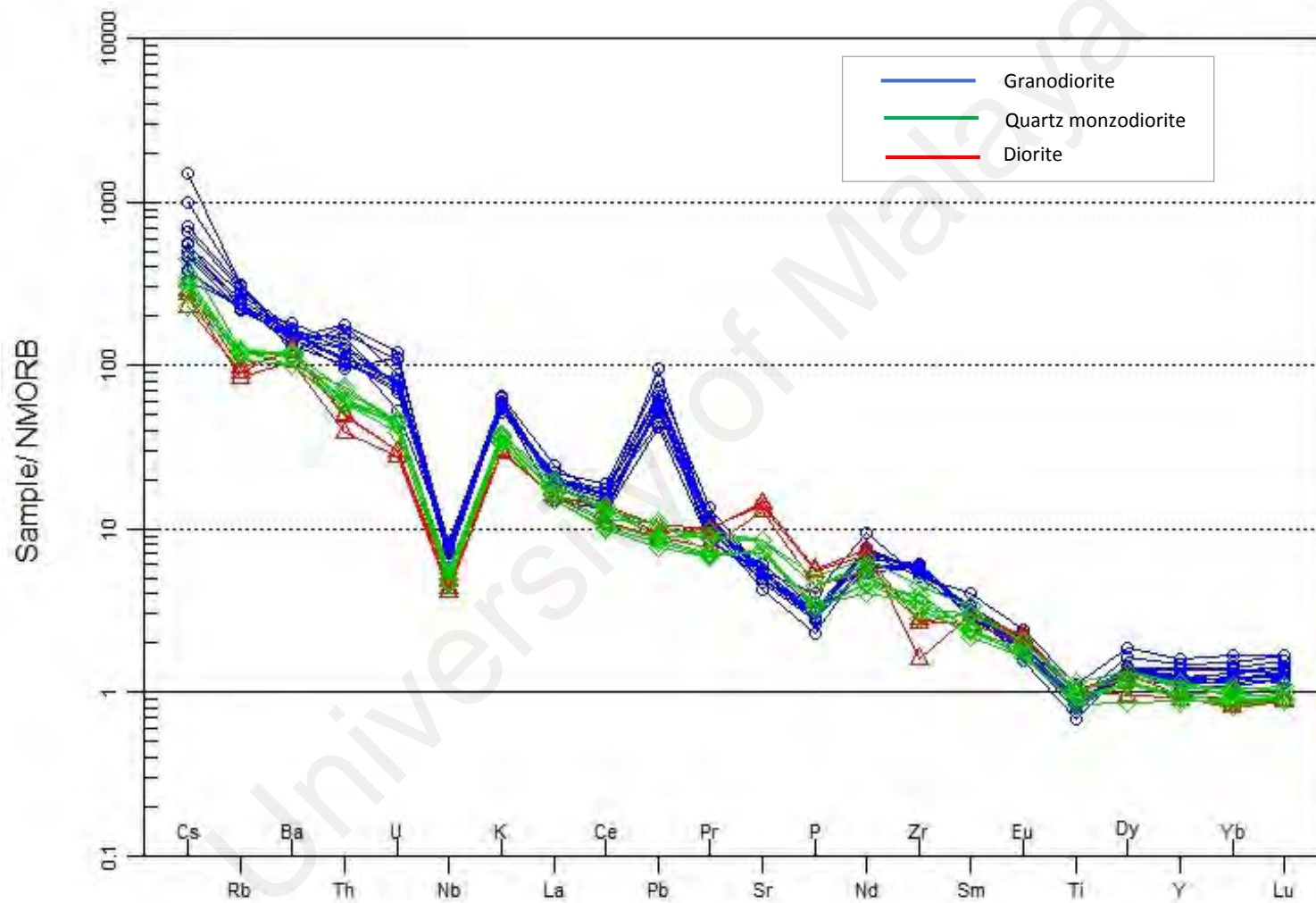
Figure 4.3 N-MORB normalized values of trace elements according to Sun and McDonough (1989) of all the three rock types, notice the significant positive Pb anomaly for granodiorite

4.5   Rare Earth Elements (REE) Geochemistry

Rare earth elements (REE) data of the dioritic rocks from study area is shown in Table 4.4. The range of sum of REE for diorite, quartz monzodiorite and granodiorite are from 198.1-238.19 ppm, 177.73-265.31 ppm and 221.07-329.49 ppm, respectively. In all the three rock types, the concentrations of the light rare earth elements (LREE) are extremely higher (167.57-306.15 ppm) compared to the heavy rare earth elements (HREE), which is much lower, ranging only (11.84-23.34 ppm). The graph of Sum LREE against Sum HREE shows a good linear trend, showing LREE content increases with increasing HREE for each of the samples from diorite→quartz monzodiorite→granodiorite (Fig. 4.4).

Sum REE when plotted against SiO_2 (Fig. 4.5) for the three rock types show no discernible trends with increasing silica contents, but there is an increase of total REE contents from diorite→quartz monzodiorite→granodiorite. REE are incompatible in most silicates and as a result, they remain in melt during fractional crystallisation, thus being enriched in late stage magmatic liquids. The behaviour of the REE has been suitably explained by Miller and Mittlefehldt (1982). They suggested that the variable removal of accessory phases like sphene, allanite, apatite and monazite which contains bulk of REE determine the trends of these REE with increasing fractionation.

To better depicts and show the relationship of the REEs among the three types of rocks, normalization of the REEs are done where REE abundances of the samples are divided with the values of the chondritic meteorites. Chondritic meteorites are chosen because they are believed to be similar in chemical composition to the primitive earth. Chondritic meteorites are not believed to show fractionation among the REE. Therefore, any variations from horizontal trends on diagrams using chondrite-normalized data can be considered to represent fractionation of the REE in the petrographic system under examination.

The chondrite-normalized REE values (normalization factors from Nakamura, 1974) are shown in Table 4.5 and the chondrite-normalized REE patterns for selected samples are shown in (Fig. 4.6). Diorite, quartz monzodiorite and granodiorite display a similar chondrite-normalized REE patterns. The chondrite-normalized REE patterns are fractionated [$(La/Yb)_N$ = 6.52-11.92]. They are characterized by LREE enrichment with $(La/Sm)_N$ = 2.88-4.42 and weakly fractionated HREE with $(Gd/Yb)_N$ = 1.32-2.18, suggesting garnet-free sources (Wilson, 2007). From the least to most fractionated rocks (diorite→quartz monzodiorite→granodiorite), a slight narrow but very consistent increase in negative Eu (Eu/Eu* = 0.602-1.008) anomaly can be seen (Fig. 4.7). The dioritic rocks from study area however have a narrow range of Eu/Eu* ratios and weak negative Eu anomalies. Diorite has the lowest Eu anomaly value ranging only from 0.908-1.008 and for quartz monzodiorite, 0.776-0.938. Eu anomaly decreased more markedly for granodiorite ranging from 0.602-0.943. This negative Eu anomaly probably resulted from fractional crystallisation of plagioclase during magmatic evolution.

Table 4.4 Rare earth elements data (in ppm) for dioritic rocks from study area

Sample	PD2	PD1	PD4	DYG1	DYG2	LANG1	LANG4A	LANG4B	LANG8	BAIL1A	BAIL1B	BAIL2	BAIL3	BER3	BER8
Rock type	DIKE	DR	DR	DR	DR	QMZD	QMZD	QMZD	QMZD	QMZD	QMZD	QMZD	QMZD	QMZD	QMZD
La	36.5	39.2	39.8	44.7	39.8	47.2	46.5	49.5	46.3	39.9	37	40	37.7	41.2	43.5
Ce	91.8	103.4	100.6	94.9	81.9	96.7	98.3	103.4	97.1	81.2	74.2	81.5	77	83.9	90.9
Pr	10.36	13.34	13.05	11.39	10.19	11.92	11.5	12.85	11.65	9.18	8.92	9.44	8.93	9.47	10.68
Nd	34.1	50.7	53.9	43.9	39.8	45.9	43.9	47.3	41	37	34	34.5	29.5	33.8	42.7
Sm	5.36	8.02	7.86	7.35	6.82	8.02	7.7	8.79	7.95	6.53	6.22	6.3	5.71	6.39	6.96
Eu	1.05	2.28	2.19	2.12	2.04	2.13	2.12	2.02	2.11	1.68	1.77	1.59	1.67	1.83	1.99
Gd	4.71	6.91	7	6.31	5.68	6.82	6.57	7.28	6.82	5.34	5.46	5.56	5.25	5.63	6.4
Tb	0.79	0.98	0.97	0.85	0.82	1.02	0.95	1.01	0.97	0.83	0.81	0.84	0.79	0.89	0.97
Dy	5.07	5.83	5.36	5.05	4.31	5.86	6.11	6.1	5.47	5.24	5.11	4.58	3.96	5.23	5.47
Ho	0.83	0.86	0.89	0.95	0.94	1.15	1.04	1.17	1.07	0.99	0.9	0.99	0.96	0.94	1.2
Er	3.11	3.11	2.82	2.67	2.58	3	3.11	3.61	3.31	2.65	2.66	2.6	2.81	3.08	3.33
Tm	0.47	0.41	0.4	0.39	0.37	0.45	0.43	0.49	0.5	0.4	0.38	0.4	0.37	0.43	0.45
Yb	3.15	2.74	2.56	2.76	2.45	2.64	3.26	3.17	2.84	2.79	2.51	2.91	2.67	3.08	3.24
Lu	0.51	0.41	0.41	0.38	0.4	0.44	0.47	0.49	0.44	0.4	0.41	0.44	0.41	0.41	0.5
Sum LREE	183.88	223.85	224.4	210.67	186.23	218.69	216.59	231.14	212.93	180.83	167.57	178.89	165.76	182.22	203.13
Sum HREE	13.93	14.34	13.41	13.05	11.87	14.56	15.37	16.04	14.6	13.3	12.78	12.76	11.97	14.06	15.16
Sum REE	197.81	238.19	237.81	223.72	198.1	233.25	231.96	247.18	227.53	194.13	180.35	191.65	177.73	196.28	218.29

Table 4.4 Rare earth elements data (in ppm) for dioritic rocks from study area (cont)

Sample	TBO5	TBO6	TBO3	TBO4	TM3	TM4	TM6	TM7	MYA2	JONG1	JONG2	MIAM2	TMR2	TMR3	TMR4
Rock type	MZD	MZD	QMZN	QMZN	QMZN	QMZN	QMZN	QMZN	QMZN	QMZN	QMZN	QMZN	QMZN	QMZN	QMZN
La	43	43.8	52.3	49.7	43.7	54.7	47	37.6	47.2	45.9	47.6	60.6	50.8	48.1	50.3
Ce	112.2	113.8	122	124	108.4	142.1	113.9	98.7	96.2	94	97.5	114.6	129.4	121.4	131
Pr	14.2	14	14.51	14.85	14.01	17.7	13.64	12.16	11.2	10.83	11.28	13.63	15.67	14.61	15.81
Nd	56.1	53.9	52.5	55.3	52	69.2	51.4	44.4	41.3	38.7	42.8	48.2	55.5	54.9	55
Sm	9.18	9.33	8.5	8.73	8.06	10.56	8.13	7.68	8.2	7.3	7.7	8.43	8.83	8.23	8.91
Eu	2.28	2.25	1.91	2.16	2.05	2.44	1.98	2.2	1.82	1.9	1.74	1.59	2.04	1.86	1.99
Gd	8.13	7.95	6.89	8.01	7.24	9.45	7.38	6.69	7.11	6.58	7.04	7.81	7.62	7.51	7.45
Tb	1.31	1.3	1.11	1.27	1.19	1.51	1.14	1.08	1.02	0.95	1.11	1.16	1.18	1.11	1.19
Dy	7.68	6.9	5.96	7.47	6.49	8.54	6.22	6.29	6.22	5.62	6.39	6.28	6.35	6.18	6.59
Ho	1.25	1.23	1.03	1.34	1.13	1.47	1.11	0.98	1.19	1.15	1.45	1.39	1.12	1.14	1.13
Er	4.33	4.17	3.7	4.71	3.9	5.18	3.89	3.41	3.64	3.48	4.19	4.07	3.57	3.96	3.99
Tm	0.6	0.59	0.53	0.69	0.6	0.77	0.55	0.53	0.53	0.48	0.64	0.57	0.58	0.62	0.57
Yb	4.4	3.78	3.48	4.6	3.66	5.11	3.58	3.31	3.74	3.66	4.25	4.2	3.66	3.91	3.98
Lu	0.65	0.65	0.55	0.76	0.6	0.76	0.59	0.55	0.56	0.52	0.71	0.64	0.59	0.66	0.62
SumLREE	245.09	245.03	258.61	262.75	235.46	306.15	243.43	209.43	213.03	205.21	215.66	254.86	269.86	256.61	270.46
SumHREE	20.22	18.62	16.36	20.84	17.57	23.34	17.08	16.15	16.9	15.86	18.74	18.31	17.05	17.58	18.07
SumREE	265.31	263.65	274.97	283.59	253.03	329.49	260.51	225.58	229.93	221.07	234.4	273.17	286.91	274.19	288.53

Table 4.5 Chondrite normalized REE values according to Nakamura (1974)

Sample	LaN	CeN	PrN	NdN	SmN	EuN	GdN	TbN	DN	HoN	TmN	YbN	LuN	Eu/Eu*	LaN/YbN	LaN/SmN	CeN/YbN	CeN/SmN	ErN	EuN/YbN
PD1	118.79	119.54	119.11	80.48	39.51	29.61	25.04	20.85	17	12.29	13.67	12.45	12.06	0.9	9.54	3.01	9.6	3.03	13.82	2.38
PD4	120.61	116.3	116.52	85.56	38.72	28.44	25.36	20.64	15.63	12.71	13.33	11.64	12.06	0.91	10.36	3.11	10	3	12.53	2.44
DYG1	135.45	109.71	101.7	69.68	36.21	27.53	22.86	18.09	14.72	13.57	13	12.55	11.18	0.96	10.8	3.74	8.75	3.03	11.87	2.19
DYG2	120.6	94.68	90.98	63.17	33.6	26.49	20.58	17.45	12.57	13.43	12.33	11.14	11.76	1.01	10.83	3.59	8.5	2.82	11.47	2.38
LANG1	143.03	111.79	106.43	72.86	39.51	27.66	24.71	21.7	17.08	16.43	15	12	12.94	0.89	11.92	3.62	9.32	2.83	13.33	2.31
LANG4A	140.91	113.64	102.68	69.68	37.93	27.53	23.8	20.21	17.81	14.86	14.33	14.82	13.82	0.92	9.51	3.71	7.67	3	13.82	1.86
LANG4B	150	119.54	114.73	75.08	43.3	26.23	26.38	21.49	17.78	16.71	16.33	14.41	14.41	0.78	10.41	3.46	8.3	2.76	16.04	1.82
LANG8	140.3	112.25	104.02	65.08	39.16	27.4	24.71	20.64	15.95	15.29	16.67	12.91	12.94	0.88	10.87	3.58	8.7	2.87	14.71	2.12
BAIL1A	120.91	93.87	81.96	58.73	32.17	21.82	19.35	17.66	15.28	14.14	13.33	12.68	11.76	0.8	9.53	3.76	7.4	2.92	11.78	1.72
BAIL1B	112.12	85.78	79.64	53.97	30.64	22.99	19.78	17.23	14.9	12.86	12.67	11.41	12.06	0.94	9.83	3.66	7.52	2.8	11.82	2.01
BAIL2	121.21	94.22	84.29	54.76	31.03	20.65	20.14	17.87	13.35	14.14	13.33	13.23	12.94	0.83	9.16	3.91	7.12	3.04	11.56	1.56
BAIL3	114.24	89.02	79.73	46.83	28.13	21.69	19.02	16.81	11.55	13.71	12.33	12.14	12.06	0.94	9.41	4.06	7.33	3.1	12.49	1.79
BER3	124.85	96.99	84.55	53.65	31.48	23.77	20.4	18.94	15.25	13.43	14.33	14	12.06	0.94	8.92	3.97	6.93	3.08	13.69	1.7
BER8	131.82	105.09	95.36	67.78	34.29	25.84	23.19	20.64	15.95	17.14	15	14.73	14.71	0.92	8.95	3.84	7.14	3.07	14.8	1.7
TBO5	130.3	129.71	126.79	89.05	45.22	29.61	29.46	27.87	22.39	17.86	20	20	19.12	0.81	6.52	2.88	6.49	2.87	19.24	1.48
TBO6	132.73	131.56	125	85.56	45.96	29.22	28.8	27.66	20.12	17.57	19.67	17.18	19.12	0.8	7.72	2.89	7.67	2.86	18.53	1.7
TBO3	158.48	141.04	129.55	83.33	41.87	24.81	24.96	23.62	17.38	14.71	17.67	15.82	16.18	0.77	10.02	3.78	8.92	3.37	16.44	1.57
TBO4	150.61	143.35	132.59	87.78	43	28.05	29.02	27.02	21.78	19.14	23	20.91	22.35	0.79	7.2	3.5	6.86	3.33	20.93	1.34
TM3	132.42	125.32	125.09	82.54	39.7	26.62	26.23	25.32	18.92	16.14	20	16.64	17.65	0.82	7.96	3.34	7.53	3.16	17.33	1.6
TM4	165.76	164.28	158.04	109.8	52.02	31.69	34.24	32.13	24.9	21	25.67	23.23	22.35	0.75	7.14	3.19	7.07	3.16	23.02	1.36
TM6	142.42	131.68	121.79	81.59	40.05	25.71	26.74	24.26	18.13	15.86	18.33	16.27	17.35	0.79	8.75	3.56	8.09	3.29	17.29	1.58
TM7	113.94	114.1	108.57	70.48	37.83	28.57	24.24	22.98	18.34	14	17.67	15.05	16.176	0.94	7.57	3.01	7.58	3.02	15.16	1.9
MYA2	143.03	111.21	100	65.56	40.39	23.64	25.76	21.7	18.13	17	17.67	17	16.47	0.73	8.41	3.54	6.54	2.75	16.18	1.39
JONG1	139.09	108.67	96.7	61.43	35.96	24.68	23.84	20.21	16.38	16.43	16	16.64	15.29	0.84	8.36	3.87	6.53	3.02	15.47	1.48
JONG2	144.24	112.72	100.71	67.94	37.93	22.6	25.51	23.62	18.63	20.71	21.33	19.32	20.88	0.73	7.47	3.8	5.83	2.97	18.62	1.17
MIAM2	183.64	132.49	121.7	76.51	41.53	20.65	28.3	24.68	18.31	19.86	19	19.09	18.82	0.6	9.62	4.42	6.94	3.19	18.09	1.08
TMR2	153.94	149.6	139.91	88.1	43.5	26.49	27.61	25.11	18.51	16	19.33	16.64	17.35	0.76	9.25	3.54	9	3.44	15.87	1.59
TMR3	145.76	140.35	130.45	87.14	40.54	24.16	27.21	23.62	18.02	16.29	20.67	17.77	19.41	0.73	8.2	3.6	7.9	3.46	17.6	1.36
TMR4	152.42	151.45	141.16	87.3	43.89	25.84	26.99	25.32	19.21	16.14	19	18.09	18.24	0.75	8.43	3.47	8.37	3.45	17.73	1.43
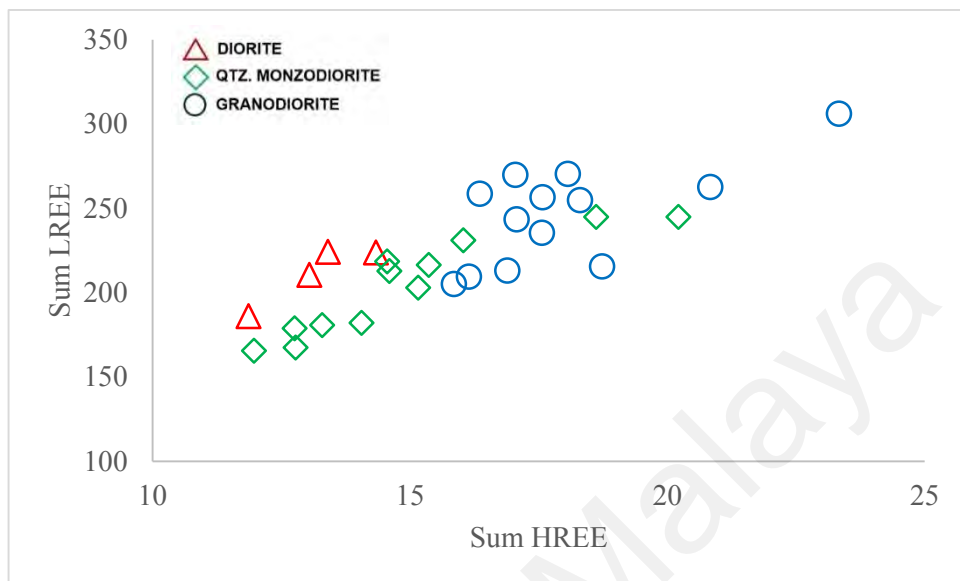
Figure 4.4 Sum LREE vs. Sum HREE
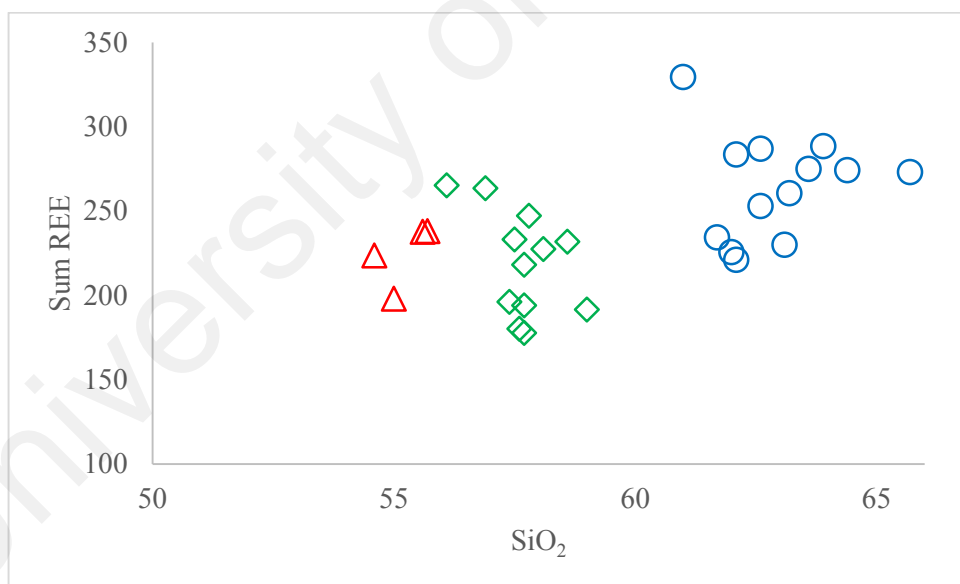
Figure 4.5 Sum REE vs. SiO$_2$
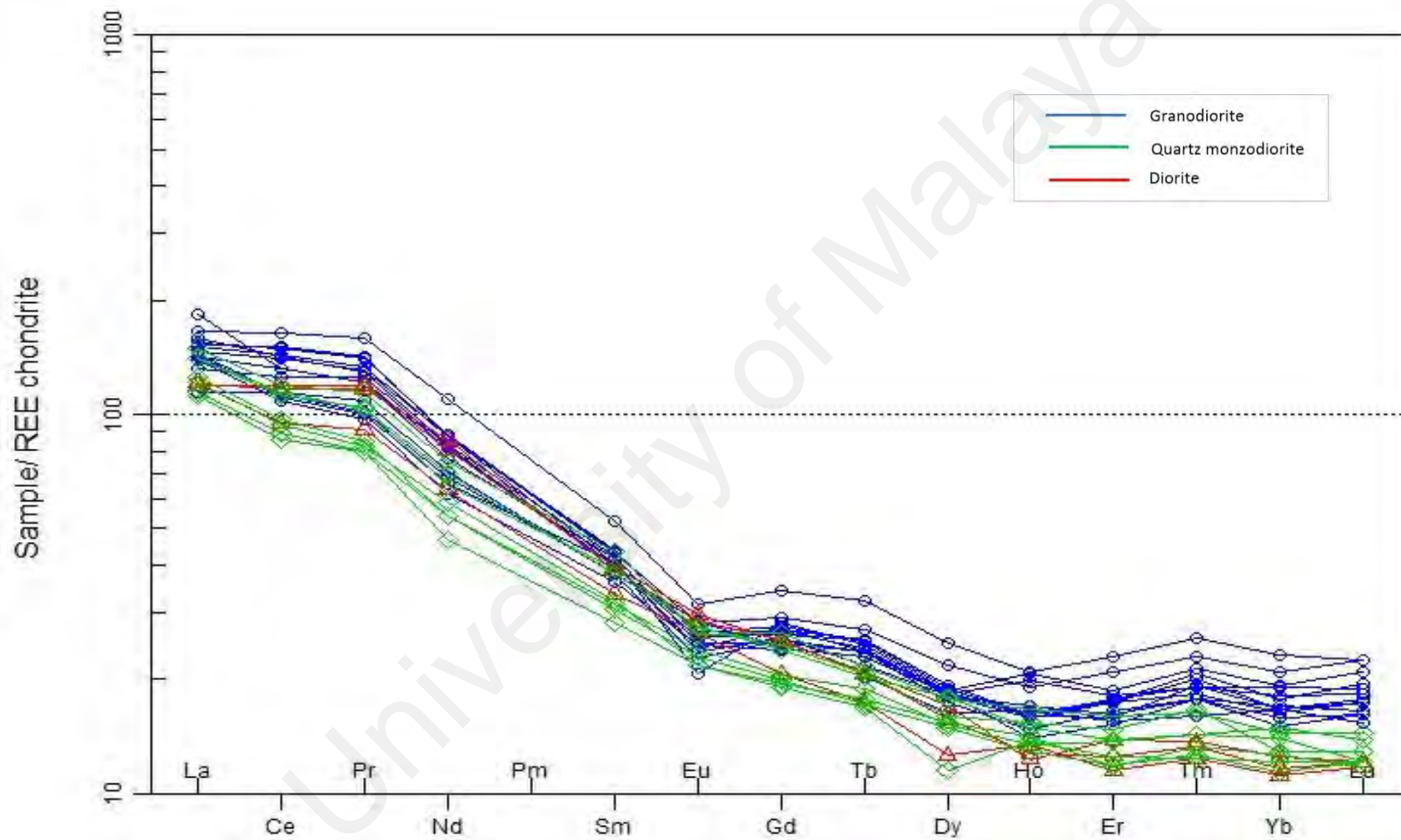
Figure 4.6 Chondrite-normalized REE plot. Normalization values after Nakamura (1974)
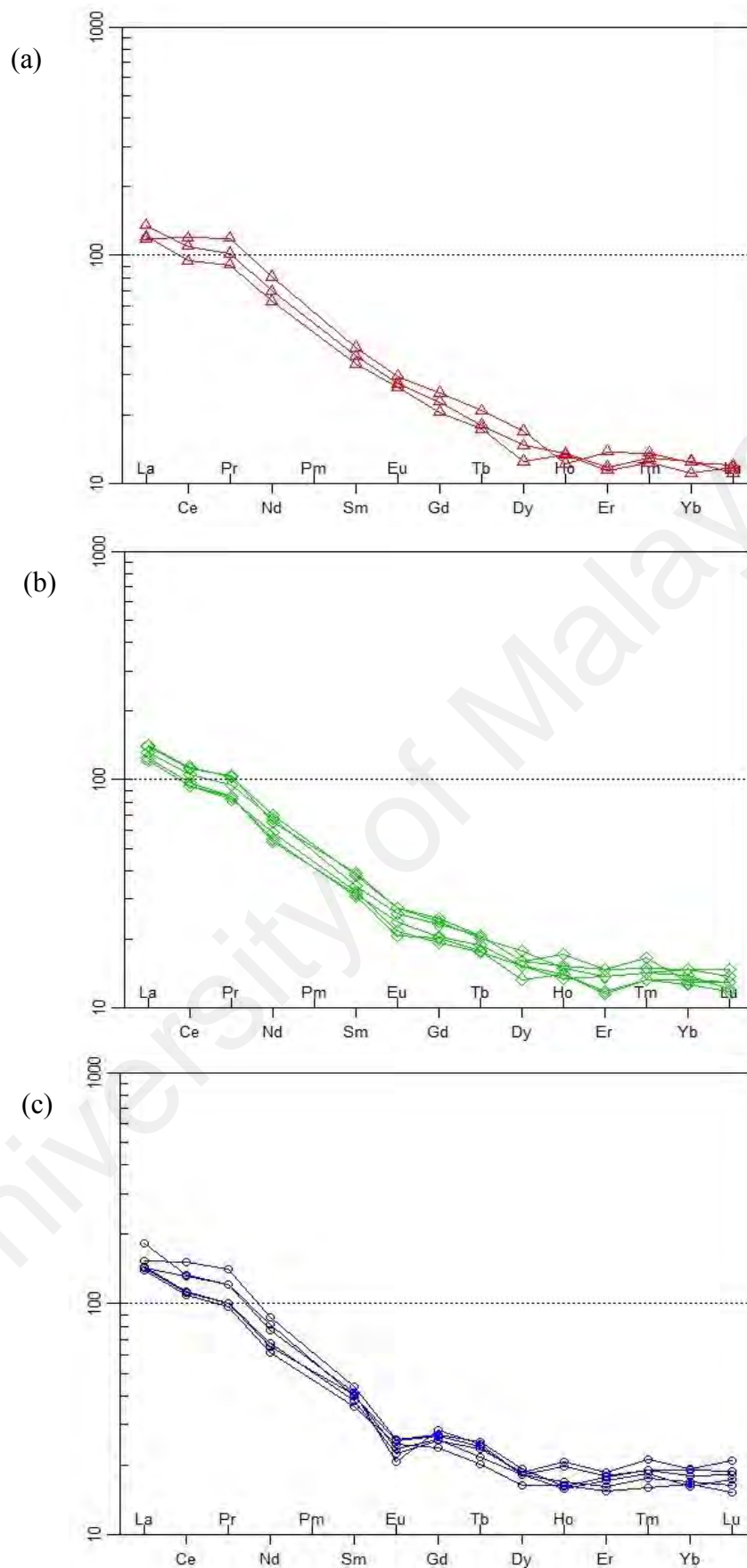
Figure 4.7 Chondrite normalized REE patterns for each of the rock type from study area. (a) diorite (b) quartz monzodiorite (c) granodiorite. Notice the more pronounced negative Eu anomaly for (c)

4.6　Large Ion Lithophile (LIL) Elements Modelling

Large ion lithophile elements (LIL) such as Ba, Rb and Sr are useful to determine major precipitating phase during magma fractionation in intermediate and acid rocks. Each LIL elements behave differently for each major mineral phase, where Rb substitutes for K in K-feldspar, hornblende and biotite, Ba substitute preferentially into K-feldspar and biotite while Sr substitutes readily for Ca in plagioclase and K in K-feldspar.

As it has been earlier identified from Harker diagram that there are at least two different magmatic pulse of the dioritic rocks from study area, that is (1) mafic-end members; diorite-quartz monzodiorite and (2) felsic-end members; granodiorite, the LIL modelling of these two different members will be plotted separately. From the modelling, it can be seen that both members show different trends of minerals fractionation with increasing magmatic differentiation.

For the more mafic-end members, it can be seen from the pair Rb-Sr and Ba-Rb, Fig. 4.9a and Fig. 4.10a respectively, the overall trends are consistent with fractionation of plagioclase and hornblende. For granodiorite, the more felsic units, all the trends are consistent with fractionation of plagioclase, biotite and K-feldspar. A good linear trend seen from the pair of Sr-Ba (Fig. 4.8b) suggest that crystal fractionation via crystallisation of plagioclase, K-feldspar and biotite play an important role during magmatic evolution of granodiorite.

The importance of the major precipitating phase; hornblende and plagioclase; plagioclase, biotite and K-feldspar in the differentiation is consistent with LIL modelling. Inter elements variation diagram in log scale for the pairs Sr-Ba, Rb-Sr and Ba-Rb are shown in Fig. 4.8, 4.9, 4.10 respectively. Also shown in each of the diagram is the vector diagram representing the net change in composition of liquid after 30% Rayleigh fractionation by removing hornblende, plagioclase, biotite or K-feldspar. Thus, the LIL log – log plot suggest that crystal fractionation plays an important role during the

magmatic evolution of both mafic and felsic end members of dioritic rocks from study area.

4.7   Inter-Elements Variation Diagram

From the plot of Sr vs. Ba, granodiorite clearly shows a decrease of Ba concomitant with Sr with increasing SiO_2, suggesting that K-feldspar, biotite and plagioclase are being removed in the differentiation sequence (Fig. 4.11). Granodiorite has the highest concentration of Ba, ranging from 764-1134 ppm and the lowest content of Sr (378.8-545 ppm). Diorite has the highest concentration of Sr, ranging as high as 1155.5-1297.6 ppm, with Ba ranging from 662-801 ppm. The range of Sr and Ba concentration for quartz monzodiorite ranges are: 606-823 ppm and 617.7-770.9 ppm respectively. Both mafic end members, diorite and quartz monzodiorite, however does not show any significant changes of Sr together with Ba, where concentration of Sr remains more or less stagnant with increasing Ba and SiO_2 concentrations.

The importance of plagioclase and K-feldspar precipitations during magmatic evolution of the felsic-end member: granodiorite are also depicted from the plotting of Ba vs. Eu/Eu* and Sr vs. Eu/Eu* after Eby (1990). Granodiorite clearly lies in a linear trend for both of this plot (Fig. 4.14 and 4.15), where Sr decreases with increasing Eu/Eu* (Eu anomaly) values while Ba concentration increases with increasing Eu/Eu* values. There is no clear trend observed for the mafic-end members: diorite and quartz monzodiorite. Also shown in each of the diagram is the vector diagram representing modelled fractionation trends after Eby (1990). This modelling however are more suitable in determining major precipitating phase for felsic rock types, as Eu/Eu* values of more mafic rocks are small, and less significant. From the Eu anomaly values, diorite has the lowest value ranging only: 0.91-1.01 and for quartz monzodiorite: 0.78-0.94, when compared to Eu anomaly of granodiorite that shows a wide range from 0.602-0.943. The

negative Eu anomaly shown (Fig. 4.7) are a result from fractional crystallisation of plagioclase during magmatic evolution.

The role of plagioclase during magmatic differentiation can also be observed from the plotting of Ba/Sr ratio vs. SiO_2 (Fig. 4.12) that shows a positive slope, demonstrating the effect of plagioclase precipitation during magmatic evolution. As K-feldspar and biotite have higher partition coefficients for Ba compared to other common minerals; and similarly plagioclase has higher or similar partition coefficients for Sr than the major minerals in andesitic to dacitic and rhyolitic magmas respectively (Rollinson, 1993), hence the Ba/Sr ratio will help to identify the relative roles of K-feldspar and plagioclase, since it increases with precipitation of plagioclase from the magma, but decreases when K-feldspar and biotite start to precipitate.

A good J-shaped trend can also be seen from the plotting of Sr vs. CaO (Fig. 4.13), where Sr increases with increasing CaO content. This positive slope supports that plagioclase is being removed during fractionation.

In the diagram of Rb vs. Sr (Fig. 4.16), there are two different trends that can be seen. Diorite clearly shows an enrichment of Sr with increasing Rb concentrations, whereas Sr generally decreases with increasing Rb for quartz monzodiorite and granodiorite. As Sr is a more compatible trace element in plagioclase, but not in pyroxene, fractionation of plagioclase would have decreased the concentration of Sr with increasing silica content (Wilson, 2007). The increasing trend (enrichment of Sr) in the diorite probably showed that plagioclase fractionation does not play a bigger role in diorite, and pyroxene, might have crystallizes first and dominates in the early stage of magmatic evolution. As pyroxene has low partition coefficient for Sr (Dunn and Sen, 1994; McKay, 1986; Nielsen et al., 1992), fractional crystallisation of pyroxene in diorite will not highly change Sr in residual magma.

Sr vs. MgO diagram (Fig. 4.17) is plotted to further observe the relationship of pyroxene and plagioclase fractionation. From this diagram, a positive slope can be seen where Sr increases together with MgO contents. This relationship suggest that plagioclase does fractionate together with pyroxene for diorite and quartz monzodiorite.

The HREE pattern of diorite, quartz monzodiorite and granodiorite that shows a progressive change from negative slope to concave-upward patterns with decreasing Gd/Yb ratio (Fig. 4.19), suggesting the fractionation of hornblende and clinopyroxene during the magma differentiation (Gau et al., 2013).

The plotting of Dy/Yb ratio vs. SiO_2 (Fig. 4.20) shows a negative trend, where a significant decrease in Dy/Yb ratio with increasing silica is attributable to the removal of hornblende and/or sphene fractionation (Davidson et al., 2007). Two separate trends of decreasing Dy/Yb ratio can be clearly seen for quartz monzodiorite and granodiorite.

As K-feldspar and biotite have higher partition coefficients for Ba compared to other common minerals, the changes in Ba concentrations when plotted against the total content of ($MgO+Fe_2O_3$) is plotted to see the major mafic mineral that controls magmatic evolution between the two mafic-end member: diorite-quartz monzodiorite and the felsic-end member: granodiorite. From the diagram of ($MgO+Fe_2O_3$) vs. Ba, (Fig. 4.18), there is no discernible trend of the Ba content for both the mafic-end members. The maximum value of Ba content for granodiorite is 1504 ppm and starts decreasing in a linear trend with increasing total ($MgO+Fe_2O_3$) content. Fractionation of biotite and K-feldspar should buffer or reduce Ba in the residual liquid (Blundy and Wood, 2003), thus causing this linear negative trend. From this diagram it also indicates that biotite and K-feldspar crystallized late or sank very slowly in co-existing melt during magmatic differentiation (Wyborn et al., 2001) and that biotite and K-feldspar does not play a major role during magmatic evolution of diorite and quartz monzodiorite.

Rb and Sr can be used as a possible measure of the degree of fractional crystallization as they are a major constituent of the rock-forming minerals and therefore can be found as dispersed trace element in igneous rocks. During fractional crystallization of a magma, Sr is initially removed from the melt phase and concentrated in calcic plagioclase, while Rb is concentrated in the residual magma. Therefore, the Rb/Sr ratio of co-magmatic igneous rocks tends to increase with increased differentiation cause by both an increase in Rb and a decrease in Sr. Rb/Sr vs SiO$_2$ diagram is shown in (Fig. 4.21). Due to their low Rb content (41.7 – 174.7 ppm) compared to the high Sr (378.8-1297.6 ppm) content, all the rocks have very low Rb/Sr ratio with average of 0.19. Rb/Sr ratio is significantly lower in the diorite and quartz monzodiorite (0.03 -0.16) compared to granodiorite (0.24 – 0.41), possibly reflecting higher volume of K-feldspar and lower volume of plagioclase in granodiorite.

Rb vs Rb/Sr variation diagram in semi log scale is plotted to see the enrichment of Rb relative to Sr in a differentiating magma (Schaff et. al., 1983). A good curve shaped fractionation trend can be seen from (Fig. 4.23). The diorite samples have the least Rb and are the least fractionated of all the samples. The quartz monzodiorite and granodiorite samples have slightly more Rb and are more fractionated.

P$_2$O$_5$ vs. Rb plot of the dioritic rocks (Fig. 4.22) shows typical I-type characteristic where P$_2$O$_5$ decreases with increasing Rb content and magmatic differentiation.

Based on K$_2$O vs. Na$_2$O diagram (Fig. 4.24), dioritic rocks from study area can be classified as 'I' type, crystallizing from meta-igneous source rock, after Chappell and White (1983). From this diagram, it can be seen that both mafic-end members: diorite-quartz monzodiorite and felsic-end member: granodiorite shows a different trend of K$_2$O enrichment with respect to Na$_2$O. K$_2$O content does not vary and were clustered for diorite and quartz monzodiorite, but clearly shows an increase of K$_2$O content with decreasing Na$_2$O for granodiorite.
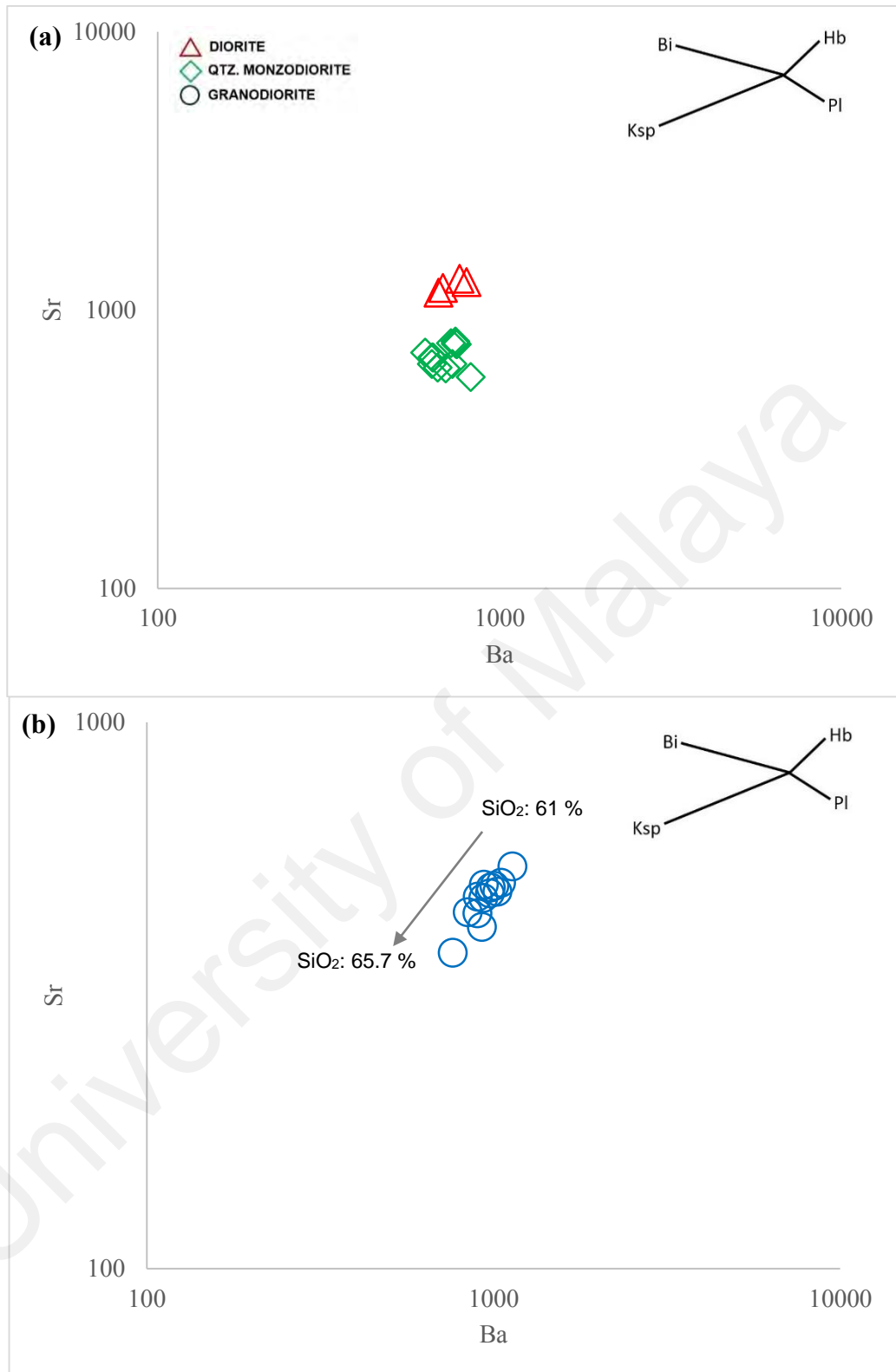
Figure 4.8   LIL modelling for the pair Sr-Ba for (a) diorite, quartz monzodiorite and (b) granodiorite. Mineral vector indicate path evolved liquids for 30% of mineral precipitating. Ksp=K-feldpsar, Pl=plagioclase, Bio=biotite and Hbl=hornblende
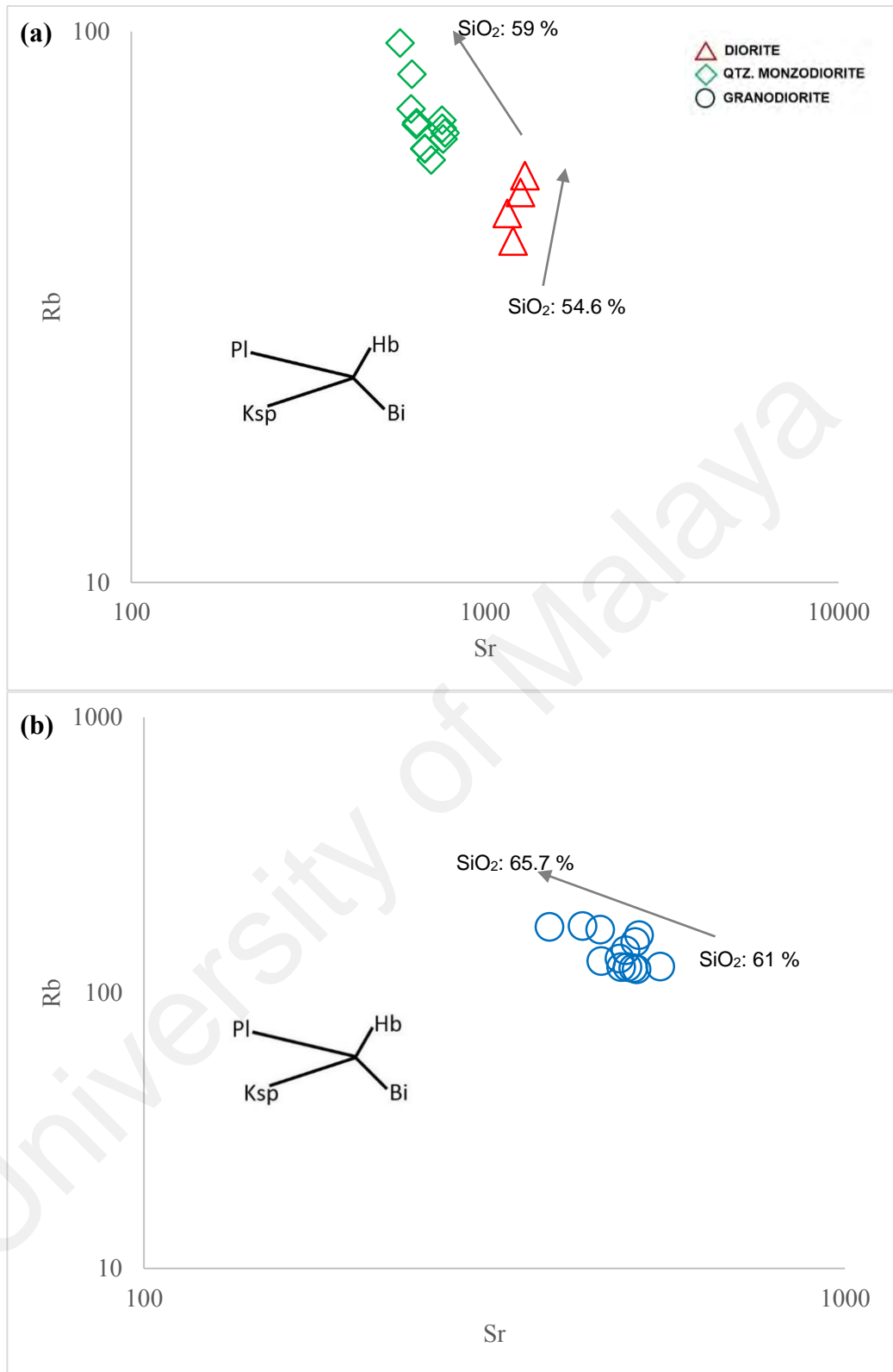
Figure 4.9   LIL modelling for the pair Rb-Sr for (a) diorite, quartz monzodiorite and (b) granodiorite. Mineral vector indicate path evolved liquids for 30% of mineral precipitating. Ksp=K-feldpsar, Pl=plagioclase, Bio=biotite and Hbl=hornblende
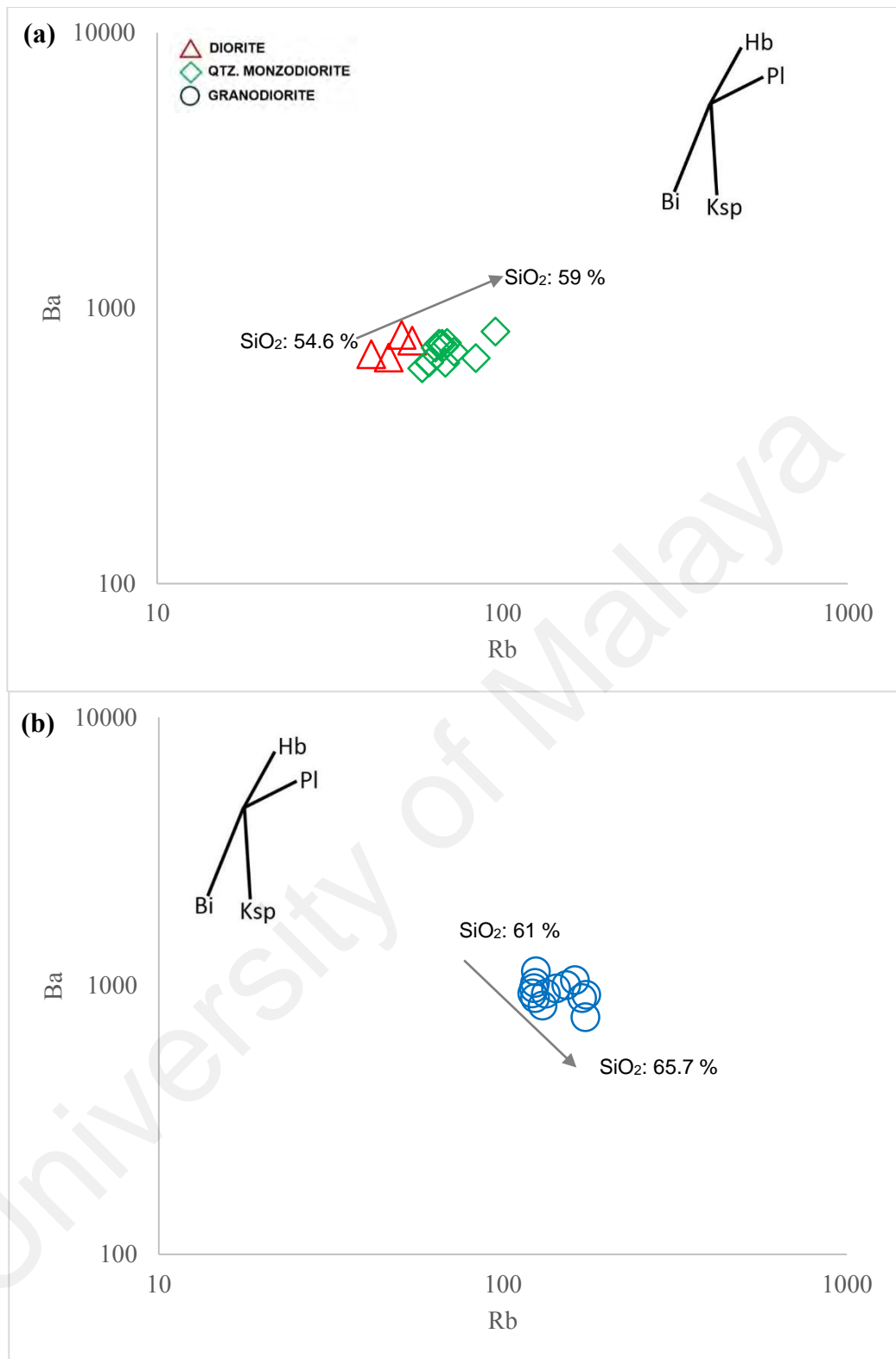
Figure 4.10   LIL modelling for the pair Ba-Rb for (a) diorite, quartz monzodiorite and (b) granodiorite. Mineral vector indicate path evolved liquids for 30% of mineral precipitating. Ksp=K-feldpsar, Pl=plagioclase, Bio=biotite and Hbl=hornblende
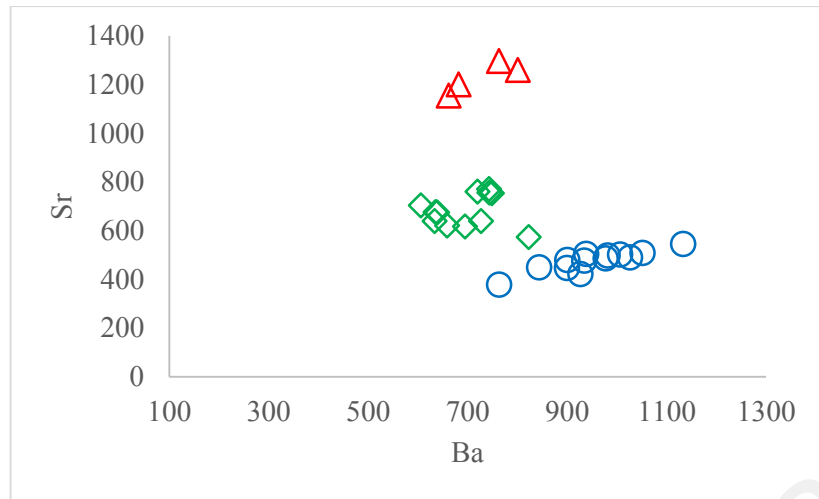
Figure 4.11   Plot of Sr vs. Ba diagram where the decrease of Ba concomitant with Sr for granodiorite suggest that K-feldspar, biotite and plagioclase are being removed in the differentiation sequence
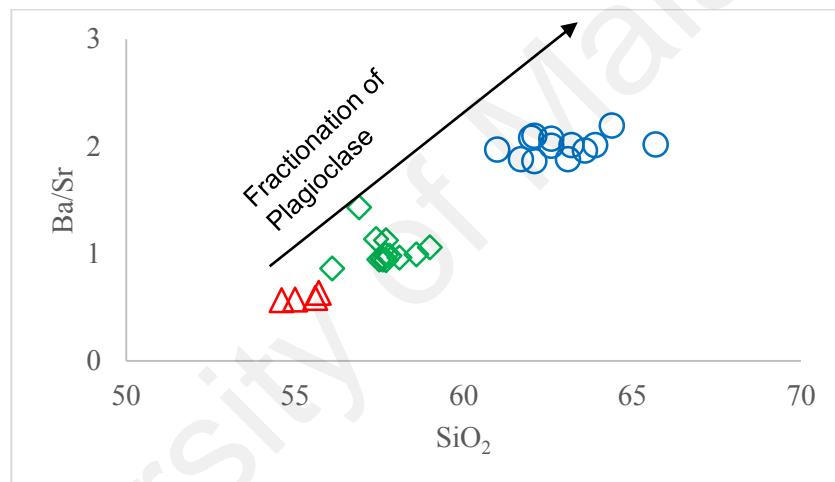
Figure 4.12   Increasing Ba/Sr ratio indicates fractionation of plagioclase rather than K-feldspar (Rollinson, 1993). Abbreviations and path of plagioclase fractionation are after Kretz (1983)
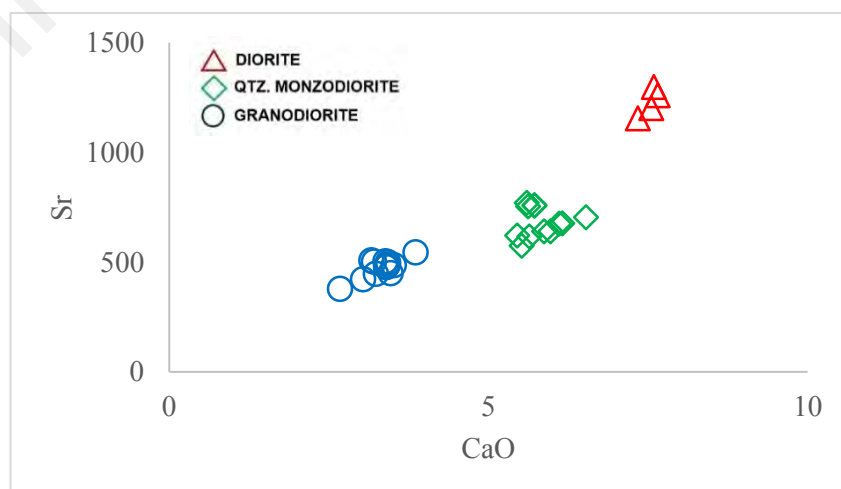
Figure 4.13   Positive slope of Sr vs CaO plot supports that plagioclase is being removed in the differentiation sequence.
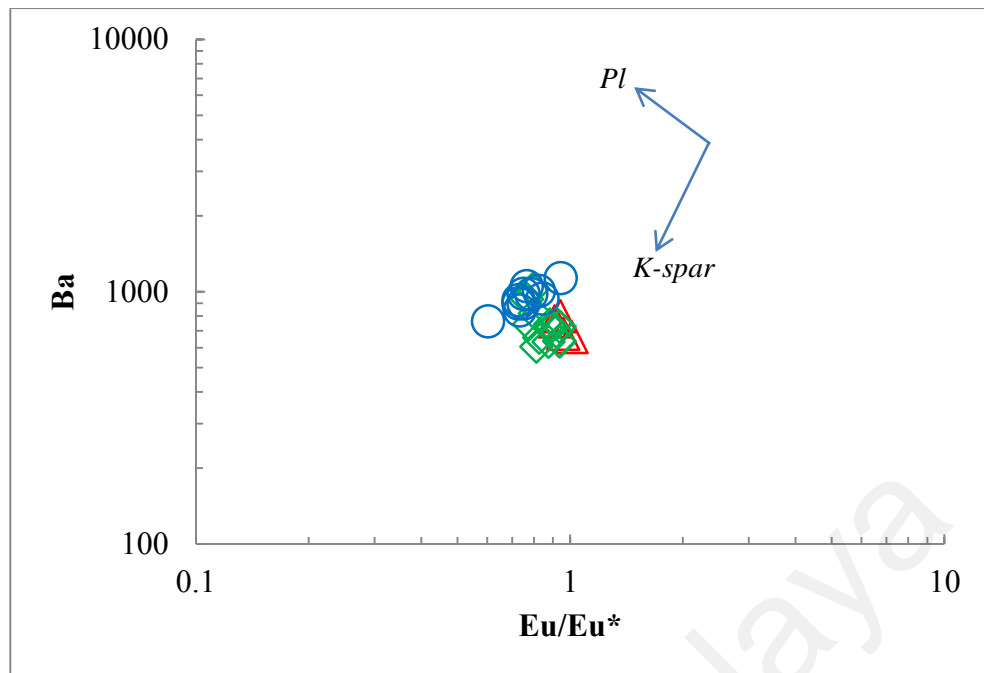
Figure 4.14   Ba vs Eu/Eu* showing the role of plagioclase and K-feldspar fractionation in the magma generation of dioritic rocks from study area. Length of vectors represents 50% of Rayleigh fractionation. Modelled fractionation trends after Eby (1990). Eu/Eu* values were obtained from the chondrite normalized after Nakamura (1974)
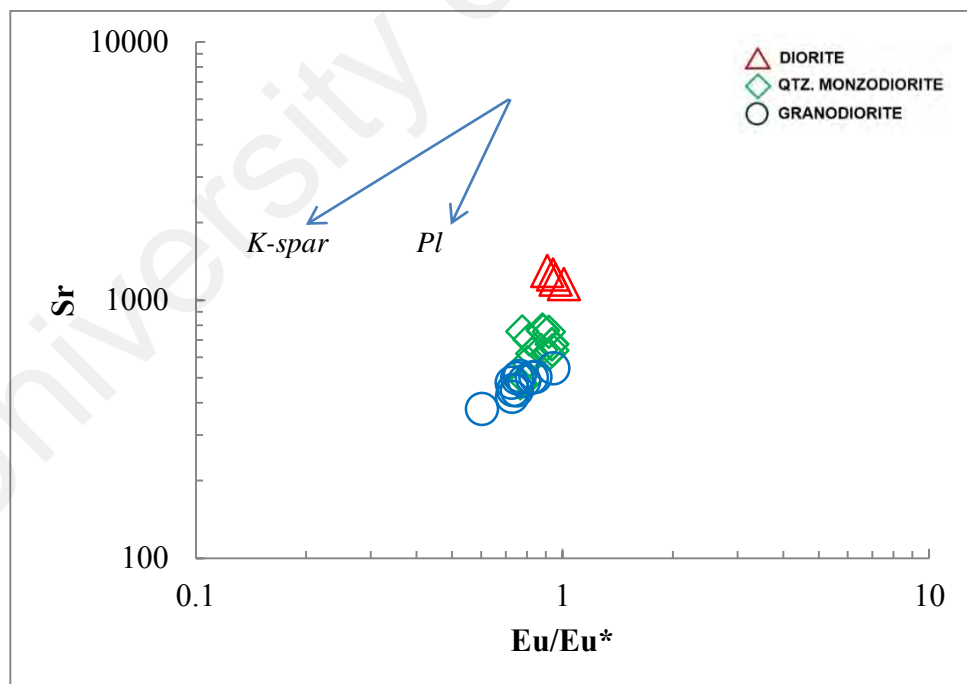
Figure 4.15   Sr vs Eu/Eu* showing the role of plagioclase and K-feldspar fractionations in the magma generation of dioritic rocks from study area. Length of vectors represents 50% of Rayleigh fractionation. Modelled fractionation trends after Eby et. al. (1990)
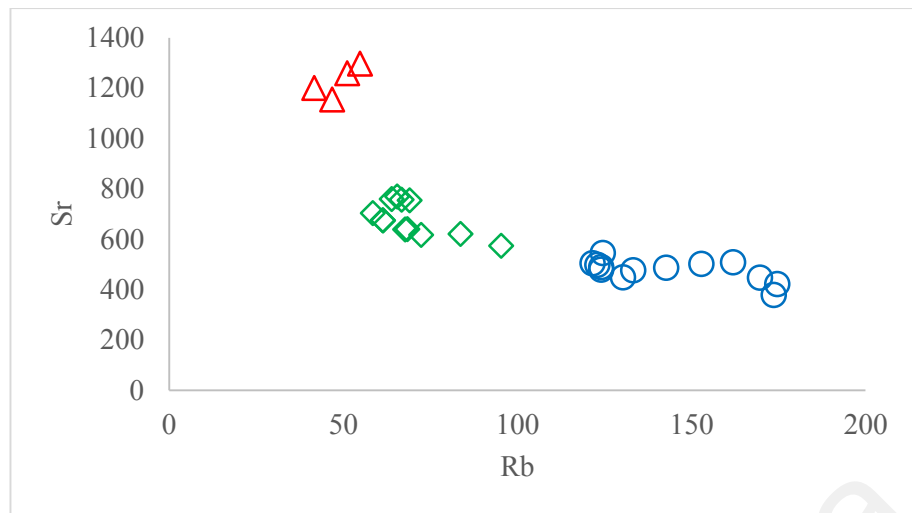
Figure 4.16   Sr vs. Rb plot
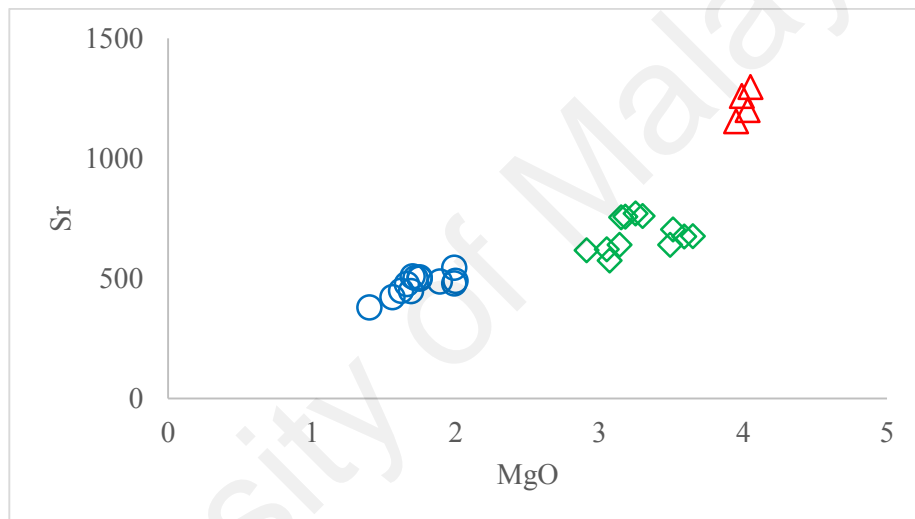
Figure 4.17   Sr vs MgO plot showing as Mg decreases, Sr decreases.
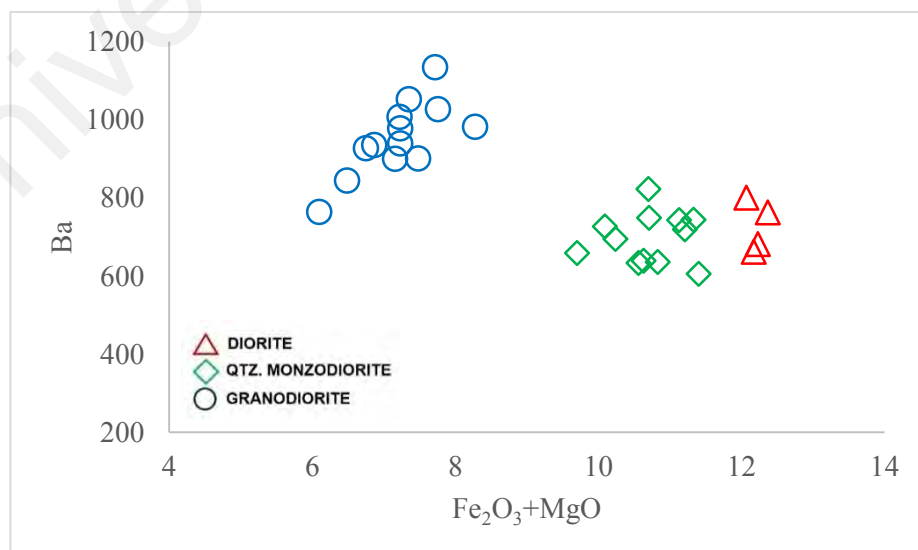
Figure 4.18   Ba vs (MgO+Fe$_2$O$_3$) diagram (after Wyborn et al., 2001)
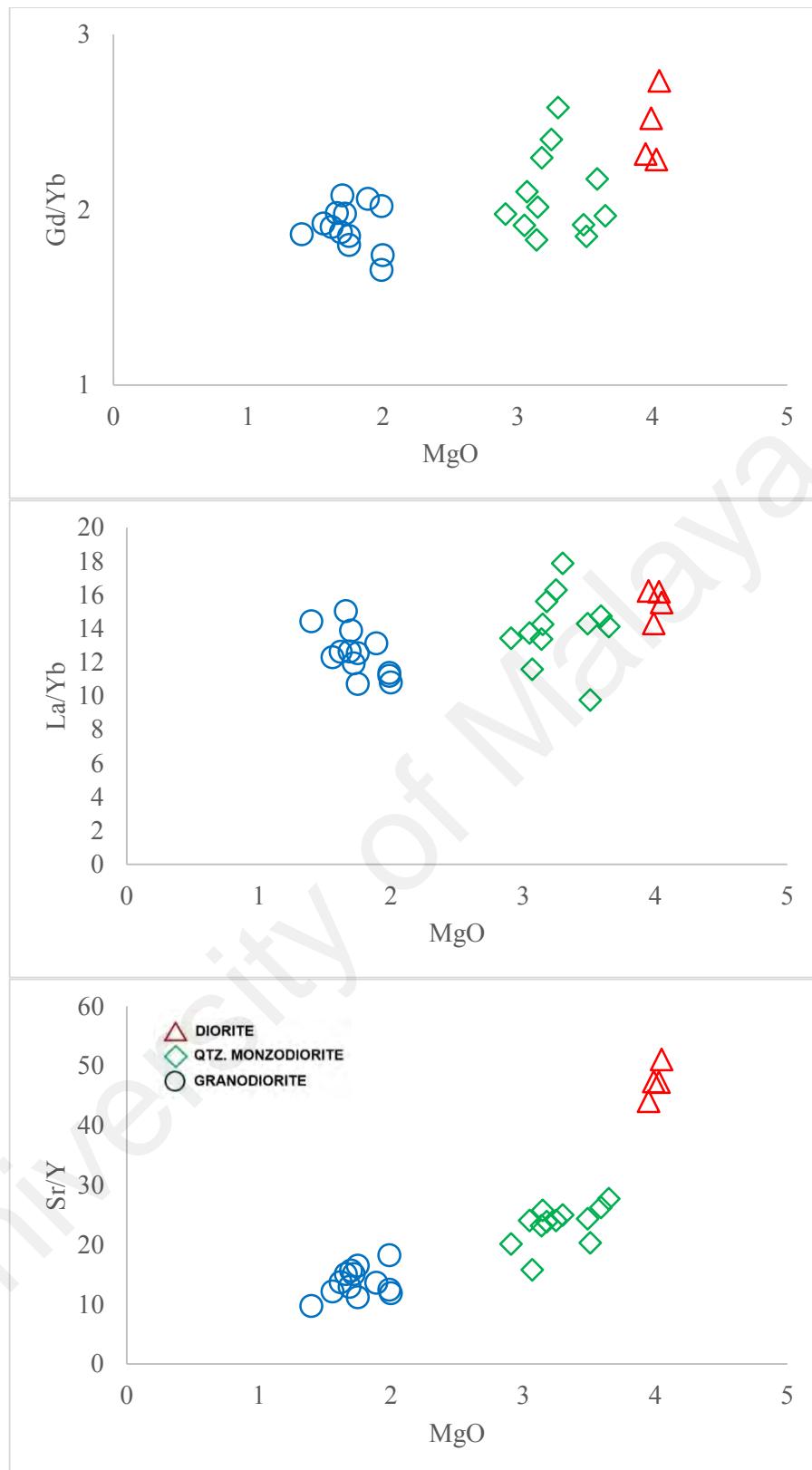
Figure 4.19   Plots of MgO vs (a)Gd/Yb, (b)La/Yb and (c) Sr/Y for the samples progressive change from from negative slope to concave-upward pattern when plotted with increasing MgO content.
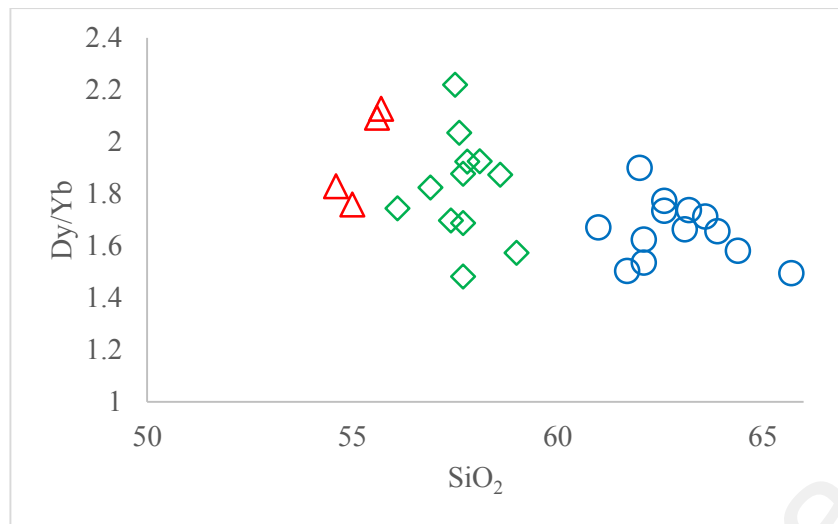
Figure 4.20   All the samples follow the fractionated trend of hornblende and titanite on the Dy/Yb vs SiO$_2$ (after Davidson et al., 2007)
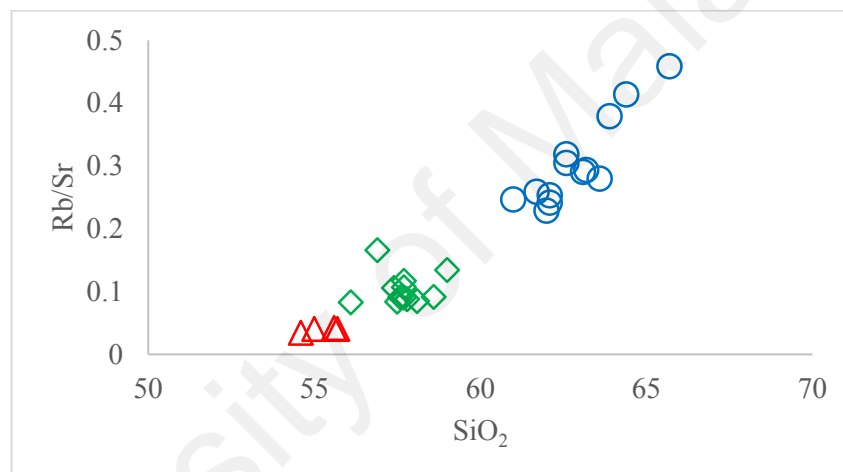
Figure 4.21   Rb/Sr vs SiO$_2$ diagram, the Rb/Sr ratio of co-magmatic igneous rocks tends to increase with increased differentiation cause by both an increase in Rb and a decrease in Sr content.
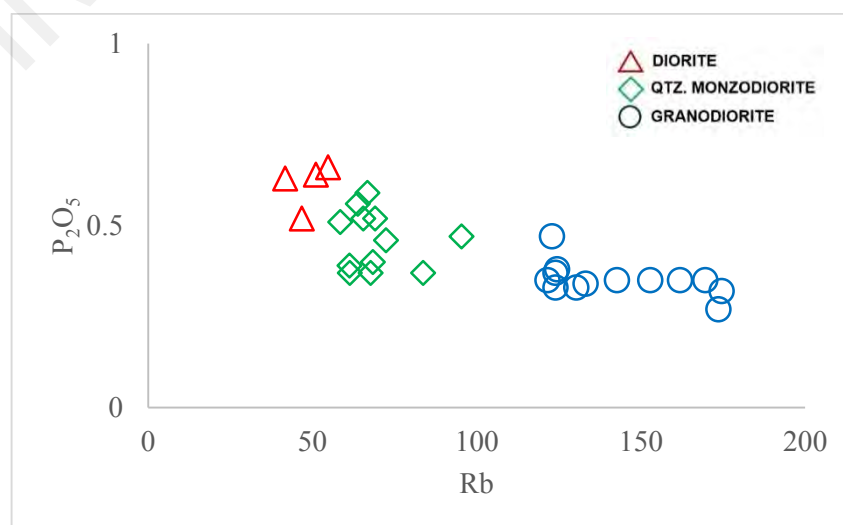
Figure 4.22   P$_2$O$_5$ vs Rb plot of the dioritic rocks from study area

116
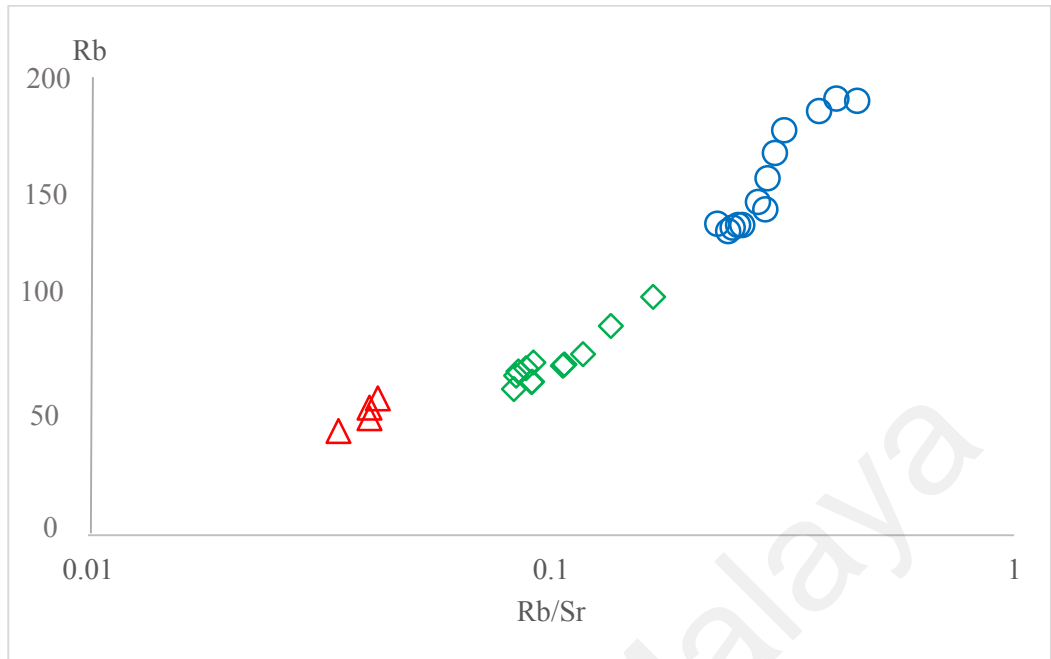
Figure 4.23   Rb - Sr variation diagram (based on Schaff et. al., 1983)
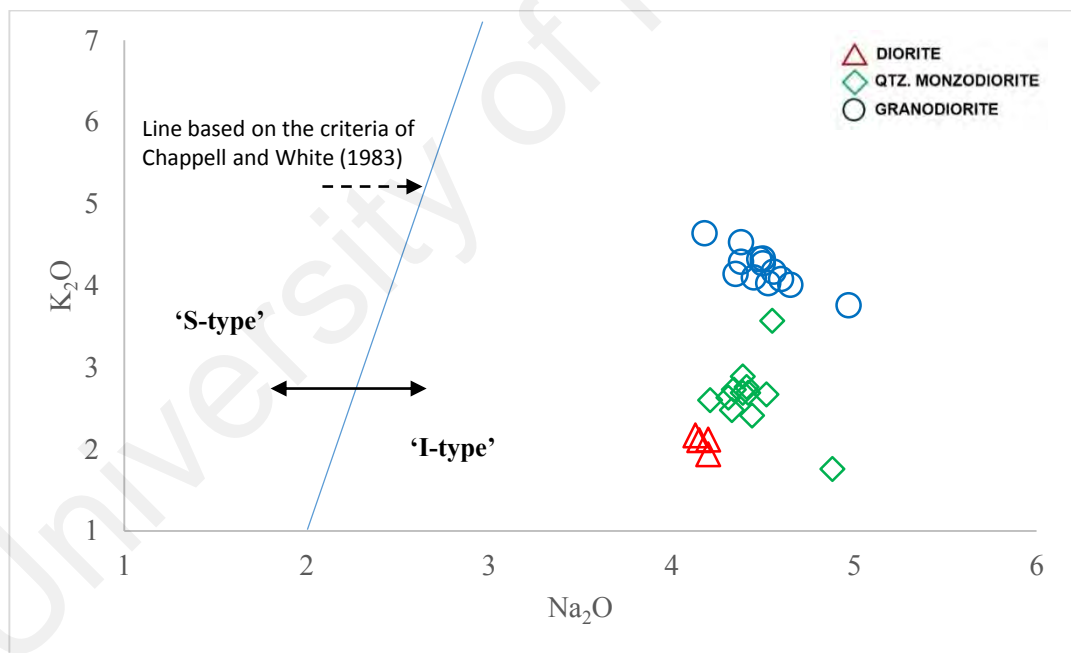
Figure 4.24 K_2O vs Na_2O plot. Field of the S and I type granite is after Chappell and White (1974)

4.8   Zircon Saturation Thermometry

Zircon saturation temperature can be calculated from whole rock geochemistry to estimate the temperature of the magma forming the rocks of study area. Accessory mineral such as zircon plays a crucial role in the petrogenesis of granitic rocks, as it control the response of isotopic systems (U-Pb, Lu-Hf, Sm-Nd) and the geochemical variation of many important trace and minor elements (e.g. Zr, P, REE, U, Th) during partial melting and subsequent fractionation of magma (Gromet & Silver 1983; Miller & Mittlefehldt 1984; Sawka 1988; Watt & Harley 1993; Bea 1996; Ayres & Harris 1997; Hoskin et al. 2000).

Whole-rock Zircon saturation temperature (T_{Zr}), developed by Watson and Harrison (1983), were estimated by using the Zr solubility in granitic melts. The software Saturnin from GCDKIT written in the freeware R language was used to perform the tedious calculations of zircon saturation in the rocks. According to the calibration, if a granitic melt is saturated with Zr, its temperature can be calculated from the measured major element and Zr contents.

The Zr saturation at a given temperature is defined by the equation of Watson & Harrison (1983):

$$Ln\ (D_{Zr/melt}) = -\ 3.80 - 0.85\ (M-1) + \underline{12\ 900} \qquad (1)$$

where;

$D_{Zr/melt}$	=	distribution coefficient for Zr between zircon and melt;
T	=	absolute temperature (K);
M	=	cationic ratio

$$\underline{Na + K + 2Ca} \quad \text{in the melt} \qquad (2)$$
$$Al.Si$$

Taking into account the theoretical concentration of Zr in stoichiometric zircon (497 644 ppm) and the definition of the distribution coefficient, the saturation concentrations of Zr (Zr_{SAT}, ppm) by:

118

$$Zr_{SAT} = \frac{496\ 644}{D_{Zr/melt}} \tag{3}$$

Computing temperature using the observed Zr concentration:

$$T\ (K) = \frac{12900}{\ln\left[\dfrac{497\ 644}{Zr}\right] + 3.8 + 0.85\ (M-1)} \tag{4}$$

The results for the rock samples are listed in Table 4.6. Calculated temperature for Zr ranges from 679.5 to 853 °C for the pluton, with average of 783.09°C. Zircon saturation temperature for the mafic-end member, diorite and quartz monzodiorite are much lower, ranging from 679.6-782.2°C while the felsic-end member, granodiorite has higher zircon saturation temperature range: 808.7-853°C. From this, it can be postulated that the temperature of magma forming diorite and quartz monzodiorite are much lower compared to granodiorite.

Table 4.6 Calculated zircon saturation temperature (T_{Zr}) for all samples from the study area

Sample	M	Zr	TZr. Sat (°C)	Zircon Saturation at specific temperature						
				700'C	750'C	800'C	850'C	900'C	950'C	1000'C
PD1	2.64	195.1	716.3	156.9	299.8	539.5	921.2	1503	2356.1	3565.1
PD4	2.64	118.1	679.5	157.1	300.2	540.2	922.4	1504.9	2359	3569.6
DYG1	2.63	214.9	724.3	155.6	297.5	535.2	914	1491.2	2337.5	3537
DYG2	2.6	205	722.5	151.9	290.4	522.5	892.2	1455.7	2281.9	3452.8
LANG1	2.36	146.7	712.7	123.7	236.5	425.5	726.6	1185.5	1858.2	2811.8
LANG4A	2.32	207.2	742.3	119.4	228.1	410.5	701	1143.7	1792.7	2712.7
LANG4B	2.41	331.2	774.2	129.5	247.6	445.4	760.7	1241.1	1945.4	2943.7
LANG8	2.34	238.2	751.9	121.8	232.7	418.8	715.2	1166.8	1829	2767.5
BAIL 1A	2.29	269.9	766.1	116.2	222	399.5	682.2	1113.1	1744.8	2640.2
BAIL 1B	2.32	233.5	752.1	119.1	227.6	409.5	699.3	1140.9	1788.3	2706
BAIL 2	2.21	290.2	777.5	109.1	208.6	375.3	640.9	1045.6	1639.1	2480.2
BAIL 3	2.34	258.9	759.1	121.3	231.8	417	712.2	1161.9	1821.3	2755.9
BER3	2.32	288.6	769.6	119.1	227.7	409.7	699.7	1141.5	1789.3	2707.5
BER8	2.28	327.5	782.8	115.8	221.4	398.4	680.3	1110	1739.9	2632.7
TBO5	2.47	227.3	739.2	136	259.9	467.7	798.7	1303.1	2042.6	3090.7
TBO6	2.44	257.2	751.1	132.8	253.7	456.6	779.7	1272.1	1994	3017.2
TBO3	1.95	423.1	831.9	87	166.3	299.2	510.9	833.6	1306.7	1977.2
TBO4	1.96	393.2	824	87.9	167.9	302.2	516	841.8	1319.6	1996.8
TM3	1.94	374.4	821	86.4	165.2	297.2	507.5	828	1297.9	1963.9
TM4	2.1	374.6	808.7	98.9	189.1	340.2	580.9	947.8	1485.7	2248.1
TM6	1.98	423.8	829.4	89.5	171	307.7	525.4	857.2	1343.7	2033.1
TM7	2.05	432.5	825.4	95.2	182	327.5	559.3	912.6	1430.5	2164.5
MYA2	1.95	446.6	836.7	87.3	166.8	300.1	512.5	836.2	1310.7	1983.3
JONG1	1.94	439.5	835.7	86.8	165.9	298.6	509.9	831.9	1304.1	1973.2
JONG2	1.94	427.5	833.1	86.7	165.8	298.3	509.4	831	1302.7	1971.1
MIAM2	1.76	450.6	853	74.4	142.2	255.9	437.1	713.1	1117.8	1691.4
TMR2	1.92	405.3	829.8	85.2	162.9	293.1	500.4	816.5	1279.9	1936.6
TMR3	1.91	419	833.9	84.3	161.1	289.8	495	807.6	1265.9	1915.4
TMR4	1.94	420.3	831.8	86.5	165.2	297.3	507.7	828.4	1298.5	1964.8
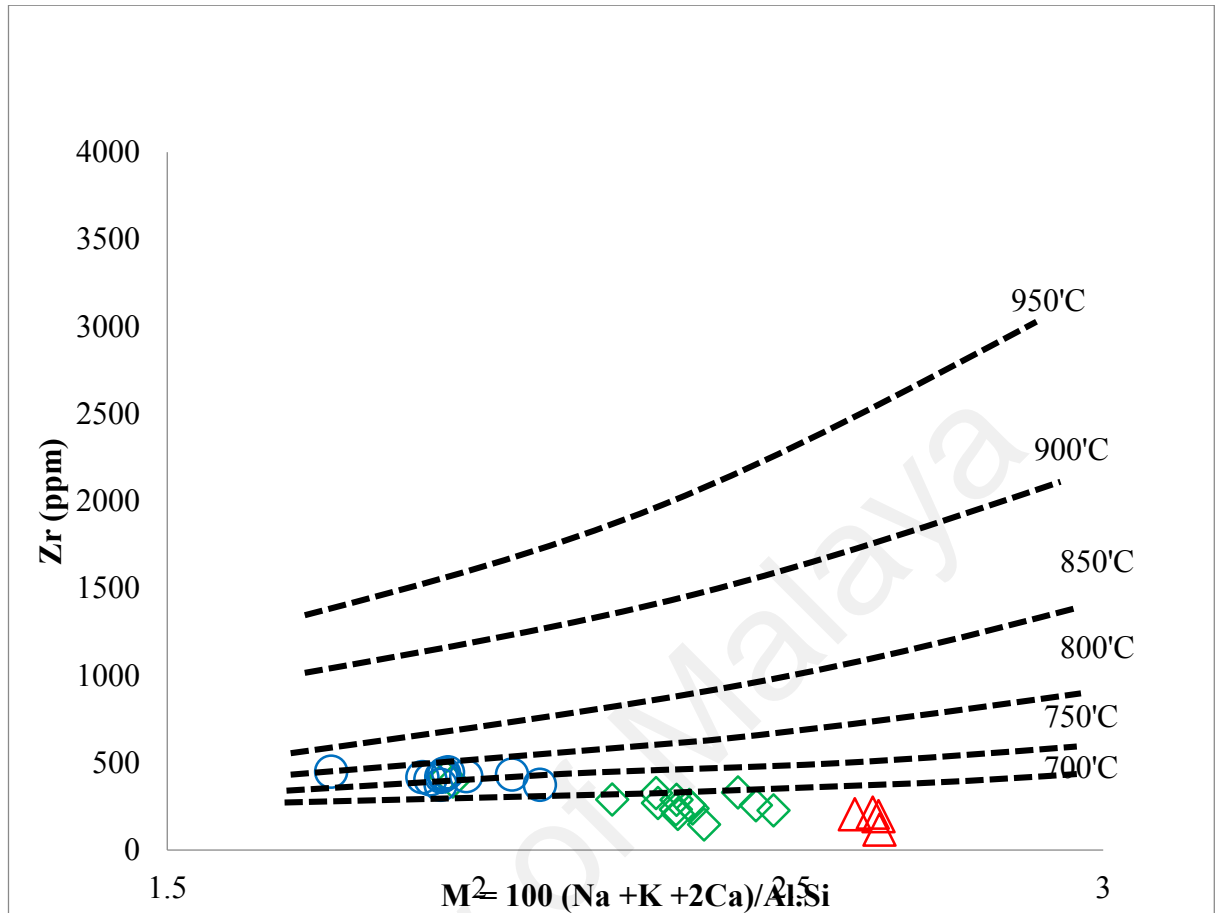
Figure 4.25   The samples show low zircon saturation temperature (T_{Zr}) ranging from diorite: 679.5-724.3 °C, quartz monzodiorite: 712.7-782.8 °C and granodiorite: 808.7-853 °C, showing increasing temperature from diorite→quartz monzodiorite→granodiorite.

4.9   Rock Classification based on Geochemical Analysis

There are several classification schemes based on geochemical data that can be used to classify, distinguished and identify the different geochemical characteristics of dioritic rocks from study area.

4.9.1   Classification Using Aluminium Saturation Index by Shand (1943)

Aluminium saturation index or ASI is the alumina saturation classification based on the molar proportions of A/CNK ($Al_2O_3/\{CaO+Na_2O+K_2O\}$). The value of ASI calculated represent the presence of specific mineral compositions in a rock, where rocks with ASI values of more than 1 shows that the magma is rich with Al_2O_3, hence high Al mineral will crystallised such as garnet, andalusite and almandine in the rock. Meanwhile rocks with ASI values of less than 1 are usually characterised by the presence of hornblende, pyroxene, and biotite (Fig 4.26). ASI index classified rocks having the ASI>1 as peraluminous and ASI<1 as metaluminous. Molar proportions of A/NK ($Al_2O_3/\{Na_2O+K_2O\}$), could also be used to classify rock, where A/NK > 1.0 is metaluminous and A/NK < 1 as peralkaline.

The rocks of study area are metaluminous in characteristics, having ASI values of less than 1, ranging from 0.74-0.93, and the A/NK value more than 1, ranging from 1.25-1.88. Graph of A/NK against A/CNK is plotted (Fig. 4.27), where all the rocks fall within the metaluminous   field.   Common   non-quartzo-feldspathic   minerals   observed   for metaluminous rocks are pyroxene, hornblende and biotite, and this is true as these three major minerals can be observed in all the rocks under petrographic observation.

4.9.2   Alphabetical Classification by Chappel and White (1974)

Chappel and White (1974) identified two different types of granite at the Lachlan Fold Belt, Eastern Australia that can be classified as 'I' type and 'S' type. This classification

scheme distinguishes different granite types that have been derived from crustal melting of igneous source rocks as 'I' type, and those derived from melting of sedimentary source rocks as 'S' type. I-type granites are characterised as hornblende and biotite bearing calc alkaline granitoids, metaluminous to mildly peraluminous, with SiO_2 ranging from 56-77%.

The graph of A/CNK vs SiO_2 also supported the I-type characteristics of the rocks from study area, where it fall within the I-type field (Fig. 4.28), with A/CNK<1 shows an increasing trend with increasing SiO_2 content. From this plot, the gap between both mafic end members: diorite, quartz monzodiorite and felsic end member: granodiorite can be clearly seen. Na_2O vs. K_2O plot (Fig. 4.24) also distinguishes the dioritic rocks from study area as being 'I' type, where all the rocks fall in the 'I' type field based on the criteria of Chappell and White (1983).

4.9.3 Classification Based On Alkaline Index by Peacock (1931)

Peacock (1931) recognized two curves intersected at the plotting of $Na_2O + K_2O$ and CaO vs SiO_2 shows a different value of SiO_2 for different rock suites. The value of SiO_2 where the two curves intersected are now known as the Peacock Index or Alkali-Lime Index (ALI) and is used to divide rock suites into the following:

Alkali-Lime Index	Name of Suite
< 51	Alkali
51 – 56	Alkali – calcic
56 – 51	Calc – Alkalic
> 61	Calcic

On a graph of Na_2O+K_2O and CaO vs SiO_2 is plotted (Fig. 4.29), the value of SiO_2 obtained from the intersection of Na_2O+K_2O and CaO is 56.0. Thus, based on the ALI, all the rocks at the study area falls within the alkali-calcic/calc-alkalic suite. It is notable that subduction related volcanic and plutonic rocks fall into the calc-alkalic suite of

Peacock, and the term calc-alkaline is often given to the suite of rocks found associated with subduction zones.

By using the Modified Alkaline Lime Index (MALI) by Frost et al., (2001), all the rocks at the study area also falls within the alkali-calcic and calc-alkalic field (Fig. 4.30) as in the Alkaline Lime Index by Peacock (1931).

4.9.4   Classification based on Hastie et al., (2007)

A modified classification for the previous plot of Peccerillo & Taylor (1976) by Hastie et al., (2007) using less mobile elements, Co and Th, also distinguishes three different types of magma series, which is the high-K calc-alkaline-shoshonite series, calc-alkaline series and tholeiitic series. All the rocks at study area fall within the field of high − K calc-alkaline series (Fig. 4.31).

4.9.5   Classification based on Peccerillo and Taylor (1976)

Peccerillo & Taylor (1976) plots of K_2O vs. SiO_2 are widely used to distinguish various series of tholeiitic, calc-alkaline, high-K calc-alkaline and shoshonitic rocks. Diorite and quartz monzodiorite plot in the high-K calc-alkaline series while granodiorite falls in shoshonite series due to high K_2O content of the samples, ranging from 1.76-4.64% (Fig. 4.32).

4.9.6   Classification Based On Irvine and Baragar (1971)

Following Irvine and Baragar (1971), AFM ternary diagram is used to divide the subalkaline rocks into calc-alkaline and tholeiitic series on the basis of their iron contents, where A=Na_2O+K_2O, F=total Fe expressed as FeO, and M=MgO (all in wt. %). F approximately equals FeO + Fe_2O_3 (Irvine and Baragar, 1971). In the AFM diagram, tholeiitic suites commonly show a strong trend of iron enrichment in the early stages of

differentiation, whereas calc-alkaline suites do not undergo iron enrichment due to the early crystallization of Fe-Ti oxides and trend straight across the diagram toward alkali enrichment.

Based on the AFM diagram (Fig. 4.33) all the rocks at the study area fall within the calc-alkaline series trend. This trend is typical of co-magmatic calc-alkaline intrusive suites. As crystallization continues, the magmas become progressively enriched in alkalis relative to iron and magnesium. This diagram also shows the relationship between all the rocks at the study area whereby they are all co-magmatic and form from the magmatic evolution through fractional crystallization. The fractionation progression as interpreted from the AFM diagram is; (from least to most fractionated) diorite→quartz monzodiorite→granodiorite.
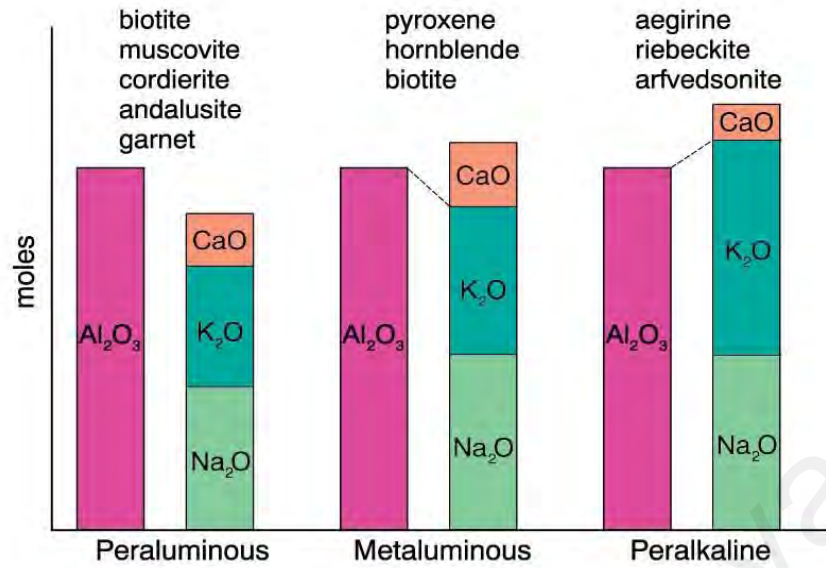
Figure 4.26 Common non-quartzo-feldspathic minerals for each type of classes based on ASI, after Clarke (1992)
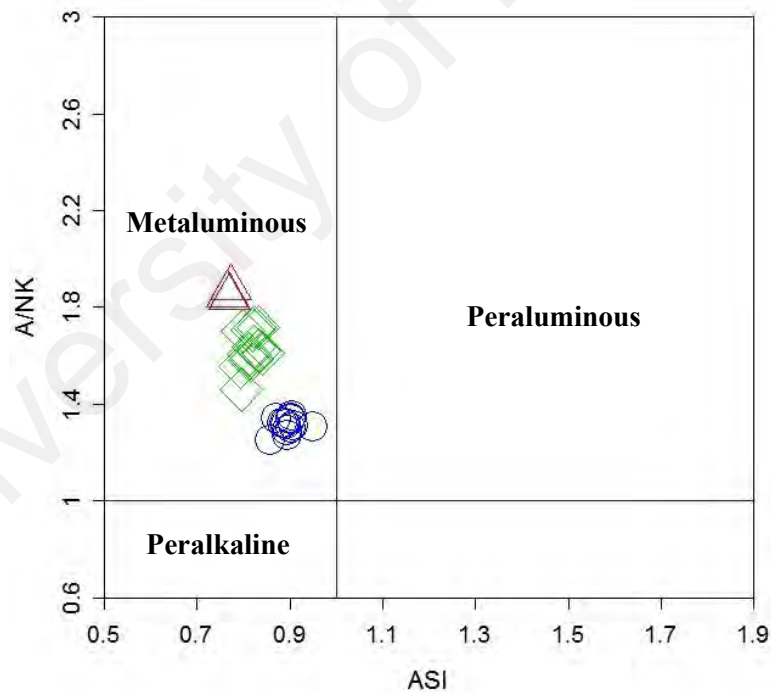
Figure 4.27 Rock classification using Shand (1947) based on the ASI values. The values of A/NK are plotted against A/CNK. All of the rocks at the study area fall within the Metaluminous field.
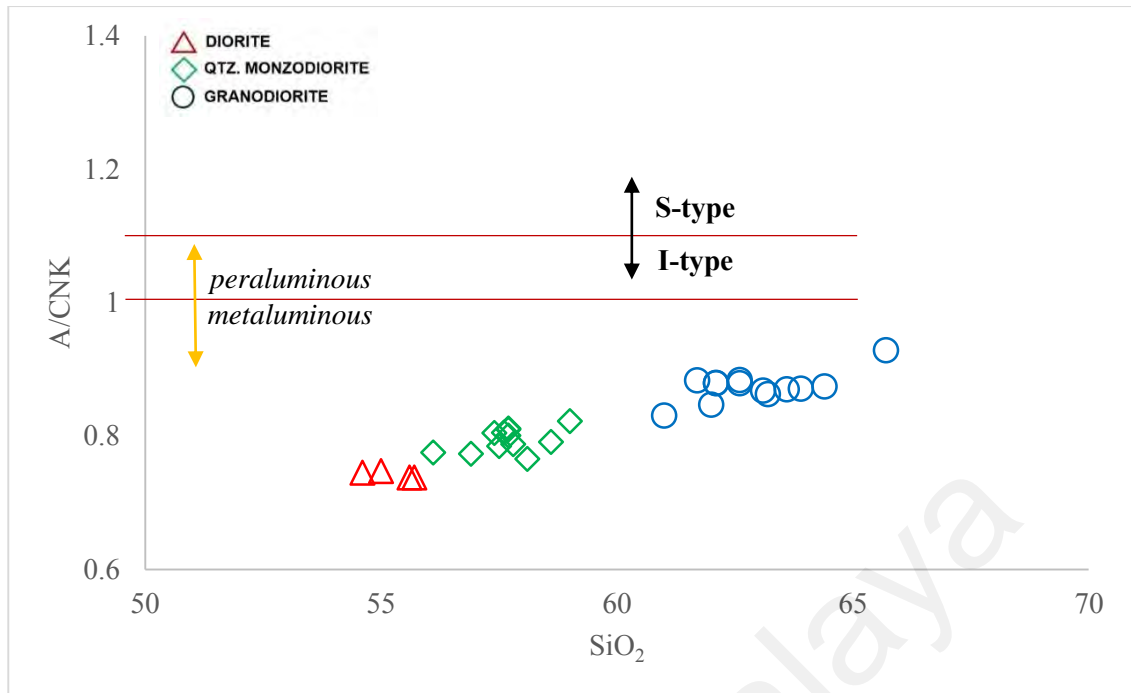
Figure 4.28 Classification made based on Chappel & White that separates I and S type granitoids together with the peraluminous and metaluminous characteristics based on A/CNK against SiO_2 plot. The value of ASI index (A/CNK values) increases with increasing SiO_2 content from diorite→quartz monzodiorite→granodiorite.
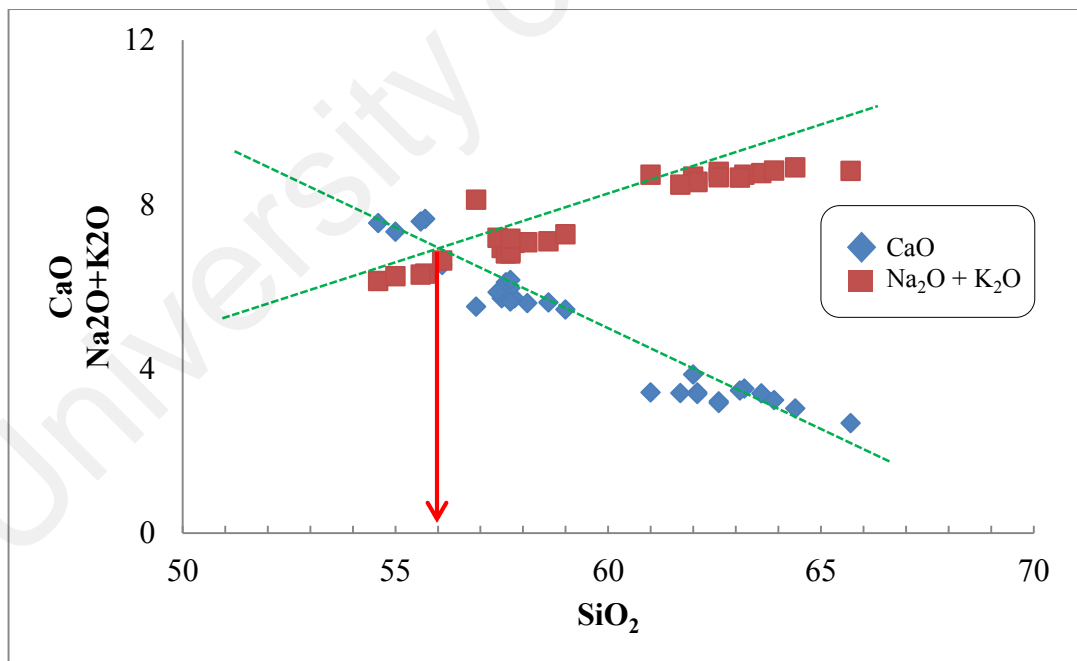
Figure 4.29 $Na_2O + K_2O$ and CaO vs SiO_2 plot based on Alkaline Lime Index by Peacock (1931). Also shown is the intersection of $Na_2O + K_2O$ and CaO line.
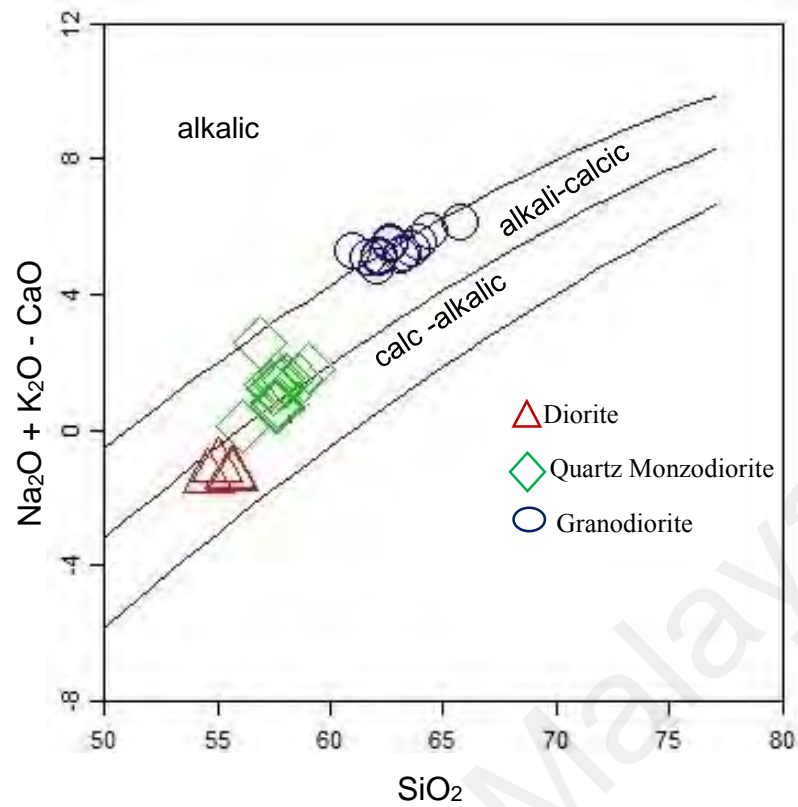
Figure 4.30 Na$_2$O + K$_2$O and CaO vs SiO$_2$ plot classification based on Modified Alkali Lime Index (MALI) by Frost et al., (2001). All the rocks plotted fall within the Alkali – Calcic and Calc – Alkalic field.
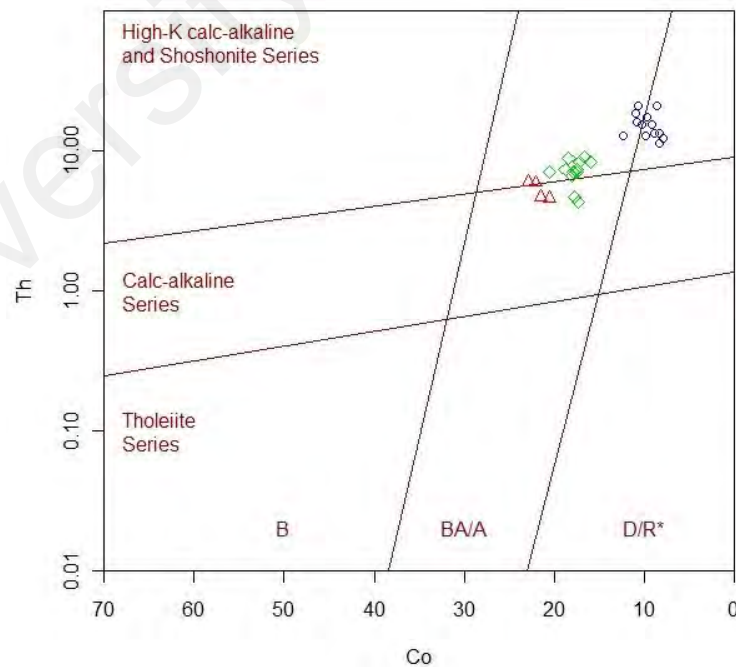
Figure 4.31 Magma series classification based on Hastie et al., (2007) where the samples plot within the calc-alkaline series and the high-K calc-alkaline and shoshonite series.
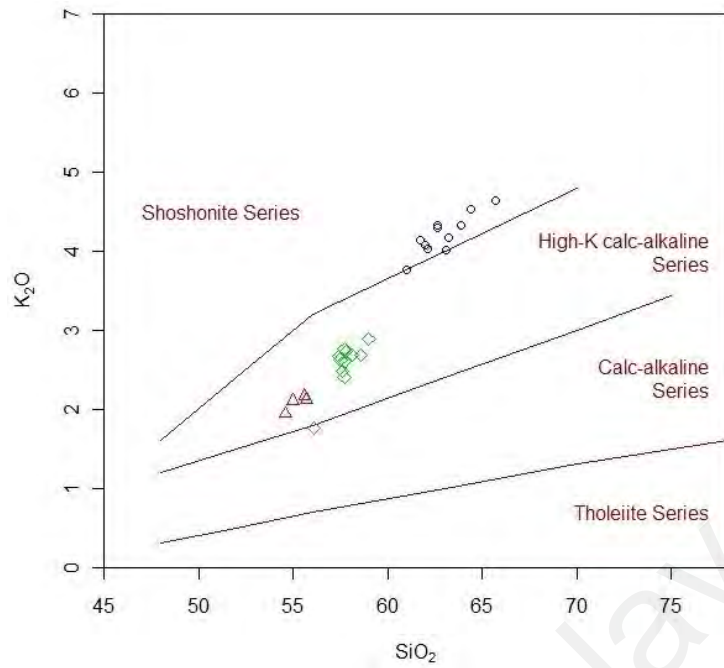
Figure 4.32 K_2O vs SiO_2 plot based on Peccerillo and Taylor (1976)
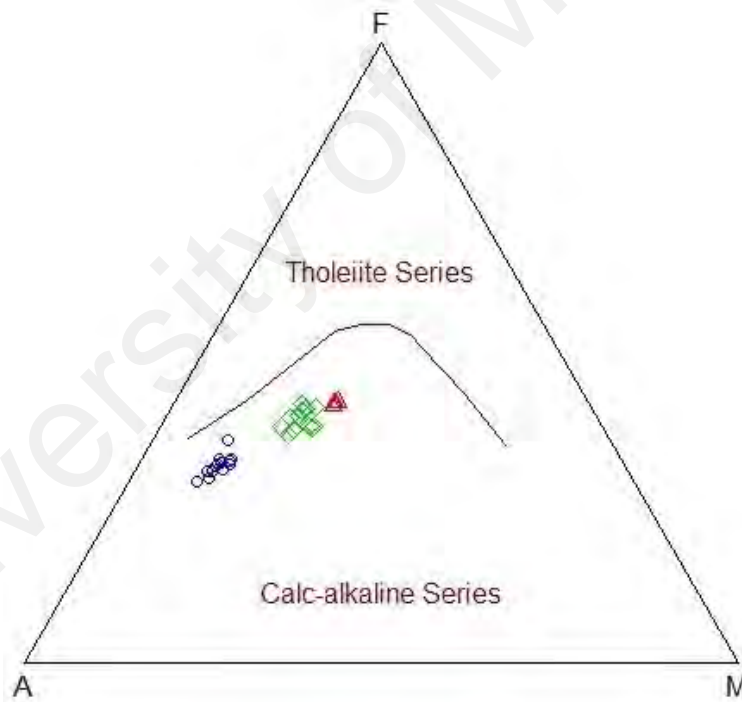
Figure 4.33 Magma series classification based on the AFM content according to
Irvine & Baragar (1971). All the rocks plotted fall within the calc-alkaline magma series.

4.10   Geotectonic Classification based on Geochemical Analysis

Several classifications can be made to distinguish tectonic environment of igneous rock based on selected major and trace element geochemical data.

4.10.1 Classification by Pearce et al., 1984

Pearce et al., (1984) uses trace elements Rb vs. (Y+Nb), Ta vs. Yb, Nb vs. Y and Rb vs. (Ta+Yb) for the construction of granite tectonic discrimination diagram. Four groups of different tectonics can be identified, which is Oceanic Ridge Granite (ORG), Volcanic Arc Granite (VAG), Within Plate Granite (WPG) and Collisional Granite (CG). Three out of the four plots classified the rocks from study area as the Volcanic Arc Granite (Fig. 4.34). From all the three plots, it can be seen that all the rock types show well defined pseudo-linear trends, with similar trends of SiO_2 contents increasing from right to left along each of these. VAG are often characterised by enrichments of K, Rb and Ba relative to Nb, Ce, Zr, Y and the absence of a negative Ba anomaly on a normalised multi-element spider diagram.

4.10.2 Classification by Schandl and Gorton (2002)

According to Schandl and Gorton (2002), four different tectonic regimes were identified for felsic to intermediate rocks, which is oceanic arcs, active continental margins (ACM), within-plate volcanic zones (WPVZ) and within plate basalt (WPB). High-field-strength-element ratio tectonic discrimination diagrams of: (a) Th/Yb vs. Ta/Yb, (b) Th vs. Ta, (3) Th/Hf vs. Ta/Hf and (4) Th/Ta vs. Yb diagrams for the entire rock samples plot in the active continental margin settings (Fig. 4.35). The intermediate rocks from study area have mineralogical field and geochemical characteristics typical of volcanic arc granites related to an active continental margin. However, in a setting of

active continental margin, the evolution of magmas through thickened section of continental crust produces added complexities.

4.10.3 Classification by Maniar and Piccoli (1989)

Granite tectonic discrimination diagram by Maniar and Piccoli (1989) using major elements can be classified to seven tectonics environment; (1) Island Arc Granite (IAG), (2) Collisional Arc Granite (CAG), (3) Continental Collisional Granite (CCG), (4) Post-Orogenic Granite (POG), (5) Ridge Related Granite (RRG), (6) Continental Epi-orogenic Uplift Granite (CEUG) and (7) Oceanic Plagiogranite (OP). IAG, CAG, CCG and POG are classified as orogenic granite, while RRG, CEUG and OP are classified as anorogenic granite. The plotting of FeO_t vs. MgO and FeO_t+MgO vs. CaO (Fig. 4.36) all the samples plot within the IAG-CAG-CCG field. From both of these plots, the gap between the two members can be clearly seen. However, it is important to mention that this granite classification by Maniar and Piccoli (1989) are more useful for igneous rocks with more than 2% of quartz under petrographic observation and more than 60 wt. % of SiO_2 from geochemical analysis.

4.10.4 Classification by Harris et al., (1986)

Trivariate plot of Hf-Rb/30-Ta×3 by Harris et al., (1986) distinguishes four group types of intermediate to acid intrusive rock tectonic settings; (Group 1) calc-alkaline volcanic arc intrusions (Group 2) syn-collisional peraluminous intrusions (Group 3) late and post-collisional calc-alkaline intrusions and (Group 4) post collision alkaline intrusions. All the rock samples are plotted in (1) calc-alkaline volcanic arc field (Fig. 4.37).

Rocks that fall within the Group 1 of calc-alkaline volcanic arc field are mostly derived from mantle modified by a subduction component and which are characterized by

selective enrichments in LIL elements. They typically form a high-level calc-alkaline suite ranging from gabbros to biotite granites, in which diorites, tonalites and granodiorites are the dominant rock types. Group-I intrusions are similar in field relations, mineralogy and geochemistry to intrusions found in active continental margins and are thus assumed to be of volcanic-arc origin.
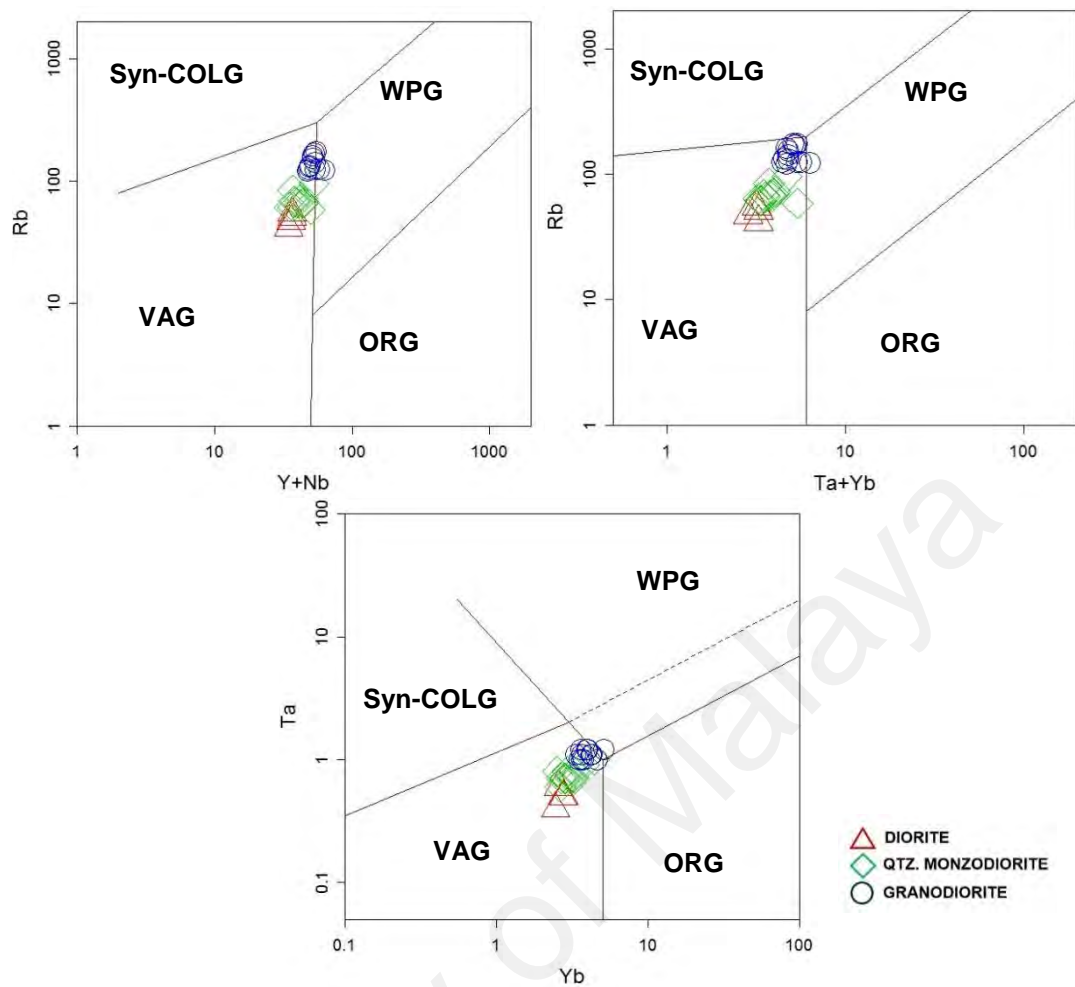
Figure 4.34 Discrimination diagram after Pearce et al (1984) Syn-COLG: Syn
Collisional Granite; WPG: Within Plate Granite; VAG: Volcanic Arc Granite; ORG:
Oceanic Ridge Granite
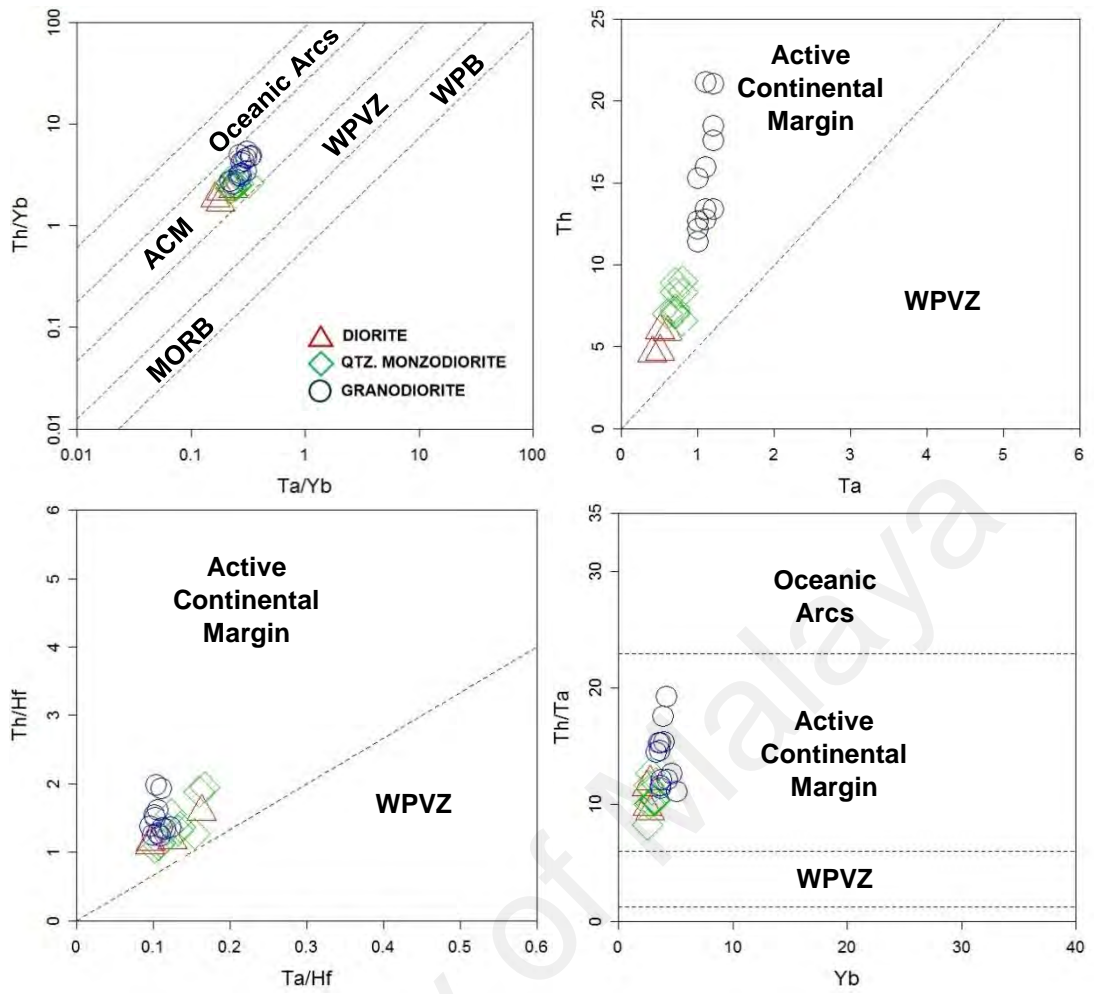
Figure 4.35   Tectonic discrimination diagram based on Schandl and Gorton (2002)
ACM: Active continental margin; WPVZ: Within Plate Volcanic Zone; WPB: Within
Plate Basalt; MORB: Mid-Oceanic Ridge Basalt.
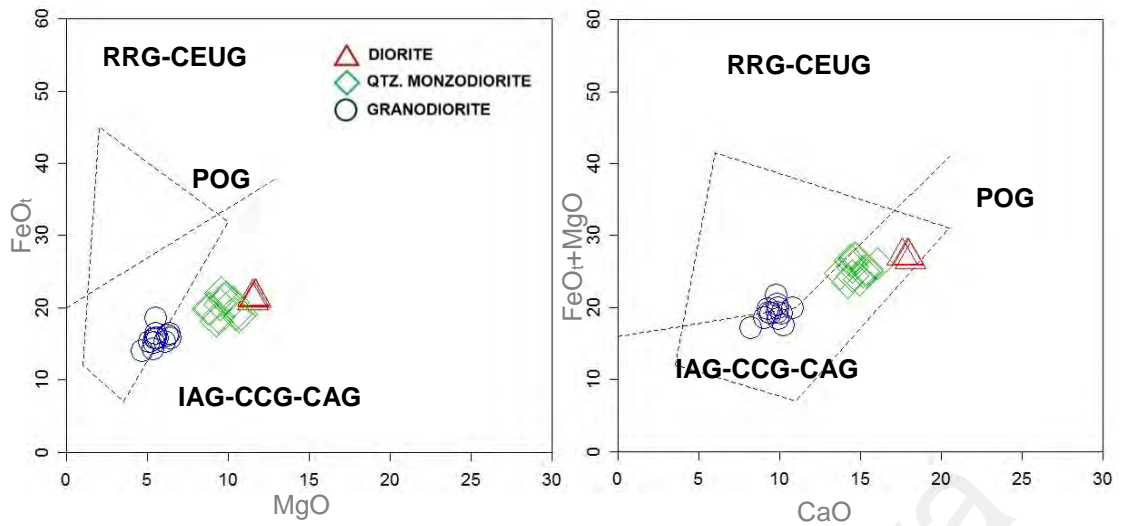
Figure 4.36   Granite tectonic discrimination diagram by Maniar and Piccoli (1989). IAG: Island Arc Granite; CAG: Collisional Arc Granite; CCG: Continental Collisional Granite; POG: Post-Orogenic Granite; RRG: Ridge Related Granite; CEUG : Continental Epi-orogenic Uplift Granite; OP: Oceanic Plagiogranite
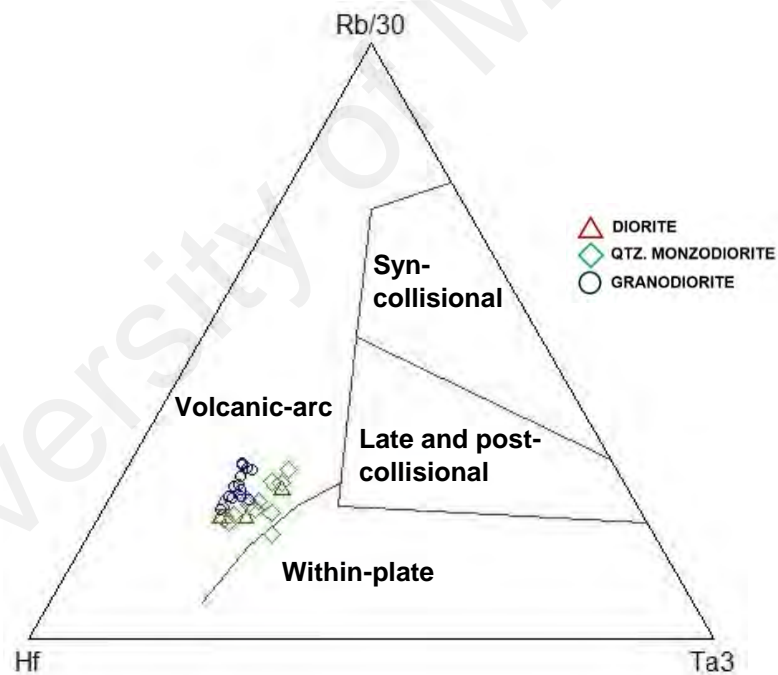
Figure 4.37 Ternary plot Hf - Rb/30 - Ta*3 by Harris et al. (1986), all rock samples fall in the Volcanic Arc (VA) field.

4.11 Summary

Based on major and trace elements geochemistry, Harker diagram, LIL modelling, inter-elements variation diagram, spidergram, REE trends, rock classifications and geotectonic classification diagram based on geochemical data available, several conclusions can be made:

1. The range of SiO_2 for the rocks are: diorite (54.6-55.6%), quartz monzodiorite (56.1-59 %) and granodiorite (61-65.7 %). Although the range of SiO_2 does not overlap between from these different rock types, diorite and quartz monzodiorite show similar range and values for most major and trace elements concentration. Granodiorite however, shows a significantly different compositions.

2. Geochemistry of major and trace elements clearly shows a different composition between the mafic-end members: diorite and quartz monzodiorite; and felsic-end member: granodiorite.

3. Mafic-end members are characterized by higher Fe_2O_3 (6.65-8.32 %) CaO (5.45-7.65 %), MgO (2.91-4.05 %) and the TAS of these mafic-end members are lower, ranging only from 6.41-7.28 %. They are characterised by low concentrations for most trace elements, with an exceptionally higher and variable Sr concentrations: 574.9-1297.6 ppm.

4. Granodiorite have a significantly higher TAS contents: 8.49-8.91 %, having high K_2O concentrations (3.76-4.64 %) compared to mafic-end members (1.76-2.17 %). Granodiorite are also characterized by low Fe_2O_3 (4.7-6.53 %), CaO (2.68-3.86 %) and MgO (1.4-2 %). Most trace elements concentrations are highest in granodiorite: Ba (764-1134 ppm), Rb (121.7-174.7 ppm), Zr (374.4-450.6 ppm), with a significantly low Sr concentrations (378.8-545 ppm).

5. A 2% silica gap between both members, different range of major and trace elements concentrations and different trends seen on Harker diagram for major and trace

elements suggest that both members are made up of at least two different individual batches of melt.

6. The linear-like trend and geochemical variations seen from Harker plot suggest the importance of fractional crystallisation for these two members, where diorite-quartz monzodiorite are the results of fractional crystallisation from the same magma whereas granodiorite crystallizes from a different magma.

7. N-MORB normalized diagram further distinguishes the difference between these two members where there is no positive Pb spike for the mafic-end member possibly reflecting their mantle components, and granodiorite shows distinct positive Pb-anomaly, where Pb are normally enriched at crustal sources and consistent with the involvement of crustal compositions.

8. There is also a different in the calculated zircon saturation temperature, where it ranges much lower for diorite and quartz monzodiorite, ranging from 679.6-782.2°C while the felsic-end member, granodiorite has higher zircon saturation temperature range: 808.7-853°C. The higher range of T_{Zr} for granodiorite (808.7-853°C) could be explained by the higher abundances of biotite and amphibole in granodiorite, as breakdown of these two minerals occur most likely at T>800°C (Miller et al., 2003).

9. Generally, the pluton is I-type, metaluminous, with the mafic-end member showing high-K calc-alkaline trend while the felsic-end member shows shoshonitic trend.

10. Geotectonic classification diagram classify the tectonic regime of the dioritic rock as calc-alkaline volcanic arc (VAG) origin with field relations, mineralogy and geochemical characteristics which are typically associated with active continental margin (ACM) settings. They are characterized by mantle modified by subduction components, selective enrichments in LIL elements, enrichments of K, Rb and Ba relative to Nb, Ce, Zr, Y and the absence of a negative Ba anomaly on a normalised multi-element spider diagram.

11. Both members are controlled by different mineral proportions on LIL log plot (mafic-end members: clinopyroxene, hornblende, plagioclase and felsic-end member: plagioclase, K-feldspar, biotite).

12. A multi sources and different origins for both end members can be seen from geochemical plots and classification diagrams, suggesting they were probably made up of individual batches of melt. However, continuous trend seen for both members on Rb/Sr vs SiO_2, Sr vs CaO and REE patterns suggests that a connection exist between all the rocks at some stage of their magmatic evolution.

CHAPTER 5: COMPARISON OF DIORITIC ROCKS FROM AUR AND PEMANGGIL ISLANDS

5.1 Introduction

This chapter focuses on the comparison of the dioritic rocks from Aur and Pemanggil Islands. Both islands are underlain by dioritic rocks, intermediate in composition, and have been dated as Late Cretaceous (~80Ma) age. As these Cretaceous plutons of Aur and Pemanggil Islands form a linear chain aligned NNW and SSE to one another, this implies that their formation and interpretations are of regional tectonic significance. Through this chapter, the brief general geology and petrographic characteristics of dioritic rocks of Pemanggil Island were described. Similar and contrasting characteristics of dioritic rocks from both islands based on geochemical data, together with the petrogenesis and genetic relationship will be discussed.

5.2 General Geology of Pemanggil Island and the Petrographic Characteristics

Pemanggil Island is located 15 km northwest to Aur Island. Plutonic igneous rocks covers almost 80% of Pemanggil Island, forming a hilly topography, and the island is heavily forested. Rock exposed at Pemanggil Island is in the form of in-situ rock boulders with various sizes and shapes. Three types of diorite can be found at Pemanggil Island, which is: (1) pyroxene hornblende diorite, (2) porphyritic pyroxene-hornblende diorite and (3) microdiorite. Fragments of volcanic rock measuring 10 to 20 cm across can be seen in the dioritic rock, and these rocks intruded into the volcanic rock probably of Permian age. Pyroxene hornblende diorite occurs mainly in the northern part and the porphyritic pyroxene hornblende diorite occurs mainly in the southern part of Pemanggil Island. Microdiorite however can be found showing sharp contact with the pyroxene hornblende diorite. The dioritic rocks of Pemanggil Island are relatively homogenous. Enclave is rarely found except for some small scale hornblende schlieren found within

the pyroxene hornblende diorite at the eastern part of the island (Abdul Hamid et al., 2002).

Modal compositions indicate that all the three different diorites of Pemanggil Island fall and can be classified as diorite or gabbro according to Streckeisen (1976), (Abdul Hamid et al., 2002). Hand specimens of the porphyritic pyroxene hornblende diorite of Pemanggil Island shows a distinct porphyritic texture, with abundance plagioclase as the matrix, size ranging from 0.5 cm to 2 cm. All the three different rock types have plagioclase as the most abundance minerals, being more than 86% of the rock mineral compositions. Summary of the petrographic description of the dioritic rock of Pemanggil Island is shown in (Table 5.2).

Dioritic rocks of Aur Island, when plotted within the QAP diagram however fall within the diorite, quartz monzodiorite and granodiorite field (Fig. 3.1b). Mineralogy of rocks from both islands consist of the same minerals, which is; plagioclase, quartz, alkali feldspar, biotite, clinopyroxene and hornblende. Accessory minerals are apatite, zircon, and opaque minerals. The summaries of similar and contrasting petrographic characteristics of rocks from Pemanggil and Aur islands are shown in (Table 5.3).

Table 5.1   Summarize general geology and field observation of
Aur and Pemanggil Islands

Area	Aur Island	Pemanggil Island
Rock types	Diorite Quartz Monzodiorite Granodiorite	Pyroxene hornblende diorite Porphyritic pyroxene hornblende diorite
Dike	Aplite dike - cutting through diorite body at Dayang Island (located north to Aur Island) - sharp contact	Microdiorite - cutting through porphyritic pyroxene hornblende diorite at Teluk Pakleh (southern of Pemanggil Island) - sharp contact
Types of enclave		
Enclave	Mafic Microgranular Enclave (MME) - rounded to angular shape - sharp contact with host rock - fine grained igneous texture - can be found within quartz monzodiorite and granodiorite body - petrography shows the mineralogy of enclave consist mainly of biotite, hornblende and clinopyroxene, to diorite in composition	Felsic Microgranular Enclave (FME) - ovoid shape - sharp to gradational contact with host rock - fine grained igneous texture - found only at the southern of Pulau Pemanggil, within the microdiorite - origin : disrupted fine grain margin
Xenolith	None	Fragments of volcanic rock measuring between 10 to 20 cm within dioritic rock
Schlieren	None	Hornblende schlieren found in pyroxene hornblende diorite - oblate shape, coplanar orientation - origin : disrupted enclave
Rock outcrop	In – situ rock boulders - commonly fractured, jointed - grooves on rock boulders are commonly observed - no contact has been found between the different rock varieties	In – situ rock boulders - commonly fractured, jointed - grooves on rock boulders are commonly observed - no contact has been found between the two different varieties of dioritic rock

Table 5.2   Summary of petrographic descriptions of Pemanggil Island

Rock Type	Porphyritic pyroxene hornblende diorite	Pyroxene hornblende diorite	Microdiorite
Occurrences	southern part of the island	northern part of island	Syn – plutonic dyke
Macroscopic description	Highly porphyritic	Equigranular, bigger mafic clots	Fine grained
Microscopic description Major minerals	Plagioclase, augite, hornblende, biotite, quartz, K-feldspar	Plagioclase, augite, hornblende, biotite, quartz, K-feldspar	Plagioclase, hornblende, biotite
Accessory minerals	Opaque minerals	Opaque minerals, zircon	Opaque minerals
Texture	Highly porphyritic - Plag as phenocryst (euhedral – anhedral shape, 0.5 to 2.0 cm)	Hypidiomorphic granular	Fine grained, equigranular
Other petrographic features	Hornblende rim surrounding augite	Hornblende rim surrounding augite	Biotite form from alteration of hornblende

Table 5.3   Comparison of petrographic descriptions of Aur and Pemanggil Island dioritic rocks

	Aur Island	Pemanggil Island
Distribution of igneous rock	Covering whole island	Covering whole island
QAP classification (Streckeisen, 1976)	Diorite Quartz Monzodiorite Granodiorite	Gabbro Diorite
Texture	Hypidiomorphic granular Ophitic, sub-ophitic texture texture	Porphyritic : Pyroxene hornblende diorite Equigranular : Pyroxene hornblende diorite Fine grained equigranular : microdiorite
Plagioclase	Zoning, polysynthetic albite twinning Intergrowth of plagioclase Opaque, apatite inclusion	Zoning, polysynthetic albite twinning Opaque and zircon inclusion
Pyroxene	Augite - surrounded by hornblende rim - showing distinct cleavage	Augite - surrounded by hornblende rim - anhedral

	subhedral to anhedral shape - not observed in granodiorite	- present in both varieties of pyroxene hornblende diorite, not in microdiorite
Hornblende	Green to pale green pleochroism Subhedral to anhedral shape Usually forming mafic clots together with biotite and pyroxene	Green to pale green pleochroism Subhedral to anhedral shape Inclusions in other mineral, i.e plagioclase
Biotite	Euhedral to anhedral Opaque, apatite inclusion	Subhedral to anhedral Opaque inclusion
Alkali feldspar and quartz	Late mineral, interstitial Anhedral	Late mineral, interstitial Anhedral Percentage less than 5% in the three different rock types Myrmekit texture observed in microdiorite
Accessory minerals	Opaque minerals, apatite, zircon, sphene - opaque minerals are abundant, scattered, as inclusions in other minerals - minor amount of sphene; observed in granodiorite	Opaque minerals, zircon - no apatite, sphene observed - opaque minerals are abundant, scattered
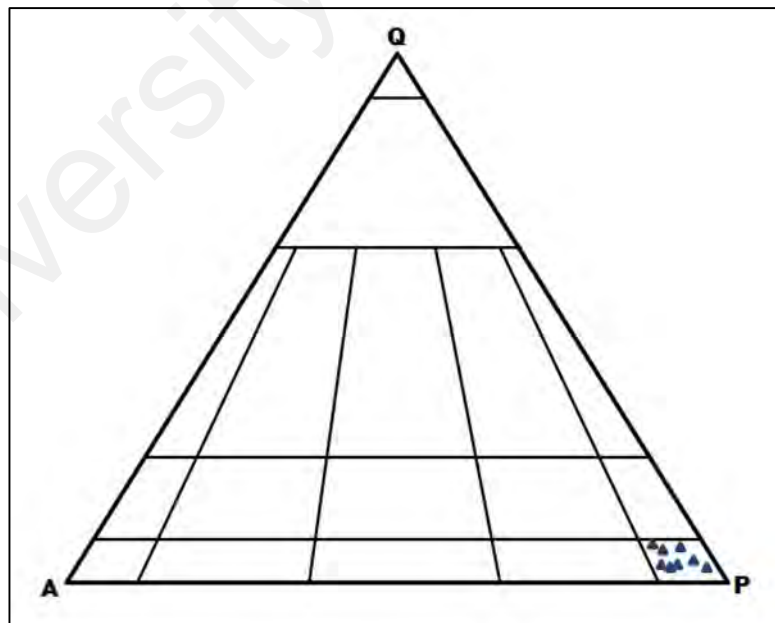
Figure 5.1   Rock classification of the dioritic rocks at Pemanggil Island, falls within the diorite based on the modal mineral percentages of QAP, after Streickensen (1976). (Taken from Mohd Marzuki Asmuri, 2002; Mohd Basri Ismail, 2002)

143

5.3   Geochemical Comparisons of Aur and Pemanggil Dioritic Rocks

The range for selected major and trace elements for the dioritic rocks from both islands are shown in Table 5.4. From this table, it can be seen that the ranges for most major and trace elements are almost the same and there are not much different in the concentrations of rocks from both islands. However, concentrations of some major and trace elements are noticeably different between these two.

Al_2O_3 and P_2O_5 of dioritic rocks from Pemanggil Island are higher compared to Aur Island, ranging 14.56 to 19.71 % and 0.28 to 0.92 % respectively. The ranges for Al_2O_3 and P_2O_5 for Aur Island respectively are; 15.36 to 17.06 % and 0.27 to 0.66 %. K_2O contents of Aur Island are higher ranging from 1.94 to 4.64 % whereas K_2O content for Pemanggil Island ranges are: 1.33 to 4.18 %.

Another distinct observations are the different range of some trace elements, where Sr concentrations for Pemanggil dioritic rocks are very high, ranging from 861-2234 ppm with an average of 1368. Sr concentrations for Aur dioritic rocks range only from 378.8 to 1297.6 ppm with a much lower average: 665. W and Zr contents of Pemanggil are also higher than Aur dioritic rocks, where the ranges for W is 4-65.2 ppm with average 11.78 and for Zr: 104.1-526.4 ppm with average 366.97. W contents for Aur are only 0.7-5.1 ppm with average of 1.94 and for Zr: 118.1-450.6 ppm with average 318.62. However, Pb contents for Aur dioritic rocks are higher than Pemanggil, ranging from 2.4-28.5 ppm with average 10.6, whereas Pb contents for Pemanggil ranges only from 2.1-10.8 ppm with an average of 5.44.

5.3.1   Major and Trace Elements Geochemistry

To better depicts the differences between the dioritic rocks from both islands, selected major and trace element are plotted together in Harker diagram to evaluate the trends of these elements with increasing SiO_2 contents. From Harker diagram for major elements

(Fig 5.2), K_2O is the only elements showing linear positive trend with increasing silica contents for rocks from both islands. Al_2O_3, CaO, MgO, Fe_2O_3, TiO_2 and P_2O_5 for both islands generally decreases with increasing magmatic differentiations, suggesting the importance of fractional crystallisation and the removal of ferromagnesium and Ca-bearing plagioclase during magmatic evolution.

While Aur dioritic rocks clearly shows a compositional gap and two different groups from the Fe_2O_3, CaO and MgO plots, Pemanggil dioritic rocks shows a clear linear trends for these elements without any distinct gap. On Al_2O_3 plot, Pemanggil dioritic rocks show distinct negative linear trend while Aur dioritic rocks show a separate negative trend for the mafic and felsic-end members. Rb, Ta, Th and U show linear positive trend for dioritic rocks from both islands. Sr shows a distinct negative linear trend for Pemanggil dioritic rocks, while Aur dioritic rocks exhibit a complicated trends.

Normalised multi-element diagram (spider diagram) of trace elements for dioritic rocks from both islands were plotted together. Pemanggil dioritic rocks exhibit complicated trends for Pb anomaly, where samples with SiO_2=51.3-55.5 % show negative Pb anomaly, and with increasing SiO_2 contents (53.9-64.5 %) there's a slight and gradual increase of positive Pb anomaly (Fig. 5.4a). Aur dioritic rocks show a distinct difference of Pb anomaly for the different members, where felsic-end members (SiO_2=61-65.7 %) show distinct positive Pb anomaly, while there is no anomaly for Pb for the mafic-end members (SiO_2=54.6-59 %), where Pb concentrations remain stagnant.

Dioritic rocks from both islands show variable depletion at Rb, Nb, P, Zr, Sm, Eu and Ti. They are characterized by high concentrations of incompatible trace elements (LILE and LREE) and pronounced by significant Nb, Zr, P and Ti anomalies, resembling those of volcanic arc granitoids. Negative Ti anomaly is commonly related to ilmenite or titanite fractionation, whereas negative P anomaly is attributed to apatite separation.

Both dioritic rocks from Pemanggil and Aur Islands have similar chondrite-normalized REE patterns. They are significantly enriched in LREE and weakly fractionated HREE (Fig. 5.5 a, b). The chondrite-normalized REE patterns for Pemanggil dioritic rocks are fractionated, $(La/Yb)_N$ = 9.79-15.81. They are characterized by weak LREE enrichment with $(La/Sm)_N$ = 3.31-4.92, fractionated HREE with $(Gd/Yb)_N$ = 1.57-2.62 and negative Eu anomaly (Eu/Eu* = 0.663-1.14). Dioritic rocks from both islands have a narrow range of Eu/Eu* ratios and weak negative Eu anomalies.

Table 5.4 Range and average of selected major and trace elements of the dioritic rocks from Pemanggil and Aur Islands

	Pemanggil diorite		Aur diorite	
Major Elements (wt. %)	Range	Average	Range	Average
SiO_2	51.3-64.5	57.99	54.6-65.7	59.69
Al_2O_3	16.23-19.16	17.5	15.36-17.06	16.21
Fe_2O_3	4.28-8.02	6.15	4.7-8.32	6.65
CaO	3.69-7.85	5.22	2.68-7.65	4.94
MgO	1.21-3.24	2.14	1.4-4.05	2.69
Na_2O	4.24-5.14	4.82	4.13-4.97	4.43
K_2O	1.33-4.18	3.34	1.94-4.64	3.27
MnO	0.07-0.13	0.1	0.08-0.16	0.12
TiO_2	0.74-1.72	1.21	0.87-1.44	1.18
P_2O_5	0.28-0.92	0.58	0.27-0.66	0.43
Trace Elements (ppm)				
Ba	318-1180	822	662-1134	816-31
Rb	18.7-146.3	89	41.7-174.7	99.5
Sr	861.8-2234.6	1368.28	378.8-1297.6	665.47
Zr	104.1-526.4	366.97	118.1-450.6	318.62
Y	21.3-42.2	27.93	24.4-44.6	31.64
Zn	21-63	40.21	26-90	39.86
Pb	2.1-10.8	5.44	2.4-28.5	10.6
Ni	9.5-31.9	13.24	4.2-14.3	9.4
Nb	7.2-23.5	17.08	8.9-19.4	14.31
Ta	0.4-1.5	1.12	0.4-1.2	0.87
Th	2.4-20.1	11.76	4.6-21.2	10.62
Hf	2.2-11.9	8.39	3.7-11.7	7.6
U	0.7-6.9	3.74	1.2-5.1	2.76
V	46-157	97.05	61-208	115.83
W	4-65.2	11.78	0.7-5.1	1.94
Mo	0.6-4.5	1.68	0.6-4.1	1.76
Cu	9.5-50.2	34.34	9.5-51.6	24.03
Co	10.2-22.2	14.12	7.9-22.9	14.72
Cs	0.8-8.2	4.21	1.2-10.5	3.06
Ga	17.5-21.3	19.55	16.1-18.7	17.66
As	1-6.1	3.11	0.7-8.6	3.41
A/CNK	0.78-0.9	0.83	0.74-0.93	0.82
K_2O+Na_2O	5.59-9.07	8.15	6.14-8.91	7.7
K_2O/Na_2O	0.25-0.95	0.7	0.36-1.11	0.74
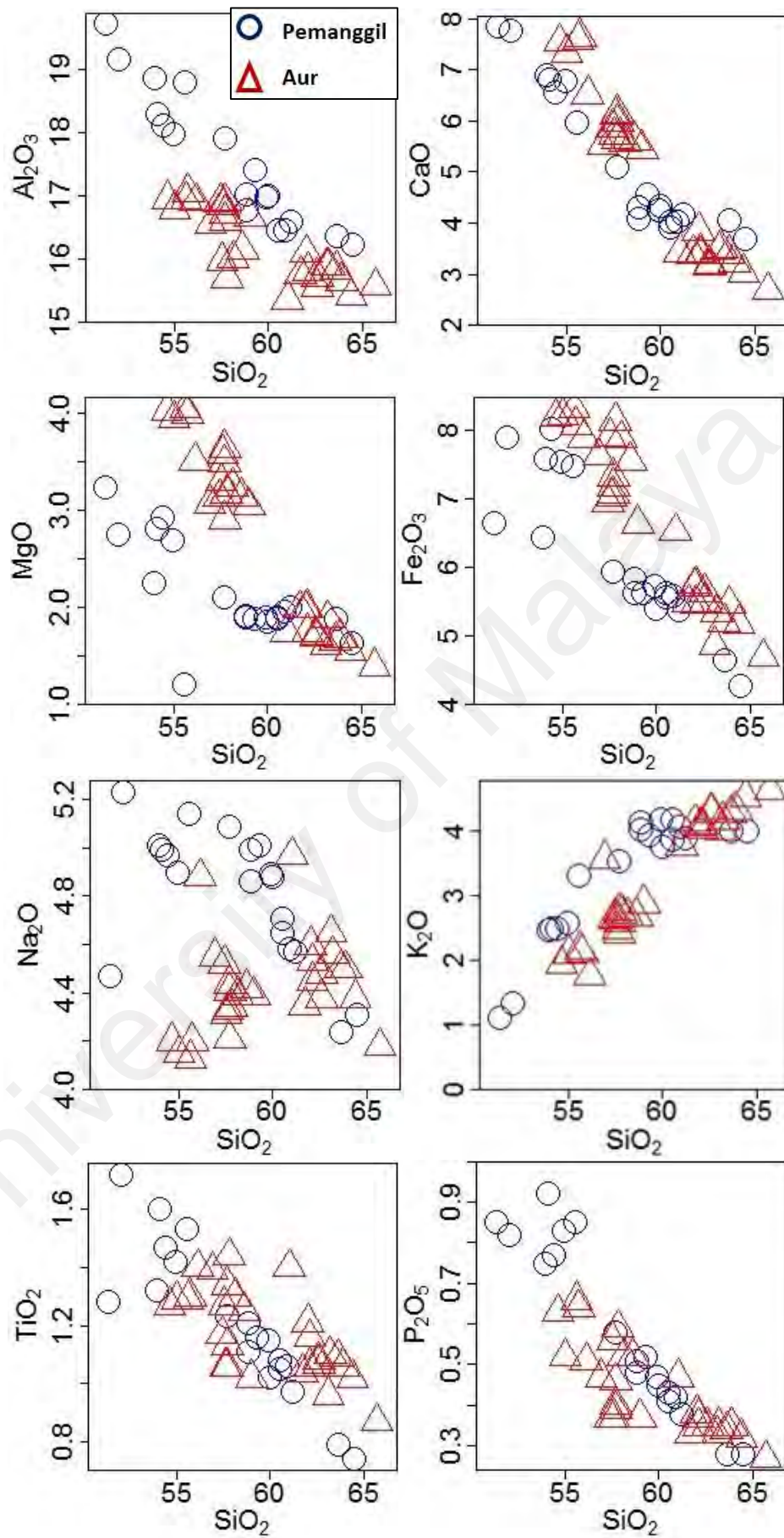
Figure 5.2 Harker variation diagram for major elements
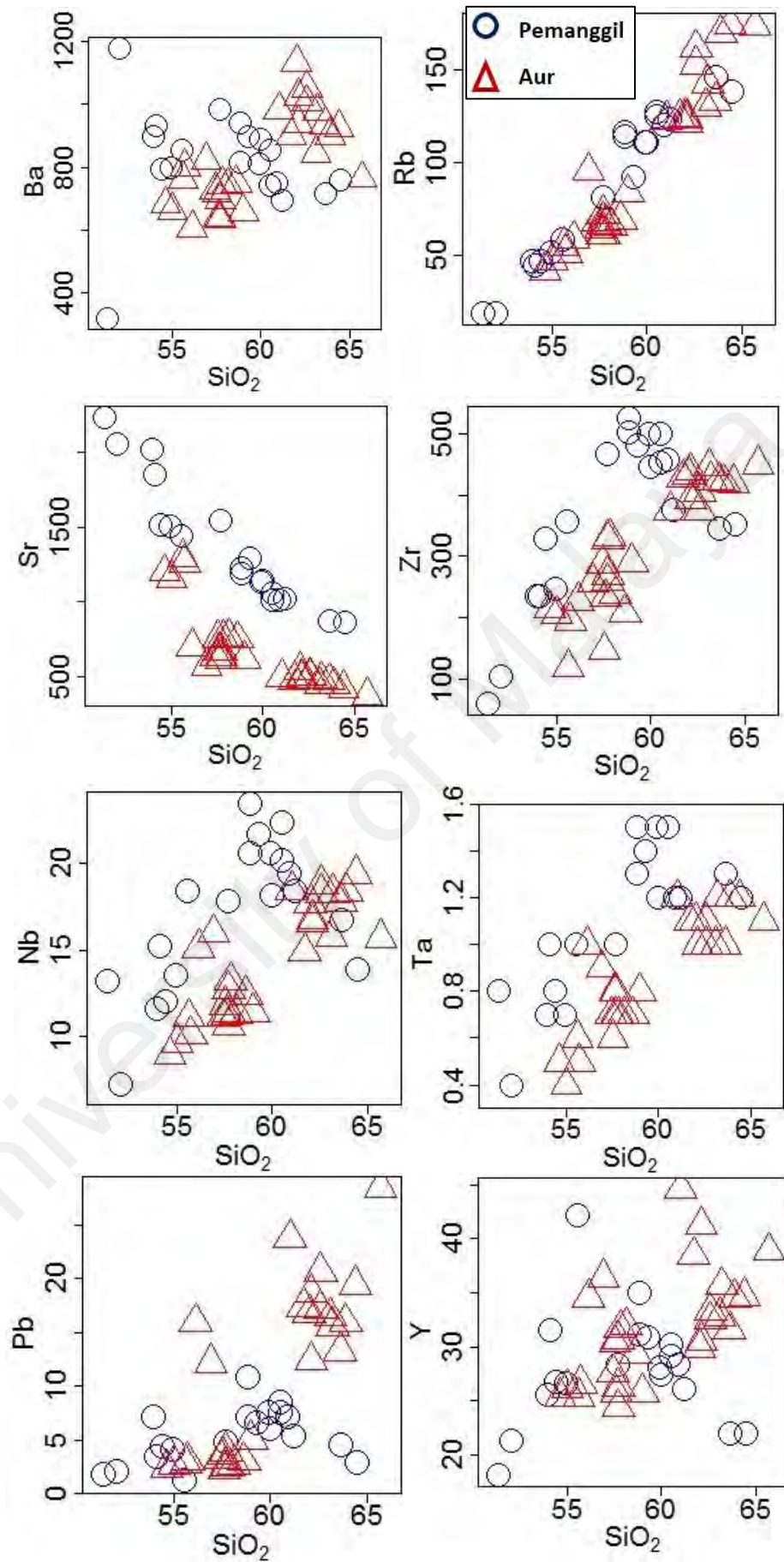
Figure 5.3 Harker variation diagram for selected trace elements
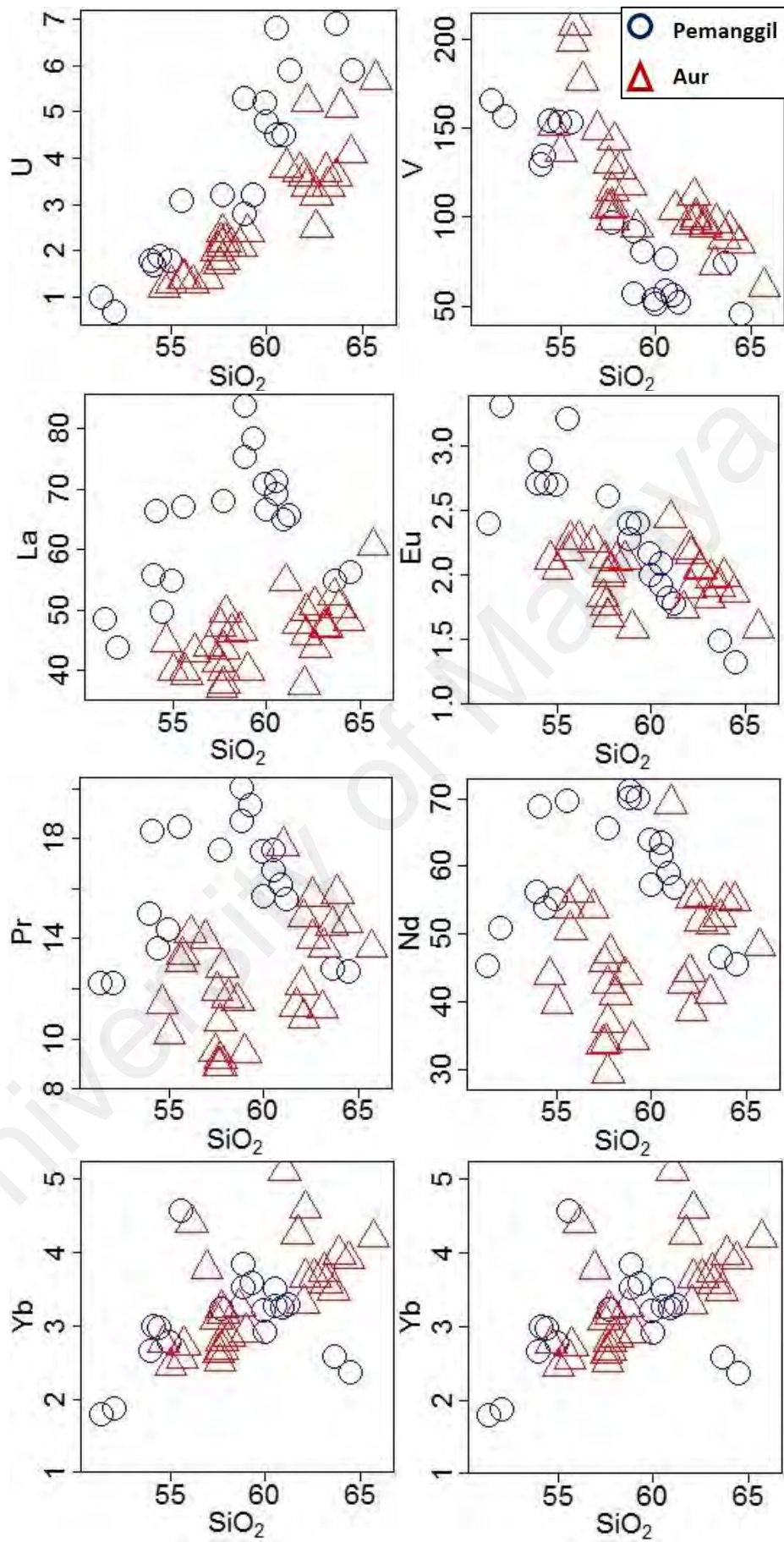
Figure 5.3 Harker variation diagram for selected trace elements (cont.)
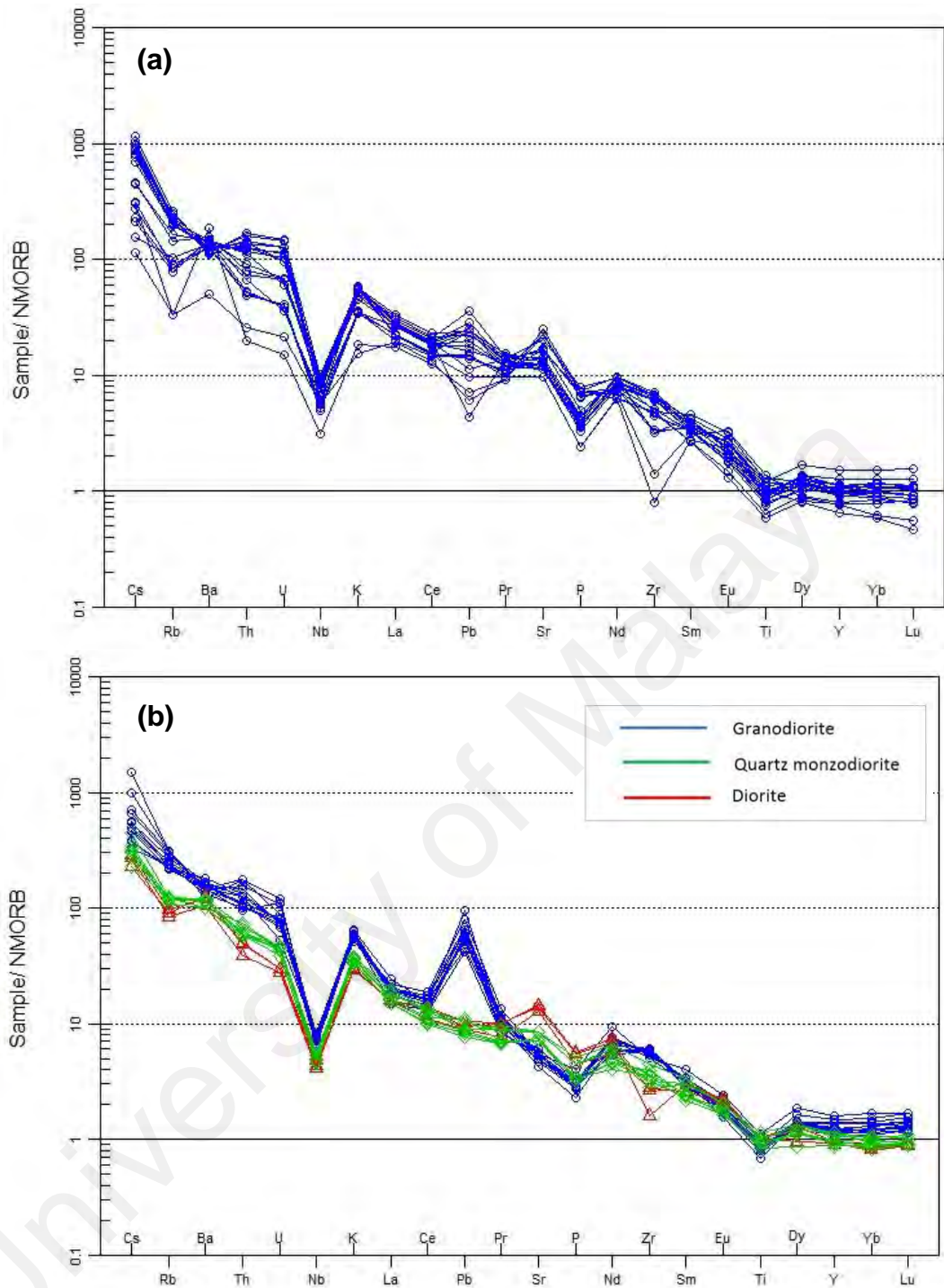
Figure 5.4 N-MORB normalized values of trace elements according to Sun and McDonough (1989) for (a) Pemanggil and (b) Aur
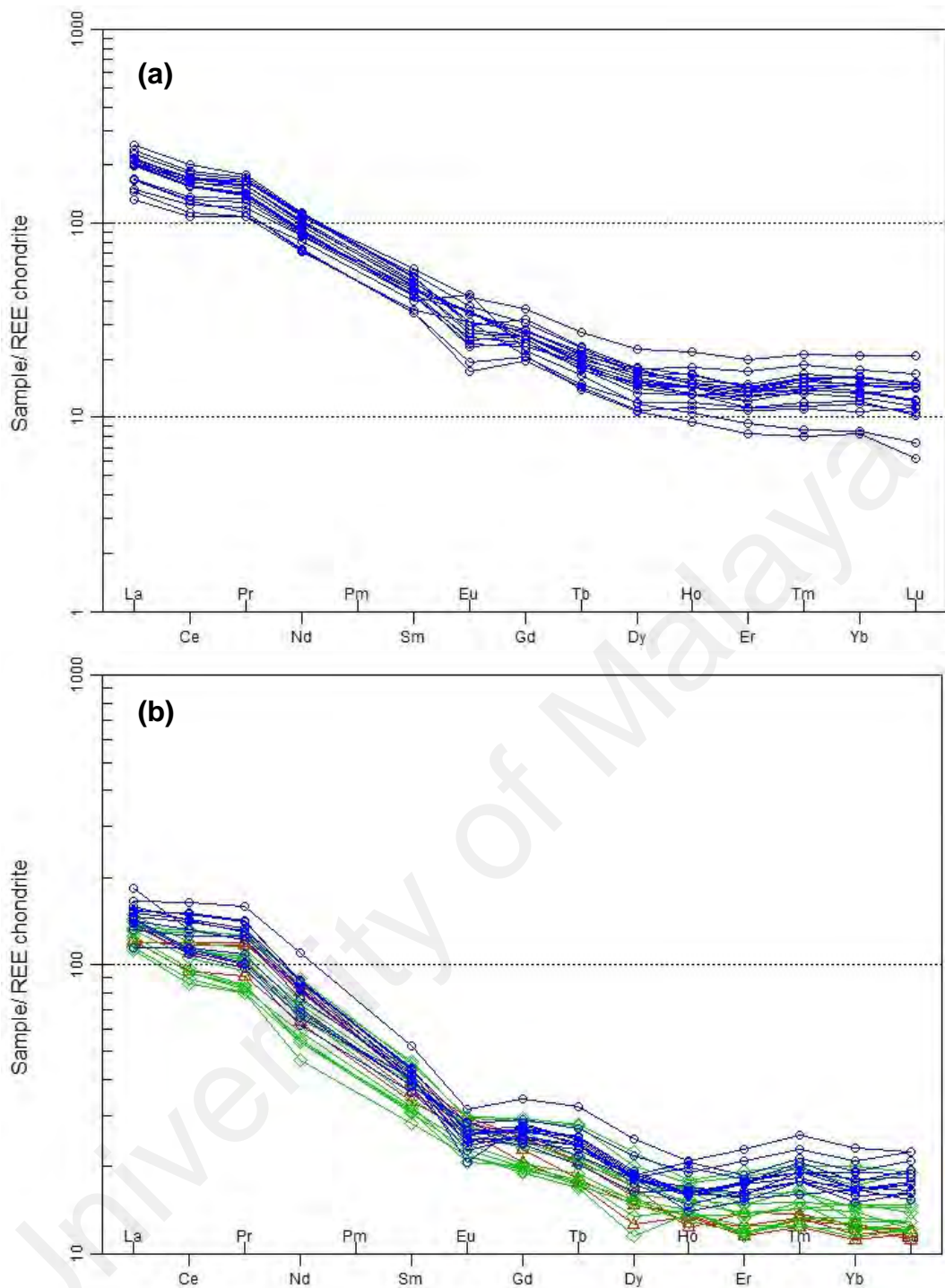
Figure 5.5   Chondrite-normalized REE plot. Normalization values after Nakamura (1974) for (a) Pemanggil and (b) Aur

5.3.2   LIL Modelling and Inter Elements Variation Diagrams

(a)   LIL Modelling

From the plotting of selected large ion lithophile elements (LIL) modelling, dioritic rocks from both islands show different trends of minerals fractionation with increasing magmatic differentiation.

For Pemanggil dioritic rocks, the overall trends are consistent with fractionation of plagioclase, biotite and K-feldspar. A good linear trends of all the rock samples seen from the pair of Sr-Ba and Rb-Sr in log scale (Fig. 5.6 and Fig. 5.8), suggest that crystal fractionation via crystallisation of biotite, plagioclase and K-feldspar play an important role during magmatic evolution of Pemanggil dioritic rocks.

LIL modelling for Aur dioritic rocks show different trends of mineral fractionation with increasing magmatic differentiation. For the more mafic-end members, (diorite and quartz monzodiorite), the overall trends are consistent with fractionation of plagioclase and hornblende. For granodiorite, the more felsic units, a good linear trend seen from the pair of Sr-Ba suggest that crystal fractionation via crystallisation of plagioclase, K-feldspar and biotite play an important role during magmatic evolution.

(b) Inter-elements variation diagrams

The plotting of Sr vs CaO for dioritic rocks from both islands show a linear positive trend for Pemanggil and a positive curve trend for Pulau Aur, where Sr increases with increasing CaO content. (Fig. 5.10). The distinct linear and curve shaped trend of rocks of Pemanggil and Aur respectively further support that the magma source of these two islands comes from a different source. The positive trend seen from Sr vs. CaO plot from both island supports that plagioclase is being removed during the differentiation sequence.

A Sr vs Ba plot for both islands are shown in Fig. 5.11. Both Pemanggil and Aur dioritic rocks have about the same concentrations of Ba, but Sr concentrations of Pemanggil dioritic rocks are distinctly higher. Pemanggil dioritic rocks show a good positive correlation, where Sr value increases with increasing Ba. Aur dioritic rocks show different trends where both mafic end members (diorite and quartz monzodiorite) does not show any significant changes of Sr together with Ba, where concentration of Sr remains more or less stagnant with increasing Ba. The felsic-end member of Aur dioritic rocks: granodiorite, clearly shows an increase of Ba concomitant with Sr.

The importance of plagioclase and K-feldspar precipitations during magmatic evolution can be depicted from the plotting of Sr vs. Eu/Eu* (Eu anomaly) after Eby, (1990). Sr trends of dioritic rocks from both islands when plotted against the Eu/Eu* values (Fig. 5.13), clearly depicts the difference of mineral fractionating for both islands. Pemanggil dioritic rocks clearly lies in a linear trend, where Sr decreases with increasing Eu/Eu* values. Whereas for Aur dioritic rocks, only the felsic-end member: granodiorite lies on a linear trend where Sr decreases with increasing Eu anomaly values. There is no clear trend observed for the mafic-end members: diorite and quartz monzodiorite. Also shown in each of the diagram is the vector diagram representing modelled fractionation trends after Eby (1990).

The plot of selected ratios of HREE elements (La/Yb, Sr/Y and Gd/Yb) against MgO is useful in constraining the role of clinopyroxene and hornblende fractionation during crystallisation (Gau et al., 2013). The HREE pattern of dioritic rocks from Pemanggil and Aur Islands shows a progressive change from negative slope to concave-upward patterns with decreasing Gd/Yb ratio (Fig. 5.12), suggesting the fractionation of hornblende and clinopyroxene during the magma differentiation of dioritic rocks from both islands.

Rb/Sr vs SiO$_2$ plot for both Pemanggil and Aur dioritic rocks show a linear trend of increasing Rb/Sr ratio with increasing SiO$_2$ contents (Fig. 5.14). Rb/Sr ratio for

Pemanggil range much lower (0.009-0.167) compared to Aur dioritic rocks, which have a higher range of Rb/Sr ratio (0.035-0.459). The higher Rb/Sr ratio Aur dioritic rocks reflects the highly evolved nature of the Aur magma compared to the Pemanggil magma.
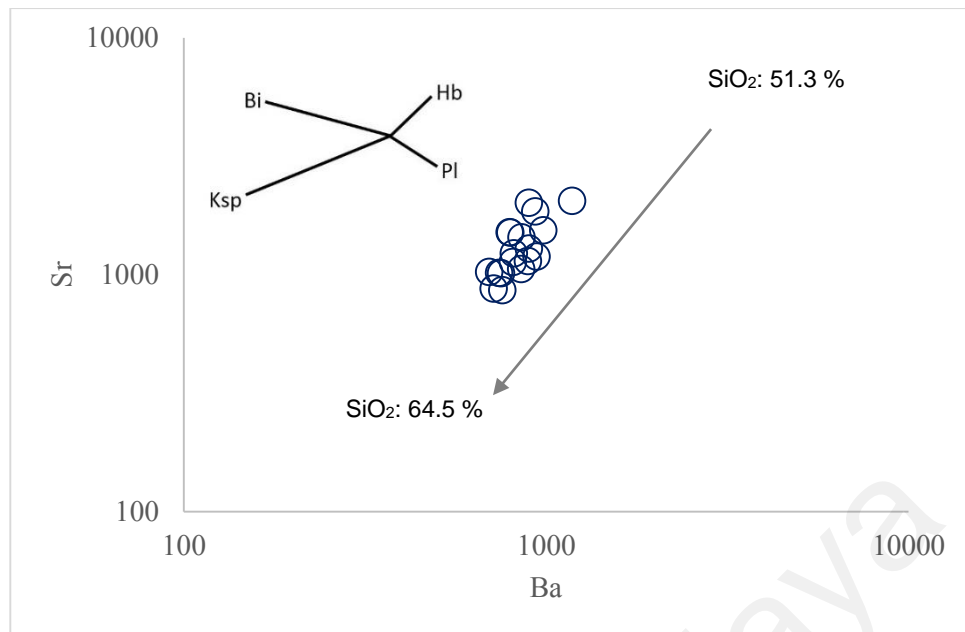
Figure 5.6 LIL modelling for the pair Sr-Ba for Pemanggil dioritic rocks. Mineral vector indicate path evolved liquids for 30% of mineral precipitating. Ksp=K-feldpsar, Pl=plagioclase, Bio=biotite and Hbl=hornblende

Figure 5.7 LIL modelling for the pair Sr-Ba for Aur dioritic rocks. Notice that only the felsic end member: granodiorite that follows the trend of Plag+Bio+K-spar fractionation. Mineral vector indicate path evolved liquids for 30% of mineral precipitating. Ksp=K-feldpsar, Pl=plagioclase, Bio=biotite and Hbl=hornblende.

Figure 5.8 LIL modelling for the pair Rb-Sr for Pemanggil dioritic rocks. Mineral vector indicate path evolved liquids for 30% of mineral precipitating. Ksp=K-feldspar, Pl=plagioclase, Bio=biotite and Hbl=hornblende.
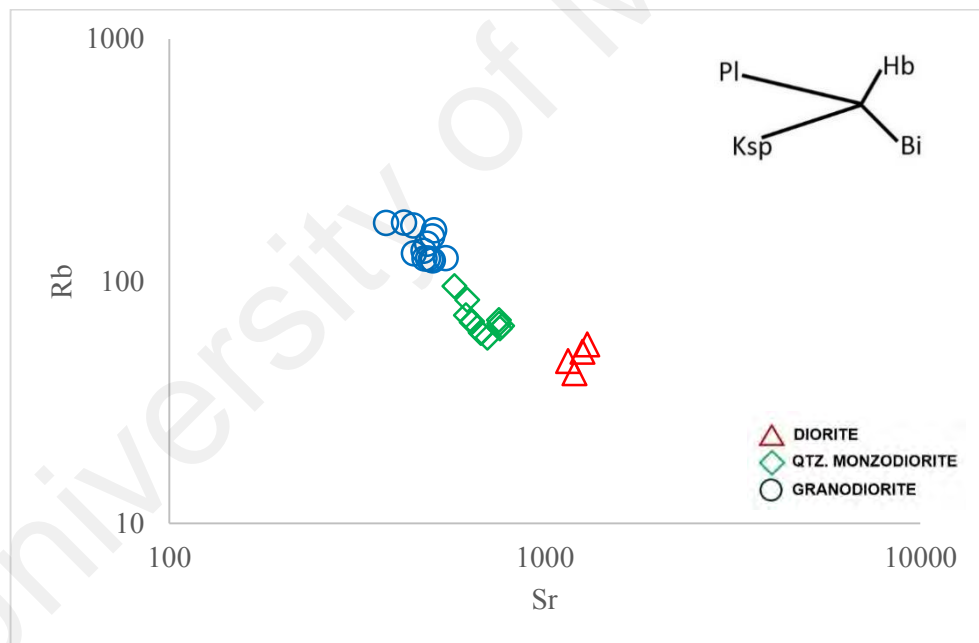
Figure 5.9 LIL modelling for the pair Rb-Sr for Aur dioritic rocks. Mineral vector indicate path evolved liquids for 30% of mineral precipitating. Ksp=K-feldpsar, Pl=plagioclase, Bio=biotite and Hbl=hornblende.

157
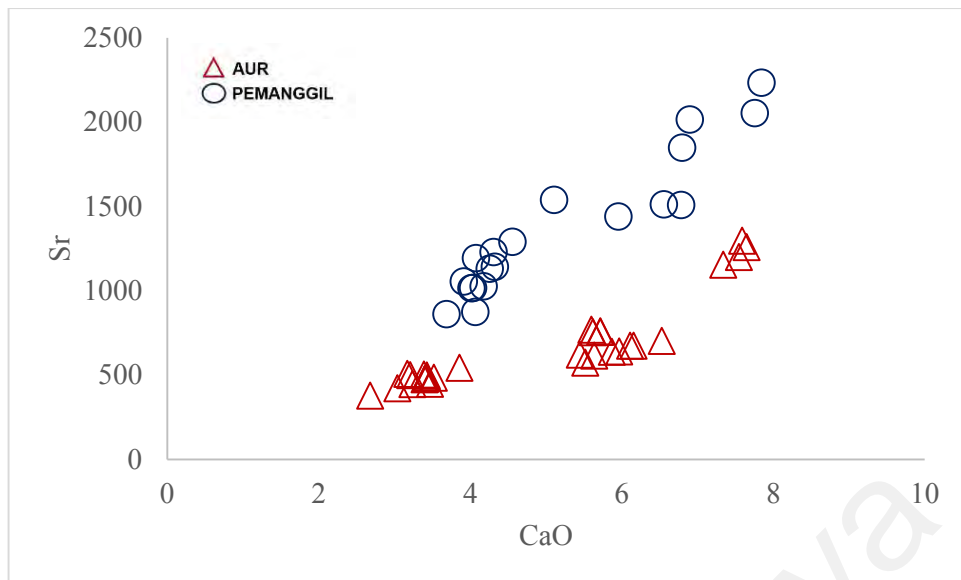
Figure 5.10 Sr vs CaO plot of Aur and Pemanggil Islands, showing positive trend, where Sr increases with increasing CaO. The distinct J-shaped of Aur dioritic rocks and the linear trend for rocks of Pemanggil dioritic rocks indicate that the two rocks are not related to each other.
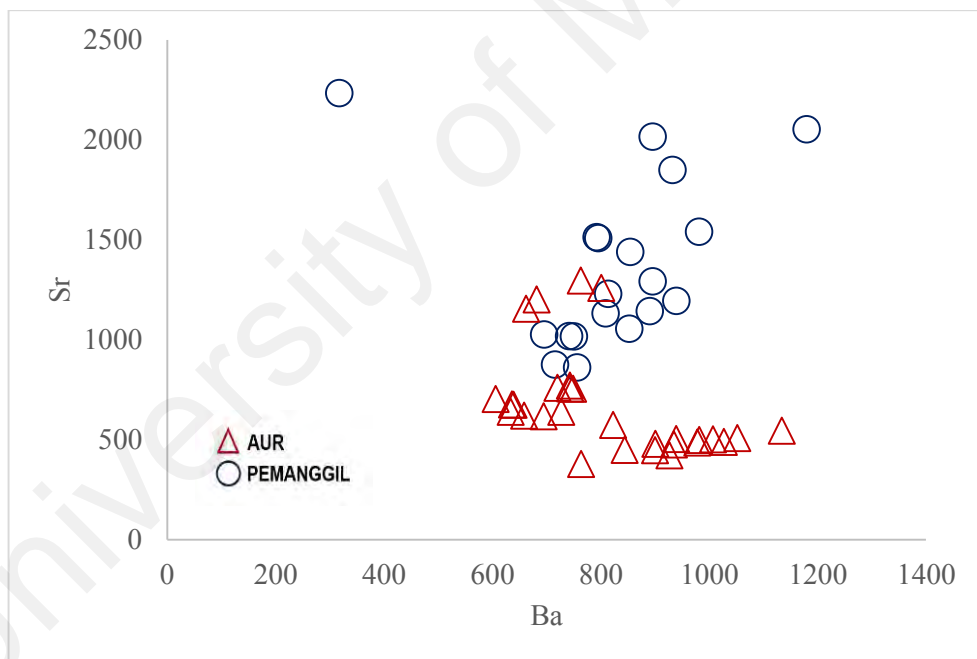
Figure 5.11 Sr vs. Ba plot. Pemanggil dioritic rocks show a linear positive correlation, where Sr value increases with increasing Ba. This linear trend supports that K-feldspar, biotite and plagioclase are being removed in the differentiation sequence. Aur dioritic rocks exhibit a complicated trends where there are different trends for the three types of rocks.

158
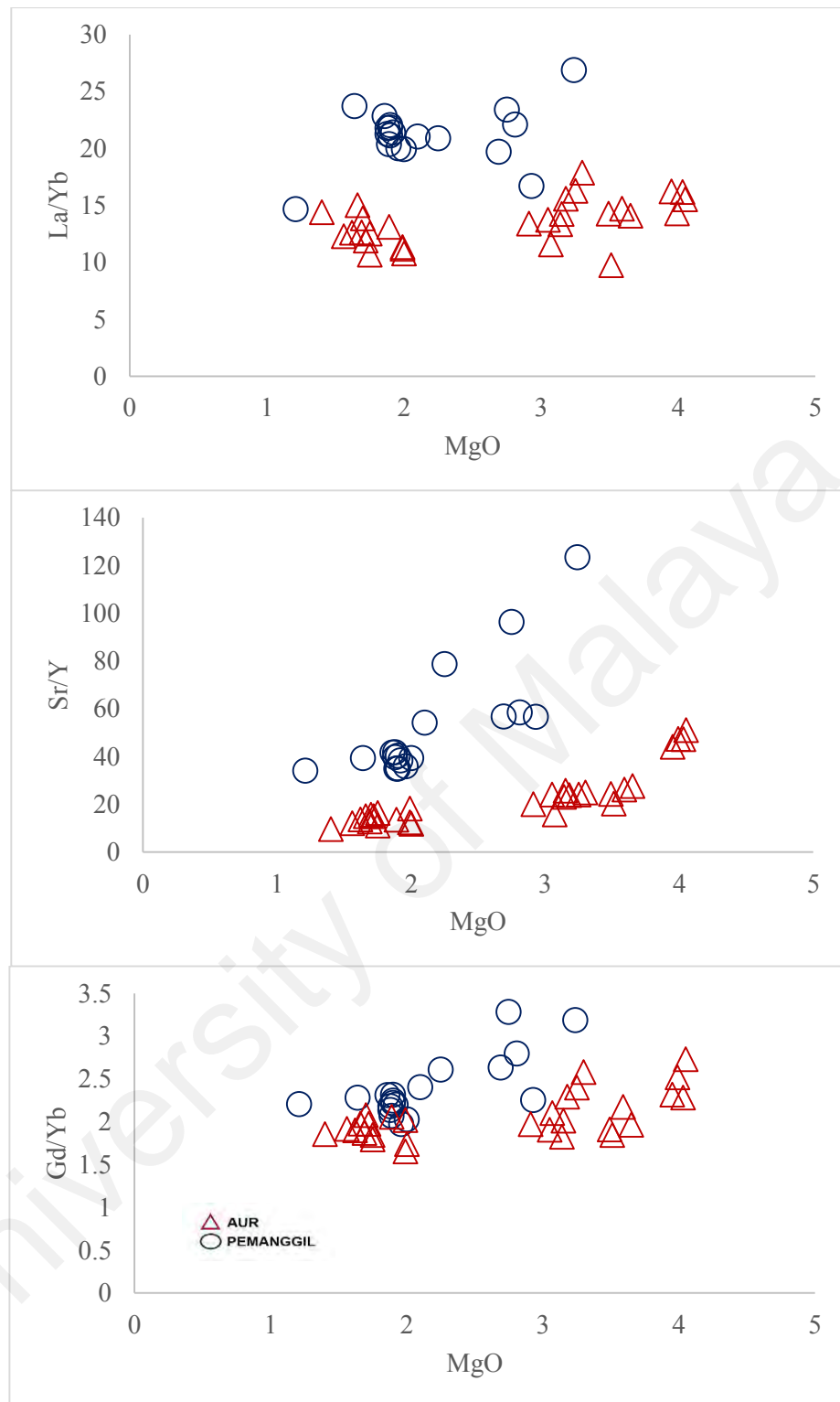
Figure 5.12 Plots of MgO vs (a)Gd/Yb, (b)La/Yb and (c) Sr/Y for both Pemanggil and Aur Islands show a progressive change from from negative slope to concave-upward pattern when plotted with increasing MgO content, supporting that clinopyroxene and hornblende fractionation during crystallisation.
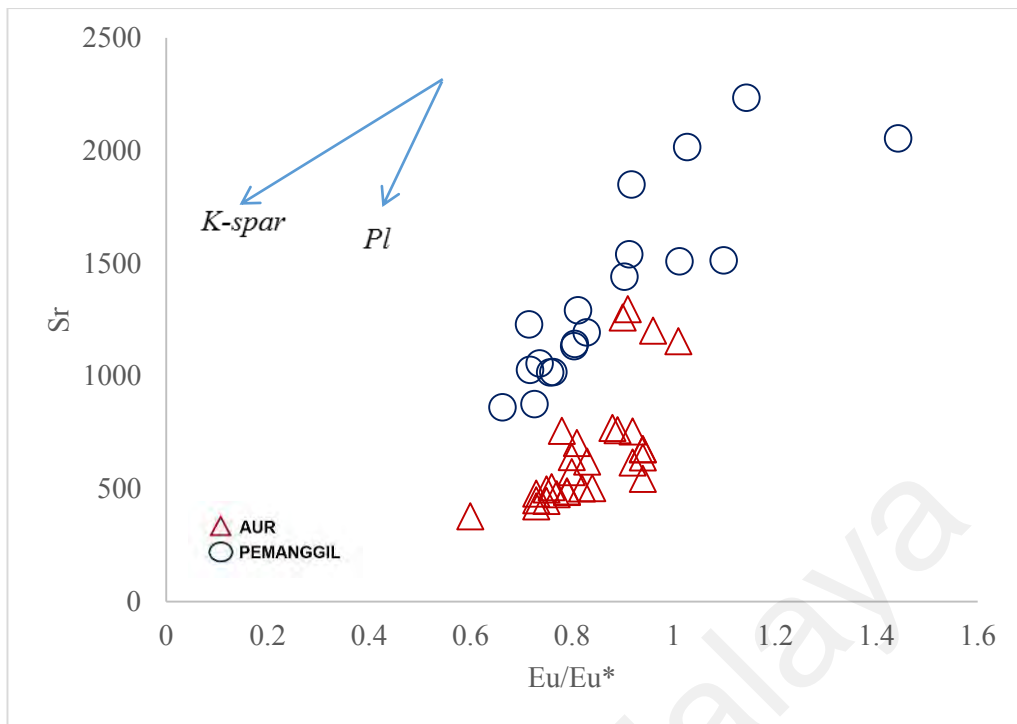
Figure 5.13 Sr vs Eu/Eu* plot showing the role of plagioclase and K-feldspar fractionations in the magma generation of dioritic rocks from both islands. Length of vectors represents 50% of Rayleigh fractionation. Modelled fractionation trends are after Eby (1990)
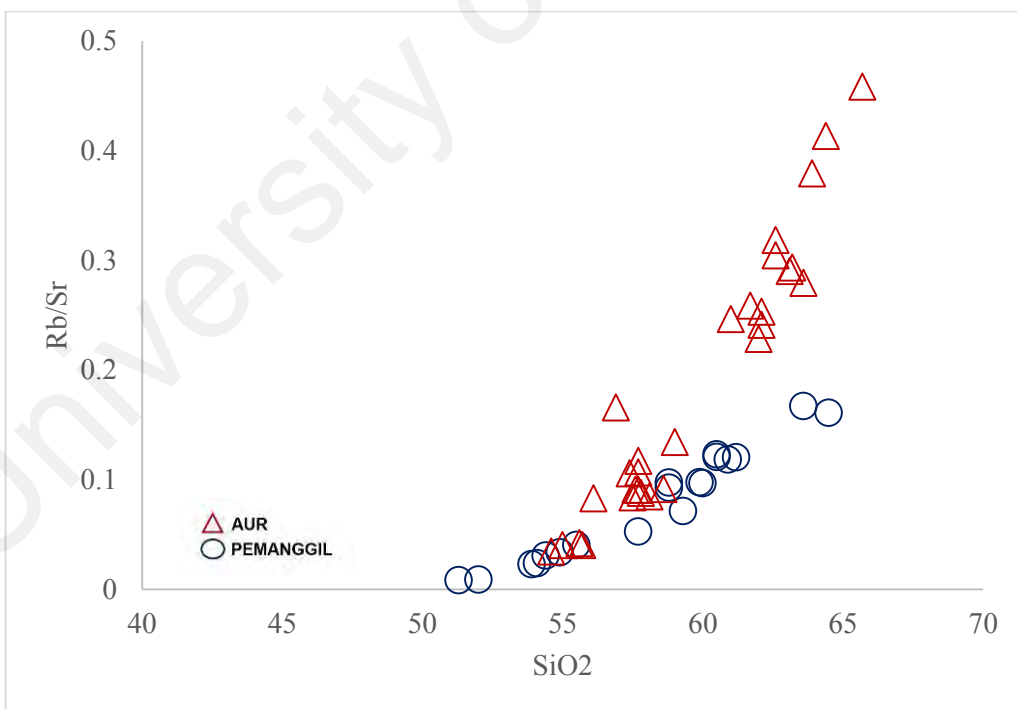
Figure 5.14 Rb/Sr vs. SiO_2 plot. Dioritic rocks from both islands show increasing Rb/Sr ratio with increasing SiO_2.

5.3.3 Geochemical and Geotectonic Classifications based on Geochemical Data

This section emphasizes on the geochemical classification and geotectonic classifications based on geochemical data for both Pemanggil and Aur Islands.

In the rock classification based on the K_2O vs. SiO_2 plot as defined by Peccerilo and Taylor (1976), majority of the samples from both islands fall in the field of high-K calc-alkaline series and shoshonite series (Fig. 5.15a). While there are distinct gap for Aur dioritic rocks where the mafic-end members fall in the High-K calc-alkaline series and the felsic-end member fall in the Shoshonite series, majority of Pemanggil samples fall in the Shoshonite series due to their high K_2O content ranging from 2.47-4.18 wt. %.

All the dioritic rocks are metaluminous in nature, having ASI values of less than 1, ranging from 0.435-0.895 for Pemanggil and 0.74-0.93 for Aur. All the rocks fall in the metaluminous field in the ASI classification diagram by Shand (1943) (Fig. 5.15b). The calc-alkaline nature of the dioritic rocks from study areas can be seen from the AFM ternary diagram (Fig. 5.15c) by Irvine and Baragar (1971).

Based on the geotectonic discrimination diagram by Pearce et al., (1984), dioritic rocks from both areas show similar and well-defined pseudo-linear trends where all the samples plots in the Volcanic Arc Granite (VAG) field (Fig. 5.16).

Schandl and Gorton (2002) classified four tectonic regimes for felsic to intermediate rocks based on HFSE ratios. All the samples from Pemanggil and Aur are classified and plot in the active continental margin (ACM) setting (Fig. 5.17).

Trivariate plot of Hf-Rb/30-Ta×3 by Harris et al., (1986) is useful in distinguishing tectonic setting for intermediate to acid intrusive rocks. Samples from both islands are plotted in the calc-alkaline volcanic arc field (Fig. 5.18).
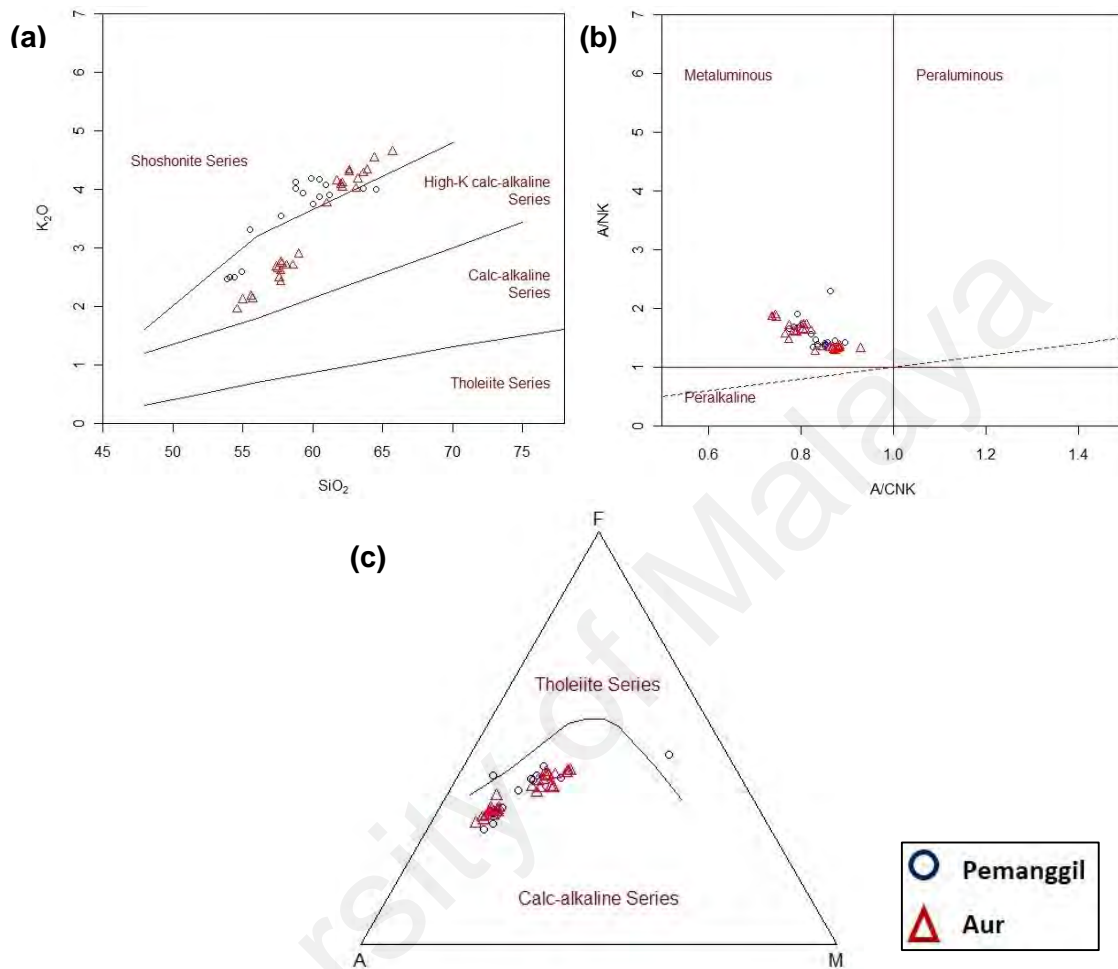
Figure 5.15 (a) K$_2$O vs SiO$_2$ plot based on Peccerillo and Taylor (1976)
(b) Rock classification using Shand (1947) based on the ASI values. All of the samples
from both islands fall within the 'Metaluminous' field. (c) Magma series classification
based on the AFM content according to Irvine & Baragar (1971). All the rocks fall
within the calc-alkaline magma series.
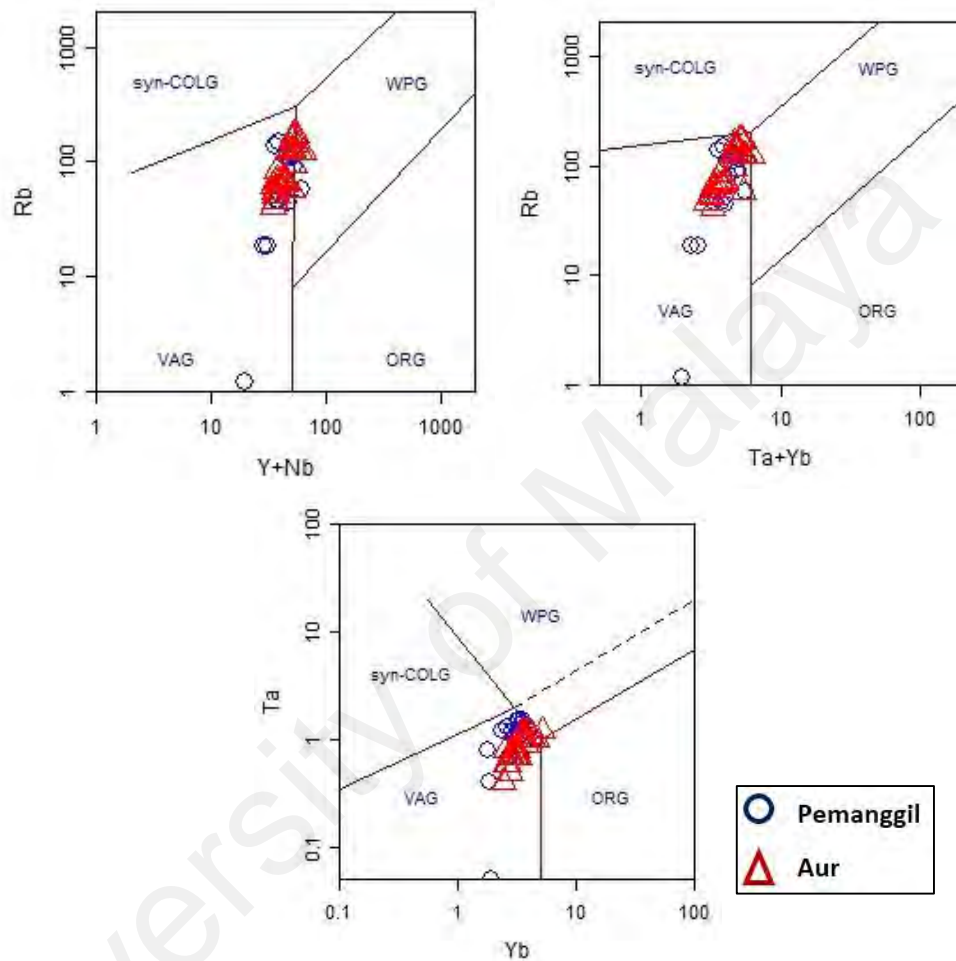
Figure 5.16   Tectonic discrimination diagram after Pearce et al (1984). All samples from both islands show well defined pseudo-linear trends, with similar trends of SiO_2 contents increasing from right to left along each of the diagrams.
Syn-COLG: Syn-Collisional Granite; WPG: Within Plate Granite;
VAG: Volcanic Arc Granite; ORG: Oceanic Ridge Granite
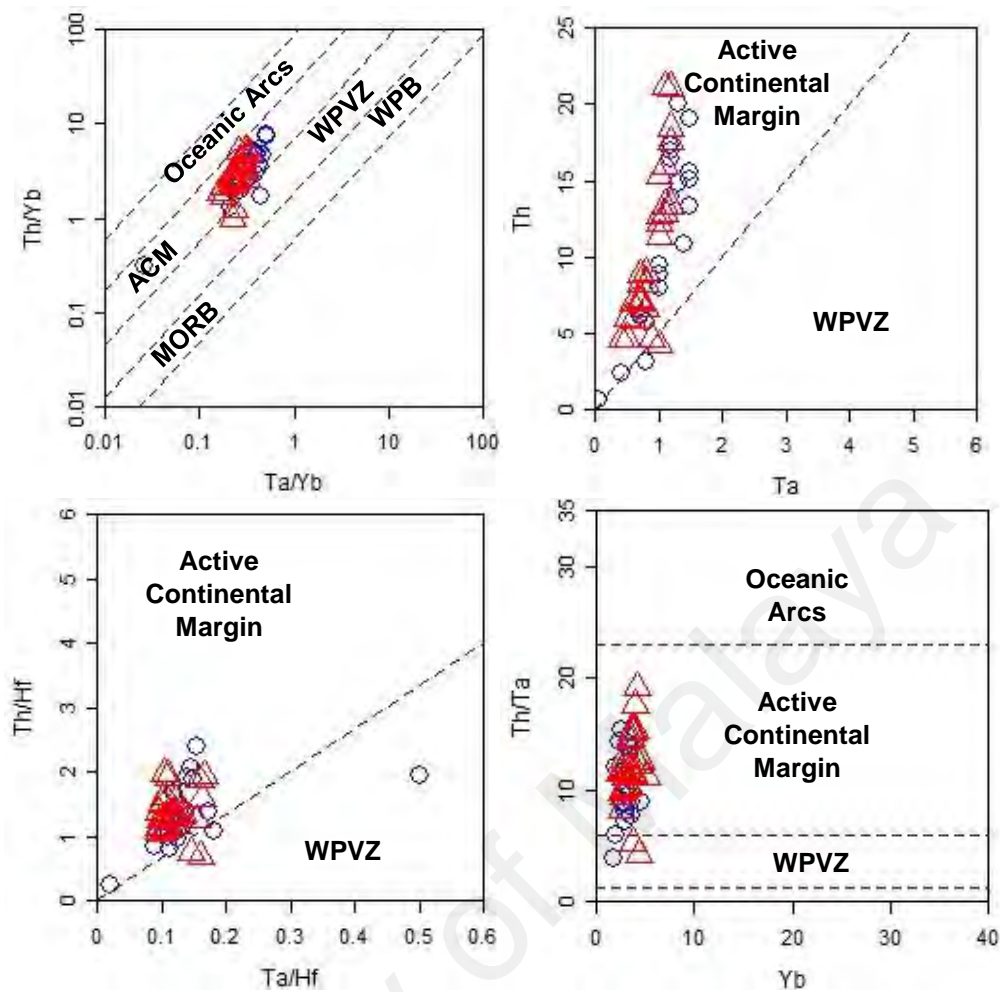
Figure 5.17 Tectonic discrimination diagram based on Schandl and Gorton (2002).
All the rocks from Pemanggil and Aur Islands fall within the Active Continental Margin
(ACM) tectonic settings.
*ACM: Active continental margin; WPVZ: Within Plate Volcanic Zone; WPB: Within
Plate Basalt; MORB: Mid-Oceanic Ridge Basalt.*
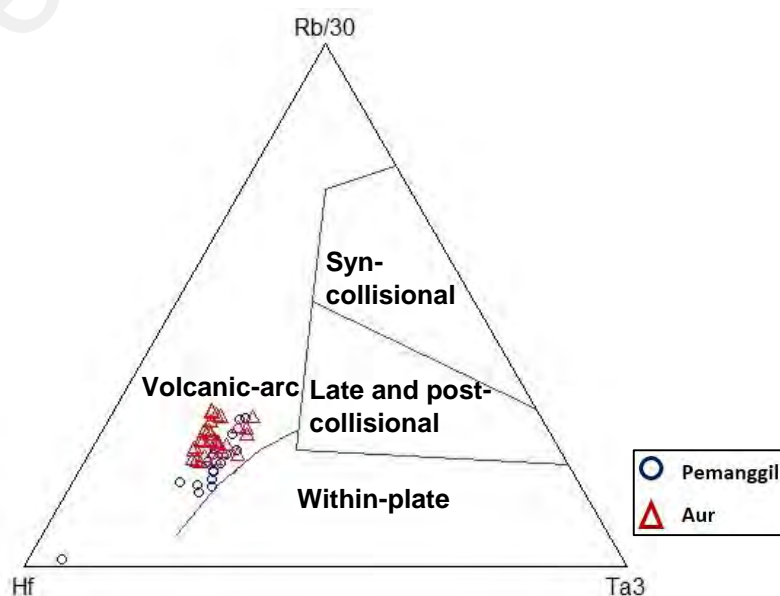
Figure 5.18 Ternary plot Hf - Rb/30 - Ta*3 by Harris et al. (1986), all rock samples fall
in the Volcanic Arc (VA) field.

5.4 Summary

Based on major and trace elements geochemistry, Harker diagram, LIL modelling, inter-elements variation diagram, REE trends and geotectonic classification diagram based on geochemical data available for Pemanggil and Aur Islands, several comparisons can be made:

1. Geochemistry shows that Pemanggil and Aur dioritic rocks are made up of different batches of melt.

2. All samples from Pemanggil dioritic rocks show similar concentrations and good linear trend on Harker plot, LIL modelling and inter-element variation diagram, suggesting that they were from the same individual magma. Linear trend and geochemical variations seen from Harker plot suggest the result of fractional crystallisation from one source of magma.

3. Aur dioritic rocks clearly show a different compositions and trends between the mafic-end members (diorite and quartz monzodiorite) and felsic-end member (granodiorite), suggesting that both members are made up of at least two different individual batches of melt. Both members are controlled by different mineral proportions on LIL log plot (mafic-end members: clinopyroxene, hornblende, plagioclase and felsic-end member: plagioclase, K-feldspar, biotite).

4. LIL modelling shows that crystal fractionation via crystallisation of biotite, plagioclase and K-feldspar play an important role during magmatic evolution of Pemanggil dioritic rocks.

5. Pemanggil dioritic rocks are characterised by enriched and higher Sr, ranging from 861.8-2234.6 ppm with an average of 1368.28. Sr concentrations for Aur dioritic rocks are lower and different for both end members. Sr concentrations for mafic-end members are higher, ranging from 574.9-1297.6 ppm and significantly low Sr range for the felsic-end member: 378.8-545 ppm.

6. Higher Rb/Sr ratio for Aur dioritic rocks reflects the highly evolved nature of the Aur magma compared to the Pemanggil magma.

7. N-MORB normalized diagram further distinguishes the difference between Pemanggil and Aur. Pemanggil dioritic rocks exhibit complicated trends for Pb anomaly, where samples with SiO_2=51.3-55.5 % show negative Pb anomaly, and with increasing SiO_2 contents (53.9-64.5 %) there's a slight and gradual increase of positive Pb anomaly.

8. Aur dioritic rocks show a distinct difference of Pb anomaly for the different members, where felsic-end members (SiO_2=61-65.7 %) show distinct positive Pb anomaly, while there is no anomaly for Pb for the mafic-end members (SiO_2=54.6-59 %), where Pb concentrations remain stagnant.

9. Dioritic rocks from both islands show variable depletion at Rb, Nb, P, Zr, Sm, Eu and Ti. They are characterized by high concentrations of incompatible trace elements (LILE and LREE) and pronounced by significant Nb, Zr, P and Ti anomalies, resembling those of volcanic arc granitoids. They show similar chondrite normalized REE patterns and have a narrow range of Eu/Eu* ratios and weak negative Eu anomalies.

10. Geotectonic classification diagrams classify the tectonic settings for Pemanggil and Aur dioritic rocks as calc-alkaline volcanic arc granite (VAG) origin with field relations, mineralogy and geochemical characteristics typical of active continental margin (ACM) settings. Both islands show similar trends on most of tectonic discrimination diagram, and the rocks are characterized by mantle modified by subduction components, selective enrichments in LIL elements, enrichments of K, Rb and Ba relative to Nb, Ce, Zr, Y and the absence of a negative Ba anomaly on a normalised multi-element spider diagram.

11. The continuous trend seen from Sr vs. CaO, REE patterns, rock classification diagrams, tectonic classification diagram suggest that a connection exist between all the rocks from Pemanggil and Aur Island at some stage of their magmatic evolution.

CHAPTER 6: DISCUSSION AND CONCLUSION

6.1 Introduction

This chapter will focus on the discussion of the magmatic processes involved, petrogenesis and consequently the possible tectonic setting for the magmatism of a much younger and Late Cretaceous age of the Aur dioritic rocks. Discussions and conclusions derived were made based on field observation, petrographic analysis, geochemical analysis and the comparison with the dioritic rocks of Pemanggil Island.

6.2 Petrogenetic Considerations of Coeval Mafic and Felsic Magma Association

Mafic and felsic magma associations can be seen on the Eastern Belt, where smaller gabbroic bodies that are marginal to larger granitic masses can be found. Mafic rocks associated with the Permian to Triassic granite constitute less than 5% of the total surface exposures. These associations can be observed from the olivine eucrite at the Linden Hill Stock, gabbro-norite-diorite at Kemuning Hill and gabbro-diorite on Pemanggil and Aur Islands (Ghani, 2009).

Whereas the occurrences of these mafic magma found at Linden and Kemuning Hills from Peninsular Malaysia are older, and of Triassic age (Liew, 1983), the occurrences of mafic magmas found offshore Peninsular Malaysia are much younger, where unpublished U-Pb zircon data of the dioritic rocks from both Pemanggil and Aur Island give an age of about 80 ± 1Ma. (Ghani, unpublished data). Cretaceous magmatism are also recorded from the biotite K-feldspar granites of the Tioman Island that yields a zircon age of 80 ± 1Ma (Searle et al., 2012).

Origin of two coeval magmas with differing compositions are still a matter of discussions, and these mafic-felsic associations are mostly common in post-collisional to post-orogenic magmatic suites, thus reflecting the contrasting rates of magma generation and differentiation (B. Bonin, 2004). Late Cretaceous magmatism of Peninsualar

167

Malaysia are described as post-orogenic (e.g. Cobbing et al., 1986; Metcalfe, 2000), in which the collision between Sibumasu and Indochina block of Peninsular Malaysia has long subside, and considering a likely delay of up to ten or more million years between generation of granitic magmas and crystallization (emplacement ages), subduction of the Paleo-Tethys has most likely ceased in the Middle Triassic (Metcalfe, 2013).

Aur pluton clearly display the mafic and felsic magma interaction with the presence of rounded to ellipsoidal MME heterogeneously distributed throughout the pluton. The presence of MME as evident from study area might have indicated that magma mixing and/or mingling between these two different magma in generation of the rocks. It is notable that during the post-collision and post-orogenic magmatism, commingling of mafic and felsic magmas are documented by mafic enclaves and syn-plutonic dikes (B. Bonin, 2004).

6.3   Petrogenesis

As identified from petrographical and geochemical data, it is evident that there are at least two different magmatic pulses of magma forming the composite Aur intermediate plutons which consist of the mafic-end member: diorite and quartz monzodiorite and the felsic-end member: granodiorite. The anti-rapakivi texture and presence of MME may have suggested that magma mixing and/or mingling processes might have play an important role during the magmatic evolutions of the rocks.

From petrographic observations, mafic-end members: diorite and quartz monzodiorite show the typical ophitic and sub-ophitic texture often found in mafic rock, their major mafic phase are consist of clinopyroxene, orthopyroxene, with minor biotite and hornblende whereas the felsic-end member: granodiorite shows a markedly different observation. Granodiorite shows the typical granitic hypidiomorphic granular texture, with hornblende and biotite as its major mafic phase (details on Chapter Three). Magma

mixing texture; anti-rapakivi can only be observed in granodiorite, suggesting that there must have been an interaction between these two magmas at one point during magmatic evolution.

Different trends seen on Harker diagram, LIL modelling, N-MORB normalized spidergram and inter-elements variation diagram further supports that there are at least two different magmatic pulses, with a distinct geochemical characteristics of these two members. Silica gap, although small, (2 wt. % SiO_2) are not due to under sampling, but rather due to their different geochemical compositions. Mafic-end members are characterized by higher Fe_2O_3 (6.65-8.32 %) CaO (5.45-7.65 %), MgO (2.91-4.05 %) and a notably high and variable Sr concentrations: 574.9-1297.6 ppm. The felsic-end member: granodiorite have a distinct high K_2O content (3.76-4.64 %) compared to mafic-end members (1.76-2.17 %), higher Ba (764-1134 ppm), Rb (121.7-174.7 ppm), Zr (374.4-450.6 ppm), low in Fe_2O_3 (4.7-6.53 %) CaO (2.68-3.86 %), MgO (1.4-2 %) and Sr (378.8-545 ppm) concentrations compared to the mafic melt. In addition, calculated zircon temperature range (T_{Zr}) of granodiorite range much higher, 808.7-853°C compared to diorite and quartz monzodiorite: 679.5-782.8°C.

6.3.1 The Origin of Mafic-end Members

Since HFSE (such as Nb and Ta) are depleted in the lithospheric mantle relative to the LREE, high Nb/La ratios ($\sim$>1) indicate an OIB-like asthenospheric mantle source for basaltic magmas and lower ratios ($\sim$<0.5) indicate a lithospheric mantle source (Bradshaw and Smith, 1994; and Smith et al., 1999). Accordingly, Nb/La ratio of the mafic rock, range from (0.2-0.37), suggesting a lithospheric mantle source. The high Mg# values of more than 40 for diorite and quartz monzodiorite (43.6-50.25) indicate that there must be some mantle-derived components in their sources (Rapp and Watson, 1995). N-MORB normalized diagram after Nakamura (1976) also shows no positive Pb spike for the mafic-

end member, possibly reflecting their mantle components, as Pb abundances are very low in the mantle and should the mafic-end members have a crustal components, N-MORB spidergram would have shown a positive Pb spike (C. Yuan et al., 2010).

6.3.2 The Origin of Felsic-end Members

Granodiorite occupies volumetrically large areas of Aur Island, covering the central and southern part of the island, suggesting that they were not derived from the mafic melts by fractionation. Marked negative Eu-anomalies (Eu*/Eu=0.602-0.943) at 61-65.7 wt. % SiO_2 preclude derivation from a mafic melt via fractional crystallisation, and indicate some feldspar fractionation during their formation. The high K_2O contents of granodiorite, that it even falls on the shoshonite field on the classification diagram by Peccerillo and Taylor (1976) indicates that the K-bearing calc-alkaline rocks were at crustal levels during their generation. In addition, the elevated LREE and trace elements contents of granodiorite e.g., Th (11.4-21.2 ppm), Pb (12.4-28.5 ppm), U (2.5-5.1 ppm) and Eu/Eu* (<1.0) indicates an upper crustal components is involved in the generation of granodiorite. Rocks derived from upper crustal sources should have relatively higher Th (>10 ppm), Pb (>20 ppm), U (>2 ppm) and Eu/Eu* (<1) (S. Liu et al., 2009). Mafic-end members are characterised by different range and lower values of Th (4.3-9 ppm), Pb (2.4-5.1 ppm), U (1.2-2.4 ppm) and Eu/Eu* (0.776-1.008). Moreover, the distinct positive Pb-anomaly of granodiorite, where Pb are normally enriched at crustal sources and consistent with the involvement of crustal compositions (Rudnick and Fountain, 1995; C. Yuan et al., 2010). Crustal involvement may have been important, especially in the evolution of the granodiorite. The higher range of T_{Zr} for granodiorite (808.7-853°C) could be explained by the presence of biotite and amphibole in granodiorite, as breakdown of these two minerals occur most likely at T>800°C (Miller et al., 2003).

6.3.3 Magmatic Processes

The presence of certain disequilibrium textures, a wide and different range of whole rock geochemical compositions suggest that a number of distinct differentiation processes took place involving partial melting, magma mixing, fractional crystallization and possibly crustal contamination.

Distinction between fractional crystallization, batch partial melting and magma mixing can be made graphically using incompatible trace elements with different bulk solid/melt partition coefficients D (Schiano et al., 2010). For two incompatible elements H (a high incompatible element, typical H elements are Rb, Ba, Th and U) and M (a moderately incompatible element, typical M elements are Nd, Sm, Sr, Hf and Zr), the fractional crystallization equation gives (Treuil and Joron 1975; Allègre and Minster 1978):

$$C_H = C_{HO}/f$$
and
$$C_M = C_{MO}/f$$

where C_H and C_M are the concentrations of elements H and M of the liquid, respectively; C_{H0} and C_{M0} are the concentrations of elements H and M of the source, respectively; and f is the weight fraction of the residual liquid. Therefore,

$$(C_H/C_M) = (C_{H0}/C_{M0}) = \mathbf{a} \text{ where '}\mathbf{a}\text{' is a constant:}$$

In the plot of C_H/C_M versus C_H, partial melting is expressed by a straight line with a slope, whereas fractional crystallization would produce an almost horizontal line (Fig. 6.1). It is noted that the data plot along a linear line, suggesting magma mixing and/or partial melting as the dominant factors to form both the mafic and felsic end members.

Moreover, plots of the most incompatible elements Ba and Rb versus the compatible element Ni (Fig. 6.2) (after Jian-Wei et al., 2009), indicates that partial melting rather than fractional crystallization dominated the genesis of the dioritic rocks of Aur Island. Among the key features of both mafic and felsic end members are the enrichment of

LILE, LREE, depletions of HREE and the pronounced negative Nb-Ti anomalies on primitive mantle normalized diagram (Fig. 4.11) which are known to be the characteristics of subduction-related magmas. Among the important feature of subduction related metasomatism is the formation of hydrous mineral phase such as biotite and amphibole (Beccaluva et al., 2004), which are abundant in granodiorite. These characteristics are commonly attributed to the mantle source, which has been previously enriched in LILEs over HFSE by metasomatic activity of fluids derived from the subducted slab or sediments (e.g. Pearce, 1983; Hawkesworth et al., 1997; Elburg et al., 2002; Cameron et al., 2003). High LIL/HFSE ratios and negative Nb and Ti anomalies can also be characteristics of magma originated from an enriched sub-continental lithospheric mantle (SCLM) caused by earlier subduction events. Mantle enrichment events could have probably formed at great depth during the period of subducting Paleo-Tethys Ocean during the Middle-Late Triassic. During such case, a large amount of fluids and/or sediments could have caused metasomatization of the depleted mantle.
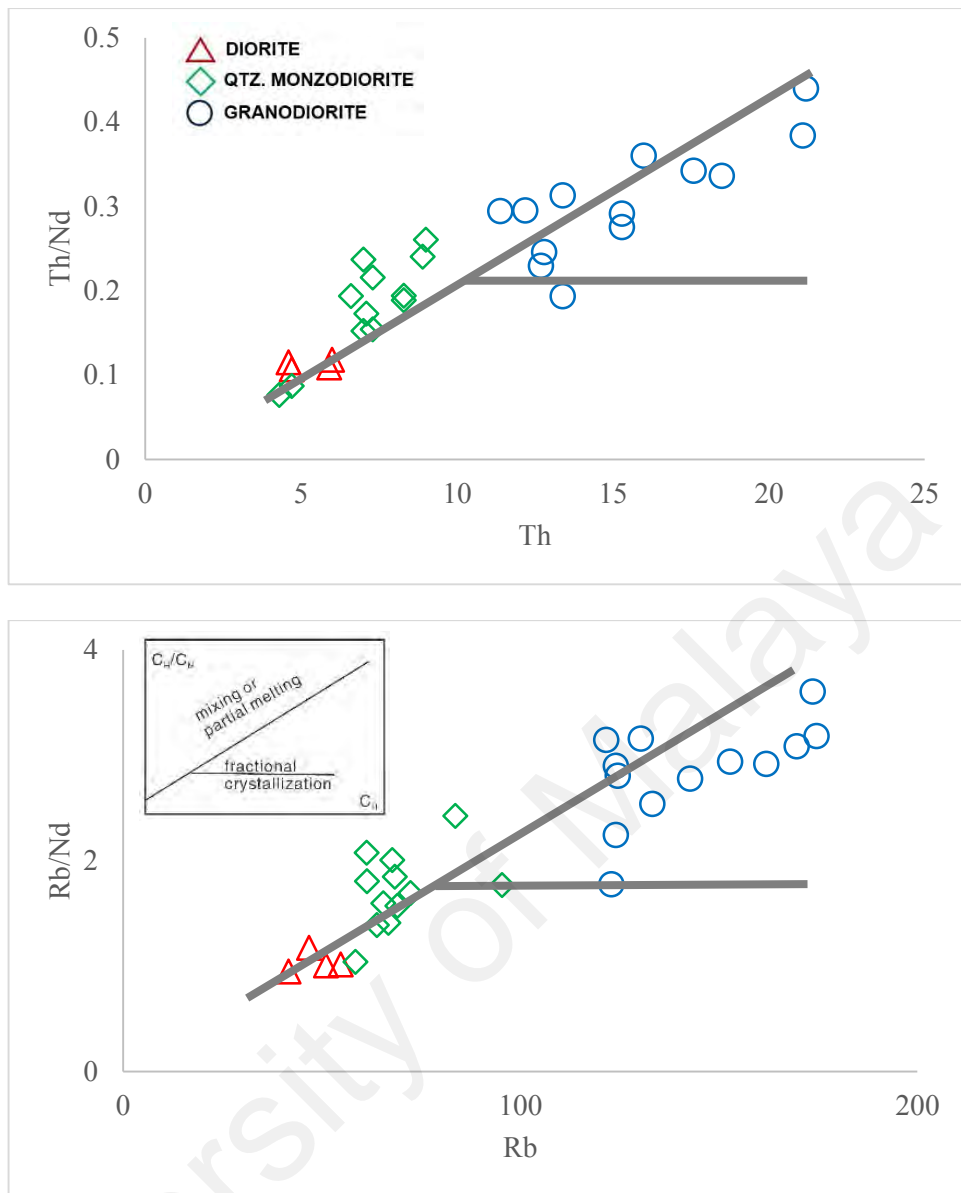
Figure 6.1   Plots of (a) Th/Nd vs Th and (b) Rb/Nd vs Rb for the dioritic rocks from Aur Island. The data define arrays that are each consistent with a series of magma mixing and/or different degrees of partial melting. Also shown in (b) is a schematic C_H/C_M vs C_H diagram showing theoretical correction curves during fractional crystallization, partial melting and mixing process. (after Gou et al., 2013)
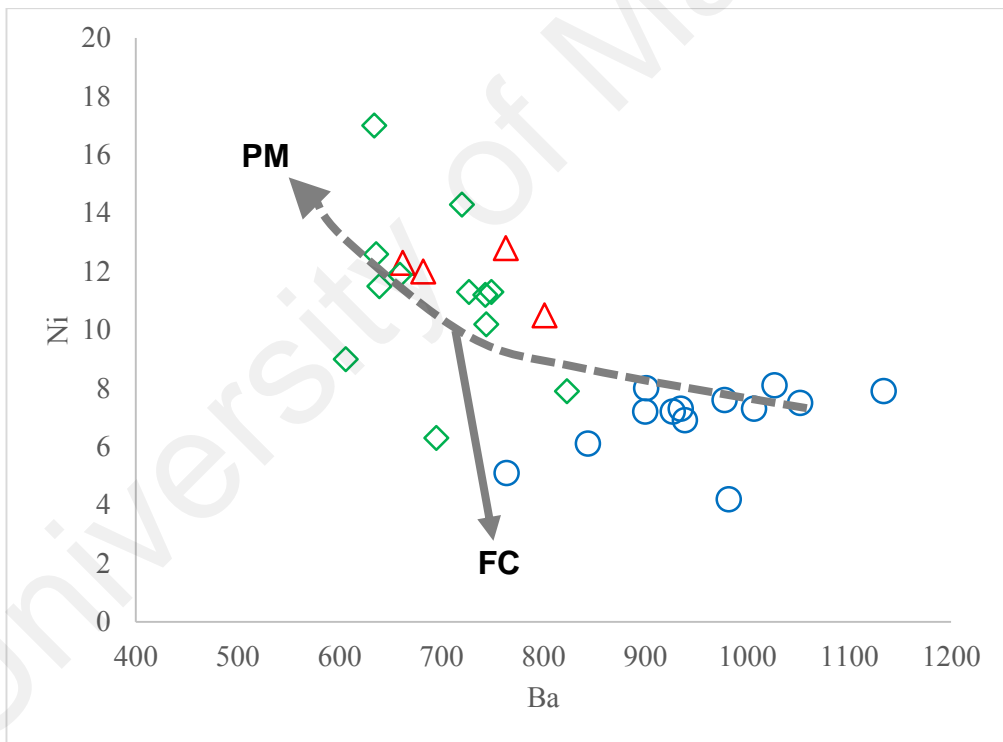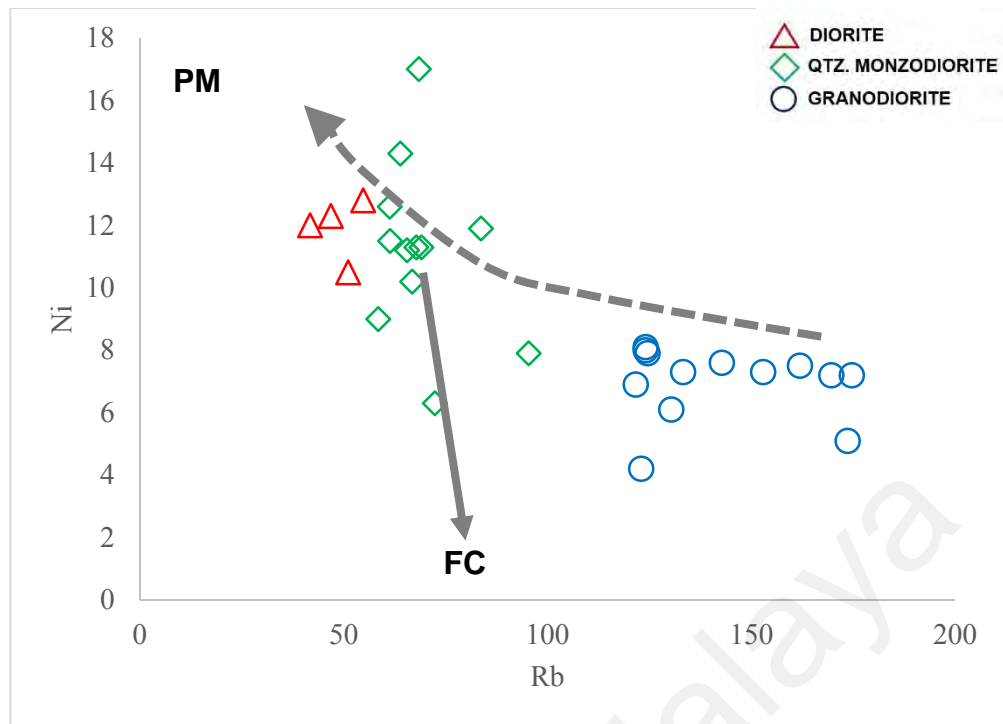
Figure 6.2   Plots of the most incompatible elements Ba and Rb versus the compatible element Ni, indicating partial melting (PM) rather than fractional crystallization (FC) dominated the genesis of the dioritic rocks of Aur Island (after Jian-Wei et al., 2009)

6.4   Tectonic Settings

The Cretaceous plutons of Tioman, Pemanggil and Aur Islands form a linear chain aligned NNW and SSE to one another. This fact implies that partial melting to produce the granitic melt was not a local petrologic event, but rather their formation and interpretations are of regional tectonic significance. Mantle-derived basaltic dikes particularly the lower limit (~79 Ma) are broadly coeval with these Cretaceous granitic magmatism (Cobbing et al., 1992) which occurs as individual scattered plutons in Central and Eastern Belt.

As not many detailed studies were done on the occurrences of Cretaceous plutons of Peninsular Malaysia, lack of precise geochronological and systematic geochemical data, the tectonic implications of these Cretaceous plutons still remain poorly constrained. Post-collisional and post-orogenic magmatism on Peninsular Malaysia are not yet fully understood, in which the magmatism of Peninsular Malaysia has only been focused during the subduction of Palaeo-Tethys Ocean and the collisions between Sibumasu and Indochina from Early Permian-Late Triassic period (Sevastjanova et al., (2001); Barber and Crow, (2003); Metcalfe (2011), Sone and Metcalfe (2008); Searle et al., (2012); G. Oliver et al., (2013).

Although the genesis of these Cretaceous magmatism in relation to tectonic processes are still unclear, several authors have put forth brief explanations on the occurrences of these smaller and isolated Cretaceous plutons.

In the recent U–Pb zircon ages for granitoids of the Malay Peninsula presented by Searle et al. (2012), these smaller and isolated bodies of Cretaceous plutons with I-type affinities found within the Peninsular Malaysia are common with the Cretaceous magmatism of the Western Thailand-Myanmar/Burma province that consists of hornblende-biotite I-type granodiorite-granites. He suggested that these Cretaceous magmatism could be the far field effects of both eastern (Meso-Tethyan) and western

(Paleo-Pacific) subduction processes in the Sundaland region, thus causing this subduction-influenced, late stage and post collisional granites emplacement of the Tioman Island granite in the East and Phuket in the west.

Another explanation for the emplacement of Cretaceous plutons in Peninsular Malaysia as proposed by different authors was that there is a significant thermo-tectonic event during Cretaceous, where during the Middle to Late Cretaceous, there has been a significant time of folding and faulting in Peninsular Malaysia (Harbury et al., 1990; Krahenbuhl, 1991; Mustaffa Kamal Shuib, 2009a, 2009b), with most faults that cut the Main Range granites are dated as Cretaceous (Harun, 2002). Reactivation of these faults as sinistral strike slip faults that occurred in the Late Cretaceous are synchronous with the emplacement of granitoids (e.g. Kemahang and Noring Granites, Stong Complex) and the deformation of Jurassic–Cretaceous red bed sequences (Mustaffa Kamal Shuib, 2009b). These granitoid bodies were emplaced in the Cretaceous and are probably the result of this Cretaceous thermo-tectonic event.

Recent thermochronological analyses by M. A. Cottam et al., (2013) of granites from Peninsular Malaysia records a thermal perturbation and significant heating of the crust between ~105 Ma and ~87 Ma. Following previous authors, (e.g. Hall and Morley, 2004; Smyth et al., 2007; Hall, 2009; Clements et al., 2011; Morley, 2012) as Peninsular Malaysia that consists of Sibumasu and Indochina block are the fundamental continental core of Sundaland, M.A. Cottam et al., (2013) interpreted this period of thermal pertubation as the consequences of a major continental collision during Late Cretaceous, when Australian microcontinental fragment(s) collided with the southern margin of Sundaland. Subduction of a cold dense slab along Sundaland margin during Mesozoic probably caused viscous mantle flow that drove regional subsidence during Late Jurassic and Early Cretaceous, creating a dynamic topographic low (DTL) (e. g. Clements et al.,

2011). Termination of subduction by Late Cretaceous would have caused regional uplift and exhumation, with rising mantle adding significant heat into the crust.

Subduction-related igneous-tectonic activity of Late Cretaceous of West Borneo Basement blocks have been found associated with Serabang Formation and near Lupar River (Lupar Line), (Moss, 1998). Collisions between Southern and Northern Sundaland during Early-Late Cretaceous (~130 Ma to ~80Ma) are marked by these suture lines of Serabang and Lupar Line (**Fig. 6.3**). Several authors have presumed the possibility of extrapolation of Lupar and Serabang Line through Natuna Island (Indonesia) and Sundaland region during the Late Cretaceous based on the existence of serpentinite, diabase, tuff, gabbro, diorite and Norite of Bunguran beds of Natuna Island. (Haile, 1970; White and Wing, 1978).
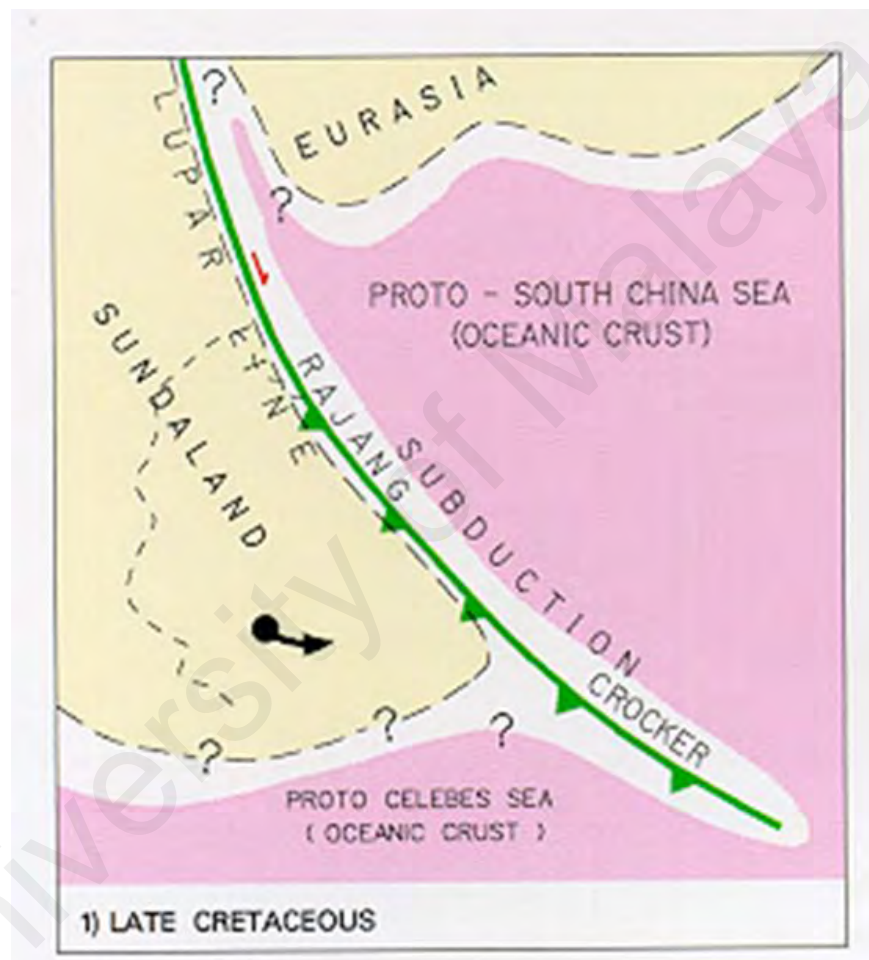
Figure 6.3   Possibility of Lupar Line extension during the Late Cretaceous through Sundaland region (Haile, 1970; White and Wing, 1978)
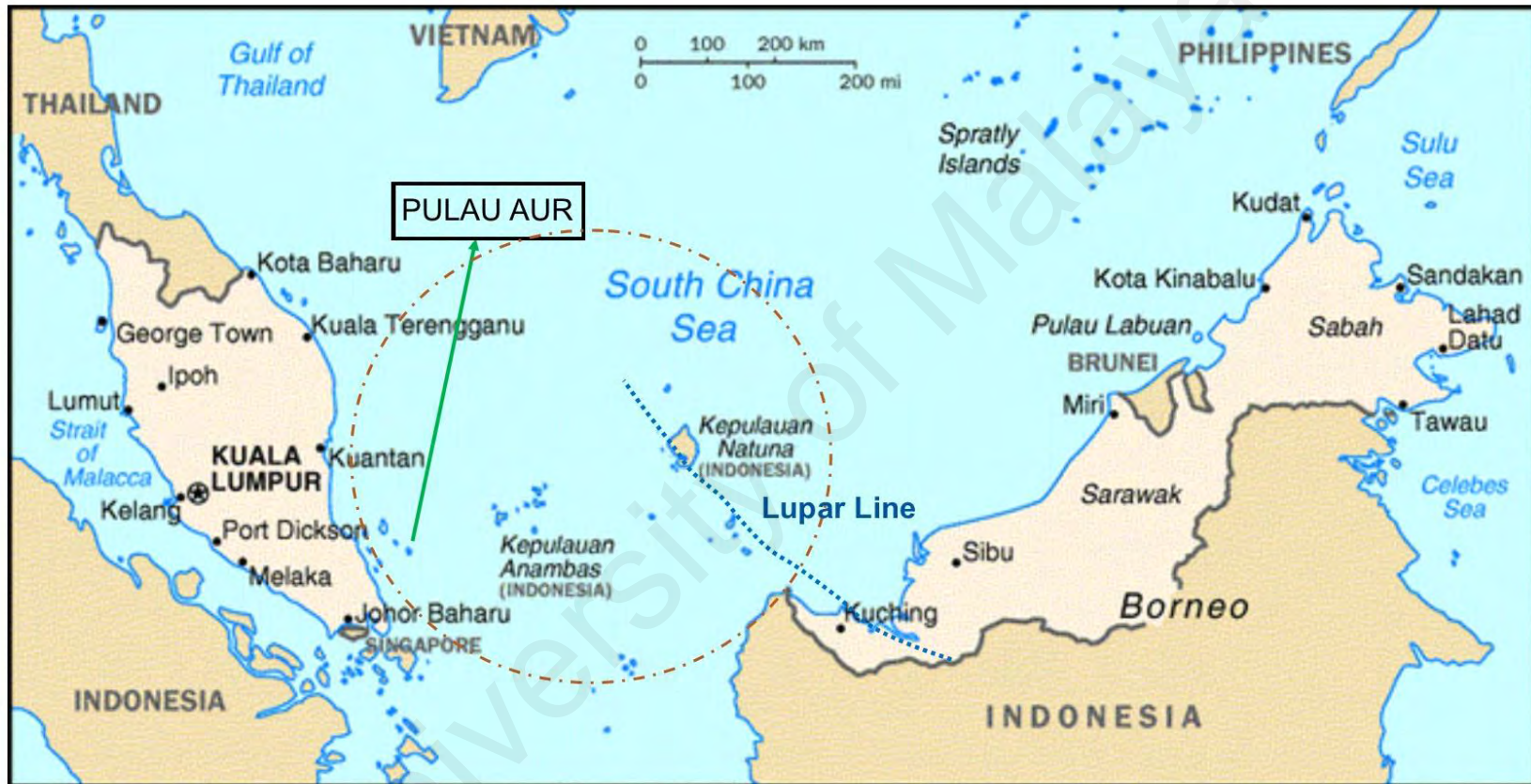
Figure 6.4 Map showing the relative location of the study area, Aur Island, Natuna Islands and the relative extension of Lupar Line
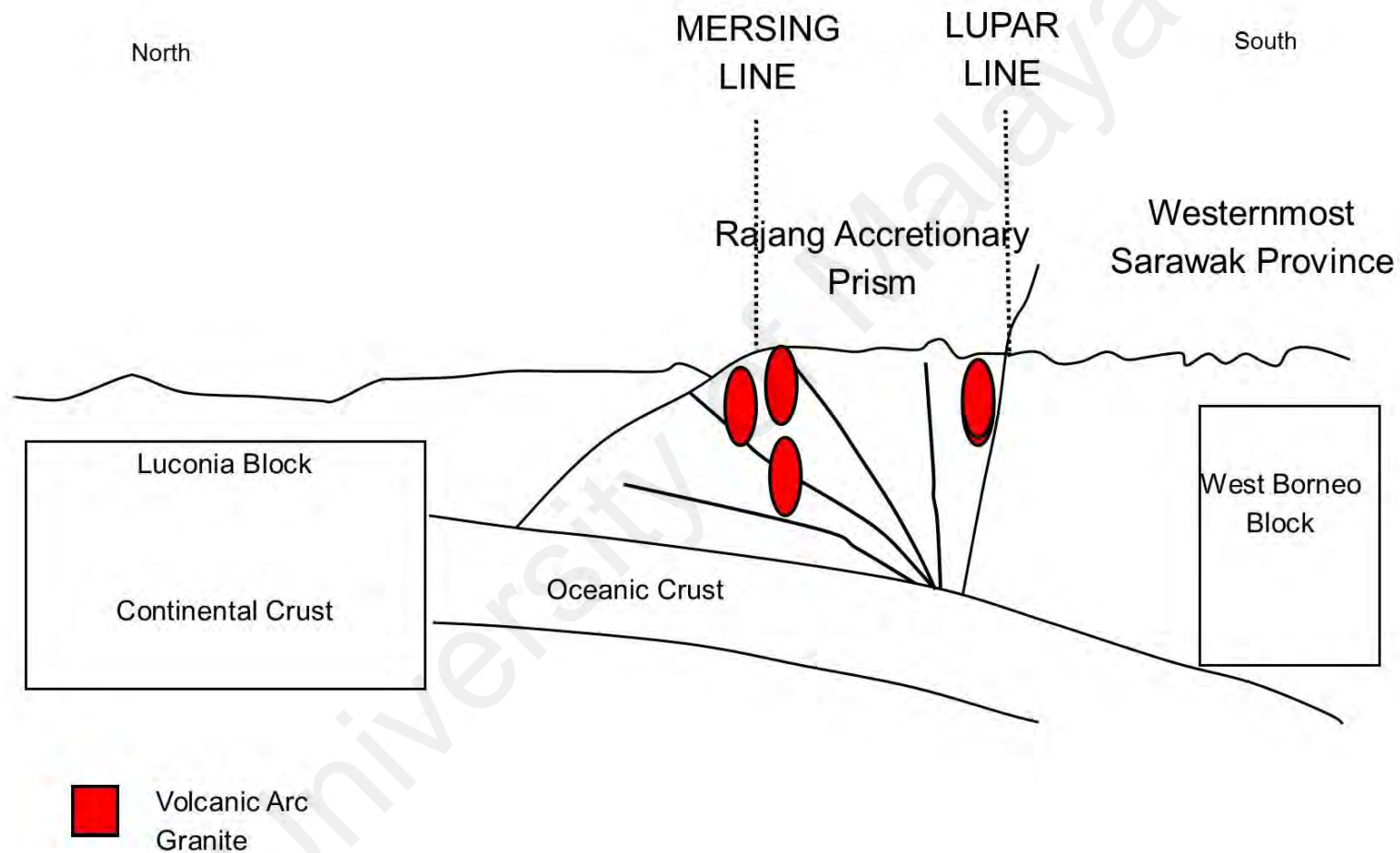
Figure 6.5 Diagrammatic cross section to suggest the plate tectonic model for Early to Late Cretaceous convergent tectonics as collisions between Northern and Southern Luconia and West Borneo Block occurred. Modified after Tjia (2000).

6.5 Conclusions

Based on modal mineralogy and mineral assemblages from petrographic observation, the rocks from study area form two different units; the mafic-end member and the felsic-end member. The magma from which the mafic-end member unit crystallizes are much more mafic, resembling possible mantle source contribution, due to the abundances of clinopyroxene as its major mafic phase. Clinopyroxene is dominant mafic minerals in diorite and quartz monzodiorite, but totally disappears in granodiorite.

The more felsic-end member: granodiorite are more siliceous and richer in alkaline minerals due to the presence of perthite, anti-rapakivi texture, and the increasing abundances and size of quartz and K-feldspar observed in granodiorite. The major mafic phase are made up of hornblende and biotite.

Magma from which the two-end members have crystallised are I-type, coming from igneous source melt, due to the presence of major minerals like: clinopyroxene, hornblende, biotite, and accessory minerals like: sphene and apatite. The anti-rapakivi texture and presence of MME may have suggested that magma mixing and/or mingling processes might have play an important role during the magmatic evolutions of the rocks

From geochemical data, generally, the pluton is I-type, metaluminous, with the mafic-end member showing high-K calc-alkaline trend while the felsic-end member shows shoshonitic trend. Mafic-end members are characterized by higher Fe_2O_3 (6.65-8.32 %) CaO (5.45-7.65 %), MgO (2.91-4.05 %) and the TAS of these mafic-end members are lower, ranging only from 6.41-7.28 %. They are characterised by low concentrations for most trace elements, with an exceptionally higher and variable Sr concentrations: 574.9-1297.6 ppm. Granodiorite have a significantly higher TAS contents: 8.49-8.91 %, having high K_2O concentrations (3.76-4.64 %) compared to mafic-end members (1.76-2.17 %). Granodiorite are also characterized by low Fe_2O_3 (4.7-6.53 %), CaO (2.68-3.86 %) and MgO (1.4-2 %). Most trace elements concentrations are highest in granodiorite: Ba (764-

1134 ppm), Rb (121.7-174.7 ppm), Zr (374.4-450.6 ppm), with a significantly low Sr concentrations (378.8-545 ppm).

A 2% silica gap between both members, different range of major and trace elements concentrations and different trends seen on Harker diagram for major and trace elements suggest that both members are made up of at least two different individual batches of melt. Both members are controlled by different mineral proportions on LIL log plot: (a) mafic-end members: clinopyroxene, hornblende, plagioclase (b) felsic-end member: plagioclase, K-feldspar, biotite.

A multi sources and different origins for both end members can be seen from petrographical data, geochemical plots and classification diagrams, suggesting they were probably made up of individual batches of melt. Geochemistry shows that Pemanggil and Aur dioritic rocks are made up of different sources of magma. However, continuous trend seen for both members on Rb/Sr vs SiO_2, Sr vs CaO and REE patterns suggests that a connection exist between all the rocks at some stage of their magmatic evolution.

All the samples show negative Nb-Ti anomalies, which reflect involvement of subduction related component (Pearce et al., 2005; Hemond et al., 2006). Slab derived fluid is enriched in highly mobile elements (Ba, U, Pb) due to low T dehydration at shallow emplacement levels, and partial melting of mantle metasomatized by such fluid would produce magmas with high Ba/Th ratios of more than 50 (Pearce et al., 2005). This high Ba/Th ratio can be seen in all rock samples, especially for diorite and quartz monzodiorite (61.1-175) and granodiorite (36-82.4)

Geotectonic classification diagram classify the tectonic regime of the dioritic rock as calc-alkaline volcanic arc (VAG) origin. They are characterized by mantle modified by subduction components, selective enrichments in LIL elements, enrichments of K, Rb and Ba relative to Nb, Ce, Zr, Y and the absence of a negative Ba anomaly on a normalised multi-element spider diagram.

Based on petrography and geochemical data, following the tectonic model of Moss (1998), Haile (1970), White and Wing (1978) the writer proposed that it is possible that the Late Cretaceous plutons of Tioman, Pemanggil and Aur Islands which form a linear chain aligned NNW and SSE parallel to one another, could be the far field effects and extrapolation of Lupar and Serabang Line of West Borneo Basement blocks which marked the subduction-related igneous-tectonic activity during the collisions between Southern and Northern Sundaland during Early-Late Cretaceous (~130 Ma to ~80 Ma).(Figure 6.5).

REFERENCES

Ahrens, L. H., Pinson, W.H. & Kearns, M.M., (1952). Association of rubidium and potassium and their abundance in common igneous rocks and meteorites. *Geochem. Acta,* 229- 294p.

Atherton, M. P., (1993). Granite magmatism. *Journal of Geological Society of London* **250**.

Ayre, M., Harris, N. (1997). REE fractionation and Nd-isotope dis-equilibrium during crustal anatexis: constraints from Himalayan leucogranites. *Chemical Geology,* **139**, 249-269.

Barbarin, B., Didier, J. (1992). Genesis and evolution of mafic microgranular enclaves through various types of interaction between co-existing felsic and mafic magmas. *Transactions of the Royal Society of Edinburgh Earth Sciences,* **83**, 145-153.

Barbarin, B., (1999). A review of the relationships between granitoid types, their origins and their geodynamic environments. *Lithos* **46**, 605-626.

Batchelor RA, Bowden P (1985) Petrogenetic interpretation of granitoid rock series using multicationic parameters. *Chem Geol* **48**, 43-55.

Bea, F. (1996). Residence of REE, Y, Th and U in granites and crustal protoliths; implications for the chemistry of crustal melts. *Journal of Petrology,* **37**, 521-552.

Beccaluva, L., Bianchini, G., Bonadiman, C., Siena, F., Vaccaro, C. (2004). Coexisting anorogenic and subduction-related metasomatism in the mantle xenoliths from the Betic Cordillera (southern Spain). *Lithos,* **75**, 67‑87.

Beckinsale, R.D. (1979). Granite magmatism in the Tin belt of Southeast Asia. *In:* Atherton, M.P. & tArney, J. (eds) *Origin of Granite Batholiths: Geochemical Evidence.* Shiva, Nantwich, 34‑44.

Bignell, J.D. & Snelling, N.J. (1977). *Geochronology of Malaysian Granites.* Overseas Geological and Mineral Resources, **47**.

Blundy, J., Wood, B. (2003). Partitioning of trace elements between crystals and melts. *Earth and Planetary Science Letters,* **210**, 383‑397.

Bradshaw, T.K., Smith, E.I. (1994). Polygenetic Quaternary volcanism at Crater Flat, Nevada. *Journal of Volcanology and Geothermal Research,* **63**, 165‑182.

Bonin, B. (2004). Do coeval mafic and felsic magmas in postcollisional to within-plate regimes necessarily imply two contrasting, mantle and crustal, sources? A review. *Lithos* 78:1–24

Cameron, B.I., Walker, J.A., Carr, M.J., Patino, L.C., Matias, O., Feigenson, M.D. (2003). Flux versus decompression melting at stratovolcanos in southeastern Guatemala. *Journal of Volcanology Geothermal Research,* **119**, 21‑50.

Castro, A., Moreno-Ventas, I., De La Rosa, J. (1990). Microgranular enclave as indicators of hybridization processes in granitoid rocks, Hercynian belt, Spain. *Geological Journal*, **25**, 391-404.

Chappell, B.W. (1996). Magma mixing and the production of compositional variation within granite suites: evidence from the granites of southeastern Australia. *Journal of Petrology,* **37**, 449-470.

Chappel, B.W., & White, A. J. (1974). Two contrasting granite types. *Pasific Geology*, **8**, 173-174p.

Chen, Y.D., Price, R.C., White, A.J.R. (1989). Inclusions in three S-type granites from southeastern, Australia. *Journal of Petrology,* **30**, 1181-1218.

Clarke, D. B., (1992). *Granitoid rocks*. Chapman and Hall, London.

Clements, B., Burgess, P.M., Hall, R., Cottam, M.A. (2011). Subsidence and uplift by slab-related mantle dynamics, a driving mechanism for the Cretaceous and Cenozoic evolution of continental SE Asia? In: Hall, R., Cottam, M.A., Wilson, M.E.J. (Eds.), The SE Asian Gateway: History and Tectonics of the Australia-Asia Collision, vol. 355. Geological Society London Special Publications, pp. 37-51.

Cobbing, E.J., Pittfield, P.E.J., Derbyshire, D.P.F. & Mallick, D.I.J. (1992). *The Granites of the Southeast Asian Tin Belt.* Overseas memoirs of the British Geological Survey, **10**.

Cobbing, E.J., Mallick, D.I.J., Pitfield, P.E.J., Teoh, I.H. (1986). The granites of the

Southeast Asian Tin Belt. *Journal of the Geological Society of London* **143**, 537-550.

Cottam, M. A., Hall, R., Ghani, A. A (2013). Late Cretaceous and Cenozoic tectonics of the Malay Peninsula constrained by thermochronology. *Journal of Asian Earth Sciences,* **76**, 241-257.

Darbyshire, D.P.F. (1988). Geochronology of Malaysian granites. NERC Isotope Geological Report, British Geological Survey, **3**, 60 pp.

Davidson, J., Turner, S., Handley, H., Macpherson, C., Dosseto, A. (2007). Amphibole 'sponge' in arc crust? *Geology,* **35**, 787-790.

Didier, J., Barbarin, B. (1991). The different types of enclaves in granites nomenclature. In: Didier, J., Barbarin, B. (Eds.), Enclaves and Granite Petrology Developments in Petrology, **13**, 19-24.

Dorais, M.J., Whitney, J.A., Roden, M.F. (1990). Origin of mafic enclaves in the Dinkey Creek Pluton, Central Sierra Nevada batholith, California. *Journal of Petrology,* **31**, 853-881.

Dunn, T., Sen, C. (1994). Mineral/matrix partition coefficients for orthopyroxene, plagioclase, and olivine in basaltic to andesitic systems: a combined analytical and experimental study. *Geochimica et Cosmochimica Acta,* **58**, 717–733.

Eby, G.N. (1990). The A-type granitoids: a review of their occurrence and chemical characteristics and speculations on their petrogenesis. *Lithos*, **26**, 115-134.

Elburg, M.A., Bergen, M.V., Hoogewerff, J., Foden, J., Vroon, P., Zulkarnain, I., Nasution, A. (2002). Geochemical trends across an arc-continent collision zone: magma sources and slab-wedge transfer processes below the Pantar Strait volcanoes, Indonesia. *Geochimica et Cosmoschimica Acta,* **66**, 2771‑2789.

Frost, T.P., Mahood, G.A., (1987). Field, chemical, and physical constraints on mafic-felsic magma interaction in the Lamark Granodiorite, Sierra Nevada, California. *Geological Society of America Bulletin,* **99**, 272-291.

Frost, B. R., Barnes, C. G., Collins, W. J., Arculus, R. J., Ellis, D. J. & Frost, C. D. (2001). A geochemical classification for granitic rocks. *Journal of Petrology,* **42**, 2033-2048.

Garson, M.S., Young, B., Mitchell, A.H.G & Tait, B.A.R. (1975). *The Geology of the tin belt on Peninsula Thailand around Phuket, Phang-Nga and Takua Pa*. Institute of Geological Sciences, London, Overseas Memoir, **1**, 112.

Ghani, A.A. (2009). Plutonism. *In:* Hutchison, C.S. & Tan, D.N.K.(eds) *Geology of Peninsular Malaysia*. Geological Society of Malaysia, Kuala Lumpur, 211-231.

Gou, J.F., Zhou, M.F. (2013) Magma mixing in the genesis of the Kalatongke dioritic intrusion: Implications for the tectonic switch from subduction to post-collision, Chinese Altay, NW China. *Lithos,* **162-163**, 236-250.

Gromet, L.P., Silver, L.T. (1983). Rare earth elements distribution among minerals in a granodiorite and their petrogenetic implications. *Geochim. Cosmochim. Acta,* **47**, 925-939.

Haile, N. S. (1970). Notes on the geology of the Tambelan, Anambas and Bunguran (Natuna) islands, Sunda Shelf, Indonesia, including radiometric age determinations. *U. N. ECAFE C.C.O.P. Technical Bulletin* **3**, 55-90.

Hall, R., Morley, C.K. (2004). Sundaland Basins. In: Clift, P., Wang, P., Kuhnt, W., Hayes, D.E. (Eds.), Continent-Ocean Interactions within the East Asian Marginal Seas, vol. 149. AGU Geophysical Monograph, Washington, DC, pp. 55–85.

Harris, N.B.W., Pearce, A.J., Tindle, A.G. (1986) in Coward, M.P., Ries, A.C. (Eds) (1986), *Collision Tectonics,* Geological Society Special Publication, 19, pp. 67-81.

Hastie, A. R., Kerr, A. C., Pearce, J. A. & Mitchell, S. F. (2007). Classification of altered volcanic island arc rocks using immobile trace elements: development of the Th-Co discrimination diagram. *Journal of Petrology,* **48,** 2341-2357.

Hawkesworth, C.J., Turner, S.P., McDermott, F., Peate, D.W., van Calsteren, P. (1997). U‑Th isotopes in arc magmas: implications for element transfer from the subducted crust. *Sciences,* **276**, 551‑555.

Hémond, C., Hofmann, A.W., Vlastélic, I., Nauret, F. (2006). Origin of MORB enrichment and relative trace element compatibilities along the Mid-Atlantic Ridge between 10° and 24°N. *Geochemistry Geophysics Geosystems*, **7**, Q12010. doi:10.1029/2006GC001317.

Hoskin, P.W.O., Kinny, P.D., Wyborn, D., Chappell, B.W. (2000). Identifying accessory mineral saturation during differentiation in granitoid magmas: an integral approach.   *Journal of Petrology,* **41**, 1365-1396.

Hutchison, C.S. (1989). *South-East Asian Oil, Gas, Coal and Mineral Deposits*. Oxford Monographs on Geology and Geophysics, **13**.

Hutchison, C.S., & Tan, D.N.K. (2009). *Geology of Peninsular Malaysia*. University of Malaya, Geological Society of Malaysia, Kuala Lumpur.

Irvine, T. N. & Baragar, W. R. A. (1971). A guide to the chemical classification of the common volcanic rocks. *Canadian Journal of Earth Sciences,* **8,** 523-548.

Jian-Wei, L., Xin-Fu, Z., Mei-Fu, Z., Chang-Qian, Ma., Sergio de Souza, Z., Vasconcelos, P. (2009), Late Mesozoic magmatism from the Daye region, Eastern China: U-Pb ages, petrogenesis and geodynamic implications. *Contributions to Mineralogy and Petrology,* **157**, 383-409.

Krahenbuhl, R. (1991) Magmatism, tin mineralization and tectonics of the Main Range, Malaysian Peninsula: consequences for the plate tectonic model of Southeast Asia based on Rb-Sr, K-Ar and fission track data. *Bulletin of the Geological Society of Malaysia* **29**, 1-100.

Kumar, S., Rino, V., Pal, A.B. (2004). Field evidence of magma mixing from microgranular enclaves hosted in Palaeoproterozoic Malanjkhand granitoids, central India. *Gondwana Research*, **7**, 539-548.

Kumar, S. (1995). Microstructural evidence of magma quenching inferred from enclaves hosted in the Hodrusa granodiorites, Western Carpathians. *Geologica Carpathica*, **46**, 379-382.

Lameyre, J., Bonin, B. (1991). Granites in the main plutonic series. In: Didier, J., Barbarin, B. (Eds.), Enclaves and Granite Petrology Developments in Petrology, **13**, 3-17.

Lameyre, J., Bowden, P. (1982). Plutonic rock type series: discrimination of various granitoids series and related rocks. *Journal of Volcanology and Geothermal Research,* **14**, 169-186.

Lee, C. P. (2009). Paleozoic stratigraphy. In: Hutchison C. S., D.N.K. (Eds), Geology of Peninsular Malaysia. University of Malaya and the Geological Society of Malaysia, 55-85.

Liang, Qi., Jing, Hu., Conrad Gregoire, D. (2000). Determination of trace elements in granites by inductively coupled plasma mass spectrometry. *Talanta,* **51**, 507-513.

Liew, T.C., McCulloch, M.T. (1985). Genesis of granitoid batholiths of Peninsular Malaysia and implications for models of crustal evolution: evidence from Nd-Sr isotopic and U–Pb zircon study. *Geochimica et Cosmochimica Acta*, **49**, 587-600.

Liew, T.C., Page, R.W. (1985). U–Pb zircon dating of granitoid plutons from the west coast province of Peninsular Malaysia. *Journal of the Geological Society of London*, **142**, 515–526.

Liu HT, Sun SH, Liu JM, Zhai MG (2009). The Mesozoic high-Sr granitoids in the northern marginal region of North China craton: geochemistry and source region. *Acta Petrol Sin* **18**, 257–274.

Maniar, P.D. & Piccoli, P.M. (1989). Tectonic discriminations of granitoids. *Geological Society of America Bulletin,* **101,** 635-643.

McKay, G.A. (1986). Crystal/liquid partitioning of REE in basaltic systems: extreme fractionation of REE in olivine. *Geochimica et Cosmochimica Acta,* **50**, 69–79.

Metcalfe, I. (1998). Palaeozoic and Mesozoic geological evolution of the SE Asian region: multidisciplinary constraints and implications for biogeography. In: Hall, R., Holloway, J.D. (Eds.), Biogeography and Geological Evolution of SE Asia. Backhuys Publishers, Amsterdam, The Netherlands, 25-41.

Metcalfe, I. (2000). The Bentong-Raub Suture Zone. *Journal of Asian Earth Sciences* **18**, 691-712.

Metcalfe, I. (2011). Tectonic framework and Phanerozoic evolution of Sundaland. *Gondwana Research* **19**, 3-21.

Metcalfe, I. (2013). Tectonic evolution of the Malay Peninsula. *Journal of Asian Earth Sciences* **76**, 196-213.

Metcalfe, I. (2013). Gondwana dispersion and Asian accretion: Tectonic and palaeogeographic evolution of eastern Tethys. *Journal of Asian Earth Sciences* **66**, 1-33.

Miller, C.F., Mittlefehldt, D.W. (1984). Extreme fractionation in felsic magma chambers; a product of liquid-state diffusion or fractional crystallisation? *Earth and Planetary Science Letters,* **68**, 151-158.

Mitchell, A.H.G. (1977). Tectonic settings for the emplacement of the Southeast Asian tin granites. *Geological Society of Malaysia Bulletin*, **9**, 123‑140.

Mohd. Basri Abdul Hamid, (2002). *Kajian Petrologi dan Geokimia Selatan Pulau Pemanggil, Mersing, Johor Darul Takzim.* Unpublished B. Sc. Thesis, University Malaya.

Mohd. Rozi Umor, (2009). Petrogenesis dan Geokimia Batuan Igneous Jalur Tengah Semenanjung Malaysia. Published PhD thesis, University Malaya.

Moorhouse, W.W. (1959). The Study of Rocks in Thin Section: Harper and Bros., New York, 514.

Morley, C.K. (2012). Late Cretaceous–Early Palaeogene tectonic development of SE Asia. *Earth Science Reviews*, **115**, 37–75.

Moss, S. J. (1998), Embaluh Group turbidites in Kalimantan: evolution of a remnant oceanic basin in Borneo during the Late Cretaceous and Paleogene. *Journal of the Geological Society of London,* **155**, 509-524.

Muhamad Marzuki Asmuri, (2002). *Kajian Lapangan, Petrologi dan Geokimia di Utara Pulau Pemanggil, Mersing, Johor Darul Takzim.* Unpublished B. Sc. Thesis, University Malaya.

Mustaffa Kamal Shuib (2009). Structures and deformation. In: Hutchison C.S. and Tan D.N.K. (Eds.), Chapter 13, Geology of Peninsular Malaysia. University of Malaya and the Geological Society of Malaya. 271-308.

Nakamura, N. (1974). Determination of REE, Ba, Fe, Mg, Na and K in carbonaceous and ordinary chondrites. *Geochim. Cosmochim. Acta.* **38**, 757-773.

Nielsen, R.L., Gallahan, W.E., Newberger, F. (1992). Experimentally determined mineral melt partition coefficients for Sc, Y and REE for olivine, orthopyroxene, pigeonite, magnetite and ilmenite. *Contributions to Mineralogy and Petrology,* **110**, 488-499.

Oliver, G., et al., (2013) U-Pb zircon geochronology of Early Permian to Late Triassic rocks from Singapore and Johor: A plate tectonic reinpretation, *Gondwana Research,* **26**, 132-143.

Peacock, M. A., (1931). Classification of igneous rock series: *Journal of Geology*, **39**, 54-67p.

Pearce, J.A. (1983). Role of the sub-continental lithosphere in magma genesis at active continental margins. In: Hawkesworth, C.J., Norry, N.J. (Eds.), Continental Basalts and Mantle Xenoliths. Shiva, Cheshire, UK, pp. 230-249.

Pearce, J. A., Harris, N. W. & Tindle, A. G. (1984). Trace element discrimination diagrams for the tectonic interpretation of granitic rocks. *Journal of Petrology,* **25,** 956-983.

Pearce, J.A., Stern, J.R., Bloomer, S.H., Fryer, P. (2005). Geochemical mapping of the Mariana arc-basin system: Implications for the nature and distribution of the subduction components. *Geochemistry Geophysics Geosystems*, **6***, Q07006. doi:10.1029/2004GC00895.

Peccerillo, A. & Taylor, S. R. (1976). Geochemistry of Eocene calc-alkaline volcanic rocks from the Kastamonu area, Northern Turkey. *Contributions to Mineralogy and Petrology,* **58,** 63-81.

Poli, G.E., Tommasini, S. (1991). Model for the origin and significance of microgranular enclaves in calc-alkaline granitoids. *Journal of Petrology*, **32**, 657-666.

Rollinson, H.R. (1993). *Using Geochemical Data: Evaluation, Presentation, Interpretation*. Longman, New York. 352p.

Sawka, W.N. (1988). REE and trace element variations in accessory minerals and hornblende from the strongly zoned McMurry Meadows Pluton, California. *Trans, Roy. Soc. Edinb., Earth Sci,* **79**, 157-168.

Schaff, R. G., Blum, J. D., Wunnicke, E., Sheffield B. (1983). Petrology, Geochemistry, and Isotope Geochronology of the Gilmore Dome and Pedro Dome Plutons, *Alaska Report of Investigations,* 83-2.

Schandl, E.S., Gorton, M.P. (2002). Application of high field strength elements to discriminate tectonic settings in VMS environments. *Economic Geology,* **97,** 629-642.

Searle, M.P., Whitehouse, M.J., Robb, L.J., Ghani, A.A., Hutchison, C.S., Sone, M., Ng, S.W.P., Roselee, M.H., Chung, S.L., Oliver, G.J.H. (2012) Tectonic evolution of Sibumasu-Indochina terrane collision zone in Thailand and Malaysia-constraints from new U-Pb zircon chronology of SE Asian tin granitoids. *Journal of the Geological Society London,* **169**, 489–500.

Sevastjanova, I., Clements, B., Hall, R., Belousova, E. A., Griffin, W.L., Pearson, N. (2011). Granitic magmatism, basement ages, and provenance indicators in the Malay Peninsula: Insights from detrital zircon U-Pb and Hf-isotope data. *Gondwana Research,* **19**, 1024-1039.

Shand, S. J., (1943). *Eruptive rocks. Their genesis, composition, classification and their relation to ore deposits*. 3rd edition. New York, Wiley & Sons.

Shelley, D., 1992. Igneous and metamorphic rocks under microscopes: classification, textures, microstructures and mineral preferred orientations. Chapman and Hall, 445p.

Sheth, H. C., Ignacio, S., Alvarado, T., Surendra, V.P., (2002)., What is the calc alkaline rock series*? International Geology Review*, Vol. 44, 686–701p.

Smith, E.I., Sanchez, A., Walker, J.D., Wang, K. (1999). Geochemistry of mafic magmas in the Hurricane Volcanic field, Utah: implications for small- and large- scale chemical variability of the lithospheric mantle. *Journal of Geology,* **107**, 433-448.

Smyth, H.R., Hamilton, P.J., Hall, R., Kinny, P.D. (2007). The deep crust beneath island arcs: inherited zircons reveal a Gondwana continental fragment beneath East Java. *Earth and Planetary Science Letters*, **258**, 269–282.

Streckeisen, A. L. (1976). To each plutonic rock its proper name. *Earth Science Review*, **12**, 1-33.

Sun, S.S., McDonough, W.F. (1989). Chemical and isotopic systematics of oceanic basalts: implications for mantle composition and processes. In: Saunders, A.D., Norry, M.J. (Eds.), Magmatism in Ocean Basins Geological Society of London Special Publication 42, pp. 313–345.

Sone, M. & Metcalfe, I. (2008). Parallel Tethyan sutures in mainland Southeast Asia: new insights for the Palaeo-Tethys closure and implications for the Indosinian orogeny. *Comptes Rendus, Géoscience*, **340**, 166–179.

Tan S. B., (1977). *Geology and Geochemical Studies of Pulau Aur, Pulau Pemanggil and the Southern Rim of Pulau Tioman including the adjacent seafloor, Johore-Pahang.* Unpublished B. Sc. Thesis, University Malaya.

Tate, R.B., Tan, D.K., Ng, T.F. (2008). Geological Map of Peninsular Malaysia. In: Hutchison C.S. and Tan D.N.K. 2009 (Eds.), *Geology of Peninsular Malaysia*. University of Malaya and the Geological Society of Malaya. 479.

Tjia, H. D. (2000). Tectonic and Structural Development of Cenozoic Basins of Malaysia *Geological Society of Malaysia Annual Geological Conference* 2000 September 8-9 2000.

Vernon, R.H., Johnson, S.E. and Melis, E.A. (2004). Emplacement-related microstructures in the margin of a deformed pluton: the San Jose tonalite, Baja, California, Mexico. *Journal of Structural Geology*, **26**, 1867-1884.

Vernon, R.H. (1983). Restite, xenoliths and microgranitoid enclave in granites. *Journal and Proceedings of the Royal Society of New South Wales,* **116**, 77-103.

Watson, E.B., Harrison, T.M. (1983). Zircon saturation revisited: temperature and composition effects in a variety of crustal magma types. *Earth and Planetary Science Letters,* **64**, 295‑304.

Watt, G.R., Harley, S.L. (1993). Accessory phase controls on the geochemistry of crustal melts and restites produced during water-undersaturated partial melting. *Contributions to Mineralogy and Petrology,* **114**, 550-566.

White, A.J.R., Chappell, B.W. (1977). Ultrametamorphism and granitoid genesis. *Tectonophysics,* **43**, 7-22.

White, A. J. R. and Wing, R. S. (1978. Structural development of the South China Sea with particular reference to Indonesia. *Proceedings of the 7ᵗʰ annual convention Indonesian petroleum association*, Jakarta, 159-164.

Willbourn, E. S. (1926-1927). The Beatrice Mine, Sebilin, Federated Malay States. *Mineralogical Magazine,* **35**, 329-338; **36**, 9-15.

Williams, H., Turner, F.J., Gilbert, C.M. (1974). Petrography. San Fransisco, W. H. Freeman, 406.

Wilson, M., (2007). *Igneous Petrogenesis*. Chapman & Hall, London, p. 411.

Wyborn, D., Chappell, B.W., James, M. (2001). Examples of convective fractionation in high-temperature granites from the Lachlan Fold Belt, *Australian Journal of Earth Sciences*, **48:4**, 531-541.